


This item was submitted to Loughborough University as a PhD thesis by the author and is made available in the Institutional Repository (<https://dspace.lboro.ac.uk/>) under the following Creative Commons Licence conditions.




creative commons  
COMMONS DEED


**Attribution-NonCommercial-NoDerivs 2.5**


**You are free:**

- to copy, distribute, display, and perform the work

**Under the following conditions:**

 **Attribution.** You must attribute the work in the manner specified by the author or licensor.


 **Noncommercial.** You may not use this work for commercial purposes.

 **No Derivative Works.** You may not alter, transform, or build upon this work.

- For any reuse or distribution, you must make clear to others the license terms of this work.
- Any of these conditions can be waived if you get permission from the copyright holder.

**Your fair use and other rights are in no way affected by the above.**

This is a human-readable summary of the [Legal Code \(the full license\)](#).

[Disclaimer](#) 

For the full text of this licence, please go to:  
<http://creativecommons.org/licenses/by-nc-nd/2.5/>

**The Effect of Transient Dynamics of the Internal  
Combustion Compression Ring upon its Tribological  
Performance**

*By*

**Christopher E. Baker B.Eng. (Hons.)**

**Thesis submitted in partial fulfilment of the  
requirements for the Degree of Doctor of  
Philosophy**

**Loughborough University**

**Wolfson School of Mechanical and  
Manufacturing Engineering**

**Autumn 2013**



**Dedicated to my Mum and Dad, for everything.**

## **Abstract**

The losses in an internal combustion engine are dominated by thermal and parasitic sources. The latter arises from mechanical inefficiencies inherent within the system, particularly friction in load bearing conjunctions such as the piston assembly. During idle and at low engine speeds, frictional losses are the major contributor to the overall engine losses as opposed to the dominant contribution of thermal losses under other driving conditions. Given the relatively small size and simple structure of the top compression ring, it has a disproportionate contribution to the total frictional losses. This suggests further analysis would be required to understand the underlying causes of compression ring behaviour throughout the engine cycle. The available literature on tribological analyses of compression rings does not account for the transient ring elastodynamics. They usually assume a rigid ring for film thickness and power loss predictions, which is not representative of the ring's dynamic response. A combined study of ring elastodynamic behaviour and its tribological conjunction is a comprehensive approach.

Literature regarding incomplete ring dynamics has been available since the 1960s. However, most research contributions only provide predictions of mode shapes and natural frequencies. Furthermore, the complete ring dynamics under forcing conditions is rarely discussed. The thesis presents the methodology for the full ring elastodynamic response, both in-plane and out-of-plane (axial). The theory behind the coupling of ring dynamics and tribology is also developed and outlined. Transient tribodynamic results are then compared with those of a rigid ring. The effect of variation in engine speed is also discussed, as well as the variation with lubricant temperature. Where possible, verification of the numerical analysis is presented, comparing the predictions with experimental results and other published results. The comparisons show good correlation of the presented numerical methodology, verifying and confirming the aims set out at the start of the thesis. The thesis contributions to knowledge include combined ring elastodynamics and transient mixed thermo-hydrodynamics. The comprehensive combined experimental/numerical approach presented in the thesis is also novel.

**Keywords:** Internal Combustion engine, Compression ring, Elastodynamics, Transient tribology

## Acknowledgements

I would like to thank my supervisors, Professor Homer Rahnejat and Dr Stephanos Theodossiades, for their invaluable supervision, support, advice and encouragement throughout my research.

I acknowledge the EPSRC for their financial support, without which this research would not have been possible. I am grateful to the industrial and academic participants of the Encyclopaedic project, for contributing to an interesting and challenging endeavour.

Particular thanks go to Professor Brian Fitzsimons of Aston Martin Lagonda for providing the engine data for modelling purposes, Dr Sebastian Howell-Smith from Prodrive for the materials used in experimental analysis, and to Dr Chris Warrens of BP Castrol for the lubricant data and company insight.

I am grateful to Dr Ramin Rahmani for his support and advice throughout my research, his experience in numerical analysis was a huge help. Thanks also to Mike Theaker, for providing the experimental data in this thesis.

Finally, a massive thank you goes to my family, friends and loved ones, for their patience, understanding and support throughout my research.

## Contents

Abstract.....	ii
Acknowledgements.....	iii
Contents.....	iv
List of Figures .....	vii
List of Tables .....	xiv
Nomenclature .....	xv
Subscripts .....	xviii
Glossary of Terms .....	xix
1. Introduction.....	1
1.1. Preamble .....	1
1.2. Project overview.....	5
1.3. Aim and objectives .....	8
1.3.1. Contributions to Knowledge .....	8
1.4. Structure of the thesis.....	9
2. Literature Review .....	11
2.1. Preamble .....	11
2.2. Tribology.....	11
2.2.1. Boundary and Mixed Lubrication.....	14
2.3. The Dynamics of Incomplete Rings .....	15
2.4. Tribological Analysis of Compression Rings .....	19
2.4.1. Conformability and lubrication along the Compression Ring.....	20
2.4.2. Friction and Lubrication Concerns within the Ring-Cylinder Contact .....	23
2.4.3. Surface Roughness, Modification and Topography.....	25
2.5. Closure.....	27

3.	Compression Ring Dynamics .....	28
3.1.	Introduction.....	28
3.2.	Ring In-plane Dynamic Response .....	28
3.3.	Ring Out-of-plane Dynamic Response .....	40
3.4.	Coupling of the Ring Dynamics Methodology to the Tribological Analysis .....	51
3.5.	Closure.....	57
4.	Tribology of the compression ring.....	58
4.1.	Introduction.....	58
4.2.	Lubrication and Lubricant Rheology .....	58
4.2.1.	Regimes of Lubrication .....	58
4.2.2.	Parameters Affecting Lubricant Properties .....	59
4.3.	The Reynolds Equation.....	61
4.3.1.	Derivation of the Reynolds Equation.....	61
4.3.2.	Solving the Reynolds Equation .....	64
4.4.	The Energy Equation .....	66
4.4.1.	Convection Only.....	68
4.4.2.	Conduction Only .....	68
4.4.3.	The Peclet Number .....	68
4.5.	Asperity Interaction.....	70
4.6.	Method of Solution .....	71
4.7.	Closure.....	73
5.	Tribodynamic Numerical Analysis of the Top Compression Ring.....	75
5.1.	Introduction.....	75
5.2.	Rigid Ring Tribology.....	75
5.3.	Quasi-static ring deformation .....	79
5.4.	In-plane transient ring dynamics .....	81

## Contents

---

5.5.	Ring dynamics in two planes .....	88
5.6.	Closure.....	116
6.	Verification of the Numerical Methodology .....	118
6.1.	Introduction.....	118
6.2.	Results available in the Literature.....	118
6.3.	Experimental Validation .....	124
6.4.	Film Thickness Measurement .....	126
6.5.	Friction Measurement.....	131
6.5.1.	Motored Case.....	133
6.5.2.	Engine fired case .....	138
6.6.	Closure.....	145
7.	Conclusions.....	146
7.1.	Overall conclusions .....	146
7.2.	Achievement of aims.....	147
7.3.	Contributions to Knowledge .....	148
7.4.	Suggestions for future work.....	149
8.	References .....	152
9.	Appendices .....	163
9.1.	Appendix A – SAE technical paper .....	163
9.2.	Appendix B – STLE Annual Conference extended abstract.....	178
9.3.	Appendix C – ASME journal paper .....	186



**List of Figures**

Figure 1.1: Greenhouse Gas Emissions for leading nations in 1990 and 2010. Data from UNFCCC report, 2012 ([www.unfccc.int](http://www.unfccc.int)) ..... 1

Figure 1.2: Global transport carbon dioxide emissions in 2000 (King, 2007)..... 3

Figure 1.3: Average CO<sub>2</sub> emissions from new cars and cars in use in the UK (King, 2007) ..... 3

Figure 1.4: Typical piston and ring-pack assembly ([http://confident-instruments.com/images/piston\\_assy\\_sectioned\\_anno.JPG](http://confident-instruments.com/images/piston_assy_sectioned_anno.JPG)) ..... 6

Figure 1.5: A typical Stribeck Curve ..... 7

Figure 2.1: The degrees of freedom used by Lang (1962) ..... 16

Figure 2.2: Degrees of freedom used by Ojalvo (1962) ..... 17

Figure 2.3: Diagram of the ring within the groove, highlighting ring twist (Tian, 2002a) ..... 18

Figure 2.4: Blow-by in a poor fitting cylinder bore (Andersson et al, 2002) ..... 21

Figure 2.5: An exaggerated example of bore cross-section deformation (Tomanik, 1996).... 22

Figure 3.1: a) In-plane degrees of freedom of an incomplete ring and ..... 29

Figure 3.2: Mode shape comparison (a) Analytical ( $f = 972.06\text{Hz}$ ) and (b) FEA ( $f=969.76\text{Hz}$ ). 34

Figure 3.3: FEA versus numerical analysis ring deflection. Results correspond to the displacement of a point opposite the ring gap, with an excitation frequency of (a): 300Hz, and (b): 3500Hz..... 38

Figure 3.4: FEA versus numerical analysis FFT. Results correspond to a point opposite the ring gap, with an excitation frequency of 300Hz. (a): FEA data, and (b): numerical data ..... 39

Figure 3.5: Out-of-plane ring motion, exhibiting the relevant degrees of freedom (Ojalvo, 1962) ..... 41

Figure 3.6: Out-of-plane ring mode shape comparison, (a) Analytical method ( $f = 93.33\text{Hz}$ ) and (b) FEA model ( $f=93.33\text{Hz}$ ). ..... 46

Figure 3.7: Out-of-plane rigid body mode shapes ..... 47

Figure 3.8: FEA and Numerical response when circumferentially constant load is applied. Max. Load equivalent = 10kPa, frequency of excitation = 700Hz. .... 48

Figure 3.9: Numerical and FEA response for the force profile of equation (55) at (a) the ring gap and (b) part-way around the ring. The excitation frequency is 700Hz..... 49

Figure 3.10: FEA versus numerical analysis FFT. Results correspond to a point opposite the ring gap, excitation frequency = 700Hz (a) numerical, (b) FEA ..... 50

Figure 3.11: Cross-sectional free body diagram of the top compression ring. ....	51
Figure 3.12: Coupled in-plane tribo-dynamics algorithm.....	54
Figure 3.13: Coupled tribo-dynamics algorithm for both planes of motion .....	56
Figure 4.1: Principle of the wedge film (Gohar and Rahnejat, 2008) .....	61
Figure 4.2: Forces on a unit element of fluid (Balakrishnan, 2002).....	62
Figure 4.3: Cross-section diagram of the compression ring-cylinder liner conjunction, highlighting the forces present.....	65
Figure 4.4: Temperature distribution at the contact (Gohar and Rahnejat, 2008).....	67
Figure 4.5: Average temperature rise throughout the engine cycle for a rigid ring analysis..	70
Figure 4.6: Flowchart of the solution procedure.....	73
Figure 5.1: Gas pressure profiles at given engine speeds .....	76
Figure 5.2: Minimum film thickness variation (rigid ring analysis) at various engine speeds.	78
Figure 5.3: Total friction power loss variation (rigid ring analysis) at various engine speeds.	78
Figure 5.4: Lubricant mass flow rate variation (rigid ring analysis) at various engine speeds	78
Figure 5.5: Force profile and corresponding Fourier series .....	79
Figure 5.6: Film profile and ring deflection at various crank angle intervals around the TDC and firing point (engine speed = 2000rpm) .....	80
Figure 5.7: Minimum film thickness comparison of rigid and elastic ring analysis.....	82
Figure 5.8: Frictional power loss comparison of rigid and elastic ring analysis .....	82
Figure 5.9: Lubricant mass flow rate comparison of rigid and elastic ring analysis at ring's middle cross section. Temperature = 40°C.....	83
Figure 5.10: Circumferential and axial profiles of the lubricant pressure and film shape at points A and B of figure 7 .....	83
Figure 5.11: Effect of engine speed on the minimum film thickness predictions for both rigid and in-plane elastic ring analysis .....	84
Figure 5.12: Effect of engine speed on frictional power loss predictions for both rigid and elastic ring analysis .....	84
Figure 5.13: Effect of engine speed on lubricant flow rate predictions for both rigid and elastic ring analysis .....	85
Figure 5.14: Effect of lubricant temperature on the minimum film thickness at different engine speeds for both rigid and elastic analysis. Lubricant temperature = 80°C.....	86
Figure 5.15: Effect of temperature on the minimum film thickness (elastic ring analysis). ...	86

Figure 5.16: Effect of temperature on friction power loss (elastic ring analysis) .....87

Figure 5.17: Effect of temperature on lubricant mass flow rate (elastic ring analysis) .....87

Figure 5.18: Power loss comparison between rigid and in-plane elastic ring analysis, with respect to oil temperature and engine speed .....88

Figure 5.19: Twist of a worn ring’s axial profile .....89

Figure 5.20: Minimum film thickness comparisons for the rigid, in-plane and full dynamic analyses at 1000rpm, lubricant temperature = 40°C .....90

Figure 5.21: Total friction power loss comparisons for the rigid, in-plane and full dynamic analyses at 1000rpm, lubricant temperature = 40°C .....90

Figure 5.22: Minimum film thickness comparisons for the rigid, in-plane and full dynamic analyses at 1500rpm, lubricant temperature = 40°C .....91

Figure 5.23: Total friction power loss comparisons for the rigid, in-plane and full dynamic analyses at 1500rpm, lubricant temperature = 40°C .....91

Figure 5.24: Minimum film thickness comparisons for the rigid, in-plane and full dynamic analyses at 2000rpm, lubricant temperature = 40°C .....92

Figure 5.25: Total friction power loss comparisons for the rigid, in-plane and full dynamic analyses at 2000rpm, lubricant temperature = 40°C .....92

Figure 5.26: Minimum film thickness comparisons for the rigid, in-plane and full dynamic analyses at 1500rpm, lubricant temperature = 80°C .....93

Figure 5.27: Minimum film thickness comparisons for the rigid, in-plane and full dynamic analyses at 2000rpm, lubricant temperature = 80°C .....94

Figure 5.28: Minimum film thickness comparisons for the rigid, in-plane and full dynamic analyses at 2000rpm, lubricant temperature = 120°C .....94

Figure 5.29: Compression ring motion within the groove throughout the engine cycle. Engine speed = 1500rpm .....95

Figure 5.30: Compression ring 3D profiles at different stages of the engine cycle. Engine speed = 1500rpm .....96

Figure 5.31: The 3D profile when the ring of forced from the groove face due to combustion pressure, even when the piston is increasing in axial velocity. This causes a larger ring deformation (note the scale). Engine speed = 1000rpm, lubricant temperature = 40°C .....97

Figure 5.32: The effect of lubricant temperature on film thickness with a fully dynamic ring. Engine speed = 1500rpm .....98

Figure 5.33: The effect of lubricant temperature on film thickness with a fully dynamic ring. Engine speed = 2000rpm .....98

Figure 5.34: The effect of lubricant temperature on Friction Power Loss with a fully dynamic ring. Engine speed = 2000rpm .....99

Figure 5.35: The effect of engine speed on film thickness with a fully dynamic ring. Lubricant temperature = 80°C .....99

Figure 5.36: Ring displacement throughout the engine cycle. Engine speed = 1500rpm, lubricant temperature = 120°C.....100

Figure 5.37: The effect of engine speed on film thickness with a fully dynamic ring. Lubricant temperature = 120°C .....101

Figure 5.38: The effect of engine speed on friction power loss with a fully dynamic ring. Lubricant temperature = 120°C .....101

Figure 5.39: The effect of engine speed on film thickness with a rigid ring. Lubricant temperature = 120°C .....102

Figure 5.40: The effect of engine speed on friction power loss with a rigid ring. Lubricant temperature = 120°C .....102

Figure 5.41: Modified new ring axial profile to represent a ring part-way through its life cycle .....103

Figure 5.42: Film thickness results using an ‘intermediate’ ring profile. Lubricant temperature = 120°C .....103

Figure 5.43: Power Loss results using an ‘intermediate’ ring profile. Lubricant temperature = 120°C.....104

Figure 5.44: New and worn ring axial profiles .....104

Figure 5.45: Minimum film thickness results for the elastic analysis comparing new and worn ring profiles. Lubricant temperature = 40°C.....105

Figure 5.46: Frictional power loss results for the elastic analysis comparing new and worn ring profiles. Lubricant temperature = 40°C.....106

Figure 5.47: Comparisons between rigid and elastic results for a new and worn ring. Lubricant temperature = 80°C, engine speed = 2000rpm .....107

Figure 5.48: Comparison between new and worn ring results. Engine speed = 4000rpm, lubricant temperature 120°C.....108

Figure 5.49: Comparison between new and worn ring results. Engine speed = 6000rpm, lubricant temperature 120°C.....108

Figure 5.50: Comparison between worn ring power loss results at various engine speeds. Lubricant temperature 120°C.....109

Figure 5.51: Power loss comparison between rigid, in-plane and fully dynamic elastic ring analysis, with respect to oil temperature and engine speed .....110

Figure 5.52: Stribeck curve comparisons between rigid and elastic ring analysis. Engine speed = 1000rpm, temperature = 40°C.....111

Figure 5.53: Stribeck curve comparisons between rigid and elastic ring analysis. Engine speed = 2000rpm, temperature = 40°C.....112

Figure 5.54: Stribeck curve comparisons between rigid and elastic ring analysis at higher temperatures. Engine speed = 2000rpm, temperature = 120°C.....113

Figure 5.55: Friction coefficient contributions from viscous and asperity losses, for a rigid ring. Engine speed = 1000rpm, temperature = 40°C.....114

Figure 5.56: Friction coefficient contributions from viscous and asperity losses, for an elastic ring. Engine speed = 1000rpm, temperature = 40°C.....114

Figure 5.57: Friction coefficient contributions from viscous and asperity losses, for a rigid ring. Engine speed = 2000rpm, temperature = 120°C.....115

Figure 5.58: Friction coefficient contributions from viscous and asperity losses, for an elastic ring. Engine speed = 2000rpm, temperature = 120°C.....115

Figure 5.59: Stribeck curve comparisons between new and worn ring analyses, for a fully dynamic ring. Lubricant temperature = 40°C .....116

Figure 6.1: Predicted time-averaged temperature distributions on the cylinder liner wall (Nikian et al, 2006).....119

Figure 6.2: Experimental data in comparison with the presented methodology (2000rpm). .....120

Figure 6.3: Experimental data in comparison with the presented methodology (2400rpm). .....120

Figure 6.4: Comparison between experimental data (Takiguchi (2000)) and rigid ring, in-plane and full dynamic analysis. Engine speed = 2000rpm, lubricant temperature = 120°C121

Figure 6.5: Ring displacement throughout the engine cycle, alongside ring axial velocity and cylinder gas pressure. Engine speed = 1500rpm, lubricant temperature = 120°C.....122

Figure 6.6: Compression ring lift through TDC from an FEA model (Kurbet and Kumar, 2004). The trend shown is the same as predicted by the numerical model .....122

Figure 6.7: (a) – Experimental schematic diagram and (b) results of the measured groove position of the second compression ring (Takiguchi, 2000).....123

Figure 6.8: The ultrasonic transducer attached to the wet side of the liner (Avan et al, 2010) .....126

Figure 6.9: Oil film measurement between the ring and the liner. The sensor’s size means an ‘average’ film thickness is measured, resulting in a de-convolution process being required to find the minimum value. MOFT = Minimum Oil Film Thickness .....127

Figure 6.10: Rigid and elastic ring numerical analysis compared to measured data. Engine speed = 3200rpm, Load = 36Nm, lubricant temperature = 73°C .....128

Figure 6.11: Rigid and elastic ring numerical analysis compared to measured data. Engine speed = 3200rpm, Load = 36Nm, lubricant temperature = 100°C .....129

Figure 6.12: Rigid and elastic ring numerical analysis compared to measured data. Engine speed = 3200rpm, Load = 25Nm, lubricant temperature = 73°C .....130

Figure 6.13: Representation of the sensor size for both sets of film thickness results. A sensor width approximately 10% larger than the ring’s width (a) allows for reasonable de-convolution results, whereas double the ring’s width (b) reduces the reliability of these results.....131

Figure 6.14: Sensor position for friction measurements. The transducers were arranged in pairs (two above, two below) 120° apart .....132

Figure 6.15: Cross-section view of the floating liner assembly, showing the seal ring in green (Gore et al, 2012) .....132

Figure 6.16: Experimental data before and after averaging. Engine speed = 2000rpm, motored running conditions .....133

Figure 6.17: Friction comparison between numerical analysis and total measured friction in a motored engine. Engine speed = 2000rpm, Lubricant temperature = 35°C .....134

Figure 6.18: Friction comparison between numerical analysis and total measured friction in a motored engine. Engine speed = 2500rpm, lubricant temperature = 25°C.....135

Figure 6.19: Friction comparison between numerical analysis and total measured friction in a motored engine. Engine speed = 3000rpm, lubricant temperature = 25°C.....136

Figure 6.20: Measured friction results for different engine speeds.....137

Figure 6.21: Numerical comparisons to motored experimental data as a percentage of average friction .....138

Figure 6.22: Friction comparison between numerical analysis and total measured friction in a fired engine. Engine speed = 2000rpm, lubricant temperature = 40°C, dyno load = 30Nm .....139

Figure 6.23: Friction comparison between numerical analysis and total measured friction in a fired engine. Engine speed = 2500rpm, lubricant temperature = 40°C, dyno load = 30Nm .....140

Figure 6.24: Friction comparison between numerical analysis and total measured friction in a fired engine. Engine speed = 3000rpm, lubricant temperature = 40°C, dyno load = 30Nm .....140

Figure 6.25: Comparison between numerical analysis and un-averaged friction from figure 6.26. Engine speed = 2000rpm, lubricant temperature = 40°C, dyno load = 30Nm .....141

Figure 6.26: Comparison between numerical analysis and un-averaged friction from figure 6.27. Engine speed = 2500rpm, lubricant temperature = 40°C, dyno load = 30Nm .....141

Figure 6.27: Comparison between numerical analysis and un-averaged friction from figure 23. Engine speed = 3000rpm, lubricant temperature = 40°C, dyno load = 30Nm .....142

Figure 6.28: Comparison between averaged numerical analysis and un-averaged friction from figure 6.25. Engine speed = 2000rpm, lubricant temperature = 40°C, dyno load = 30Nm .....142

Figure 6.29: Numerical comparisons to experimental fired data as a percentage of average friction. Lubricant temperature = 40°C, dyno load = 30Nm .....143

Figure 6.30: Comparison between numerical analysis and averaged friction. Engine speed = 2500rpm, lubricant temperature = 40°C, dyno load = 130Nm.....144

## List of Tables

Table 1.1: New Engine and Transmission Efficiency Savings, and Indicative Production Costs (King, 2007) .....	4
Table 3.1: Ring properties used in numerical and FEA analyses .....	33
Table 3.2: FEA model properties.....	34
Table 3.3: Natural frequency predictions for both numerical analysis and an FEA model .....	34
Table 3.4: Out-of-plane compression ring natural frequencies. ....	46
Table 5.1: Lubricant Parameters.....	75
Table 5.2: Roughness parameters for initial numerical results.....	75
Table 5.3: Ring Properties for initial numerical results .....	76
Table 6.1: Honda CRF450 engine properties .....	125
Table 6.2: Ring and lubricant properties used in numerical analysis .....	125
Table 6.3: Average friction comparison between experimental measurements and numerical analyses, motored case.....	138
Table 6.4: Average friction comparison between experimental measurements and numerical analyses, fired case .....	143



## Nomenclature

$A$  – Cross-sectional area of the ring

$A_a$  – Asperity contact area

$A_c$  – Nominal contact area of the ring's face-width

$A_{n1}$ - $A_{n6}$  – Modal function constants

$a$  – EHL contact radius

$b$  – Ring face-width

$C_{n1}$ ,  $C_{n2}$  – Time response constants

$C_z$  – Twisting stiffness

$d$  – Ring thickness

$d_n$  – Modal function constant

$E$  – Young's modulus of elasticity

$E'$  – Composite modulus of elasticity

$e_n$  – Modal function constant

$F_e$  – Ring tension

$F_g$  – Applied Gas force

$F_{groove}$  – Groove friction

$F_R$  – Net (residual) radial force

$F_T$  – Tangential shear force

$F_{5/2}$  – Greenwood and Tripp statistical function

$f_n$  – Modal function constant

$g$  – Ring gap

$h$  – Film thickness

$h_0$  – Minimum film thickness

$I$  – Second area moment of inertia of the ring cross-section

$i, j$  – Mode number (orthogonality condition)

$k$  – Stiffness parameter

$l$  – Connecting rod length

$M_x, M_z$  – Internal moments

$m$  – Ring mass per unit length

$p$  – Pressure

$p_e$  – Elastic pressure due to ring tension

$p_g$  – Gas pressure

$p_l$  – Top ring's leading edge pressure

$p_t$  – Top ring's trailing edge pressure

$Q_n$  – General forcing function

$R$  – Ring nominal radius

$R_b$  – EHL ball radius

$r$  – Crank-pin radius

$s$  – Ring axial profile

$t$  – Time

$U_{ent}$  – Speed of entraining motion

$U$  – Out of plane modal response

$u$  – Out of plane displacement

$V$  - Tangential modal response

$v$  – Tangential displacement

$W$  – Radial modal response

$W_a$  – Asperity load share

$W_h$  – Lubricant reaction

$w$  – Radial displacement

$x$  – Direction of entraining motion

$y$  – Circumferential degree of freedom

$\alpha$ – Incomplete Ring subtended angle

$\beta$  – Ring twist

$\beta_0$  – Thermal expansivity of lubricant

$\Delta$  - Global deformation of ring/liner

$\delta$  – Local deformation

$\delta_n$  – Modal function constant

$\zeta$  - Asperity distribution per unit area

$\eta$  – Lubricant viscosity

$\eta_0$  – Ambient lubricant viscosity

$\theta$  – Temperature

$\theta_0$  – Ambient temperature

$\kappa$  - Average asperity tip radius

$\lambda_n$  – Frequency parameter

$\lambda_s$  – Stribeck oil film parameter

$\mu_n$  – Modal function constant

$\xi_n$  – Time response of ring deflection

$\pi$  – Pi

$\rho$  – Lubricant density

$\zeta$  – Coefficient of boundary shear strength

$\sigma$  – Roots of the eigenvalue problem

$\sigma_c$  – Composite roughness of the counterfaces

$\tau$  – Viscous shear stress

$\tau_0$  – Eyring shear stress of the lubricant

$\tau'$  – Time segment

$\phi$  – Crank angle

$\varphi$  – Direction along the ring periphery

$\omega_f$  – Excitation frequency

$\omega_n$  – Natural frequency

### **Subscripts**

$c$  – Composite

$n$  – mode shape index

## **Glossary of Terms**

BDC – Bottom Dead Centre

DQM - Differential Quadrature Method

EHL – Elasto-Hydrodynamic Lubrication

ENCYCLOPAEDIC - Refinement of Engine in-cycle Losses of Parasitic and Errant Dynamic Nature

FEA – Finite Element Analysis

FFT – Fast Fourier Transform

GHG – Greenhouse Gas

IC – Internal Combustion

MOFT – Minimum Oil Film Thickness

TDC – Top Dead Centre

UNFCCC - United Nations Framework Convention on Climate Change

## 1. Introduction

### 1.1. Preamble

The demand for motor vehicle production worldwide is increasing by the year. This trend is predominantly seen in developing countries, as well as in developed nations such as the UK. However, the majority of current vehicles rely on petrol or diesel as fuel for propulsion. Along with other fossil fuels, these resources are clearly limited in supply. Alongside their finite availability, the burning of fossil fuels releases carbon into the atmosphere as a by-product of combustion, which is widely accepted as being a contributing factor to the global warming. A report by the Intergovernmental Panel on Climate Change (IPCC) stated that: "The observed widespread warming of the atmosphere and ocean, together with ice mass loss, support the conclusion that it is *extremely unlikely* that global climate change of the past 50 years can be explained without external forcing and *very likely* that it is not due to known natural causes alone" (IPCC, 2007). A very recent study, also by the IPCC, suggested that scientists are 95% certain that humans are the "dominant cause" of global warming since the 1950s (BBC, 2013). Due to these worldwide concerns, a number of legislations and studies have been undertaken, with the aim of reducing the emissions exhausted by motor vehicles, and improving their efficiency.

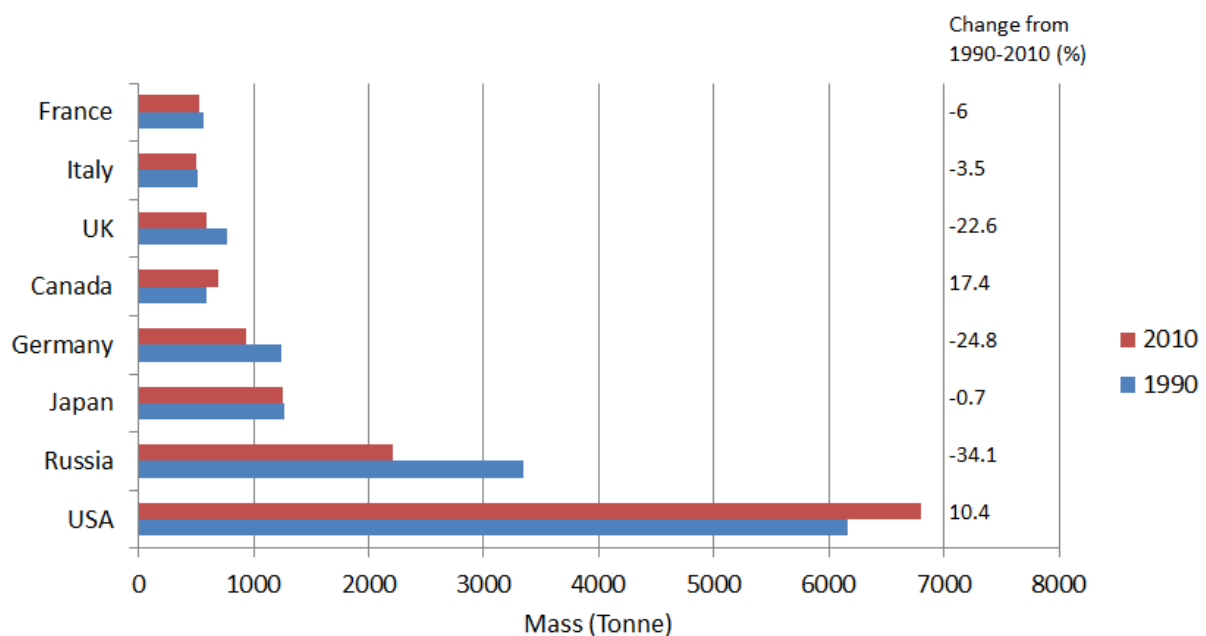


Figure 1.1: Greenhouse Gas Emissions for leading nations in 1990 and 2010. Data from UNFCCC report, 2012 ([www.unfccc.int](http://www.unfccc.int))

The United Nations Framework Convention on Climate Change (UNFCCC) was adopted on 9<sup>th</sup> May, 1992. The purpose of this Convention was to raise awareness of the problem of global warming, and to decide how best to deal with the inevitable temperature rises of the Earth's surface. In addition to this, the more recent Kyoto Protocol was adopted in 1997, and entered into force in 2005 (UNFCCC.int/kyoto\_protocol/items/2830.php). This Protocol sets emissions targets for 37 industrialised countries and the European community. The target greenhouse gas (GHG) reduction averages at 5% compared to 1990 levels between 2008 and 2012. Figure 1.1 shows the GHG emissions for the leading industrialised nations in 1990 and 2010.

Whereas the UNFCCC simply encourages the United Nations members to address GHG emissions, the Kyoto Protocol signifies a commitment by the participating countries. This commitment pressurises all industry sectors to reducing their "Carbon footprint" as much as possible, and there is nowhere this is more applicable than in the automotive industry.

The automotive sector represents a significant portion of the UK's manufacturing industry, and so faces stringent measures to improve efficiency and GHG production. In Europe, the Euro 5 emissions Standards were introduced in an effort to restrict in particular the nitrogen oxide (NO<sub>x</sub>) and particulate matter, which can have an adverse effect on people's health (<http://www.euractiv.com/en/transport/euro-5-emissions-standards-cars/article-133325>). Car manufacturers must meet these standards for their vehicles to be approved for sale within the European Union. Currently vehicles such as the Smart Car and the Volkswagen Polo BlueMotion are market leaders in terms of carbon dioxide emissions. As well as this, the King Review in 2007 highlighted the need for road vehicles to reduce carbon dioxide emissions (King, 2007). According to the review, in the year 2000 cars and vans were the cause of 7% of global carbon dioxide emissions, as well as making up almost half of all global transport emissions. Considering the projected increased demand for road vehicles in the future, particularly in developing countries, this represents a significant proportion of the world's carbon dioxide emissions. Three goals were put forward to aid progression in the push for CO<sub>2</sub> reduction. These were cleaner fuels, more efficient vehicles and smart driver choices.

This thesis is part of a project which is concerned with the development of more efficient internal combustion automobiles. As fossil fuels are a finite resource, this is viewed as a short-to-medium term solution, with vehicles powered by alternative fuels currently being researched. Some hybrid models are even in production today. As approximately 3 million internal combustion engines are produced in the UK every year (King, 2007), an improvement in fuel efficiency would have a significant impact on the GHG emissions. It is also acknowledged that internal combustion engines will remain the dominant means of propulsion for the foreseeable future. Even at the point when a viable permanent alternative to the IC engine is established, the active vehicles and power stations worldwide will in all likelihood still be overwhelmingly reliant on fossil fuels. Figure 1.2 presents the CO<sub>2</sub> emission contributions from various vehicles, which demonstrates that cars and vans contribute significantly more than any other mode of transport.

King, Julia. *The King Review of low-carbon cars: part I: the potential for CO<sub>2</sub> reduction*, 2007

(Chart 1.2)

Figure 1.2: Global transport carbon dioxide emissions in 2000 (King, 2007)

Figure 1.3 shows how engineering advancements have reduced CO<sub>2</sub> emissions in new cars compared to older models (King, 2007). Modifications such as improved fuel injection mean the fuel is combusted more efficiently, whilst the introduction of cruise control reduces sharp increases in engine speed. These benefits have even overcome the average weight gain of 20% seen in midsize vehicles, showing a 0.6% improvement in fuel efficiency (Owen and Gordon, 2003).

King, Julia. *The King Review of low-carbon cars: part I: the potential for CO<sub>2</sub> reduction*, 2007

(Chart 4.1)

Figure 1.3: Average CO<sub>2</sub> emissions from new cars and cars in use in the UK (King, 2007)



Table 1.1 shows a breakdown of different technologies, which can be applied to current IC engines to improve efficiency. If these improvements are able to be implemented on a large scale, the cost per vehicle will be relatively low. From this table, it can be seen that focusing on friction reduction could be the most cost effective method of improving engine performance, with a negligible cost per vehicle yet up to 5% reduction in friction. This thesis focuses on the reduction of mechanical friction within the engine, namely at the piston and ring-pack to cylinder-liner conjunction. Parasitic losses occur wherever moving parts are sliding against each other within the piston mechanism. 100% efficiency is impossible in real world systems, as all sliding surfaces will cause some losses, regardless of design or lubricant quality. These frictional losses account for approximately 25% of the power lost in a typical internal combustion engine. Of this, almost half of the frictional losses are accounted for within the piston mechanism. Therefore, the piston mechanism is responsible for 10-12% of power lost within the vehicle.

Table 1.1: New Engine and Transmission Efficiency Savings, and Indicative Production Costs  
(King, 2007)

King, Julia. *The King Review of low-carbon cars: part I: the potential for CO2 reduction*, 2007  
(Table 4.1)

Frictional losses increase, proportional to the total friction lost, under stop-start conditions such as driving in urban, built up areas (Uras, 1983). When high volumes of traffic are present in populated areas, over 50% of travel time is done at speeds below 20mph (Eddington Transport Study, 2006); meaning frictional losses are significant contributors to engine inefficiencies. This suggests a promising scope for improvement, as very few previous attempts at improving efficiency include a comprehensive analysis of the piston. High performance engines place even higher loads upon the piston, which creates yet more losses. With directives such as the Kyoto Protocol demanding reduced emissions and improved efficiency, clearly conflicting requirements are present between the various aspects to consider in engine design.

Whilst this thesis is concerned with the ring pack-cylinder liner conjunction specifically, it is part of a larger research project, to be undertaken at a national level. This incorporates a number of disciplines such as tribology, dynamics, contact mechanics, lubricant rheology and surface engineering, with the goal of providing novel advances to the problem of piston-connecting rod-crankshaft engine losses. Due to the input of all these fields of expertise, this approach can be described as multi-physics. The project is described as Refinement of Engine in-cycle Losses of Parasitic and Errant Dynamic Nature, to be known as Encyclopaedic (Encyclopaedic.org, 2009). Investigations of the surface roughness and asperity interactions within the contact area will be on a scale of nanometres, whereas the displacement dynamics involved with the piston motion could be considered of orders of magnitude higher (mm for the piston primary motion and  $\mu\text{m}$  for its secondary motion). The project will therefore be taking a multi-physics, multi-scale approach, a method which has not hitherto been undertaken on such a scale.

### **1.2. Project overview**

The power loss in Internal Combustion engines can be divided into two key categories, thermodynamic and parasitic. Thermodynamic losses include those due to heat, for example, heat expelled from the exhaust and heat losses from components due to the combustion process. These losses account for between 50-60% of the total engine losses. As mentioned previously, parasitic losses such as friction account for 25% of the power lost. These inefficiencies mean that only approximately 15% of the input power is available to propel the vehicle, overcoming road friction and any aerodynamic drag. Of the 25% lost due to friction, almost half is lost within the piston mechanism. Approximately one quarter is down to engine bearings, whilst around 15% is through valve train frictional forces. The remainder is accounted for with the sum of small inefficiencies within the system. Compression rings can be seen to be responsible for up to 5% of all losses in a standard 4-stroke internal combustion engine (Andersson, 1991). This is a significant proportion, especially considering the size of the component in question, when compared to the engine and vehicle as a whole. It can therefore be assumed that insufficient research has been performed in this subject area. This project is concerned with frictional losses within the piston mechanism, specifically the ring pack.

On pistons found in typical 4-stroke engines, three rings are usually present. These are known, from top to bottom, as the compression ring, secondary compression (or wiper) ring, and the oil control ring. Figure 1.4 shows the assembly of the piston, along with the location of the ring pack.

*Image can be found at confident-instruments.com ([http://confident-instruments.com/images/piston\\_assy\\_sectioned\\_anno.JPG](http://confident-instruments.com/images/piston_assy_sectioned_anno.JPG))*

Figure 1.4: Typical piston and ring-pack assembly ([http://confident-instruments.com/images/piston\\_assy\\_sectioned\\_anno.JPG](http://confident-instruments.com/images/piston_assy_sectioned_anno.JPG))

Each of these three rings is designed for oil control. However, this is a secondary function when considering the primary and secondary compression rings. As their name suggests, the key function of the compression rings is to seal the compression chamber. This is done to prevent a loss of pressure within the chamber, which would result in a loss of power. The escaping of gas down the side of the compression rings is known as blow-by. An effective compression ring must have good conformability with the bore, to minimise blow-by and excessive oil flow. As the compression ring is the closest ring to the chamber, it is subjected to the highest operating temperatures. These high temperatures result in thin film thicknesses compared to the other rings, as well as an increased deformation. At the top dead centre (TDC) the film thickness is reduced further, as it is difficult for the compression ring to scrape sufficient oil to form a complete film. This can cause surface contact in some cases, which leads to wear of the ring. This is also seen at the bottom dead centre (BDC), so it can also be attributed to the decrease in axial motion of the piston. At both the top and bottom of the piston's stroke, the speed of the piston will instantaneously reach zero. This reduction in velocity would cause the piston to rock to the side and make contact with the bore. This deterioration of lubrication conditions is known as boundary lubrication. Figure 1.5 shows the Stribeck curve, which indicates the different types of lubrication and when they occur. The symbol  $\mu$  represents the friction coefficient, whilst  $\lambda$  is the film thickness/roughness height ratio.

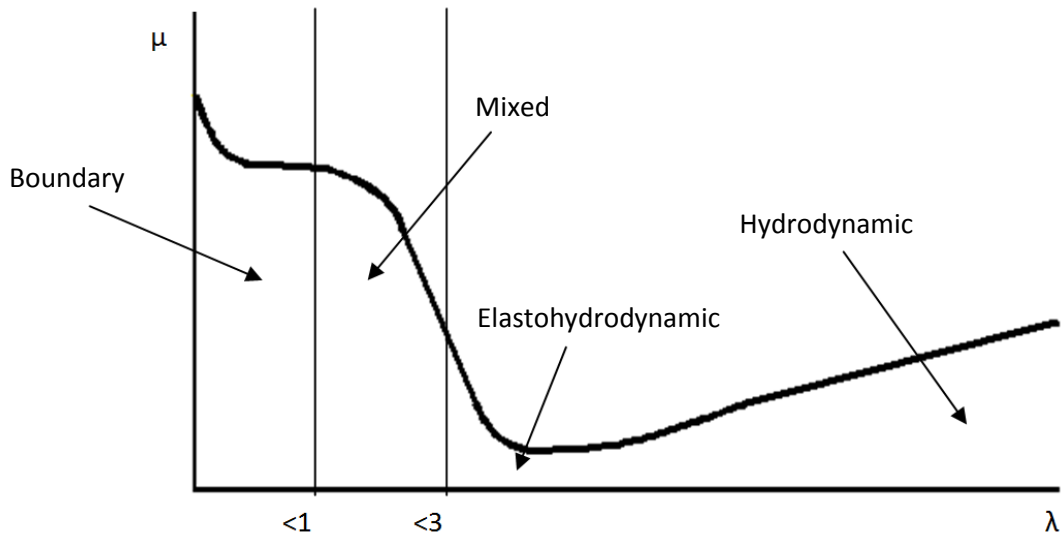


Figure 1.5: A typical Stribeck Curve

For the reasons analysed above, it can be understood that the compression ring suffers from the worst tribological conditions of the three rings. It is the compression ring to cylinder bore contact which is of most interest in this project, as the aforementioned problems give large scope for improvement.

All objects are subject to vibration, regardless of their size or shape. However, when considering 'thin' objects, any vibrations will be more visible or pronounced. This is particularly true of steel rings, due to the flexible nature of the component. The natural frequencies of the ring contribute to its resultant shape when excitation occurs, alongside the rigid body motion within the groove. Due to the thinness of the compression ring, deflections of this nature are likely to be present. These displacements will clearly affect the contact area between the compression ring and the bore, as well as the end gap of the ring, and consequently should be considered in the ring analysis. Whilst many studies have been undertaken on the compression ring, very few take into account the deflection of the ring during the piston's movement. One key element of the work to be undertaken in this thesis is to account for the complex motions of the ring, both in-plane and out-of-plane. The ring dynamics will then be superimposed onto the rigid body motion of the ring, thus giving a comprehensive ring elastodynamic model.

### **1.3. Aim and objectives**

The overall aim of the project is to develop combined analytical and experimental techniques to identify, predict and quantify sources of frictional and dynamic losses in the piston/ring-pack to connecting rod-crank sub-system. The aim of this project is to present a methodology which enables the coupling of transient ring dynamics into the tribological analysis. The results from the proposed methodology will be presented alongside the currently accepted numerical analysis. The objectives of this thesis are:

- To develop a model that predicts the inertial dynamics of the compression ring, capturing in-plane and out-of-plane modal behaviour
- To determine the global elasto-dynamics of the compression ring, giving a full transient solution. The constantly changing force profile acting upon the ring during the engine cycle will cause global deformation, which affects its modal response, and therefore the conjunctive behaviour of the system
- To complete an elastodynamic tribological analysis of the ring pack-cylinder liner conjunction. This would be coupled to the previous two points, before the addition of a combustion pressure profile. The friction and film thickness circumferentially around the ring will be calculated, with the effect of lubricant temperature also discussed.
- These numerical models will be verified by experimental analysis, with a designed-for-purpose test rig. Any relevant results published in literature will also be compared against, allowing for conclusions to be drawn.

#### **1.3.1. Contributions to Knowledge**

As stated previously, this project intends to undertake a multi-physics, multi-scale approach to solve the problem. This method has not hitherto been reported, and so will be a novel solution procedure. This thesis will contribute a numerical model, aiming to predict the dynamics and interactions of the compression ring to an acceptable level of accuracy. The inclusion of thermal effects on the system will give a comprehensive model, which in turn can be used to optimise the conditions found in the compression ring conjunction. The ultimate aim of the project is a novel solution which would point to improvements which may be made to the efficiency and power of the engine, creating a knowledge base which

can be used in future IC engine designs. Future research in this subject area will potentially build upon the progress made throughout this project, which will further advance the understanding of the piston ring pack.

### **1.4. Structure of the thesis**

The current chapter discussed the present concerns of the automotive industry and developed nations regarding the improvement in efficiency of internal combustion engines. The various methods of achieving an improvement were highlighted, which provided the impetus and reasons for undertaking the research within this thesis. The objectives of this research were then set out, with the potential contributions to knowledge detailed. This thesis is divided into 7 chapters, including the current chapter.

Chapter 2 presents a review of the currently available literature within the relevant area of interest. This review covers tribological analysis in a broader sense, as well as when applied to the piston ring-cylinder liner conjunction. Instances where the ring's motion within the groove has been investigated are highlighted. Ring dynamics literature is also surveyed. This review allows for a clear demonstration of where further research is possible, which justifies the presented thesis.

In chapter 3, the theory used to capture transient ring dynamics is discussed. The in-plane and out-of-plane dynamics methodologies are described, with finite element analysis (FEA) verification of the models also presented. This verification is for both the modal response and after applying a force to the ring model. The key references used to create this methodology are referred to throughout the chapter, alongside the modifications proposed which result in a comprehensive ring dynamics model.

The various methodologies which contribute to the tribological analysis of the top compression ring are presented in chapter 4. The Reynolds Equation is derived from the Navier-Stokes and flow equations, with the assumptions and simplifications highlighted. The solution procedure for the Reynolds Equation is also presented. Further to this, the Energy equation for thermal effects on lubricant is discussed, as well as its validity in this study. The effect of asperities on the conjunction between two lubricated surfaces is also considered, before developing the final solution procedure when considering the tribological performance of a piston ring.

Chapter 5 presents the results of the numerical analysis, using the theory detailed in the previous chapters. The effect of engine speed, lubricant temperature and ring profile is investigated. The previously accepted method of solution is compared to the proposed inclusion of transient ring elastodynamics, and conclusions are drawn.

In chapter 6, the results of the numerical analysis are compared to experimental friction and film thickness results. The experimental apparatus and procedure are explained where possible. Also, the results are presented alongside previously published experimental and numerical data from literature, with any limitations and assumptions detailed where necessary.

Finally, chapter 7 presents the main conclusions from this research. Discussion of limitations in both the numerical analysis and experimental data is presented. The objectives and aims previously set out are referred to, explaining their fulfilment, with the perceived contributions to knowledge set out. Any potential future work is highlighted, with suggested areas of study which will further enhance the research presented in this thesis.

## 2. Literature Review

### 2.1. Preamble

This thesis is concerned with the tribo-dynamic analysis of the compression ring to cylinder bore conjunction. However, a broader spectrum of subject areas has been included in this literature review. This is intended to give the reader an appreciation of the various disciplines involved, as well as other applications where the theory is prominent. A review of the literature concerned with tribology in general is shown, highlighting the key equations that will be used in this study. Also, a discussion on the relevant dynamics literature is present. Since dynamics is such a large subject area, only the vibrations of curved arches and incomplete rings feature in this report. Finally, a review of literature related to the tribological analysis of the piston, and the compression ring in particular, is shown. This allows for conclusions to be drawn regarding any parts of the tribological analysis of the compression ring which have not been explored fully. In drawing these conclusions, the position of this report's study within available literature can be seen.

### 2.2. Tribology

Osborne Reynolds (1895) derived his equation by simplification of the Navier-Stokes equations. He made a number of reasoned assumptions when deriving the equation, ignoring the inertial forces, and only retaining the viscous force of the lubricant. The Reynolds equation can be seen in equation (2.1).

$$\frac{\partial}{\partial x} \left( \frac{\rho h^3}{\eta} \frac{\partial p}{\partial x} \right) + \frac{\partial}{\partial y} \left( \frac{\rho h^3}{\eta} \frac{\partial p}{\partial y} \right) = 6 \left( u \frac{\partial \rho h}{\partial x} + v \frac{\partial \rho h}{\partial y} + 2 \frac{\partial \rho h}{\partial t} \right) \quad (2.1)$$

The simpler derivation above is also based on viscous action only. Reynolds' equation is used to obtain the pressure distribution in a conjunction, providing the other unknowns in the equation can be described. Early solutions, including Reynolds' own, were for line contact geometry. He used a long roller of radius R on a flat surface, separated by a layer of lubricant.

Some common assumptions when manipulating the Reynolds' equation include a constant lubricant density and viscosity (although the latter is only reasonable for low pressures). One may also ignore side-leakage depending on the system so  $v = 0$ , and under steady state conditions there is no squeeze term, meaning  $\partial h / \partial t = 0$ . Reynolds obtained the pressure



distribution from equation (2.1) when he assumed an infinitely long bearing. For his analytical solution he assumed a fully flooded inlet, so lubricant was readily available, and his exit boundary condition as:  $p = \frac{\partial p}{\partial x} = 0$  at  $x=x_e$ , where  $x_e$  is the film rupture position. Integrating the pressure distribution, Reynolds' obtained the line contact lubricant reaction as:

$$\frac{W_h}{L} = \frac{4.9u\eta_0R}{h_0} \quad (2.2)$$

Where  $h_0$  is the minimum film thickness. It can be seen that the contact load is inversely proportional to the minimum film size. This meant that at certain loads, the film thickness would have theoretically been less than the surface roughness of the roller. However, absence of any visible wear contradicted this theory, meaning Reynolds had not completely solved the problem.

At around the same time as Reynolds' work above, Hertz (1881) considered localised deformation of revolving ellipsoidal solids under load. The subject is now known as contact mechanics and is closely related to tribology. When considering a ball in contact with a flat surface, Hertzian theory is applicable when the contact radius,  $a$ , is much larger than the local deformation,  $\delta$ , but much smaller than the ball radius,  $R$ :  $\delta \ll a \ll R$ . The elastic deflection can create a small gap, which may be occupied by a film of lubricant, separating the contacting surfaces. This was only described half a century after Reynolds' 1896 paper by Grubin based on his work with Ertel (Grubin, 1949). The combined hydrodynamic action of the fluid film and elastic deformation of the contiguous surfaces was termed elasto-hydrodynamic lubrication, or EHL.

In the intervening period from 1896 to 1949, most tribological research was concerned with conjunctions such as journal bearings, which have relatively thick films and pressures of few tens of mega-pascals at most. The lubricant viscosity variation with pressure, generated in a narrow conjunction was described by Barus (1893) assuming isothermal conditions:

$$\eta = \eta_0 e^{\alpha p} \quad (2.3)$$

This relationship is now known as the Barus law, and  $\alpha$  is the pressure-viscosity coefficient with the unit of  $\text{Pa}^{-1}$ . When iso-viscous conditions are assumed,  $\eta = \eta_0$ , which was the

solution used by Reynolds for his long roller and later with different boundary conditions by Sommerfeld (1904) for his long bearing approximation. The physical interpretation for  $\alpha p = 0$  is that generated pressures do not affect the lubricant viscosity. However, it is evident that in lubrication with thin films, even those of a few tens of micrometres, such an assumption is untenable.

Roelands (1966) developed the Barus law to give a more accurate model:

$$\eta_r = \eta_0 e^{(\ln(\eta_0)+9.67)((1+5.1 \times 10^{-9}p)-1)} \quad (2.4)$$

Temperature can alter the properties of a lubricant dramatically. Coy (1998) used Vogel's equation to model the effect of temperature on lubricant viscosity:

$$\eta_0 = \kappa \frac{\varepsilon_1}{\varepsilon_2 + \theta} \quad (2.5)$$

where  $\kappa$ ,  $\varepsilon_1$  and  $\varepsilon_2$  are properties of the lubricant, and  $\theta$  is a given temperature. Houpert and Leenders (1985) developed Roelands' equation to include the effects of both pressure and temperature:

$$\eta_e = \eta_0 \exp \left\{ [\ln(\eta_0) + 9.67] \left[ \left( \frac{\theta - 138}{\theta_0 - 138} \right)^{\frac{\beta_0(\theta_0 - 138)}{\ln(\eta_0) + 9.67}} \left( 1 + \frac{p}{1.98 \times 10^8} \right)^{\frac{\alpha_0}{5.1 \times 10^{-9} [\ln(\eta_0) + 9.67]}} - 1 \right] \right\} \quad (2.6)$$

Where  $\beta_0$  and  $\alpha_0$  are constants and  $\theta_0$  is the ambient temperature.

Ertel and Grubin proposed that at the leading edge of the Hertzian footprint, the pressures rise to reach those of Hertzian, or  $\alpha p = 1$ . This means that there is an inlet trail of lubricant from  $x \rightarrow \infty$  for fully flooded conditions to  $x = -a$  where the trail merges to the ellipsoidal pressure distribution predicted by the classical Hertzian theory. Note that the viscosity of the lubricant then becomes  $\eta = e\eta_0$ , nearly triple its value under ambient condition. This behaviour is known as piezo-viscous action. Grubin (1949) assumes that the lubricant film is then parallel in shape, following the deflection predicted by the Hertzian theory as the generated pressures are those of Hertz. Therefore, this piezo-viscous action as well as localised contact deformation can explain the absence of wear at moderate to heavy loads, the phenomenon that Reynolds was searching for. A subsequent analysis by Petrusevich (1951) confirmed the Ertel and Grubin (1949) supposition. However, there existed the concern that the classical Hertzian pressure distribution does not conform to the continuity

of flow condition. The Dowson and Higginson (1959) numerical solution detected a pressure spike in the vicinity of contact exit, where a dip in the minimum film thickness was also observed. This means that the lubricant upon entering into the contact with rising pressures has a significantly increased viscosity. It becomes almost like an amorphous solid, and is pushed along by the relative motion of the surfaces and the pressure gradient in the direction of entrainment. As the pressures are reduced from the peak Hertzian value (often termed as primary pressure peak in elasto-hydrodynamic contacts) the lubricant viscosity also reduces dramatically. This means that locally the load carrying capacity is reduced, giving rise to a secondary pressure peak and a decrease in the film thickness is noted (minimum exit film). The size of the secondary pressure peak and its positioning within the contact is related to the operating conditions; load and speed, the inlet meniscus (supply of lubricant), mechanical properties of contacting surfaces and bulk lubricant rheology, particularly viscosity (Evans and Snidle, 1982).

### 2.2.1. Boundary and Mixed Lubrication

In an ideal world, there would be sufficient lubrication in any conjunction to facilitate motion and reduce the chances of wear occurring. However, experience tells us that these 'perfect' conditions occur rarely in any aspect of friction reduction. The gradual wearing of components suggests that contact between two surfaces can happen, even when the contact has been lubricated. Therefore, a method of predicting the effect of these contacts would enable any numerical analysis to be more accurate in its predictions.

Greenwood and Tripp (1971) examined the contact between two rough surfaces. A distribution of asperities of different radii is implemented upon a nominally flat surface, giving an expression for the asperity pressure:

$$P_a = \frac{8\sqrt{2}}{15} \pi (\zeta \kappa \sigma_{RMS})^2 \sqrt{\frac{\sigma_{RMS}}{\kappa}} E' F_{5/2}(\lambda_s) \quad (2.7)$$

In equation (2.7),  $\zeta$  is the asperity distribution in the contact area, whilst  $\kappa$  represents the average asperity tip radius.  $E'$  is the composite modulus of elasticity of the two surfaces. The dimensionless term  $F_{5/2}(\lambda_s)$  is a statistical function assuming a Gaussian distribution of asperities on the contiguous contacting surfaces (Teodorescu *et al*, 2004). Patir and Cheng (1978) studied partially lubricated contacts, and derived an average Reynolds equation for rough surfaces. This approach used flow factors which vary throughout the area examined.

The method presented by Patir and Cheng enabled surface texturing to be modelled numerically, and therefore determine which patterns should be most effective in reducing friction. This analysis has become particularly adapted in studies of the piston ring-to-cylinder liner conjunction. Some IC engine manufacturers add laser-etched patterns onto the piston, at the axial position where the ring would stop momentarily at the Top Dead Centre (TDC). As this is a position through the engine cycle where boundary interaction is most likely, extra efforts are made. For example through the mid-stroke, the film thickness between the ring and the bore is usually large enough to discount any contact between the two surfaces, and the hydrodynamic regime of lubrication is prevalent.

### **2.3. The Dynamics of Incomplete Rings**

Dynamics is the study of motion by considering the cause behind any changes in the kinematics of bodies or particles. The following section looks at various studies undertaken regarding incomplete rings on a broad scale. Whilst some of the literature reviewed is relevant to the compression ring, most of the authors do not specify an application or case study.

Early studies of ring dynamics took the form of analyzing curved bars. Lamb (1887) was among the first to perform this analysis. He discussed the in-plane flexure of a uniform bar. Based on previous work by Kirchoff, Clebsch, Thomson and Tait, a general equation for free-free end conditions was derived and solved. However, Lamb's work only considered beams with small curvatures. Den Hartog (1928) built on this work by deriving formulae for the first and second natural frequencies of an incomplete circular ring. He applied the Rayleigh-Ritz energy method to obtain these natural frequencies, for both hinged and clamped boundary conditions. Brown (1934) presented an approximate solution for the out-of-plane vibrations problem, using a modification of the Rayleigh method. He found that the calculated values using this method were higher than the ones obtained via experimentation; however they did fall within the level of expected error. Volterra and Morell (1961) later used the Rayleigh-Ritz method to find the lowest natural frequencies of elastic arcs, both in and out-of-plane. Further to this, they applied the theory to elastic hinged arcs.

Love (1944) obtained the classical equation of motion for an incomplete ring of small cross-section. He assumed an un-deformed central radial axis in order to evaluate the global

deformation of an incomplete circular ring. Love obtained various natural frequencies using the previous work of Mayer (1921). The ring was considered with different types of applied normal loads, for example for a slightly bent ring with an applied couple at its free ends in the radial plane. Other studies included the ring ends being subjected to opposing tension, as well as a couple applied at its ends perpendicular to the plane of the ring.

Archer (1960) studied the in-plane in-extensional vibrations of incomplete rings with small cross sections. The results were obtained using classical equations of motion, considering only in-plane forces. The results found by Archer between  $\pi$  and  $2\pi$  were in agreement with den Hartog's results. Shear deformation was neglected in his studies; however Timoshenko and Young (1955) proved that this was a valid assumption. Lang (1962) also studied the in-plane ring deformations and expanded it to present the full dynamic solution methodology, for both extensional and inextensional rings. Figure 2.1 shows a diagram depicting the degrees of freedom considered in this problem.

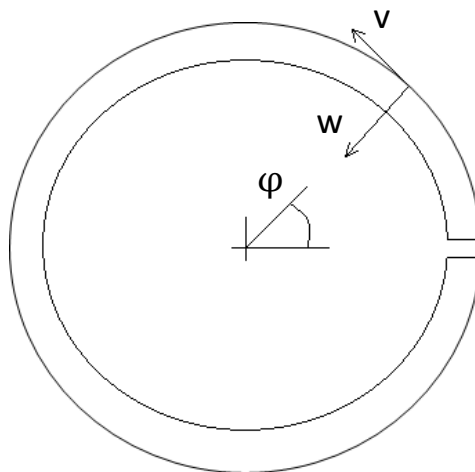


Figure 2.1: The degrees of freedom used by Lang (1962)

The boundary conditions used by Archer were clamped-clamped; however Lang (1962) provided solution forms for a variety of boundary conditions. Within the context of a compression ring application, the ring would be assumed to be free-free. In other words, there is no clamp holding the ring ends in position.

Following on from Archer's work on in-plane vibrations, Ojalvo (1962) studied the out-of-plane twist-bending vibrations of incomplete rings. He developed the equations of motion using Hamilton's Principle, to provide complementary solutions to those found by Archer. Ojalvo also concluded that there is a mutual independence between the in-plane and out-

of-plane linear motions, after inspection of the resulting expressions shows no common degree of freedom present in both in-plane and out-of-plane equations of motion. This allows the in-plane and out-of-plane solutions to be treated as separate problems from a mathematical point of view, as the in-plane equations of motion are uncoupled from the out-of-plane equations. Results were given for clamped end conditions, with Ojalvo reporting good agreement with results from Brown (1934) and den Hartog (1927). A similar method is used by Morley (1957) to find the flexural vibrations of a thin cut ring. Non-uniform beams of constant radius were examined by Lee and Chao (2000), again using the Hamilton Principle. Figure 2.2 shows the out-of-plane degrees of freedom used by Ojalvo.

Ojalvo, I. U. "Coupled twist-bending vibrations of incomplete elastic rings, "*International Journal of Mechanical Sciences* 4.1 (1962): 53-72. (figure 1)

Figure 2.2: Degrees of freedom used by Ojalvo (1962)

A number of studies have since been carried out based on the papers above, in particular Ojalvo and Archer. Williams (1973) included warping effects when producing his equations of motion, and showed results for free vibrations for complete rings and segments. His focus for the ring segments was on out-of-plane vibrations, as the in-plane natural frequencies had been discussed by Lang (1962). Wang et al (1980) applied Ojalvo's method to continuous curved beams, as opposed to single span. Rao (1971) analysed the coupled twist-bending vibrations seen in both complete and incomplete rings. He found solutions for free, supported and clamped conditions using Hamilton's principle. Rotary inertia and shearing deformation were included, to compare with classical theory which omits these values. It was found that inclusion of the shear deformation effects gives a closer prediction of the experimental natural frequencies found.

Auciello and De Rosa (1994) examined circular arches, assuming an inextensible centre axis and neglecting shear forces and rotary inertia. Their method was based on the equations of motion presented by Henrych (1981), and the results were compared to other method for

validation. These included finite element programs, the Rayleigh-Schmidt method, the Ritz and Galerkin method, and the Cells Discretisation Method.

Kang et al (1996) used the Differential Quadrature Method (DQM) to find the fundamental frequencies of circular arches, both in-plane and out-of-plane, of circular arches. The author produced results for a number of cases, including a comparison with Ojalvo (1962), with all showing a good agreement. De Rosa and Franciosi (2000) used a modification of the DQM, which allows boundary conditions to be implemented exactly. High level of precision was achieved, and again good agreement was seen when compared with previous papers. Kang (2007) then used DQM to analyse thin-walled curved beams, and showed that this method was also valid, with comparisons to other works. Challamel et al (2009) applied different loading conditions to circular arches, using Hamilton's Principle to find a solution.

Apart from vibrations, compression rings are subjected to other motion. The grooves in the piston dictate the primary movement of the rings, effectively pushing them up and down within the bore. This contact with the bore can cause a phenomenon called ring flutter. Tian et al (1998) created a ring dynamics and gas flow model, designed for a ring-pack containing three rings. Studies on a spark ignition engine found that static twist (the relative angle between rings and their grooves) has great influence on ring/groove contact characteristics, ring stability, and blow-by. Figure 2.3 shows a cross-section of the ring within the piston groove. For Tian's analysis, he assumed a layer of lubricant to be present on both surfaces of the groove, allowing a simplified Reynolds equation to be used to calculate the reaction force acting between the groove and the ring.

Tian, T., "Dynamic behaviours of piston rings and their practical impact. Part 1: ring flutter and ring collapse and their effects on gas flow and oil transport." *Proceedings of the Institution of Mechanical Engineers, Part J: Journal of Engineering Tribology* 216.4 (2002): 209-228. (figure 16)

Figure 2.3: Diagram of the ring within the groove, highlighting ring twist (Tian, 2002a)

Tian (2002a) discussed how ring flutter and ring collapse effected gas and oil flow in both SI and diesel engines. He stated that the pressure difference between the top and bottom of the ring, referring to figure 2.3, can be given as:

$$P_{12} = P_1 - P_2 \quad (2.21)$$

The critical pressure which causes ring collapse is defined as:

$$P_{12,critical} = \frac{F_t}{B_1 R} \quad (2.22)$$

Where  $F_t$  is the ring tangential force and  $R$  is the cylinder bore radius.  $B_1$  denotes the axial distance between the minimum film position and the upper edge of the face.

#### 2.4. Tribological Analysis of Compression Rings

Due to the nature of the environment in which the compression ring is required to work, a study of the system can encompass a wide variety of methodologies. The lubricant properties, entraining velocity and load are constantly changing, creating a complex arrangement (Tung and McMillan, 2004). As many as 17 influential parameters must be considered when attempting to numerically replicate the ring-liner conjunction, in order to attain results which mirror the 'real life' scenario to an acceptable level of accuracy (Taylor, 1998).

Fox et al (1997) reported that the lubricant available to the compression ring - cylinder liner conjunction has reduced as restrictions on engine emissions have been enforced on vehicle manufacturers. This reduction in lubrication increases the friction contribution of the ring pack from approximately 13% in the 1980s, to around 27% today (Richardson, 2000). A contribution between 13-40% is generally seen, depending on the engine's running conditions and specifications (Richardson, 2000). Clearly, any reduction in these frictional losses would be beneficial. If all parasitic losses are considered, a 10% improvement in mechanical losses would reduce fuel consumption by 1.5%, according to Priest and Taylor (2000).

As stated by Smedley (2004), Ramsbottom and Miller pioneered the piston ring in the mid-1800s. The work done by Miller, namely allowing the steam pressure to improve the sealing force, enabled more flexible rings to be designed. This meant improved conformability to



the cylinder bore, according to Priest and Taylor (2000). Furuhashi (1959-1961) helped to pave the way for both numerical and experimental investigations into compression ring tribology, with many studies undertaken since then.

Since Tribology encompasses a number of disciplines within the areas of physics and engineering, this section will be divided further. The following section discusses lubrication along the compression ring, along with ring and bore conformability, as well as phenomena such as blow-by. Section 2.4.2 will then review the literature concerned with frictional losses at the compression ring-bore conjunction, as well as lubrication concerns. This includes relatively recent technology relating to surface texturing, and how it can improve lubrication at the point of contact.

#### **2.4.1. Conformability and lubrication along the Compression Ring**

Conformability, in the context of a piston ring-liner system, describes how well the two parts fit together. Deformation of the bore and ring can be caused by thermal and mechanical loading, cylinder head bolt tightening and abrasion (Andersson et al, 2002). Due to its nature, the bore cannot be manufactured as a perfect cylinder. Running conditions can therefore worsen the conformance of the ring further. Whilst the in-situ ring will suffer from deformation, while the engine is running a constantly changing bore axial cross-section means flexibility is an important property of compression rings. Higher conformability between the compression ring and the cylinder means less gas will be lost through blow-by. The latter is the phenomenon where gases flow from the combustion chamber, past the ring pack to the crankcase. Figure 2.4 shows the paths these gases can follow during blow-by. The combustion gases greatly increase the bore and ring temperatures, as well as disrupting the lubricant film and separating the two surfaces. In addition to this contamination, blow-by reduces the power of the engine, as the escaping gases cause a loss of pressure within the combustion chamber. Poor conformability may also cause excessive oil flow, which causes the oil to escape with the exhaust gases.

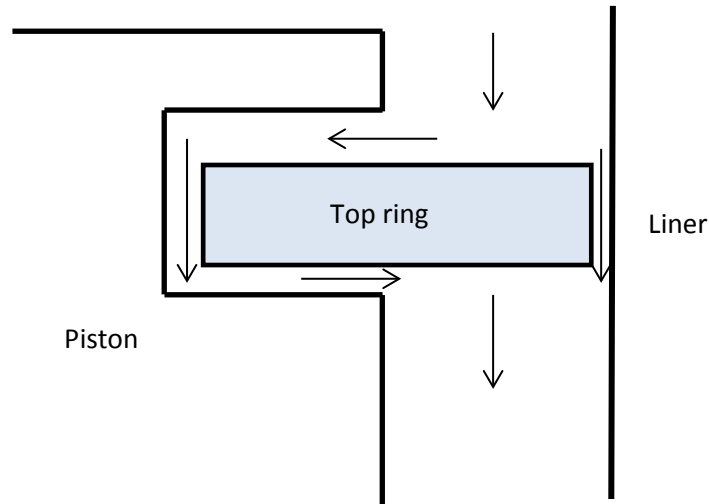


Figure 2.4: Blow-by in a poor fitting cylinder bore (Andersson et al, 2002)

Contact pressure on the ring pack comes from two sources. These are ring compression when the rings are fitted into the bore and gas pressure. The tangential force on the piston rings depends on the piston ring type. For example, the theoretical contact pressure used in the calculation of the tangential forces of rectangular and half keystone rings made of steel is approximately  $0.19 \text{ N/mm}^2$ . The spring force of the compression rings is lower than that of the oil ring (Dowson, 1993). Standards ISO 6621-4 state the values of nominal contact pressures and specific tangential forces for various piston rings. According to the work of Dowson, the loading caused by the elastic spring force on rings with gas pressure acting on the rear of the ring is typically  $10^4$ – $10^5 \text{ Pa}$ . This pressure presents only about 1 % or less of the peak gas pressure (Dowson, 1993).

Each of the rings within the ring pack is subjected to different pressures (Andersson et al, 2002). Due to the cyclic nature of a 4-stroke engine, the gas pressure on the top compression ring varies with the cylinder pressure, and is dependent on the engine stroke. These variations decrease at the secondary compression ring, with the average pressure also decreasing. The gas pressure on the oil ring can be said to be constant, and is almost equal to that of the crank chamber. The gas pressure on the compression ring increases the contact pressure, which in turn improves conformity. However, Chittenden and Priest (1993) stated that gas pressures only bear any significance for a small proportion of the engine's cycle.

Tomanik, Eduardo. "Piston ring conformability in a distorted bore." *SAE paper* 960356 (1996) (figure 2)

Figure 2.5: An exaggerated example of bore cross-section deformation (Tomanik, 1996)

Tomanik (1996) attempted to verify ring conformability criteria by experimentation. Deformed ring shapes were produced in a static jig, with areas of non-contact between the ring and the bore being measured. After processing the results, he produced a formula for calculating ring conformability. Figure 2.5 shows the areas of ring non-conformability in an example circular profile. Okamoto and Sakai (2001) presented a new calculation method for the pressure distribution on piston rings. Their method calculates the pressure from a given ring contour. This is based on a free ring, and uses the method of least squares to stabilise the results. Good agreement was found for different types of contact pressure distributions, namely strong and weak contact types, between the proposed methodology and experimental data.

Dunaevsky has undertaken many studies on ring conformability. In one of his earlier papers, a criterion for piston ring conformability to distorted cylinders is described (Dunaevsky, 1990). Fourier analysis was used to model the bore profile, and the results were supported by mass flow tests in compressors.

Dunaevsky et al (2000a, 2000b) also considered three dimensional distortions of the piston rings. They concluded that installation of the piston ring into the bore causes distortion in 3 dimensions, and that twist and 'bulging' occurs perpendicular to the ring's plane. In addition to this, the authors enhanced the capabilities of this model by accounting for contact pressure, and showing its effects on ring twist (Dunaevsky et al, 2001). They then considered the torsional ring distortion, using a Fourier series representation to model the cylinder bore geometry. The calculated twist values were compared to measured data with good compatibility. So far, Dunaevsky et al had focused on piston rings with symmetrical cross sections. The authors have also considered the differences a non-symmetrical cross section would make to the system's behaviour (Dunaevsky and Alexandrov, 2005). Therefore, a significant knowledge base has been created regarding piston ring conformability.

#### **2.4.2. Friction and Lubrication Concerns within the Ring-Cylinder Contact**

Due to varying load and surface conditions, each of the rings is subjected to differing lubrication regimes. If reducing friction was the only prerogative of an internal combustion engine, then a fully flooded contact would be desirable. However, due to the demands on today's engines regarding performance and power, this condition is not usually attainable. The most prominent lubrication regimes in the ring pack area are mixed and boundary (Andersson et al, 2002).

The majority of piston ring lubrication models are based on the Reynolds equation. The four lubrication regimes, as seen in Figure 1.5, are hydrodynamic, mixed, boundary, and elasto-hydrodynamic (EHL). Hydrodynamic lubrication usually occurs during the mid-strokes of the 4-stroke cycle, when the surface velocity is at its highest. The problems regarding lubrication are noticed at the top dead centre (TDC) and bottom dead centre (BDC). At both positions, Han and Lee (1998) noted that the ring faces were not fully lubricated. This condition meant that the Reynolds boundary condition could not be applied, and so they developed a model where the inlet is starved and the outlet has an open-end assumption. However, this model used flooded conditions at TDC and BDC. Ma et al (1997) proposed a fully flooded model and a flow-continuity model, and concluded that the latter was a more appropriate solution. They compared the results obtained numerically with those via experimentation by Hamilton and Moore (1974). Ma et al concluded that bore distortion can considerably reduce the power loss, although this distortion increases the oil consumption.

Castleman (1936) predicted that the lubrication regime surrounding piston rings was hydrodynamic, with a film thickness of approximately 5 $\mu$ m. This was in agreement with Eilon and Saunders (1957), who found similar values from friction measurements. These predictions were, however, undermined by the fact that piston rings were susceptible to wear, meaning that either metal-to-metal (asperities) contact or very thin lubricant films must occur. Wing and Saunders (1972) fitted inductance transducers to the piston for film thickness measurement. They found the oil-film thickness to be within the range 5-12 $\mu$ m. Hamilton and Moore (1974) introduced capacity gauges as a method of measuring film thicknesses and were able to resolve at much lower films, meaning more accurate film measurements were possible when the film thickness was approaching a mixed regime.

They observed values of 0.4-2.5 $\mu\text{m}$ , which are more in line with expected values at TDC and BDC especially.

Hill and Newman (1985) sought to reduce engine friction whilst maintaining performance. Their work was divided into four sections:

- Theoretical considerations – Explored the nature of piston ring friction through the three lubrication regimes experienced (boundary, mixed and hydrodynamic). The implications of the lubrication regime on piston ring design is discussed, as well as the design limitations based on factors including theoretical sealing capability, durability requirements and manufacturing considerations
- Low friction ring set design – referring to the theoretical considerations, the features of each ring pack component were reviewed
- Test results with the low friction ring set – the reduced friction set was tested, with results given for friction, oil consumption, blow-by, fuel economy and power output
- Future piston ring designs – further reductions in ring width, variation in the material composition and coatings, and the number of rings used were all examined, with any potential improvements highlighted.

Hill and Newman (1985) gave estimates of the friction reduction capable, with nearly a 26% reduction predicted for the oil ring. However this was under the assumption that the oil ring causes 60% of the ring-pack friction, which is inaccurate.

There have been many attempts to predict piston ring-to-cylinder bore tribological performance, based on pressure-induced localised deformation, caused by EHL. Ruddy et al. (1981) investigated the gas pressure within the ring pack for a large bore diesel engine, with the objective of overcoming the technical problems inherent in sealing a moving piston. The authors suggested that the ring gap could account for the gas leakage path, as a result of combined local and global deformations of the ring. Knoll and Peeken (1982) modeled the hydrodynamic lubrication of piston skirt and cylinder liner conjunction through an iterative method, using open end boundary conditions to estimate the reaction force due to the generated pressures. Balakrishnan and Rahnejat (2005) studied the transient conditions in the contact of piston skirt and ring-pack against cylinder liners during piston reversal. Their study showed changes in the regime of lubrication during reversal at or near the TDC. They

also showed that fluid film lubrication can be encouraged by the introduction of lubricant retaining surface features and modifications. Dwyer-Joyce et al (2007) verified this work via experimental analysis, where they used ultrasound to measure film thicknesses in a fired 4-stroke engine. The piston skirt-cylinder liner values obtained were in agreement with Rahnejat et al (2006). Unfortunately the sensor's resolution was not adequate for measuring the cylinder bore to compression ring film thickness.

Mishra et al (2009) analysed the ring-bore conjunction, including conformability and in-plane deformation of the ring. They assumed mixed and boundary conditions at TDC and BDC, and showed good agreement with Furuhashi and Sasaki (1983). Spencer et al (2011a) investigated the effect of the liner honing angle on the piston ring-cylinder conjunction. Honing is used in the manufacturing process, to apply the surface finish to the cylinder liner. They concluded that the honing angle had very little effect on the film thickness during the mid-stroke, but stated further work could be to investigate this procedure at TDC and BDC. Baker et al (2011b, see Appendix B) demonstrated the effect of including thermal effects on the ring's tribological performance. Internally generated (compressive heating and viscous shear) heating methods were accounted for, and comparisons made between the two methods. It was seen that when both heating mechanisms are incorporated (and the effect of combustion on lubricant temperature is not accounted for), a small difference is seen between the isothermal and thermal analyses.

#### **2.4.3. Surface Roughness, Modification and Topography**

Quan-bao et al (1988) presented a one-dimensional model of the piston ring-cylinder liner system which examined the effects of roughness on lubrication. It was concluded that inclusion of surface roughness effects would give a better approximation of the friction force values between the ring and the liner. Hu et al (1994) presented a theoretical model for a nonaxisymmetrical analysis of piston ring lubrication, which showed a variation in film thickness circumferentially. This in turn would affect the friction calculation circumferentially.

Spencer et al (2011b) attempted to optimise the surface texture of a cylinder liner, using a two-dimensional roughness model. The liner surface was measured, and a mathematical algorithm was used to model the surface numerically. They concluded that accounting for

the global surface texture and roughness should be done separately. This approach also allowed for the potential to optimise the surface texture using a mathematical model. Morris et al (2012) used the method presented by Patir and Cheng (1978) to present an analytical flow model coupled with an analytical thermal model. Rahmani et al (2012) investigated the effect of an out-of-round bore on the tribological performance, as well as a worn ring compared to a new one. The bores out of roundness caused a reduction in minimum film thickness; however the worn ring was seen to encourage an increase in film thickness in all areas of the engine cycle apart from reversal. Mishra et al (2009) used Greenwood and Tripp's method, along with measurements of a real cylinder bore, to perform a tribological analysis of a compression ring. A reasonable agreement was seen when comparing to experimental data presented by Furuhashi and Sasaki (1983), as well as previous numerical analysis (Akalin and Newaz, 2001). The discrepancy between results was attributed primarily to the inherent bore out-of-roundness and ring dynamics.

#### **2.4.4. Ring Deformation**

A number of authors have attempted to account for ring deformation during the engine cycle. Namazian and Heywood (1982) created a ring dynamics model which included a gas flow model. However, ring twist was not included in their study. Dowson et al (1979) and Ruddy et al (1979) examined the influence of ring twist, suggesting a particular contact between the ring and groove could cause flutter to occur. Their study did not include gas flow, and assumed the axial ring motion followed the piston exactly once contact between the two bodies occurred. Tian et al (1998) included both ring twist and a gas flow model. A thin layer of lubricant was assumed to cover the piston groove, and the Reynolds equation used to calculate the pressure profile along the groove. A one dimensional, analytical solution is used. However, the ring dynamics described did not calculate the elastic response of the compression ring, or account for the motion in a transient manner. Tian (2002a, b) built upon this work by showing the effect of ring flutter on gas flow and oil transport. A formula was presented, showing the critical parameters to avoid ring radial collapse. Kurbet and Kumar (2004) created a 3D finite element model of the piston and compression ring, including ring twist and piston tilt. They concluded that piston tilt has a significant effect on ring dynamics.

More recently, as part of the research presented in this thesis, an effort has been made to examine the possibility of including transient ring dynamics in the tribological analysis of the compression ring. Baker et al (2011a, see Appendix A) discussed the in-plane modal response of incomplete rings, alongside the effect of ring fitment on tribological performance. Baker et al (2012, see Appendix C) also demonstrated the effect of including ring dynamics in a tribological model, with ‘snapshots’ of deflected ring profiles presented. These snapshots were the result of extracting the force profile acting upon the ring at key locations around the firing point, and applying it to the ring’s neutral profile.

## **2.5. Closure**

There has been a vast amount of analysis performed on the dynamics of curved structures and incomplete rings. Both in-plane and out-of-plane vibrations have been solved with various analytical and numerical techniques. FEA and experimental work is largely used to verify the investigations, giving confidence that the methodologies used are sound. Similarly the area of tribology, particularly when concerning the piston cylinder-ring pack conjunction, has been the subject of numerous studies. However, a comprehensive model encompassing both ring dynamics and tribology is not yet available in the public domain. This suggests that such a model has not been created; therefore making it a potential novelty to be offered by this project.

The quasi-static dynamics of the compression ring due to gas pressure and ring tilt have been described within the literature reviewed in this report. However, one area which hasn’t been considered thus far is the transient dynamic response of the compression ring within the piston groove. This is an area where a significant contribution to knowledge is possible. Whilst the displacements compared to the piston stroke would be small, these perturbations would be of significant size compared to the film thickness values seen. The effects of inertial dynamics on the present tribological numerical analysis are not known, and so a study on the matter would add to the knowledge base shown in this chapter. This will be further enhanced by the inclusion of thermal effects, demonstrating a novel program of numerical work. Experimental data will be gathered for verification and comparison, with the aim of verifying the numerical solution for the compression ring dynamic behaviour.



### 3. Compression Ring Dynamics

#### 3.1. Introduction

The following chapter discusses the analytical methodology used to model the dynamics of the compression ring within the bore throughout the engine cycle. The motion of the ring can occur both in-plane and out-of-plane relative to its original position. However it is possible to treat these as separate problems, from a mathematical viewpoint. The in-plane dynamics are discussed first. Both methodologies are verified using an FEA model.

#### 3.2. Ring In-plane Dynamic Response

The assumptions used in the analysis of the incomplete, circular ring are as follows:

- Since the neutral radius of the ring is significantly larger than the ring's thickness, the ring can be assumed to be thin. The variable  $\frac{I}{AR^2} \approx 1.248 \cdot 10^{-5} \ll 1$ , as stated by Lang (1962), is also a measure which agrees with this assumption. In this variable, A is the cross-sectional area of the ring and R is the ring's nominal radius.
- Rotary inertia is neglected in this analysis, due to the thin nature of the ring and its relatively small mass and rotation speed.
- The neutral axis is also assumed to be inextensible ( $\frac{d}{R} \approx 0.0814 < 0.1$ ), which is a valid assumption for analysing the ring's forced response when modes lower than the fifth harmonic are only considered as important (Lang, 1962). Therefore, the following relationship couples the tangential and radial displacements:

$$w = \frac{\partial v}{\partial \varphi} \quad (3.1)$$

Figure 3.1a demonstrates the degrees of freedom used in the dynamic analysis. Figure 3.1b shows a free body diagram of the ring, exhibiting all forces and moments acting upon a ring segment (Lang, 1962):

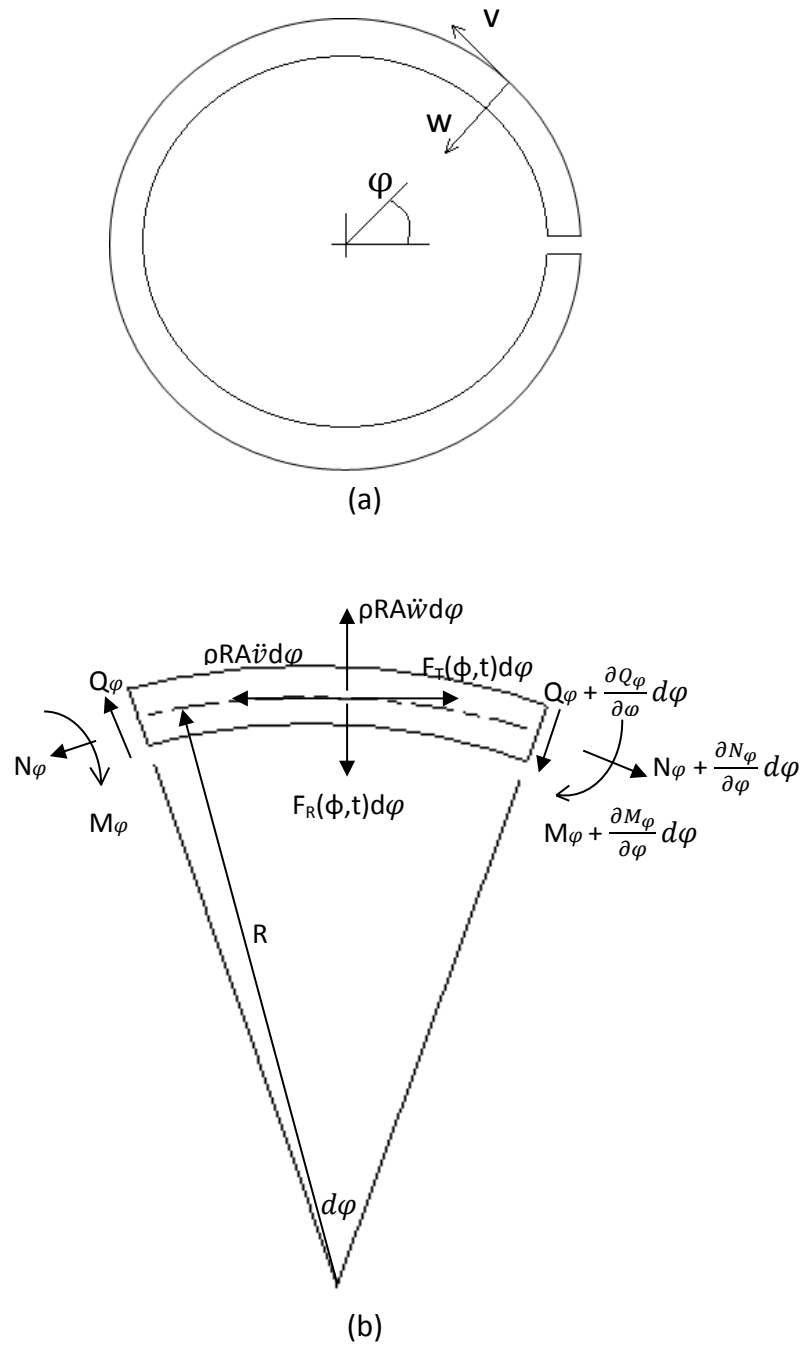


Figure 3.1: a) In-plane degrees of freedom of an incomplete ring and  
 b) Ring segment free body diagram

From figure 3.1b,  $Q(\varphi)$  is the transverse force,  $N(\varphi)$  is the circumferential normal force and,  $M(\varphi)$  is the bending moment. The force terms  $F_R$  and  $F_T$  correspond to the external excitations in the radial and tangential directions, respectively. Therefore, the equations of motion in both the tangential and radial directions are as follows (Lang, 1962):

$$\frac{\partial^6 v}{\partial \varphi^6} + 2 \frac{\partial^4 v}{\partial \varphi^4} + \frac{\partial^2 v}{\partial \varphi^2} + \frac{1}{p\omega_0^2} \frac{\partial^4 v}{\partial \varphi^2 \partial t^2} - \frac{1}{p\omega_0^2} \frac{\partial^2 v}{\partial t^2} = \frac{R^3}{EI} \left\{ \frac{\partial^2}{\partial \varphi^2} [F_R(\varphi, t)] - [F_T(\varphi, t)] \right\} \quad (3.2)$$

$$\frac{\partial^6 w}{\partial \varphi^6} + 2 \frac{\partial^4 w}{\partial \varphi^4} + \frac{\partial^2 w}{\partial \varphi^2} + \frac{1}{p\omega_0^2} \frac{\partial^4 w}{\partial \varphi^2 \partial t^2} - \frac{1}{p\omega_0^2} \frac{\partial^2 w}{\partial t^2} = \frac{R^3}{EI} \left\{ \frac{\partial^2}{\partial \varphi^2} [F_R(\varphi, t)] - \frac{\partial}{\partial \varphi} [F_T(\varphi, t)] \right\} \quad (3.3)$$

Where E is the elasticity modulus, I is the second moment of inertia and R is the ring's nominal radius. Equations (3.2-3.3) are coupled by the relationship  $w = dv/d\varphi$ . It can be seen that equations (3.2) and (3.3) are of the same form. The eigenproblem is derived by first setting the right hand side of equation (3.2) to equal zero. A solution for  $v$  is assumed, for the  $n$ th mode:

$$v(\varphi, t) = V_n(\varphi) e^{i\omega_n t} \quad (3.4)$$

Where  $V_n(\varphi)$  is the mode shape for the  $n$ th mode. Therefore, assuming  $p = \frac{I}{AR^2}$  and  $\omega_0^2 = \frac{E}{\rho R^2}$ , equation (3.2) becomes:

$$\frac{\partial^6 V_n}{\partial \varphi^6} + 2 \frac{\partial^4 V_n}{\partial \varphi^4} + (1 - \lambda_n) \frac{\partial^2 V_n}{\partial \varphi^2} + \lambda_n V_n = 0 \quad (3.5)$$

where

$$\lambda_n = \frac{mR^4}{EI} \omega_n^2 \quad (3.6)$$

Equation (3.5) has constant coefficients and it is a linear differential equation (Lang, 1962). A solution for equation (3.5) can, therefore, be assumed:

$$V_n = \sum_{i=1}^6 A_{n_i} e^{m_{n_i} \varphi} \quad (3.7)$$

Substitution of equation (3.7) into equation (3.5) leads to the following auxiliary equation (Lang, 1962):

$$\sigma_n^6 + 2\sigma_n^4 + (1 - \lambda_n)\sigma_n^2 + \lambda_n = 0 \quad (3.8)$$

Equation (3.8) is seen to be a cubic equation in  $\sigma_n^2$ , where  $\sigma$  is the root of the eigenvalue problem. The solutions to equation (3.8) are used in the mode shape functions in the following section. These mode shape solutions to equations (3.2) and (3.3) have been solved in the past by several authors, including Love (1944), Archer (1960) and Ojalvo (1962), who provide examples of calculated natural frequencies and mode shapes. The solution forms (known as modal functions) are the same for both  $v$  and  $w$  degrees of freedom and depend on the value of the frequency parameter  $\lambda_n$ .

If  $\lambda_n < \lambda_L$ , then:

$$V_n = A_{n1} \cos d_n \varphi + A_{n2} \sin d_n \varphi + A_{n3} \cos e_n \varphi + A_{n4} \sin e_n \varphi + A_{n5} \cos f_n \varphi + A_{n6} \sin f_n \varphi \quad (3.9)$$

and

$$W_n = -A_{n1} d_n \sin d_n \varphi + A_{n2} d_n \cos d_n \varphi - A_{n3} e_n \sin e_n \varphi + A_{n4} e_n \cos e_n \varphi - A_{n5} f_n \sin f_n \varphi + A_{n6} f_n \cos f_n \varphi \quad (3.10)$$

Where  $d_n$ ,  $e_n$  and  $f_n$  are the modal function constants. If  $\lambda_L < \lambda_n < \lambda_U$ , then:

$$V_n = A_{n1} \cos d_n \varphi + A_{n2} \sin d_n \varphi + A_{n3} \cos \mu_n \varphi \cosh \delta_n \varphi + A_{n4} \sin \mu_n \varphi \cosh \delta_n \varphi + A_{n5} \cos \mu_n \varphi \sinh \delta_n \varphi + A_{n6} \sin \mu_n \varphi \sinh \delta_n \varphi \quad (3.11)$$

and

$$\begin{aligned} W_n = & -d_n A_{n1} \sin d_n \varphi + d_n A_{n2} \cos d_n \varphi \\ & + A_{n3} (-\mu_n \sin \mu_n \varphi \cosh \delta_n \varphi + \delta_n \cos \mu_n \varphi \sinh \delta_n \varphi) \\ & + A_{n4} (\mu_n \cos \mu_n \varphi \cosh \delta_n \varphi + \delta_n \sin \mu_n \varphi \sinh \delta_n \varphi) \\ & + A_{n5} (-\mu_n \sin \mu_n \varphi \sinh \delta_n \varphi + \delta_n \cos \mu_n \varphi \cosh \delta_n \varphi) \\ & + A_{n6} (\mu_n \cos \mu_n \varphi \sinh \delta_n \varphi + \delta_n \sin \mu_n \varphi \cosh \delta_n \varphi) \end{aligned} \quad (3.12)$$

Finally, if  $\lambda_n > \lambda_U$ , then:

$$V_n = A_{n1} \cos d_n \varphi + A_{n2} \sin d_n \varphi + A_{n3} \cosh e_n \varphi + A_{n4} \sinh e_n \varphi + A_{n5} \cosh f_n \varphi + A_{n6} \sinh f_n \varphi \quad (3.13)$$

and

$$\begin{aligned} W_n = & -d_n A_{n1} \sin d_n \varphi + d_n A_{n2} \cos d_n \varphi + e_n A_{n3} \sinh e_n \varphi + e_n A_{n4} \cosh e_n \varphi \\ & + f_n A_{n5} \sinh f_n \varphi + f_n A_{n6} \cosh f_n \varphi \end{aligned} \quad (3.14)$$

The condition  $\lambda_n < \lambda_L$  does not arise when considering an incomplete ring. It can only occur when  $\alpha > 2\pi$ . The limits  $\lambda_U$  and  $\lambda_L$  are independent of the ring geometry, taking values of  $\lambda_L = 0.1134$  and  $\lambda_U = 17.637$ . These limit values are stated by Archer (1960) and are the boundaries across which the solution forms for  $W_n$  and  $V_n$  differ. The value of  $\lambda_n$  is determined by solving the characteristic equation (3.8).

The constants  $d_n, e_n, f_n, \delta_n$  and  $\mu_n$  depend on the roots of equation (3.8). If  $\lambda_L < \lambda_n < \lambda_U$ , the 3 roots take the form  $d_n, \delta_n + i\mu_n$ , and  $\delta_n - i\mu_n$ , meaning the second and third roots are complex conjugates. If  $\lambda_n > \lambda_U$ , then the roots are of the form  $d_n, ie_n, if_n$ . The expressions for  $V_n$  and  $W_n$  are substituted into the ring boundary conditions (free-free in this case). Equations (3.11-13) represent the normal force, bending moment and its derivative, whose values equal zero for an incomplete ring, which is free at both ends. These equations are therefore implemented at the ring ends (for  $\varphi = 0$  and  $\varphi = \alpha$ , as substituted in the expressions for  $V_n$  and  $W_n$ ):

$$\frac{d^2 V_n}{d\varphi^2} + \frac{d^4 V_n}{d\varphi^4} = 0 \quad (3.15)$$

$$-\lambda_n \frac{dV_n}{d\varphi} + \frac{d^3 V_n}{d\varphi^3} + \frac{d^5 V_n}{d\varphi^5} = 0 \quad (3.16)$$

$$\frac{dV_n}{d\varphi} + \frac{d^3 V_n}{d\varphi^3} = 0 \quad (3.17)$$

The above process gives a 6x6 matrix with respect to constants  $A_{n1} - A_{n6}$ . The  $\lambda_n$  values are found when the determinant of this matrix vanishes. The natural frequency (in rad/s) is calculated by rearranging equation (3.6), since  $\lambda_n$  is now a known variable for each mode number,  $n$ . Therefore each natural frequency of the ring depends on the frequency parameter  $\lambda_n$ , as well as to the ring's dimensions and material properties. However, it is worth noting that calculation of the frequency parameter itself is not a function of the ring's material properties. The only dimension affecting the calculation of  $\lambda_n$  is the ring's subtended angle,  $\varphi$ .

After calculation of the natural frequencies, the constants  $A_{n1}$ - $A_{n6}$  from equations (3.9-14) are required to determine the corresponding mode shapes. In order to calculate the  $A_n$  coefficients, the orthogonality conditions of the ring's modal functions must be satisfied, thus (Inman, 2001):

$$\int_0^\alpha \rho RA(V_i V_j + W_i W_j) d\varphi = 0, \quad i \neq j \quad (3.18)$$

$$\int_0^\alpha \rho RA(V^2 + W^2) d\varphi = 1, \quad i = j \quad (3.19)$$

where  $i$  and  $j$  represent different mode numbers. The boundary conditions are used to obtain expressions for  $A_{n1} - A_{n5}$  with respect to  $A_{n6}$ . These are substituted into equation (3.19), which is solved for  $A_{n6}$ . Hence, the remaining constants can be calculated, allowing the determination of the corresponding mode shape at each natural frequency.

Table 3.1 shows the modelled ring dimensions and material properties, whilst the FEA model properties are shown in table 3.2. The calculated natural frequencies are presented in table 3.3, for both the numerical method and FEA model. Excellent agreement can be seen. Figure 3.2 shows an example mode shape after applying the orthogonality conditions. A comparison is made against an FEA model of the ring for verification purposes. As shown in table 3.2, the FEA model was created using the software package NASTRAN/PATRAN, and comprises 1080 quadrilateral elements with 1355 nodes, each with 6 degrees of freedom (Baker et al, 2012). Free-free boundary conditions were assumed for the ends of the ring, as there is no restricting 'clamp' acting on the top compression ring. Again, very good agreement is observed.

Table 3.1: Ring properties used in numerical and FEA analyses

Parameter	Value
Elastic Modulus, $E$	203GPa
Ring density, $\rho$	7800kg/m <sup>3</sup>
Ring Thickness, $d$	3.5mm
Axial Face-width, $b$	1.15mm
Nominal Ring Radius, $R$	44.52mm
Ring second moment of area, $I$	2.25X10 <sup>-12</sup> m <sup>4</sup>

Table 3.2: FEA model properties

<b>Element type</b>	Quad Isomesh
<b>Number of elements</b>	1080
<b>Number of nodes</b>	1355
<b>Ring end boundary conditions</b>	Free-free

Table 3.3: Natural frequency predictions for both numerical analysis and an FEA model

<b>Mode Number</b>	<b>Analytical Method Natural Frequency (Hz)</b>	<b>FEA model Natural Frequency (Hz)</b>	<b>% Difference</b>
1	198.44	198.31	0.066
2	432.8	432.35	0.104
3	972.06	969.76	0.237
4	1803.24	1795.40	0.437
5	2892.18	2871.90	0.706
6	4224.74	4181.70	1.029
7	5793.44	5712.80	1.412

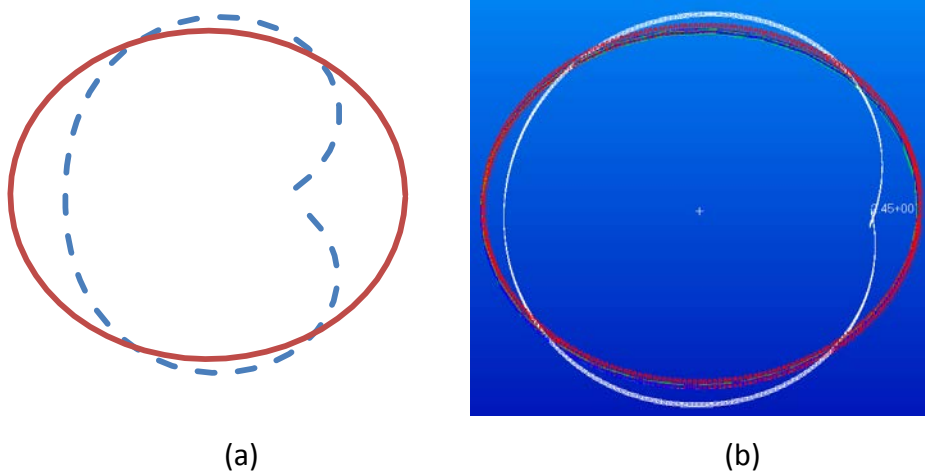


Figure 3.2: Mode shape comparison (a) Analytical ( $f = 972.06\text{Hz}$ ) and (b) FEA ( $f=969.76\text{Hz}$ ).

The particular solution of equation (3.2) takes the following form (the solution of equation (3.3) is determined using the inextensibility condition (3.1)). Thus:

$$v(\varphi, t) = \sum_{n=1}^{\infty} V_n(\varphi) \xi_n(t) \quad (3.20)$$

The time varying term of equation (3.20),  $\xi_n(t)$ , is determined through the following solution (Lang, 1962), Damping effects are not considered, due to the thin nature of the lubricant film profile:

$$\ddot{\xi}_n + \omega_n^2 \xi_n = Q_n(t) \quad (3.21)$$

where:

$$Q_n(t) = - \frac{\int_0^\alpha V_n \left\{ \frac{\partial}{\partial \varphi} F_R(\varphi, t) - F_T(\varphi, t) \right\} d\varphi}{\rho a A \int_0^\alpha (W_n^2 + V_n^2) d\varphi} \quad (3.22)$$

The  $F_T$  and  $F_R$  terms in equation (3.22) represent forces acting in the tangential and radial directions, respectively. Equation (3.22) is derived from equation (3.2) after substitution of the particular solution (3.20), rearranging the result and applying the orthogonality condition (Lang, 1962). The solution of equation (3.21) is obtained analytically as:

$$\xi_n(t) = \frac{1}{\omega_n} \int_0^t Q_n(\tau') \sin \omega_n(t - \tau') d\tau' + C_{n1} \sin \omega_n t + C_{n2} \cos \omega_n t \quad (3.23)$$

The terms  $C_{n1}$  and  $C_{n2}$  are calculated from the initial conditions, so let  $v(\varphi, t) = v_0$  and  $\dot{v}(\varphi, t) = \dot{v}_0$ , with the equivalent expressions applicable for the radial displacement. Lang (1962) found the value of these terms to be:

$$C_{n1} = \frac{\int_0^\alpha (v_0 V_n + \dot{v}_0 W_n) d\varphi}{\omega_n \int_0^\alpha (W_n^2 + V_n^2) d\varphi} \quad (3.24)$$

$$C_{n2} = \frac{\int_0^\alpha (v_0 V_n + \dot{v}_0 W_n) d\varphi}{\int_0^\alpha (W_n^2 + V_n^2) d\varphi} \quad (3.25)$$

Substitution of these terms in equation (3.23) gives the complete solution for the in-plane elastodynamic response of an incomplete ring.

Timoshenko et al (1974) detailed the in-plane rigid body response of a closed circular ring. By definition, the rigid body response of an incomplete ring would not see any deformation of the neutral radius; the response corresponds to translation and rotation around the axis



crossing its centre, vertical to the ring plane. Therefore, it is assumed that the in-plane rigid body response takes the following form in equations (3.26-27):

$$V_0 = A_0 \sin \varphi \quad (3.26)$$

And:

$$W_0 = A_0 \cos \varphi \quad (3.27)$$

Equations (3.26) and (3.27) are then used in the methodology for calculating the rigid dynamic response. The form of the transient solution, as shown by (Natsiavas, 2001):

$$\ddot{\xi}_0 = Q_0(t) \quad (3.28)$$

The solution to equation (3.28) is of a similar form to the elastodynamics solutions:

$$\xi_n(t) = \int_0^t \int_0^t Q_0(\tau') d\tau' d\tau + C_1 t + C_2 \quad (3.29)$$

Where  $C_2 = \frac{1}{\alpha} \int_0^\alpha w_0(\varphi) d\varphi$ , and  $C_1 = \frac{1}{\alpha} \int_0^\alpha \dot{w}_0(\varphi) d\varphi$

Verification of the dynamic response methodology was achieved by applying excitation to the FEA compression ring model and comparing the results to those of the analytical theory. As dictated by equation (3.22), the force profile must be differentiable in terms of the ring angle  $\varphi$  so as not to excite extensional modes. The form of the force is as follows:

$$F_R = F * \cos 2\varphi * \sin \omega_f t \quad (3.30)$$

where  $\omega_f$  is the frequency of excitation, and F is the forcing amplitude due to pressure of 1kPa applied on the ring FEA model. The pressure along the ring angle is constant. Since the in-plane load is applied radially in the case of the compression ring, applying the load as a function of the ring angle is necessary. Figure 3.3 gives a visual representation of the force profile described by equation 3.30. If the ring was to be unwrapped a sinusoidal profile would be seen, with two complete periods between the two ends of the ring.

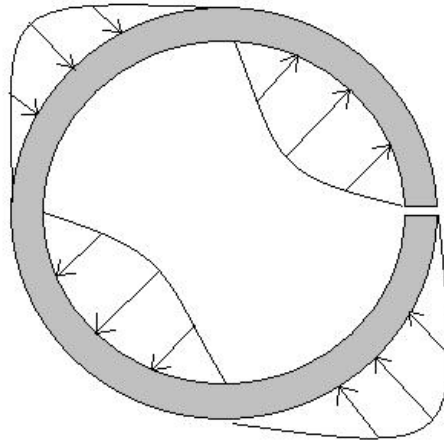
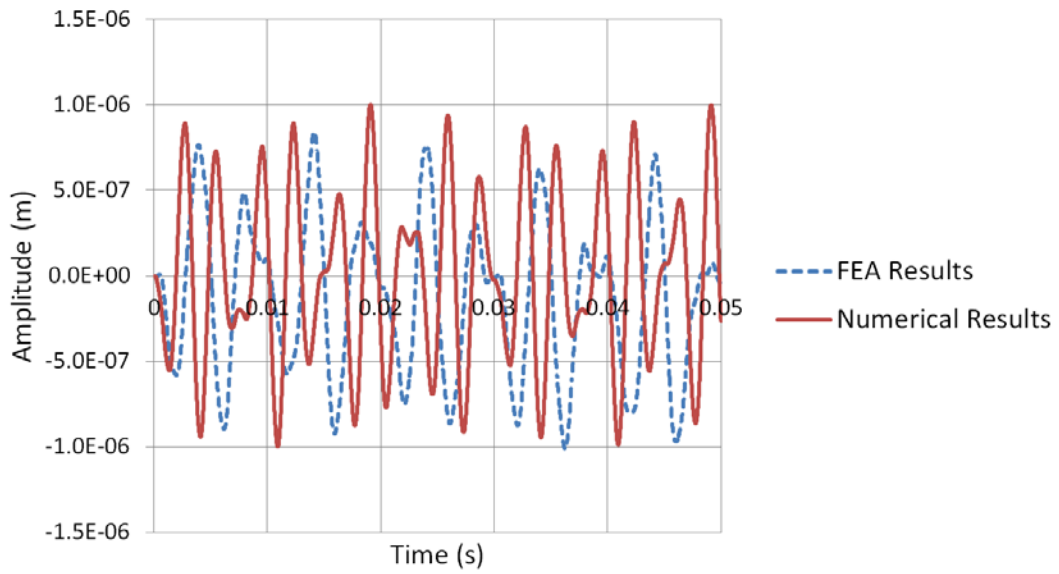
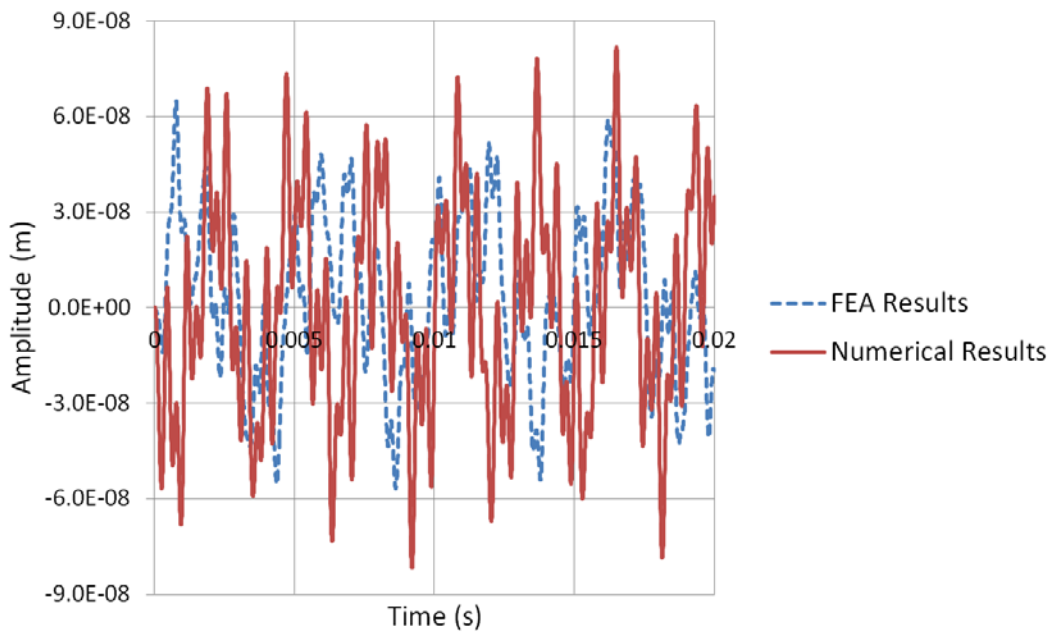


Figure 3.3: Force distribution used in FEA model

Figure 3.4 shows the displacement response at a point on the compression ring, opposite to the ring gap for two different excitation frequencies. A good agreement can be seen between the two results. Given the relatively small amplitudes seen in this study, the difference between the numerical and FEA results is within an acceptable margin of error. An example Fast Fourier Transform (FFT) of the two sets of data is shown in figure 3.5. The expected natural frequencies are shown to be present, with the excitation frequency also highlighted. The dominant natural frequency seen in figure 3.5a may explain why the shapes of the plots in figure 3.4a are slightly different, even if the amplitudes are in agreement. These results give confidence that the in-plane dynamic model has been built correctly. Results of this nature are not readily available in literature, with only the modal response analysis being usually presented. Therefore it was deemed necessary to verify the methodology in this manner.

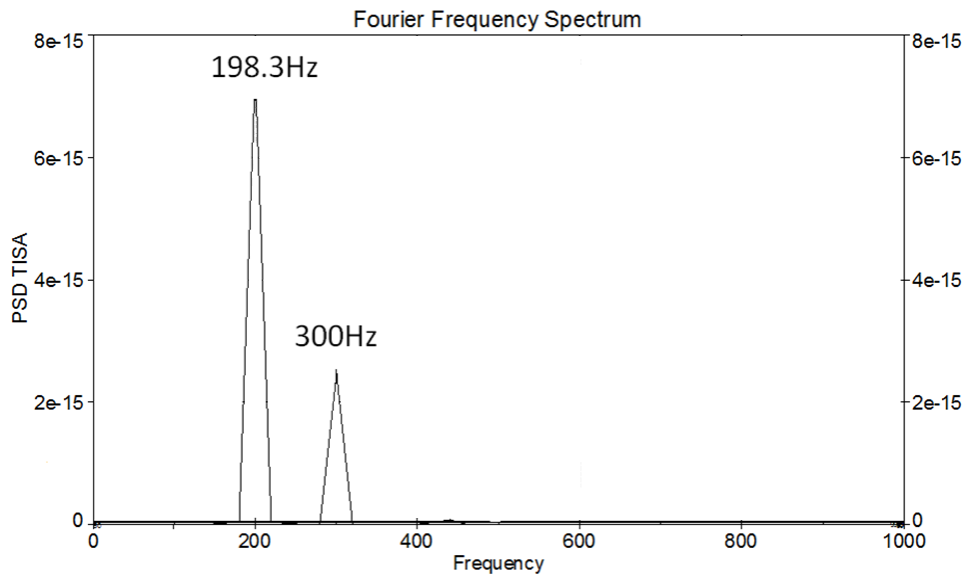


(a) 300Hz

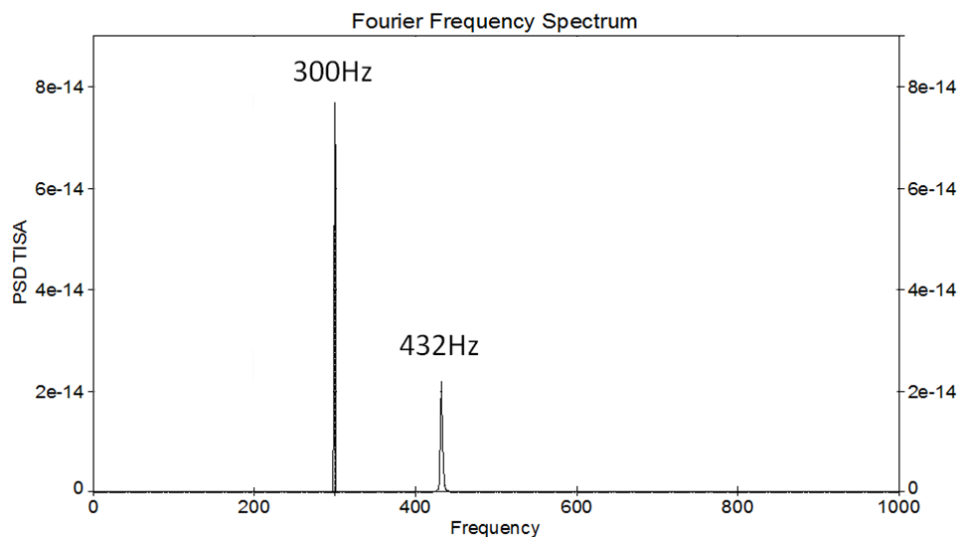


(b) 3500Hz

Figure 3.4: FEA versus numerical analysis ring deflection. Results correspond to the displacement of a point opposite the ring gap, with an excitation frequency of (a): 300Hz, and (b): 3500Hz.



(a)



(b)

Figure 3.5: FEA versus numerical analysis FFT. Results correspond to a point opposite the ring gap, with an excitation frequency of 300Hz. (a): FEA data, and (b): numerical data

Both figures 3.5a and 3.5b show the excitation frequency to be present in the FFT response. However, figure 3.5a shows the response is dominated by one of the natural frequencies for the FEA analysis. This may be due to the shape of the force profile being similar to the excited mode shape. If this was the case, even if the excitation frequency is not near a natural frequency, the force profile may cause modal excitation to occur. The differences due to element size (as the numerical solution does not require elements, as such), and the slight difference in predicted natural frequency between the FEA and numerical

methodologies (as seen in table 3.3), explain why this occurrence has not been seen in both sets of results. The greater the number of elements used, the more accurate the FEA model should be. However, a compromise has to be made regarding computing time. Also, with simple structures such as an incomplete circular ring, a point is reached where additional elements make very little difference to the response of the model. It should be noted that the numerical methodology, which will be used in the compression ring analysis, gives the expected result of the excitation frequency dominating the FFT response.

### 3.3. Ring Out-of-plane Dynamic Response

Similarly to the case of the ring in-plane analysis, the following assumptions are made when considering the out-of-plane ring dynamics:

- Since the neutral radius of the ring is significantly larger than the ring's thickness, it can be assumed that the ring is a thin structure.
- Rotary inertia is neglected in this analysis due to the thin nature of the ring and its relatively small mass and rotation speed.
- The neutral axis of the ring is also assumed to be inextensible ( $\frac{d}{R} \approx 0.0814 < 0.1$ ).

The same assumptions regarding inextensibility and shear deformation are used when discussing the out-of-plane ring dynamics, similarly to the in-plane analysis. Whereas the degrees of freedom when concerned with in-plane dynamics are the radial and tangential displacements, the out-of-plane degrees of freedom are the axial displacement,  $u$ , and twist about the neutral ring radius,  $\beta$ . The ring out-of-plane equations of motion take the following form (Ojalvo, 1962):

$$\frac{\partial^4 u}{\partial \varphi^4} - R \frac{\partial^2 \beta}{\partial \varphi^2} - k \left( \frac{\partial^2 u}{\partial \varphi^2} - R \frac{\partial^2 \beta}{\partial \varphi^2} \right) = \frac{mR^4}{EI_x} \left( \frac{\partial^4 u}{\partial t^2} - \frac{Y}{m} \right) \quad (3.30)$$

$$\frac{\partial^2 u}{\partial \varphi^2} - R\beta + k \left( \frac{\partial^2 u}{\partial \varphi^2} + R \frac{\partial^2 \beta}{\partial \varphi^2} \right) = \frac{mR^4}{EI_x} \left( \frac{\Phi_F}{m} \right) \quad (3.31)$$

where  $Y$  and  $\Phi_F$  are the out-of-plane forcing and torsional loading, respectively.

Once again, it is noted that no in-plane degrees of freedom appear in equations (3.30-31), meaning the two cases are uncoupled from an analytical point of view. The degrees of freedom used in equations (3.30-31) can be seen in figure 3.6.

Ojalvo, I. U. "Coupled twist-bending vibrations of incomplete elastic rings, "*International Journal of Mechanical Sciences* 4.1 (1962): 53-72. (figure 1)

Figure 3.6: Out-of-plane ring motion, exhibiting the relevant degrees of freedom (Ojalvo, 1962)

Since there is no torsional loading in the system we are studying, it is assumed that  $\Phi_F = 0$ . Rearranging equation (3.31) and substituting into equation (3.30):

$$\frac{\partial^4 \beta}{\partial \varphi^4} + 2 \frac{\partial^2 \beta}{\partial \varphi^2} + \beta = \frac{mR^4}{C_z} \left( \frac{1+k}{R} \right) \left( \frac{\partial^2 u}{\partial t^2} - \frac{Y}{m} \right) \quad (3.32)$$

Where  $m$  is the mass per unit length,  $C_z$  is the twisting stiffness and  $k$  is the stiffness parameter. As with equation (3.20), the out-of-plane dynamic response takes the form of a solution comprising a space-varying and a time-varying part. Also, since the force term varies spatially and with time, they have the solution form:

$$u(\varphi, t) = \sum_{n=1}^{\infty} U_n(\varphi) \xi_n(t) \quad (3.33)$$

$$\beta(\varphi, t) = \sum_{n=1}^{\infty} \beta_n(\varphi) \xi_n(t) \quad (3.34)$$

$$Y = f(t) \sum_{n=1}^{\infty} Q_n U_n(\varphi) \quad (3.35)$$

Where  $U_n(\varphi)$  is the mode shape and  $Q_n$  is the forcing function. Equations (3.33-34) represent the solution form of the out-of-plane displacement and twist, respectively. Equation (3.35) shows the form of the force function, as it can vary with respect to both

time and position around the ring. Substitution of equations (3.33-35) into equation (3.32) yields:

$$\xi_n \left( \frac{\partial^4 \beta_n}{\partial \varphi^4} + 2 \frac{\partial^2 \beta_n}{\partial \varphi^2} + \beta_n \right) = \frac{mR^4}{c_z} \left( \frac{1+k}{R} \right) \left( \dot{\xi}_n - \frac{Q_n}{m} f(t) \right) u_n \quad (3.36)$$

Separation of variables in equation (3.36) (Ojalvo, 1962) and after dividing by  $\xi_n u_n$ , it leads to the following equation:

$$-\lambda_n \left( \frac{1+k}{R} \right) = -\omega_n^2 \left( \frac{1+k}{R} \right) \frac{mR^4}{c_z} \quad (3.37)$$

Equation (3.37) provides the homogeneous and non-homogenous parts of the complete out of plane solution:

$$\frac{\partial^4 \beta_n}{\partial \varphi^4} + 2 \frac{\partial^2 \beta_n}{\partial \varphi^2} + \beta_n = -\lambda_n \left( \frac{1+k}{R} \right) u_n \quad (3.38)$$

$$\dot{\xi}_n + \omega_n^2 \xi_n = \frac{Q_n}{m} f(t) \quad (3.39)$$

Equation (3.39) is of the same form as equation (3.21) from the in-plane analysis. Therefore, the solution is expected to take a similar form. The term  $Q_n$  represents the force term applied in the out-of-plane direction and depends on the force profile. In the piston ring-cylinder liner conjunction, the out-of-plane force profile comprises the reaction force from the piston groove due to the piston's motion, gas pressure acting on the top of the ring, friction forces due to lubricant and surface interactions, as well as the ring's inertial response. Ojalvo (1962) presented solution forms for three different loading cases: time-dependent distributed loading, time-dependent concentrated loading and a loading case where the boundary conditions vary with time. The most relevant case to that of a compression ring is the time-dependent distributed loading. The solution has similarities with equation (3.20) and is a function of the mode shapes, as well as the force term:

$$Q_n = \frac{\int_0^\alpha (W(\varphi) u_n) d\varphi}{\int_0^\alpha u_n^2 d\varphi} \quad (3.40)$$

Equation (3.40) shows the force profile as it varies spatially, whereas the  $f(t)$  term in equation (3.39) gives the response with respect to time. To calculate the characteristic equation of the out-of-plane problem, equation (3.31) is rearranged and integrated twice to find an expression for  $u_n$ :

$$u_n = \left( \frac{R}{1+k} \right) \left( \iint_0^\alpha \beta_n d\varphi - k\beta_n \right) \quad (3.41)$$

A solution is assumed for  $\beta_n$ :

$$\beta_n = \sum_{K=1}^3 (A_{nK} \sin \sigma_{nK} \varphi + B_{nK} \cos \sigma_{nK} \varphi) \quad (3.42)$$

Substitution of equations (3.41) and (3.42) into equation (3.38):

$$\sum_{K=1}^3 (\sigma_{nK}^4 - 2\sigma_{nK}^2 + 1) (A_{nK} \sin \sigma_{nK} \varphi + B_{nK} \cos \sigma_{nK} \varphi) = \lambda_n \sum_{K=1}^3 \left( \frac{1}{\sigma_{nK}^2} + k \right) (A_{nK} \sin \sigma_{nK} \varphi + B_{nK} \cos \sigma_{nK} \varphi) \quad (3.43)$$

All terms involving  $\varphi$  are linearly independent; therefore the characteristic equation can be derived:

$$(\sigma_{nK}^6 - 2\sigma_{nK}^4 + \sigma_n^2) = \lambda_n (1 + k\sigma_n^2) \quad (3.44)$$

As with equation (3.8), a cubic equation is formed, the solutions to which are in terms of  $\lambda_n$ . The form of the roots of these equations can vary, as with the in-plane methodology. Burington (1958) described the general form of a cubic equation:

$$S_n^3 + pS_n^2 + qS_n + r = 0 \quad (3.45)$$

Let

$$a \equiv (3q - p^2)/3$$



$$b \equiv (2p^3 - 9pq + 27r)/27$$

$$\Delta \equiv \left( b^2/4 \right) + \left( a^3/27 \right)$$

The three roots of the cubic equation (3.45) depend on  $\Delta$ . The form of these roots varies as follows:

If  $\Delta > 0$ , there is one real root and two complex conjugates, just as with the in-plane methodology:

$$\sigma_{n1} = s1, \quad \sigma_{n2} = \mu + i\nu, \quad \sigma_{n3} = \mu - i\nu$$

The solution form is as follows:

$$\beta_n = A_{n1} \sin \sigma_{n1} \varphi + A_{n2} \sin \mu \varphi \cosh \nu \varphi + A_{n3} \cos \mu \varphi \sinh \nu \varphi + B_{n1} \cos \sigma_{n1} \varphi + B_{n2} \cos \mu \varphi \cosh \nu \varphi + B_{n3} \sin \mu \varphi \sinh \nu \varphi \quad (3.46)$$

If  $\Delta = 0$  then  $\sigma_{n2} = \sigma_{n3}$ , meaning:

$$\beta_n = A_{n1} \sin \sigma_{n1} \varphi + (A_{n2} + A_{n3}) \sin \sigma_{n3} \varphi + B_{n1} \cos \sigma_{n1} \varphi + (B_{n2} + B_{n3}) \cos \sigma_{n3} \varphi \quad (3.47)$$

If  $\Delta < 0$ , there are two possibilities. If  $k\lambda_n < 1$ , there are 3 positive, unequal roots:

$$\beta_n = A_{n1} \sin \sigma_{n1} \varphi + A_{n2} \sin \sigma_{n2} \varphi + A_{n3} \sin \sigma_{n3} \varphi + B_{n1} \cos \sigma_{n1} \varphi + B_{n2} \cos \sigma_{n2} \varphi + B_{n3} \cos \sigma_{n3} \varphi \quad (3.48)$$

Finally, if  $k\lambda_n > 1$ , there is one real and two imaginary roots:

$$\beta_n = A_{n1} \sin \sigma_{n1} \varphi + A_{n2} \sinh \sigma_{n2} \varphi + A_{n3} \sinh \sigma_{n3} \varphi + B_{n1} \cos \sigma_{n1} \varphi + B_{n2} \cosh \sigma_{n2} \varphi + B_{n3} \cosh \sigma_{n3} \varphi \quad (3.49)$$

For equations (3.46-49), the expression for the out-of-plane displacement is:

$$U_n = \left( \frac{1}{\sigma^2} + k \right) \beta_n \quad (3.50)$$

Archer (1960) stated that solutions to equation (3.47) were only valid when the total ring subtended angle was greater than  $2\pi$ . Therefore, for the case of a compression ring, equations (3.46) and (3.48) are the relevant solution forms. These are substituted into equation (3.41), which is in turn substituted into the boundary conditions (Ojalvo, 1962). The constants cancel, leaving:

$$M_x = \left( R\beta - \frac{\partial^2 \beta}{\partial \varphi^2} \right) \quad (3.51)$$

$$M_z = \left( R \frac{\partial \beta}{\partial \varphi} + \frac{\partial u}{\partial \varphi} \right) \quad (3.52)$$

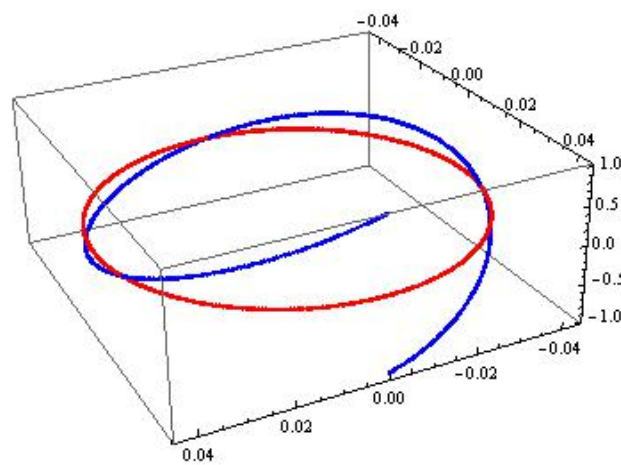
$$V = \frac{\partial \left( \frac{\partial^2 u}{\partial \varphi^2} - R\beta \right)}{\partial \varphi} - k \left( \frac{\partial u}{\partial \varphi} + R \frac{\partial \beta}{\partial \varphi} \right) \quad (3.53)$$

The boundary conditions (3.51-53) equal zero for  $\varphi = 0$  and  $\varphi = \alpha$  in the case of an incomplete ring, unrestrained at each end. Once more similarities with the in-plane analysis are seen, as this gives a set of 6 equations, each a function of the constants  $A_{n1-3}$  and  $B_{n1-3}$ . Setting the determinant of this 6x6 matrix equal to zero and finding the roots, it gives the frequency parameter specific to each mode and natural frequency.

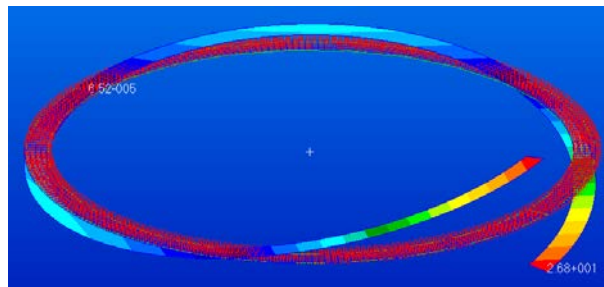
As with the in-plane analysis, an FEA model can be used to verify the methodology discussed. Table 3.4 shows a comparison of the natural frequencies for both the numerical and FEA models. The same ring properties are used from the in-plane analysis. Figure 3.7 shows a comparison between the analytical method and an FEA model of a free ring. As with the in-plane methodology, an excellent agreement is seen.

Table 3.4: Out-of-plane compression ring natural frequencies.

Mode Number	Analytical Method Natural Frequency (Hz)	FEA model Natural Frequency (Hz)	% Difference
1	92.54	93.33	0.846
2	254.29	256.42	0.828
3	534.92	538.91	0.74
4	903.02	908.57	0.611
5	1357.72	1366.52	0.644
6	1889.86	1901.72	0.624
7	2506.75	2520.66	0.552



(a)

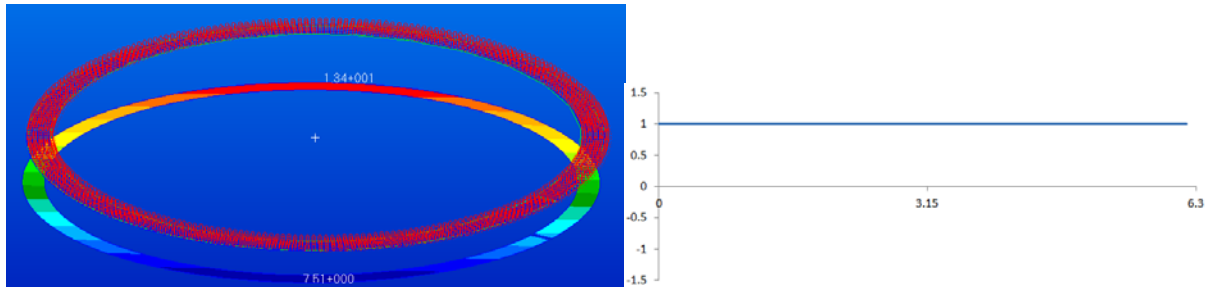


(b)

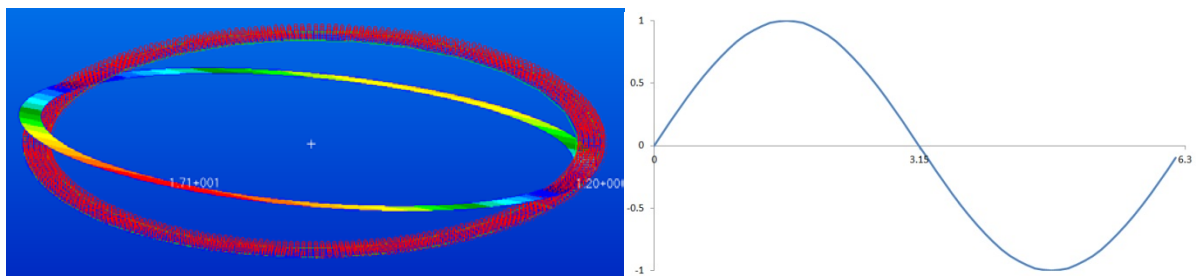
Figure 3.7: Out-of-plane ring mode shape comparison, (a) Analytical method ( $f = 93.33\text{Hz}$ ) and (b) FEA model ( $f=93.33\text{Hz}$ ).

The above methodology gives the out-of-plane elastodynamic response. Once again however, rigid body modes must be accounted for. A modal analysis of the FEA model shows three out of plane rigid body modes, as seen in figure 3.8. It can be seen that there is one purely translational mode and two ‘tilting’ rigid body modes, perpendicular to each other. Next to each FEA image, a graphical representation of the mode shape is shown, to

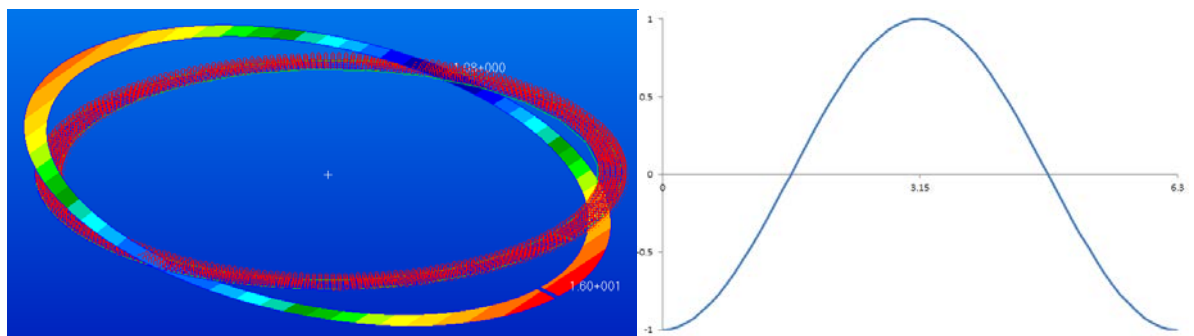
indicate the function which models the rigid body response in each case. The ring is ‘unwrapped’, with circumferential position along the x axis. It can be seen that the out of plane translation is represented by a constant term, whilst the two rotational rigid body modes follow a sinusoidal and cosine curve respectively.



(a)



(b)



(c)

Figure 3.8: Out-of-plane rigid body mode shapes

To account for these rigid body modes, an expression to describe their profile must be assumed, to replace equation (3.50), which describes the elastic mode shape  $u_n$ . For the translational mode in figure 3.8a, since the displacement is constant circumferentially, it is assumed that  $u_n = 1$ . For each of the tilting rigid body modes it can be seen that  $u_n = \sin(\varphi)$  for figure 3.8b, and  $u_n = \cos(\varphi)$  for figure 3.8c. Normalisation of these rigid body modes, as

described for the in-plane case using Natsiavas (2001), can be performed, to ensure that the size of the mode shapes is coupled to the size of the elastic mode shapes.

As with the in-plane analysis, known forces were applied to the numerical and FEA model, to verify that the numerical analysis can accurately predict the out-of-plane motion of the ring. The first test was to apply a load that varied with time only:

$$F_R = F \sin \omega_f t \quad (3.54)$$

A load profile such as this would be expected to excite a rigid body response predominantly when applied to a free-free ring, since the excitation frequency isn't near any of the ring's natural frequencies and the force profile is constant circumferentially. Figure 3.9 shows that FEA and numerical response have excellent agreement. Both the FEA and numerical results correspond to the motion of a point at the ring gap. Since the force profile doesn't change circumferentially, this response is seen at each point around the ring.

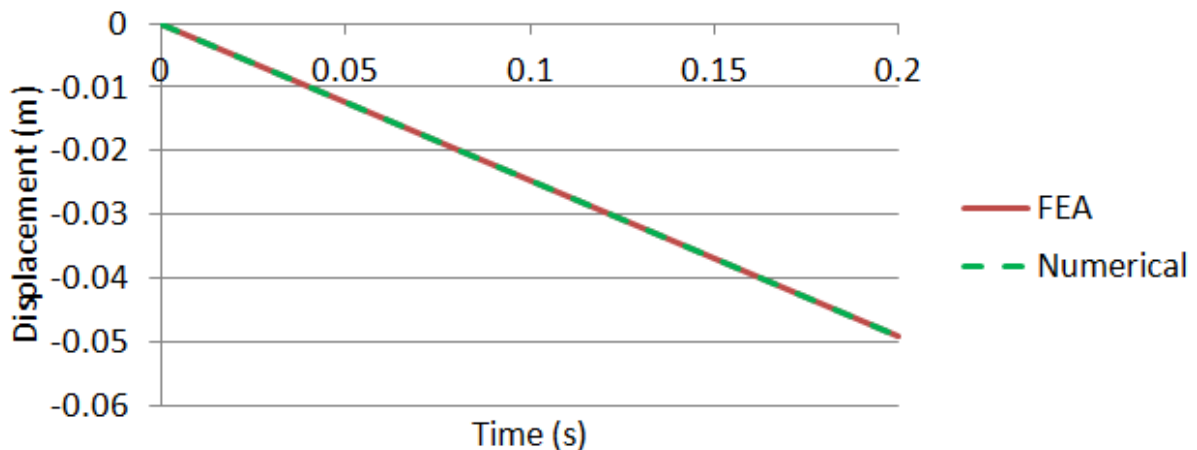


Figure 3.9: FEA and Numerical response when circumferentially constant load is applied.

Max. Load equivalent = 10kPa, frequency of excitation = 700Hz.

For further verification, more complex force profiles were applied. Equation (3.55) shows a force profile which varies with both space and time. Elastic modes will be excited more prominently, since the profile varies with respect to the ring's circumference:

$$F_R = F \cos 2\varphi \sin \omega_f t \quad (3.55)$$

Once again, very good agreement of the deflection amplitude is seen in the response of figure 3.10. However the rigid body modes are not as dominant as in the previous example. FFT analysis of the results of figure 3.10a is shown in figure 3.11.

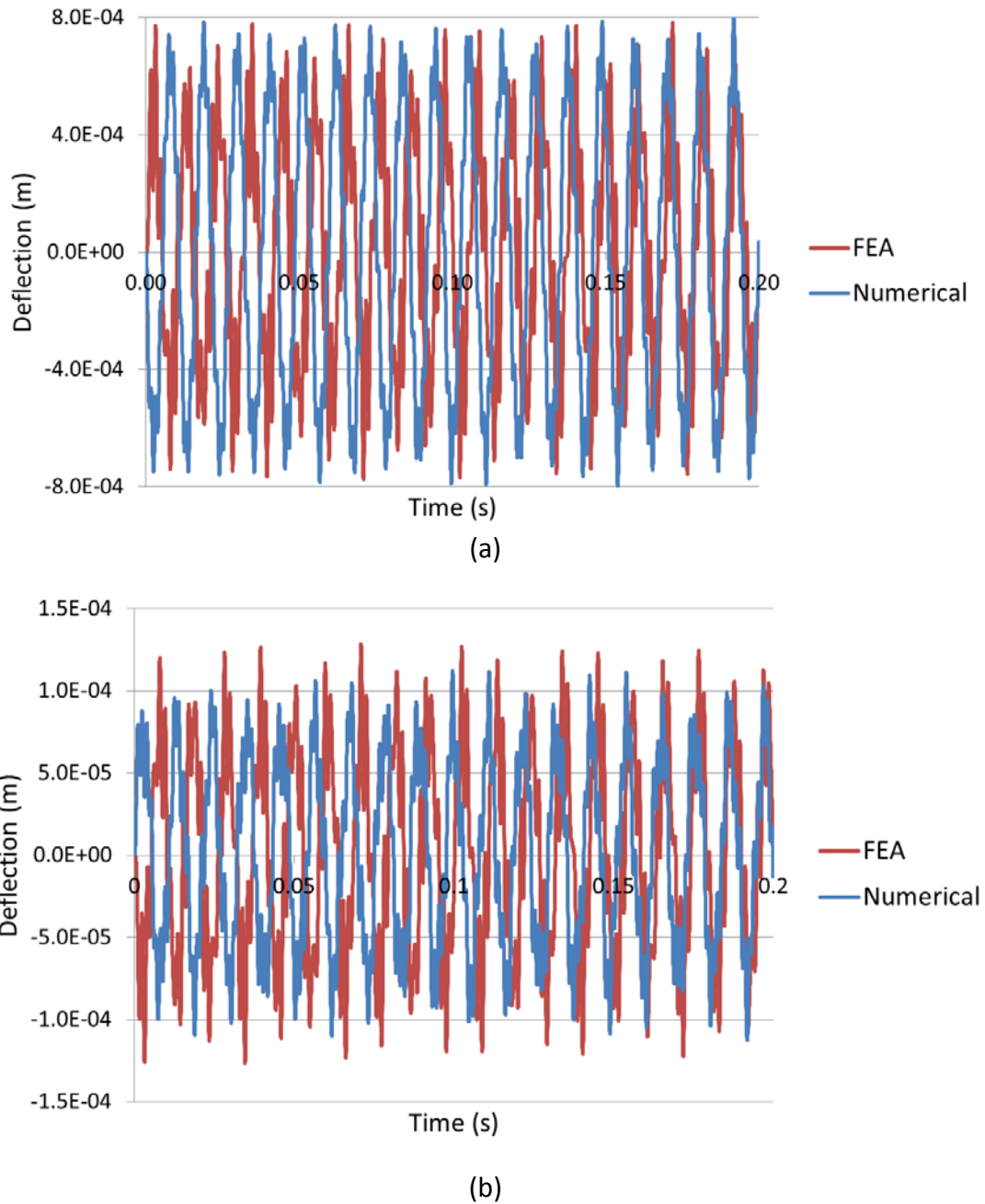
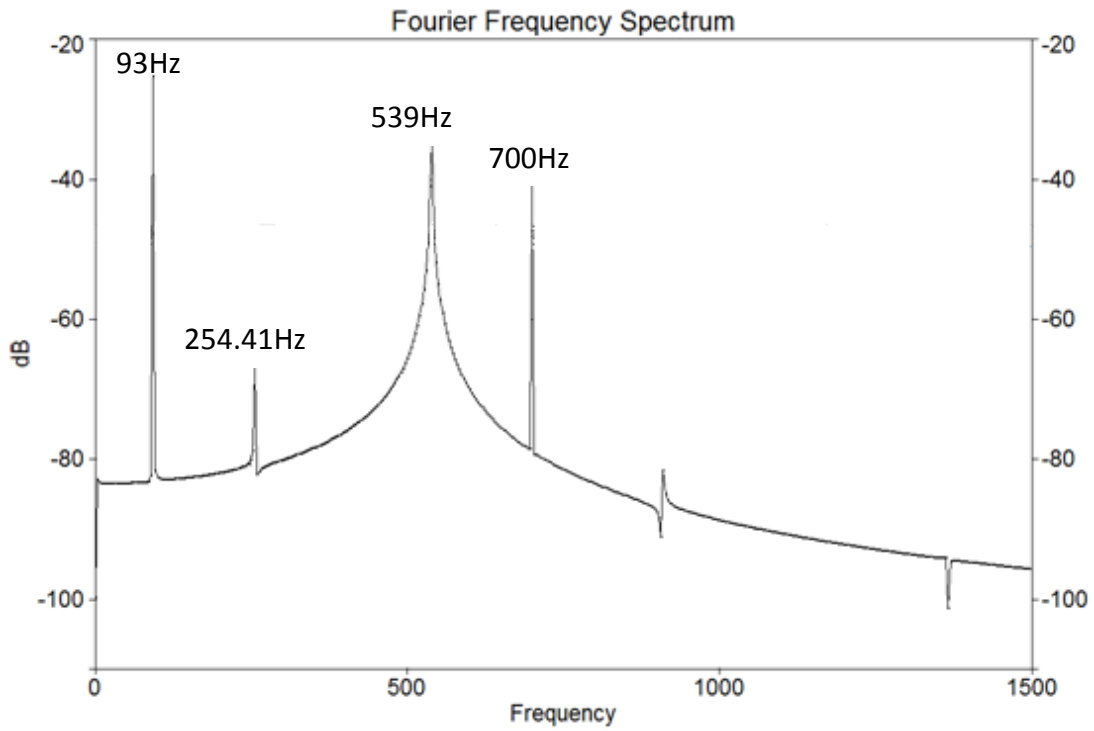
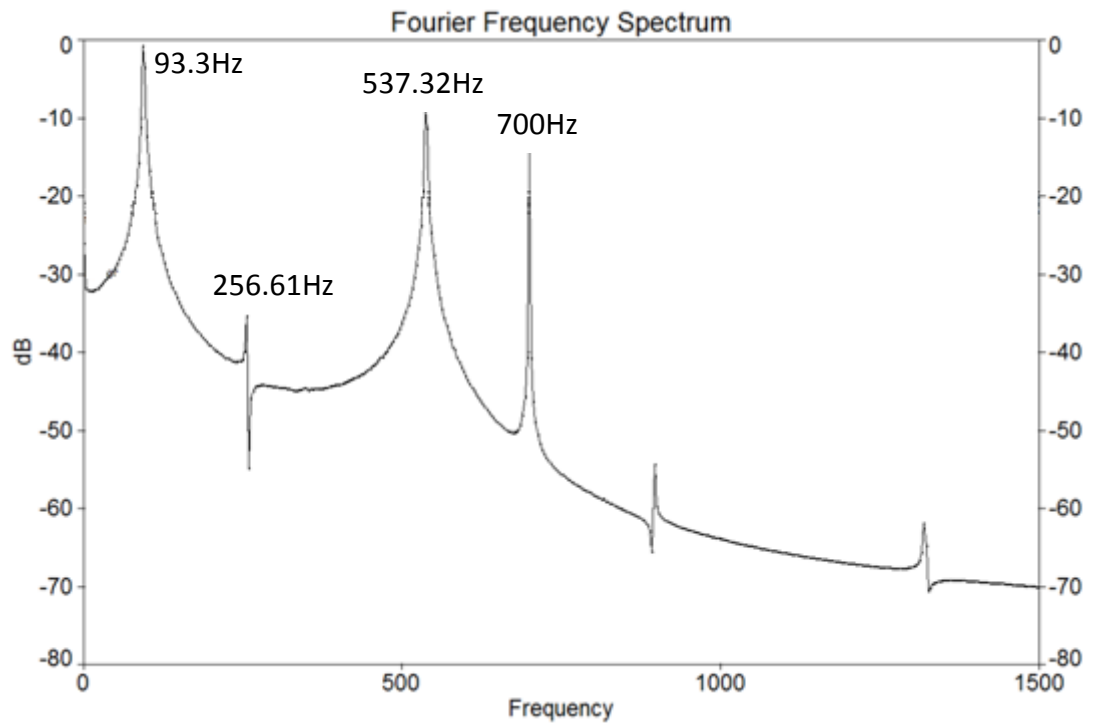


Figure 3.10: Numerical and FEA response for the force profile of equation (55) at (a) the ring gap and (b) part-way around the ring. The excitation frequency is 700Hz.



(a)



(b)

Figure 3.11: FEA versus numerical analysis FFT. Results correspond to a point opposite the ring gap, excitation frequency = 700Hz (a) numerical, (b) FEA

### 3.4. Coupling of the Ring Dynamics Methodology to the Tribological Analysis

The ring dynamic response for both in-plane and out-of-plane cases, includes a forcing term which incorporates any excitation applied in the relevant plane of the ring. It is proposed that this force profile is extracted from the tribological analysis, after calculating the external and internal forces acting upon the ring. The forces acting upon a cross section of the ring are shown in figure 3.12. Initially considering the in-plane analysis, it can be seen that the forces contributing are the ring's elastic (fitment) force, the combustion gas pressure and reaction forces from the lubricant and liner wall.

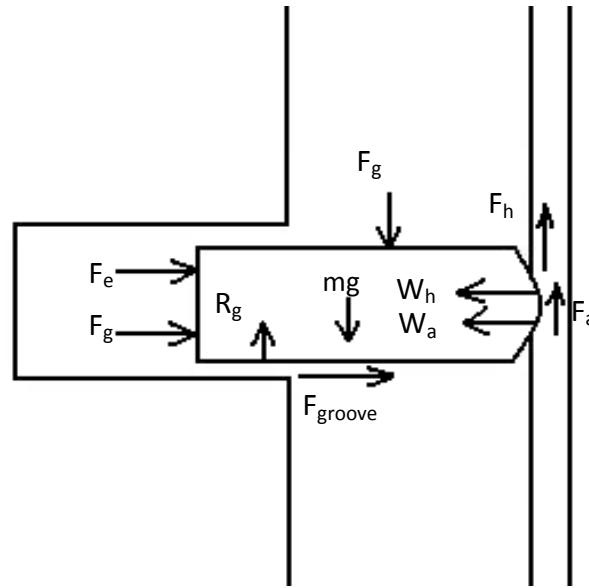


Figure 3.12: Cross-sectional free body diagram of the top compression ring.

In a quasi-static analysis with an assumed rigid ring (as it has been reported in literature), this net force is equilibrated by the generated conjunctural pressures. The latter are the result of instantaneous tribological conditions, which are determined according to the gap between the ring and the bore surface. A mixed hydrodynamic analysis is carried out, culminating in contact reactions due to the viscous action of the lubricant,  $W_h$  and asperity interactions,  $W_a$ . Thus:

$$W_h + W_a = F_e + F_g \quad (3.56)$$

The inclusion of ring elastodynamics in the compression ring analysis requires an excitation force. Therefore, instead of balancing the in-plane forces, these should be added algebraically, giving a net force profile acting upon the ring, as depicted in equation (3.57):

$$W_h + W_a - F_e - F_g = F_R \quad (3.57)$$



The  $F_R$  term in equation (3.57) is exported to the dynamics methodology in a compatible form with the analysis, as a Fourier series. The net force acting upon the ring can then be exported to the ring dynamics solution, which returns the deflections and local velocities on the ring surface. This deformed ring profile is then returned to the tribological analysis, updating the film profile (circumferentially) for the next crank angle increment. The expression for the ring-liner gap is shown in equation (3.58).

$$h(x, y, t) = h_m(t) + h_s(x, t) + \Delta_s(y, t) + \Delta_{th}(y, t) + \Delta_d(y, t) + \delta(p) \quad (3.58)$$

where, the overall gap,  $h$  (film thickness) comprises several constituents;  $h_m$  represents the variations in the minimum film thickness with time. The parameter  $h_s$  is the ring face-width profile, which can vary with time due to the inclusion of ring twist. In equation (3.58)  $\delta$  is the localised contact deformation (EHL), which is not included in this analysis.  $\Delta_s$ ,  $\Delta_{th}$  and  $\Delta_d$  represent the ‘global’ elastostatic, thermoelastic and elastodynamic deformation of either the ring and/or the liner. The initial distortion which exists in a fitted liner within the engine block or due to the tightening of the cylinder head bolts, if not accommodated by the fitted ring in the liner will yield a non-zero value for  $\Delta_s$ . A thermoelastic analysis may provide the thermally deformed bore profile for which the emerging gap can be included in  $\Delta_{th}$ .  $\Delta_d$  takes into account the change in the ring/liner gap due to deformations caused by mechanical vibrations of the bore and/or the ring under transient loads. The inclusion of thermal distortions is not within the scope of the current analysis. In addition, the effects of static deformations and ring/liner conformability have already been comprehensively studied elsewhere (2012). The ring face-width used in this study is similar to that used in Rahmani et al (2012). The profile of a new ring is assumed for most of the presented results. However, a worn ring profile is also considered. The worn ring profile is measured after a 150hr high speed engine test, representing 100,000 km normal vehicle use.

Figure 3.12 shows the algorithm for the coupling of in-plane dynamics and the tribology code. This coupled tribo-dynamics methodology will be mainly used in this thesis when performing a tribological analysis of the compression ring instead of the common assumption of ring rigidity. The previous tribological analysis of the piston ring-cylinder liner conjunction requires an iterative loop when calculating the load. Inclusion of ring dynamics removes the need for this iteration.

The approach with which the out-of-plane methodology is coupled to the tribological analysis differs slightly from the in-plane solution. The free body diagram of figure 3.11 shows the following relation:

$$F_g + mg - F_a - F_h - R_g = F_A \quad (3.59)$$

where  $F_A$  is the resultant out-of-plane force acting upon the ring.

The ring's weight is negligible when compared to the gas pressures involved, so it can be ignored in this analysis. The reaction force from the groove acting upon the ring is calculated using Tian's method (1998). A layer of lubricant is assumed to be present on the groove's surface. Tian has solved the 1D Reynolds' equation analytically:

$$\frac{d}{dx} \left( \frac{h^3}{\eta} \frac{dp_{oil}}{dx} \right) = 12 \frac{\partial h}{\partial t} \quad (3.60)$$

It can be seen that this approach neglects the effect of sliding between the ring and the groove face. If the ring is assumed to be rigid, then this assumption is reasonable. However with in-plane dynamics being included, a sliding effect can be included due to the radial motion of the ring. Therefore, equation (3.60) becomes:

$$\frac{d}{dx} \left( \frac{h^3}{\eta} \frac{dp_{oil}}{dx} \right) = 6\dot{w}(\varphi, t) \frac{\partial h}{\partial x} + 12 \frac{\partial h}{\partial t} \quad (3.61)$$

Solution of equation (3.61) by integrating between the edge of the groove and the inner edge of the ring gives the pressure profile. From this, further integration gives the force term needed for substitution into equation (3.59).

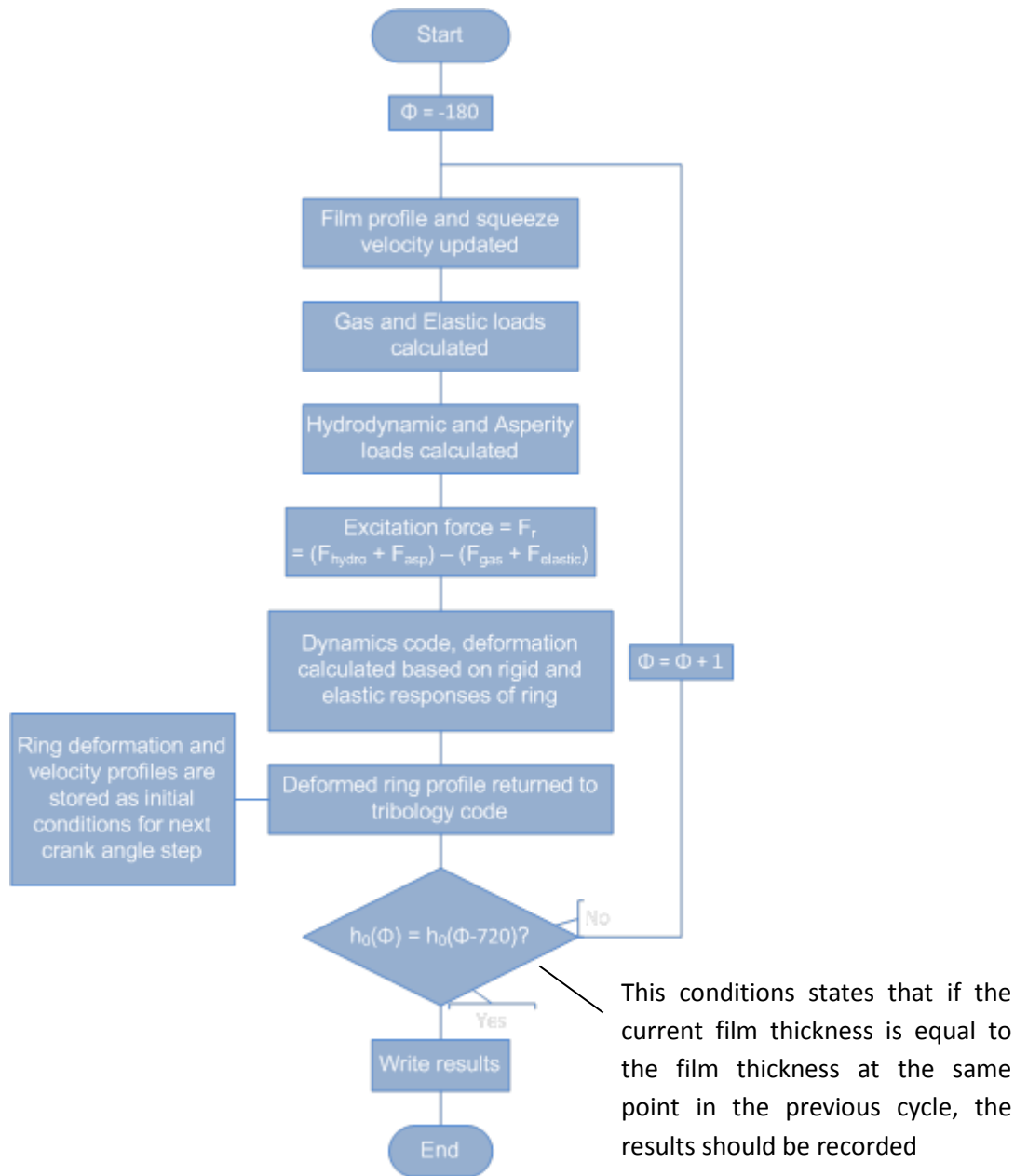


Figure 3.13: Coupled in-plane tribo-dynamics algorithm

It should be noted that the term  $F_g$  is the net gas force, which is the difference between the cylinder and crankcase gas loads. Crankcase pressure is assumed to equal atmospheric pressure for this analysis, although an inter-ring gas pressure model would change this accordingly. As with the in-plane methodology, a Fourier series will be required to convert  $F_A$  into a compatible form that can be included in the analytical solution. One of the key differences between the dynamics in the two planes is that the piston's axial velocity will affect the response of the ring in the out-of-plane direction. The effect of this will be

present in the initial conditions when solving the time-based section of the out-of-plane response.

Whilst any in-plane deformations are returned to update the film profile, this will not be possible with the out-of-plane analysis, as the film profile is not measured in this plane. Instead, the out-of-plane deformations will affect the friction calculations at each crank angle increment. In addition to this, ring twist will affect the ring's axial profile when solving Reynolds' equation. The previous analysis (assuming a new compression ring, whose profile has had a polynomial function fitted to it) used equation (3.62) to calculate the ring's axial profile:

$$y = ax^6 + bx^5 + cx^4 + dx^3 + ex^2 + fx + g \quad (3.62)$$

Using matrix algebra, the expression in equation (3.62) can be manipulated to account for the ring's twist:

$$y' = z \sin \varphi + y \cos \varphi \quad (3.63)$$

Where  $\varphi$  is the angle of twist calculated using the out-of-plane methodology, and  $z$  is the position along the ring's axial profile. Figure 3.13 shows the solution algorithm for inclusion of ring dynamics in both planes.

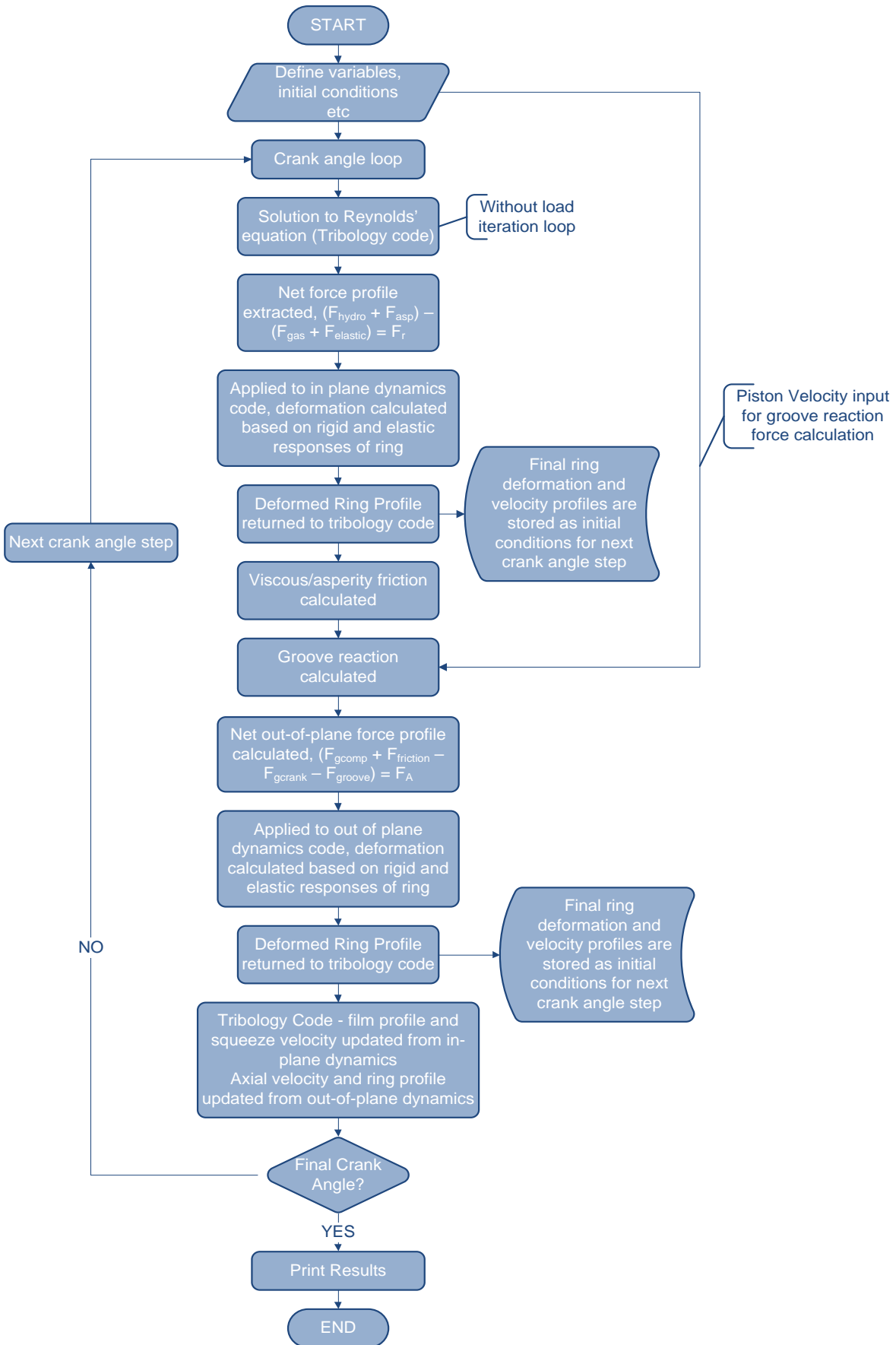


Figure 3.14: Coupled tribo-dynamics algorithm for both planes of motion

### 3.5. Closure

This chapter detailed the ring dynamics theory which will be used to model the compression ring's dynamic deflections through the engine's cycle. Elastic and rigid body solutions, in both planes, are included to give a complete elastodynamic model of the ring. Whilst the equations of motion in both planes are not new, the manipulation to account for the rigid body response in both planes has not previously been detailed or published in literature for incomplete circular rings. Verification for the elastic dynamic response has also not been previously available in literature, with results previously presented for the modal analysis only.

The proposed coupling methodology is also described, stating how the dynamic analysis fits into the current tribological model. This approach of including ring dynamics in a transient manner has not previously been published, despite it appearing to be a logical progression to attempt to capture the ring's deflection throughout the engine cycle. The algorithm demonstrating this coupling method is included, which allows the reader a greater understanding of where the ring dynamics will affect the current tribological methodology.

## **4. Tribology of the compression ring**

### **4.1. Introduction**

This chapter provides the methodology behind the equations used in the tribological analysis of the piston ring to cylinder bore conjunction. The lubricant rheology and parameters which affect it are discussed, as well as the regimes of lubrication encountered. The implementation of Reynolds equation is detailed for 2D transient analysis. Thermal effects due to shear and to a much lesser degree compressive heating are considered in some current analysis. The energy equation is discussed with the appropriate boundary conditions explained, with temperature rise predictions presented, showing whether the inclusion of the energy equation is justified. Thin films also mean that surface asperities interact on the counterfaces and affect the tribological performance of the conjunction. Therefore, asperity interactions should also be part of the solution. The solution for this allows for measured roughness data from the components, giving a more accurate prediction of the conditions encountered.

### **4.2. Lubrication and Lubricant Rheology**

#### **4.2.1. Regimes of Lubrication**

There are four categories of lubrication regime, all of which should be considered when analysing the piston ring-cylinder liner conjunction, which have been discussed in the previous chapters. The frictional contact of surfaces is known as boundary lubrication (Gohar and Rahnejat, 2008). In this regime, the coefficient of friction is relatively high due to lack of fluid film. Oxide films or additives may be present to aid friction reduction. If boundary lubrication was to occur during the combustion cycle, it would be at the reversal points of top and bottom dead centres. However, boundary lubrication is a rare occurrence, with a mixed regime of lubrication most likely.

From a theoretical point of view, mixed lubrication occurs when the surface roughness equals the lubricant film thickness. This means that the contact load is supported by both the lubricant and asperities on both the cylinder and the ring. As with boundary lubrication, high frictional forces can occur, whilst debris may also result in asperity interactions.

An increase in load or film thickness moves the contact into the elastohydrodynamic or hydrodynamic regimes of lubrication. A characteristic of EHL is high pressures within the contact, which causes an increase in lubricant viscosity as well as local surface deformation of the contiguous solids. The lubricant occupies the space in these distortions, enabling high loads to be carried with relatively low frictional losses. This type of contact often occurs in bearings, gears or cam-tappet pairs where the contact is counterformal, with quite small footprint area and with high load intensity. Soft EHL occurs with materials of low elastic modulus, for example, in synovial joints in humans and other animals, and is seen as an ideal contact for high load – low wear performance (Dowson and Neville, 2006).

Contacts with lubricant films of larger thickness fall into the hydrodynamic regime of lubrication. Under hydrodynamic conditions, the contact load is carried fully by the hydrodynamic pressures generated in the lubricant film. The loads encountered are lower than those under EHL conditions, such as those met at the mid-stroke of the engine cycle.

#### 4.2.2. Parameters Affecting Lubricant Properties

##### 4.2.2.1. Density

The density of a material or substance is the mass per unit volume, with SI units of kilograms per cubic metre. An increase in pressure sees very little change in the density of a lubricant, as verified by Dowson (1966), unless pressures are in the order of few hundred MPa. These results also indicate a linear change in density with pressure. The Dowson and Higginson (1959) relationship describing the effect of pressure on density is shown in equation (4.1):

$$\bar{\rho} = \frac{\rho}{\rho_0} = 1 + \frac{0.6 \times 10^{-9} p}{1 + 1.7 \times 10^{-9} p} \quad (4.1)$$

Temperature variations have very little effect on the density of a lubricant. However, Stachowiak and Batchelor (2001) gave the following expression to show the change of density with temperature:

$$\rho = \rho_{atm} \xi^{(\theta - \theta_0)} \quad (4.2)$$

$\xi$  is the density-temperature factor, whilst  $\theta$  and  $\theta_0$  represent the final and atmospheric temperatures respectively. Combining equations (4.1) and (4.2) gives the final expression for the density of the lubricant, accounting for the changes in contact conditions:



$$\rho = \rho_{atm}^{\xi(\theta-\theta_0)} \left[ 1 + \frac{0.6 \times 10^{-9}(p-p_{atm})}{1+1.7 \times 10^{-9}(p-p_{atm})} \right] \quad (4.3)$$

#### 4.2.2.2. Viscosity

Viscosity is the resistance of a fluid to flow. It can be expressed either as kinematic or dynamic viscosity. The dynamic viscosity of a fluid is the term most commonly seen in equations such as Reynolds. Dynamic viscosity is related to the shear modulus of a material, G:

$$G = \frac{\text{shear stress}}{\text{shear strain}} = \frac{\tau}{dx/dz} \quad (4.4)$$

The dynamic viscosity,  $\eta$ , is a ratio of the shear stress against the rate of shear strain:

$$\eta = \frac{\tau}{du/dz} \quad (4.5)$$

where  $du$  is the velocity between the top and bottom surfaces of a layer of fluid. The kinematic viscosity gives the dynamic viscosity per unit density. Viscosity is a property of the lubricant, which is affected more significantly than the density by variations in working conditions.

For an isothermal analysis, the Barus Law (1893) shows how viscosity changes with temperature:

$$\eta = \eta_0^{\alpha p} \quad (4.6)$$

Where  $\alpha$  is the pressure-viscosity coefficient, and is a property of the lubricant. However, equation (4.6) is inaccurate for sliding contacts due to viscous shear causing an increase in temperature. High pressure contacts also cause Barus' equation to over-predict. A more accurate method of predicting the viscosity within a sliding contact was derived by Roelands (1966):

$$\eta_r = \eta_0^{(\ln(\eta_0)+9.67)((1+5.1 \times 10^{-9}p)-1)} \quad (4.7)$$

This expression was developed by Houpert (1985) to include both pressure and thermal effects:

$$\eta_e = \eta_0 \exp \left\{ [\ln(\eta_0) + 9.67] \left[ \left( \frac{\theta - 138}{\theta_0 - 138} \right)^{-\frac{\beta_0(\theta_0 - 138)}{\ln(\eta_0) + 9.67}} \left( 1 + \frac{p}{1.98 \times 10^8} \right)^{\frac{\alpha_0}{5.1 \times 10^{-9} [\ln(\eta_0) + 9.67]}} - 1 \right] \right\} \quad (4.8)$$

An example detailed by Gohar and Rahnejat (2008) compares equations (4.6) and (4.8) to show the inaccuracies of Barus' equation. It is shown that  $\eta_{\text{Barus}}/\eta_{\text{Roelands}} = 188$  for a given temperature and pressure change. This shows a significant difference in predicted results, with Houpert's modification of the Roelands equation given much more reasonable values.

### 4.3. The Reynolds Equation

#### 4.3.1. Derivation of the Reynolds Equation

The Reynolds Equation is the basis of the lubrication theory, and it has been detailed by many authors on the subject area. Reynolds (1895) derived his expression for describing pressure distribution throughout a contact based on an equation derived by Navier (1823) and developed further by Stokes (in 1845). They produced a generalised equation for fluid flow, based on Newton's slow viscous fluid model. Therefore, Reynolds equation is a simplified Navier-Stokes equation with dominant action of the viscous force and assumed laminar flow in narrow conjunctions.

Figure 4.1a shows the fluid between a stationary surface and a surface moving parallel to it. With a constant flow and no change in the size of the area to flow in to, there is no pressure gradient along the surfaces. This alters when the gap shape is changed as shown in figure 4.1b. As the gap narrows, the lubricant velocity profile increases. Just as water in a river runs quickest to an area of low pressure, a bulging velocity profile indicates a lower pressure in the contact. The reverse must therefore be true when the gap is widest and pressure is increasing. This infers that there must be a point along the surface where the velocity profile is linear, as in figure 4.1a, and at this point the pressure is at a maximum. This is the basic principle on which a bearing works, and is the cornerstone of Reynolds' equation.

Gohar, R. and Rahnejat, H., (2008) *"Fundamentals of Tribology"*, London: Imperial College Press (figure 6.2)

Figure 4.1: Principle of the wedge film (Gohar and Rahnejat, 2008)

Figure 4.2 shows the axes to be used in the derivation of Reynolds equation. Generally, the x axis represents the contact width; y indicates contact length, whilst z is the distance between the two surfaces, usually the film thickness. The forces acting upon a small element of fluid are also shown, as both normal and shear stresses.

Balakrishnan, S., "Transient Elastohydrodynamic Analysis of Piston Skirt Lubricated Contact Under Combined Axial, Lateral and Tilting Motion", PhD Thesis (2002) (figure 4.5)

Figure 4.2: Forces on a unit element of fluid (Balakrishnan, 2002)

With reference to figure 4.2, the stress-strain relations for a unit element of fluid, assuming Newtonian flow, can be written as (Navier (1823), Stokes (1845)):

$$\rho \frac{Du}{Dt} = F_x - \frac{\partial p}{\partial x} + \frac{\partial}{\partial x} \left\{ 2\eta \frac{\partial u}{\partial x} + \gamma \left( \frac{\partial u}{\partial x} + \frac{\partial v}{\partial y} + \frac{\partial w}{\partial z} \right) \right\} + \frac{\partial}{\partial y} \left\{ \eta \left( \frac{\partial u}{\partial y} + \frac{\partial v}{\partial x} \right) \right\} + \frac{\partial}{\partial z} \left\{ \eta \left( \frac{\partial w}{\partial x} + \frac{\partial u}{\partial z} \right) \right\} \quad (4.9)$$

$$\rho \frac{Dv}{Dt} = F_y - \frac{\partial p}{\partial y} + \frac{\partial}{\partial y} \left\{ 2\eta \frac{\partial v}{\partial y} + \gamma \left( \frac{\partial u}{\partial x} + \frac{\partial v}{\partial y} + \frac{\partial w}{\partial z} \right) \right\} + \frac{\partial}{\partial z} \left\{ \eta \left( \frac{\partial v}{\partial z} + \frac{\partial w}{\partial y} \right) \right\} + \frac{\partial}{\partial x} \left\{ \eta \left( \frac{\partial u}{\partial y} + \frac{\partial v}{\partial x} \right) \right\} \quad (4.10)$$

$$\rho \frac{Dw}{Dt} = F_z - \frac{\partial p}{\partial z} + \frac{\partial}{\partial z} \left\{ 2\eta \frac{\partial w}{\partial z} + \gamma \left( \frac{\partial u}{\partial x} + \frac{\partial v}{\partial y} + \frac{\partial w}{\partial z} \right) \right\} + \frac{\partial}{\partial x} \left\{ \eta \left( \frac{\partial w}{\partial x} + \frac{\partial u}{\partial z} \right) \right\} + \frac{\partial}{\partial y} \left\{ \eta \left( \frac{\partial v}{\partial z} + \frac{\partial w}{\partial y} \right) \right\} \quad (4.11)$$

where  $\frac{D}{Dt}$  describes the flow with respect to time and is the complete covariant differential.

$\rho \frac{Du}{Dt}$ ,  $\rho \frac{Dv}{Dt}$  and  $\rho \frac{Dw}{Dt}$  are reliant on initial conditions, and the right hand side of equations 4.9-4.11 comprise the viscous terms, pressure gradient and body forces acting upon the fluid element in figure 4.2. The forces acting upon the same unit of fluid during flow are shown in figure 4.2. For continuity of flow and conservation of mass (Navier (1823), Stokes (1845)):

$$\frac{\partial \rho}{\partial t} + \frac{\partial}{\partial x} (\rho u) + \frac{\partial}{\partial y} (\rho v) + \frac{\partial}{\partial z} (\rho w) = 0 \quad (4.12)$$

Reynolds derived the equation governing pressure distribution in a Newtonian lubricant film. In doing so, assumptions had to be made whilst manipulating the Navier-Stokes equations:

- The lubricant viscosity and density are assumed to be constant across the film, from one surface to the other. Equations (4.9)-(4.11) can then be simplified as follows:

$$\rho \frac{Du}{Dt} = F_x - \frac{\partial p}{\partial x} + (\eta + \gamma) \frac{\partial}{\partial x} \left( \frac{\partial u}{\partial x} + \frac{\partial v}{\partial y} + \frac{\partial w}{\partial z} \right) + \eta \left( \frac{\partial^2 u}{\partial x^2} + \frac{\partial^2 u}{\partial y^2} + \frac{\partial^2 u}{\partial z^2} \right) \quad (4.13)$$

$$\rho \frac{Dv}{Dt} = F_y - \frac{\partial p}{\partial y} + (\eta + \gamma) \frac{\partial}{\partial y} \left( \frac{\partial u}{\partial x} + \frac{\partial v}{\partial y} + \frac{\partial w}{\partial z} \right) + \eta \left( \frac{\partial^2 v}{\partial x^2} + \frac{\partial^2 v}{\partial y^2} + \frac{\partial^2 v}{\partial z^2} \right) \quad (4.14)$$

$$\rho \frac{Dw}{Dt} = F_z - \frac{\partial p}{\partial z} + (\eta + \gamma) \frac{\partial}{\partial z} \left( \frac{\partial u}{\partial x} + \frac{\partial v}{\partial y} + \frac{\partial w}{\partial z} \right) + \eta \left( \frac{\partial^2 w}{\partial x^2} + \frac{\partial^2 w}{\partial y^2} + \frac{\partial^2 w}{\partial z^2} \right) \quad (4.15)$$

- The dilation term can be neglected for incompressible fluids, meaning:

$$\left( \frac{\partial u}{\partial x} + \frac{\partial v}{\partial y} + \frac{\partial w}{\partial z} \right) = 0 \quad (4.16)$$

- The oil is a thin film, and as such has negligible mass. This means gravitational forces are negligible:

$$F_x = F_y = F_z = 0 \quad (4.17)$$

- Due to the small element size, the inertial forces acting on the fluid can be ignored:

$$\rho \frac{Du}{Dt} = \rho \frac{Dv}{Dt} = \rho \frac{Dw}{Dt} = 0 \quad (4.18)$$

These assumptions reduce equations (4.13)-(4.15) as follows:

$$\frac{\partial p}{\partial x} = \eta \left( \frac{\partial^2 u}{\partial x^2} + \frac{\partial^2 u}{\partial y^2} + \frac{\partial^2 u}{\partial z^2} \right) \quad (4.19)$$

$$\frac{\partial p}{\partial y} = \eta \left( \frac{\partial^2 v}{\partial x^2} + \frac{\partial^2 v}{\partial y^2} + \frac{\partial^2 v}{\partial z^2} \right) \quad (4.20)$$

$$\frac{\partial p}{\partial z} = \eta \left( \frac{\partial^2 w}{\partial x^2} + \frac{\partial^2 w}{\partial y^2} + \frac{\partial^2 w}{\partial z^2} \right) \quad (4.21)$$

- A thin film means the assumption that the pressure across the film (the z-direction) is constant is a valid one, meaning  $\frac{\partial p}{\partial z} = 0$ .

- As the film thickness is considered small compared to surface areas, velocity variations with respect to the z axis are larger than those in the x and y directions.

Therefore:

$$\frac{\partial^2 u}{\partial x^2} + \frac{\partial^2 u}{\partial y^2} = 0; \frac{\partial^2 v}{\partial x^2} + \frac{\partial^2 v}{\partial y^2} = 0; \frac{\partial^2 w}{\partial x^2} + \frac{\partial^2 w}{\partial y^2} + \frac{\partial^2 w}{\partial z^2} = 0 \quad (4.22)$$

- The lubricant flow through the contact is laminar.
- The fluid is Newtonian, and there is no slip at the surfaces. This assumption gives the following boundary conditions:

$$z = 0; u = u_A, v = v_A = 0; z = h; u = u_B, v = v_B = 0 \quad (4.23)$$

Where A and B are the two surfaces, and u and v are surface velocities. These assumptions reduce equations (4.13)-(4.15) to the following expressions:

$$\frac{\partial p}{\partial x} = \eta \frac{\partial^2 u}{\partial z^2} \quad (4.24)$$

$$\frac{\partial p}{\partial y} = \eta \frac{\partial^2 v}{\partial z^2} \quad (4.25)$$

Integrating the above equations twice with respect to  $z$ , whilst using the boundary conditions in (4.23), gives the velocity distribution solutions. Coupling with equation (4.12) gives the full Reynolds equation:

$$\frac{\partial}{\partial x} \left( \frac{\rho h^3}{\eta} \frac{\partial p}{\partial x} \right) + \frac{\partial}{\partial y} \left( \frac{\rho h^3}{\eta} \frac{\partial p}{\partial y} \right) = 12 \left( u_{av} \frac{\partial}{\partial x} (\rho h) + v_{av} \frac{\partial}{\partial y} (\rho h) + \frac{\partial}{\partial t} (\rho h) \right) \quad (4.26)$$

The Reynolds equation is the fundamental equation of fluid film lubrication theory. The terms on the left hand side of equation (4.26) are known as the Poiseuille terms, which incorporate the pressure-induced terms. The right hand side terms are known collectively as the Couette terms, which describe the film wedge and squeeze actions.

A commonly used assumption when dealing with piston ring-cylinder liner contacts is that any entraining velocity circumferentially can be assumed to be small when compared to the axial entraining velocity. This means that  $v_{av} = 0$ , and equation (4.26) simplifies as follows:

$$\frac{\partial}{\partial x} \left( \frac{\rho h^3}{\eta} \frac{\partial p}{\partial x} \right) + \frac{\partial}{\partial y} \left( \frac{\rho h^3}{\eta} \frac{\partial p}{\partial y} \right) = 12 \left( u_{av} \frac{\partial}{\partial x} (\rho h) + \frac{\partial}{\partial t} (\rho h) \right) \quad (4.27)$$

Equation (4.27) is a standard form of the Reynolds equation, and it can be applied to many problems concerning lubricant pressure distribution and flow.

### 4.3.2. Solving the Reynolds Equation

Whilst equation (4.26) is in a standard form, further manipulation of the Reynolds equation is required to yield a usable solution form. Ultimately, the Reynolds equation is used to calculate the pressure distribution throughout a contact. Figure 4.3 shows the forces which act upon the compression ring.

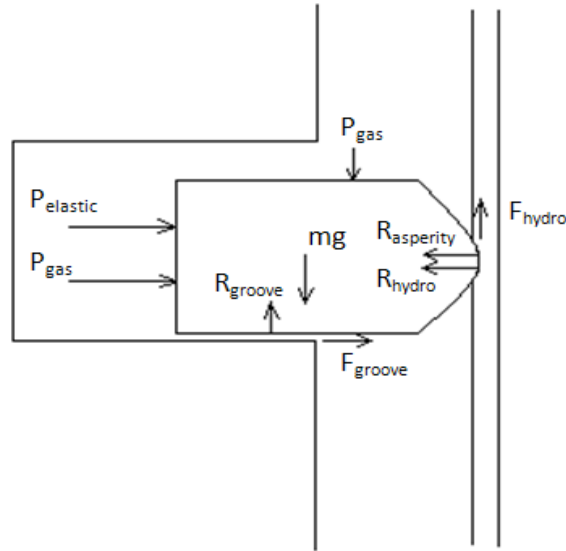


Figure 4.3: Cross-section diagram of the compression ring-cylinder liner conjunction, highlighting the forces present

In the case of a piston ring-cylinder liner analysis, the pressure distribution both circumferentially and axially must be found. The method of solution involves dividing the surface area between the ring and the liner into finite, discrete points in a grid form. Density ( $\rho$ ), viscosity ( $\eta$ ) and local deformations ( $\delta$ ) are all affected by the pressure distribution within the contact, meaning all these terms must be considered during discretisation (Rahmani et al, 2012):

$$\frac{\partial \Psi_i}{\partial x_k} = \left( \frac{\partial \Psi_i}{\partial p} \right) \left( \frac{\partial p}{\partial x_k} \right) \quad ; \begin{cases} i = 1, 2, 3 \\ k = 1, 2 \end{cases} \quad (4.28)$$

Where  $\Psi_1 = \rho$ ,  $\Psi_2 = \eta$ ,  $\Psi_3 = \delta$  and  $x_1 = x$ ,  $x_2 = y$ . Using a central difference method to perform the finite difference discretisation, the pressure at node (i,j) is described as (Rahmani et al, 2012):

$$p_{i,j} = \frac{A_{i,j} + Q_{i,j}(p_x^2 + p_y^2) + 3(M_{i,j}p_x + N_{i,j}p_y) - 6R_{i,j}}{2\left(\frac{1}{\Delta x^2} + \frac{1}{\Delta y^2}\right)} \quad ; \quad \frac{\partial p}{\partial x} = \frac{p_{i+1,j} - p_{i-1,j}}{2\Delta x}, \quad \frac{\partial p}{\partial y} = \frac{p_{i,j+1} - p_{i,j-1}}{2\Delta y} \quad (4.29)$$

The notation  $p_x$  and  $p_y$  indicates the pressure gradients  $\frac{dp}{dx}$  and  $\frac{dp}{dy}$  respectively. Where A, Q, M, N and R are as follows (Rahmani et al, 2012):

$$A_{i,j} = \frac{p_{i-1,j} + p_{i+1,j}}{\Delta x^2} + \frac{p_{i,j-1} + p_{i,j+1}}{\Delta y^2} \quad (4.30.i)$$

$$Q_{i,j} = \left[ \frac{1}{\rho} \left( \frac{\partial \rho}{\partial p} \right) - \frac{1}{\eta} \frac{\partial \eta}{\partial p} + 3 \frac{1}{h} \frac{\partial \delta}{\partial p} \right]_{i,j} \quad (4.30.ii)$$

$$M_{i,j} = \left[ \frac{1}{h} \frac{\partial h_s}{\partial x} - 2U \frac{\eta}{h^2} \left( \frac{\partial \rho}{\partial p} + \frac{1}{h} \frac{\partial \delta}{\partial p} \right) \right]_{i,j} \quad (4.30.iii)$$

$$N_{i,j} = \left[ \frac{1}{h} \frac{\partial \Delta}{\partial y} - 2V \frac{\eta}{h^2} \left( \frac{\partial \rho}{\partial p} + \frac{1}{h} \frac{\partial \delta}{\partial p} \right) \right]_{i,j} \quad (4.30.iv)$$

$$R_{i,j} = \left\{ \frac{\eta}{h^2} \left[ \left( U \frac{\partial h_s}{\partial x} + V \frac{\partial \Delta}{\partial y} \right) + 2 \left( \frac{1}{\rho} \frac{\partial \rho}{\partial t} + \frac{1}{h} \frac{\partial h_0}{\partial t} \right) \right] \right\}_{i,j} \quad (4.30.v)$$

Where U and V are the axial and tangential velocities respectively (the latter is assumed to equal zero). The symbol  $h_0$  denotes the minimum film thickness, whilst  $h_s$  is the ring's axial profile. The solution to equation (4.28) requires an initial guess. Hoffmann and Chiang (1993) described the Point Gauss-Seidel Successive Over-Relaxation iterative method, by which the pressure is updated using a relaxation factor:

$$p_{i,j}^n = (1 - \gamma)p_{i,j}^o + \gamma p_{i,j}^n \quad ; (0 < \gamma < 2) \quad (4.31)$$

The relaxation factor  $\gamma$  is dependent on the problem, with a measure of trial and error required to find the optimum value.

Convergence of the pressure at each node is determined with the use of the following convergence criteria:

$$Err_{pressure} = \frac{\sum_{i=1}^I \sum_{j=1}^J |p_{i,j}^n - p_{i,j}^o|}{\sum_{i=1}^I \sum_{j=1}^J p_{i,j}^n} \leq 1 \times 10^{-5} \quad (4.32)$$

An increase in the value of the right hand side of equation (4.32) leads to quicker convergence. However, this in turn decreases the accuracy of the calculated pressure, as it does not yield to a fully converged solution. The full solution method will be discussed later in this chapter.

#### 4.4. The Energy Equation

Due to the nature of sliding surfaces, even those with a lubricant film, preventing solid-to-solid contact, a temperature increase within the contact is an inevitable outcome, mostly due to viscous shear of a thin film of lubricant. At significantly high pressures, some heating of lubricant also takes place through its compression to enter into a diminishing gap. In

some cases, an isothermal analysis gives a reasonable film thickness prediction. However, when high shear rates are present, such as those between the piston ring and the liner, thermal effects within the contact may affect any numerical results. This increase in temperature affects the viscosity of the lubricant, as described previously. Internal heating of the lubricant occurs via two mechanisms: compression of the contact, and the viscous shearing of the film, caused by a high entraining velocity. There are also two methods by which heat can be taken away from the system: convection and conduction. Cameron (1967) presented a full derivation of the energy equation. Since neglecting side leakage is a reasonable simplification:

$$vU_{ent}\theta\frac{\partial p}{\partial x} + \eta\left(\frac{\partial U_{ent}}{\partial z}\right)^2 = \rho U_{ent}c_p\frac{\partial \theta}{\partial x} - k_t\frac{\partial^2 \theta}{\partial z^2} \quad (4.33)$$

where  $\theta$  is the temperature rise in Kelvin,  $v$  is the coefficient of thermal expansion,  $k_t$  is the thermal conductivity, and  $c_p$  is the specific heat. The four terms in equation (4.33) are conveniently divided in two heating and two cooling terms, with compressive heating and viscous shear on the left hand side of the equation, and convection and conduction cooling terms on the right hand side. Figure 4.4 shows the temperature distribution at the contact.

Gohar, R. and Rahnejat, H., (2008) *“Fundamentals of Tribology”*, London: Imperial College Press (figure 6.12)

Figure 4.4: Temperature distribution at the contact (Gohar and Rahnejat, 2008)

Throughout the full cycle of a four-stroke engine, these terms take greater or less significance, depending on the position of the piston ring. For example, at positions such as the TDC and BDC, the film thickness greatly reduces, along with the entraining velocity, meaning convection by the lubricant film has less of an effect. Therefore, convection may be neglected, when compared with conduction through the adjacent bounding solid surfaces. However, during the mid-stroke motion, the film thickness is such that convection must be considered when applying the energy equation. Different solution forms can be obtained by considering various thermal models.



#### 4.4.1. Convection Only

Relatively speaking, the compressive heating term is insignificant in a typical contact. Assuming that any heat generated within the contact is displaced only via convection (thick film assumption), whilst letting the average fluid velocity equal,  $U_{ent1} = U_{ent}/2$  and the maximum average temperature rise be  $\Delta\theta/2$ , equation (4.33) becomes:

$$\rho c_p \frac{d\theta}{dx} dx \int_0^h U_{ent} dz = \rho c_p \left( \frac{d\theta}{dx} \right) \left( \frac{U_{ent1} h}{2} \right) dx \quad (4.34)$$

Inspection of figure 4.4 shows that  $x = B$ ,  $d\theta/dx = \Delta\theta/2B$ . The total heat convected away from the contact is therefore:

$$\frac{\rho c_p U_{ent1} h}{2} \left( \frac{\Delta\theta}{2B} \right) \int_0^B dx = \frac{\rho c_p U_{ent1} h \Delta\theta}{4} = \left( \frac{U_{ent1} \rho h}{2} \right) \times c_p \times \frac{\Delta\theta}{2} \quad (4.35)$$

A simpler way of recalling the right hand side of equation (4.35) is to read the mass flow per second  $\times$  specific heat  $\times$  temperature rise.

#### 4.4.2. Conduction Only

Depending on the system being analysed, it can also be assumed that all the heat within the contact is lost through conduction only. Analysis by Gohar and Rahnejat (2008) showed very little convection for thin films, with conduction losses being over an order of magnitude larger in some instances. Assuming a linear temperature gradient across the film, from zero on the moving surface ( $z=0$ ) to  $\delta\theta/h$  on the stationary surface, gives a parabolic temperature distribution across the film. Integrating equation (4.33) with respect to  $z$ :

$$k_t \int_0^h \frac{d^2\theta}{dz^2} dz = k_t dx \frac{\delta\theta}{h} \quad (4.36)$$

Letting  $\delta\theta = x\Delta\theta/B$ , the total conducted heat through the top surface is:

$$\frac{k_t \Delta\theta}{Bh} \int_0^B x dx = \frac{k_t \Delta\theta B}{2h} \quad (4.37)$$

#### 4.4.3. The Peclet Number

The determining factor in whether convection or conduction should be included in an analysis is the heat flow ratio, also known for fluid flow studies as the Peclet number:

$$Pe = \frac{\frac{U_{ent1} h}{4} \rho c_p \Delta\theta}{\frac{k_t \Delta\theta B}{2h}} = \frac{\frac{U_{ent1} h^2}{2B}}{\left( \frac{k_t}{\rho c_p} \right)} \quad (4.38)$$

The Peclet number is the ratio of convected to conducted heat. Whenever  $Pe < 1$ , it is reasonable to assume convection is negligible within the contact. For all other cases, both methods of heat transfer must be accounted for.

A complete cycle in a four-stroke engine envelopes conditions where both conduction and convection are dominant at different stages of the cycle. Karthikeyan et al (2010) included thermal effects when analysing grease-lubricated bearings. Neglecting convection, they found the following analytic solution:

$$-k_t \frac{\partial \theta}{\partial z} = v \frac{\partial p}{\partial x} \int_0^h \theta U_{ent} dz + \eta \int_0^h \left( \frac{\partial U_{ent}}{\partial z} \right)^2 dz \quad (4.39)$$

Note that  $kt$  has units of  $\text{kJm}^{-1}\text{s}^{-1}(\text{°K})^{-1}$ . Assuming a linear heat transfer across the film,  $\theta = \theta_0 + \Delta\theta$ , where  $\theta_0$  is the inlet temperature. Substituting this into equation (4.33) and rearranging:

$$\delta\theta(x) = \frac{\theta_0 v \frac{\partial p}{\partial x} \int_0^h U dz + \eta \int_0^h U_z^2 dz}{k_t \frac{1}{h} - v \frac{\partial p}{\partial x} \int_0^h U dz} \quad (4.40)$$

Equation (4.40) shows the temperature change within a contact when only considering conduction, and is valid for thin elastohydrodynamic films (Gohar and Rahnejat, 2008). Each term in the modified energy equation was integrated individually. However at the mid-span of a piston cycle, convection must be accounted for. Using the same approach as Karthikeyan *et al* (2010), but accounting for convection:

$$\delta\theta(x) = \frac{\theta_0 v \frac{\partial p}{\partial x} \int_0^h U dz + \eta \int_0^h U_z^2 dz}{\rho c_p \frac{1}{l} \int_0^h U dz + k_t \frac{1}{h} - v \frac{\partial p}{\partial x} \int_0^h U dz} \quad (4.41)$$

Equation (4.41) accounts for both conduction and convection, and is valid for hydrodynamic films.

Figure 4.5 shows the resultant temperature increases due to the analysis above in a piston ring-cylinder liner system. With a starting lubricant temperature of 40°C, a rigid ring is assumed. As mentioned previously, it is valid to include both conduction and convection in any internal thermal analysis when studying the compression ring. However, the actual temperature rise throughout the engine cycle when including both methods is relatively small. At the point of combustion, both at 2000rpm and 4000rpm, the internal heat

generated is less than 10°C. It is clear that the temperature increase due to the combustion itself will be significantly higher than this. Also, if the starting temperature of the lubricant is higher than the 40°C used here, the effect of internal heating mechanisms would be reduced even further. It is, therefore, reasonable to assume that internal heating methods can be neglected if actual liner temperatures can be used, or if the lubricant temperature is set to a more realistic value in the numerical analysis. The inclusion of transient ring dynamics would not alter these results so as to make this assumption unreasonable.

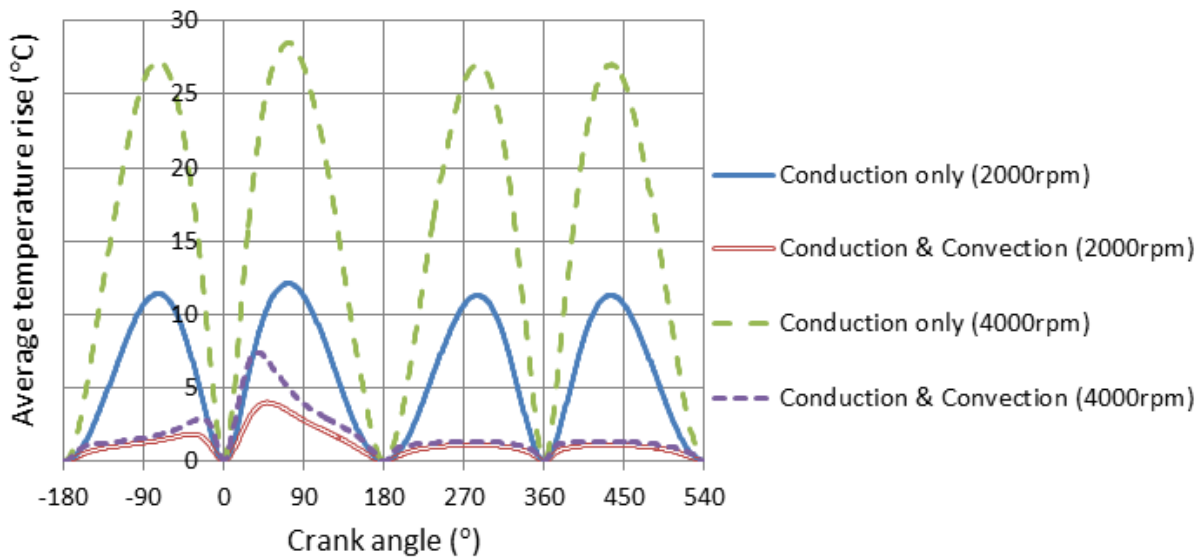


Figure 4.5: Average temperature rise throughout the engine cycle for a rigid ring analysis

#### 4.5. Asperity Interaction

In contacts of lower film thickness, there is an increased chance that the roughness features of both surfaces will affect the tribological performance of the contact. Greenwood and Tripp (1970) proposed a model for calculating the asperity loads within a contact (Priest, 2000):

$$W_a = \frac{8\sqrt{2}}{15} \pi (\zeta \kappa \sigma)^2 \sqrt{\frac{\sigma}{\kappa}} E' A F_{5/2}(\lambda) \quad (4.42)$$

In equation (4.42), the terms  $(\zeta \kappa \sigma)$  and  $(\sigma/\kappa)$  are dimensionless roughness parameters obtained through surface roughness measurements.  $\kappa$  is the asperity radius of curvature,  $\zeta$  equals the number of asperities per unit area, and  $\sigma$  represents the composite surface roughness.  $A$  is the apparent area considered, in other words the flat area before considering the effect of surface roughness. The lambda value is used in plotting the

Stribeck curve, and is the film ratio of film thickness to surface roughness average.  $F_{5/2}(\lambda)$  is the probability distribution of asperity height. In the studies described in this thesis, a fifth-order polynomial curve is fitted to this distribution (Teodorescu, 2004):

$$F_{5/2}(\lambda) = -0.0046\lambda^5 + 0.0574\lambda^4 - 0.2958\lambda^3 + 0.7844\lambda^2 - 1.0776\lambda + 0.6167 \quad (4.43)$$

Equation (4.42) gives the radial asperity load. However, out-of-plane frictional forces must also be considered.

$$f_t = f_v + f_b \quad (4.44)$$

The total friction is a summation of viscous and boundary friction. Priest (2000) defined the boundary friction as follows:

$$f_b = \tau_0 A_e + \xi W_a \quad (4.45)$$

$\tau_0$  is known as the Eyring stress, while  $\xi$  is the pressure coefficient for the boundary shear strength in asperities. This coefficient is considered to equal approximately 0.17 for steel. The actual pressure coefficient of the compression ring was also measured for this study. The values were found to be 0.3038 and 0.2012 for a brand new and end-of-life ring respectively. The values used are given along with other relevant information in the numerical models.  $A_e$  is the effective area of the contact, accounting for asperities:

$$A_e = \pi^2 (\zeta \kappa \sigma)^2 \sqrt{\frac{\sigma}{\kappa}} E' A F_2(\lambda) \quad (4.46)$$

Further to the boundary friction, viscous friction must also be considered:

$$f_v = \tau (A - A_e) \quad (4.47)$$

Where  $\tau$  is the viscous shear:

$$\tau = (\tau_x^2 + \tau_y^2)^{1/2} = \left| \pm \frac{h}{2} \bar{\nabla} p + \bar{V} \frac{\eta}{h} \right| \quad (4.48)$$

#### 4.6. Method of Solution

As stated previously, Equations (4.28-4.32) are implemented to solve the Reynolds equation. A two-stage convergence process is sought before a solution can be accepted.

Firstly, the generated pressures and lubricant rheological states are deemed to have converged, when:

$$Err_{pressure} = \frac{\sum_{i=1}^I \sum_{j=1}^J |p_{i,j}^n - p_{i,j}^o|}{\sum_{i=1}^I \sum_{j=1}^J p_{i,j}^n} \leq 1 \times 10^{-5} \quad (4.49)$$

And:

$$Err_{properties\ and\ deflection} = \frac{\sum_{i=1}^I \sum_{j=1}^J |\psi_{i,j}^n - \psi_{i,j}^o|}{\sum_{i=1}^I \sum_{j=1}^J \psi_{i,j}^n} \leq 1 \times 10^{-3} \quad (4.50)$$

Secondly, the quasi-static balance of applied forces on the ring is sought through:

$$Err_{load} = \frac{|F(\varphi) - W(\varphi)|}{F(\varphi)} \leq 1 \times 10^{-3} \quad (4.51)$$

Where  $F(\varphi)$  and  $W(\varphi)$  are the external and internal loads respectively. If this criterion is not met then the minimum nominal gap is adjusted and the entire iterative procedure is repeated:

$$h_m^n = (1 + \beta\chi)h_m^o \quad (4.52)$$

$\chi$  is the adjusting parameter:  $\chi = \frac{W(\varphi) - F(\varphi)}{\max\{W(\varphi), F(\varphi)\}}$ . Superscripts  $n$  and  $o$  denote new and old steps in the iteration process. A damping coefficient for load convergence,  $\beta$ , is used to affect faster load convergence, whilst avoiding numerical instability.

Finally, a typical analysis cycle requires an initial guess as the nominal minimum clearance. This means that the analysis should continue until cyclic behaviour in minimum clearance is achieved between successive engine cycles. Thus:

$$Err_{clearance} = \frac{|h_m(\varphi) - h_m(\varphi-720)|}{h_m(\varphi-720)} \leq 1 \times 10^{-3} \quad (4.53)$$

An algorithm of the solution process used is shown in figure 4.6. Note that this is the methodology for the tribological analysis only; with no ring dynamics included.

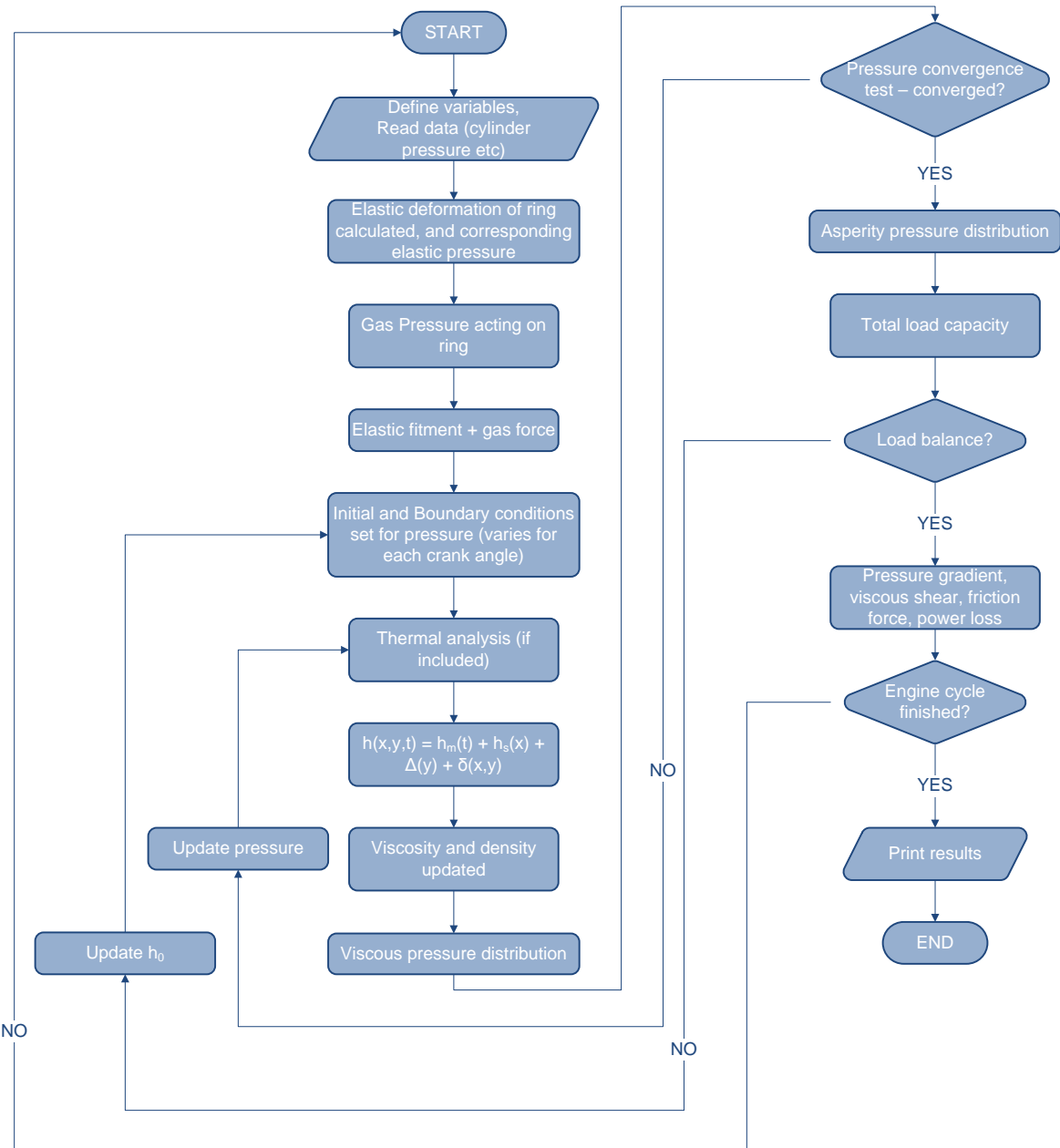


Figure 4.6: Flowchart of the solution procedure

#### 4.7. Closure

In this chapter, expressions to define lubricant properties and their variations due to contact conditions were highlighted. The Reynolds equation was derived from the Navier-Stokes equations, with any assumptions stated. The discretised solution form of the Reynolds equation is also presented. Thermal effects are accounted for by manipulation of the Energy equation, concluding in an expression valid for hydrodynamic films. The effects of surface asperities within the contact are also explained, both in load carrying and frictional terms.

This outlines the tribological analysis methodologies which are applied to the top compression ring to determine frictional losses and film thickness predictions.

## 5. Tribodynamic Numerical Analysis of the Top Compression Ring

### 5.1. Introduction

This chapter presents the results of the tribodynamic analysis of the top compression ring. Various engine conditions are presented, comparing the proposed method of transient ring dynamics with a rigid ring analysis. These include different oil temperatures, ring profiles and engine speeds. Initially, quasi-static force balance results are presented, which highlight the need for including transient ring dynamics. Then, the in-plane transient elastic motion of the ring is coupled with the tribological analysis and the results are compared. Finally, the out-of-plane ring dynamics are also coupled to the methodology, to give a fully elastodynamic compression ring tribological model.

### 5.2. Rigid Ring Tribology

The system which is modelled throughout this chapter is based upon a V12 high performance gasoline engine. The lubricant used in the analysis is SAE 10W40. Table 5.1 lists the lubricant rheological parameters. The surface roughness parameters used in the boundary friction calculations are listed in table 5.2.

Table 5.1: Lubricant Parameters

Parameter	Value	Unit
Pressure-viscosity coefficient	$2 \times 10^{-8}$	$\text{m}^2/\text{N}$
Thermal expansion coefficient	$6.5 \times 10^{-4}$	$1/^\circ\text{K}$
Lubricant density	833.8 at 40 [°C], 783.8 at 100 [°C]	$\text{kg}/\text{m}^3$
Lubricant kinematic viscosity, $\nu$	59.99 at 40 [°C], 9.59 at 100 [°C]	$\times 10^{-6} \text{ m}^2/\text{s}$

Table 5.2: Roughness parameters for initial numerical results

Parameter	Value	Unit
Ra for the liner	0.26	$\mu\text{m}$
Ra for a new ring	0.408	$\mu\text{m}$
Ra for a worn ring	0.235	$\mu\text{m}$
Roughness parameter $(\zeta\kappa\sigma_c)_c$	0.073672	-
Measure of asperity gradient $(\sigma_c/\kappa)_c$	0.309288	-
Pressure coefficient	0.3038	-



The combustion gas pressure curve at different engine speeds and 100% throttle are provided by industrial collaborators of research. Figure 5.1 shows the gas pressure profiles for some example engine speeds (for a fired engine).

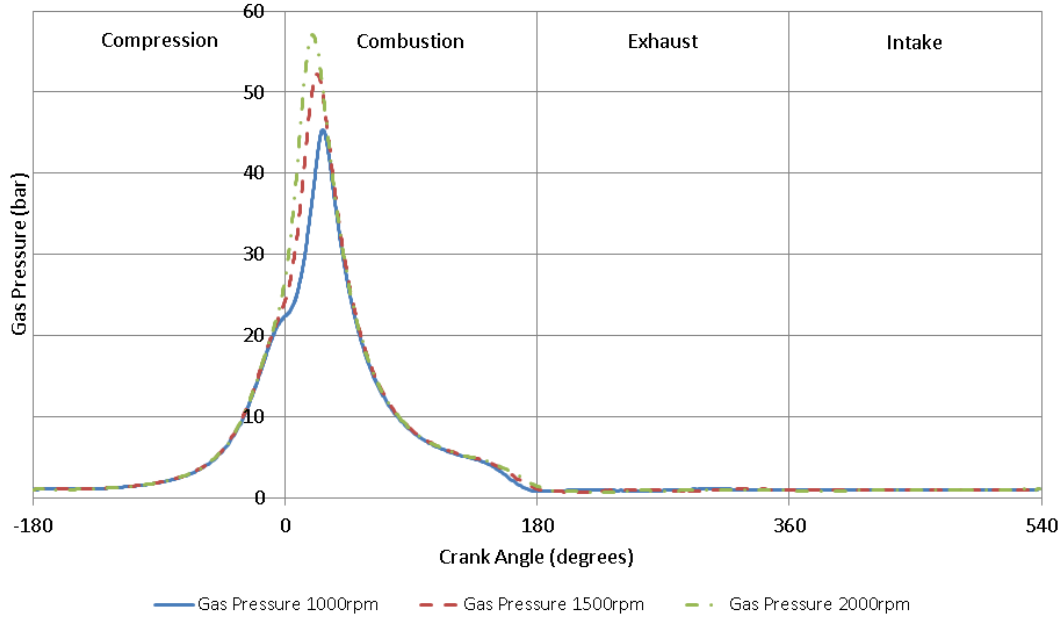


Figure 5.1: Gas pressure profiles at given engine speeds

The compression ring details are listed in table 5.3.

Table 5.3: Ring Properties for initial numerical results

Property	Value
Elastic modulus, $E$	203 GPa
Ring density, $\rho$	7800 kg/m <sup>3</sup>
Ring thickness, $d$	3.5 mm
Axial face-width, $b$	1.15 mm
Nominal fitted ring radius, $R$	44.52 mm
Ring second moment of area, $I$	2.25X10 <sup>-12</sup> m <sup>4</sup>
End gap size (free ring)	10.5mm

A fully flooded inlet condition is assumed for the presented analysis. The lubricant temperature is considered to remain constant throughout the engine cycle for each analysis. This is because the internally generated temperature rise due to compression and viscous shear was shown to be small, when compared to the measured liner and combustion temperatures, as shown previously in this thesis. For the rigid ring analysis, the film

thickness at each crank angle is calculated through an iterative process based on quasi-static equilibrium of forces acting on the ring. The external gas and elastic fitment forces act normal to the inner rim of the ring in the radial outward direction, with lubricant and asperity reaction forces acting radially inwards. The film thickness affects these reaction forces and their values are iterated upon until equilibrium is reached. Frictional losses are due to asperity interactions as well as viscous shear of the lubricant film. Greenwood and Tripp model for asperity interactions is used for asperity interactions.

Initial results are presented for the compression ring tribology without considering any ring dynamics (i.e. an assumed rigid fitted ring). Figure 5.2 shows the minimum film thickness variation over an engine cycle, at various engine speeds. The oil temperature is assumed to be constant at 40°C, and the contact inlet is regarded as fully flooded. As expected, an increase in engine speed results in higher sliding velocity and a thicker minimum film thickness. However, the parameter  $\Delta U/h$  effectively increases, therefore the viscous shear stress and consequently the viscous friction (as shown in figure 5.3) increase also. The lubricant flow rate is also enhanced with an increase in the engine speed, which is demonstrated in figure 5.4. The power stroke is where the most extreme conditions are encountered by the compression ring, with the maximum combustion pressure occurring about 20° crank angle past the top dead centre (TDC). This is reflected by a notable drop in the film thickness and an increase in frictional power loss throughout the power stroke, in comparison with the rest of the engine cycle.

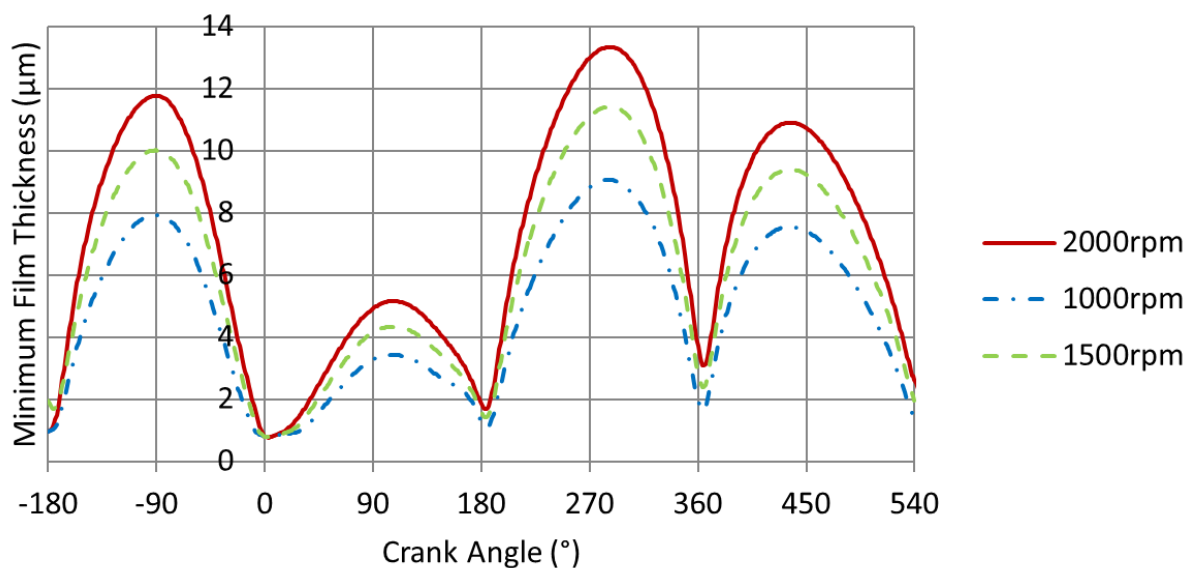


Figure 5.2: Minimum film thickness variation (rigid ring analysis) at various engine speeds

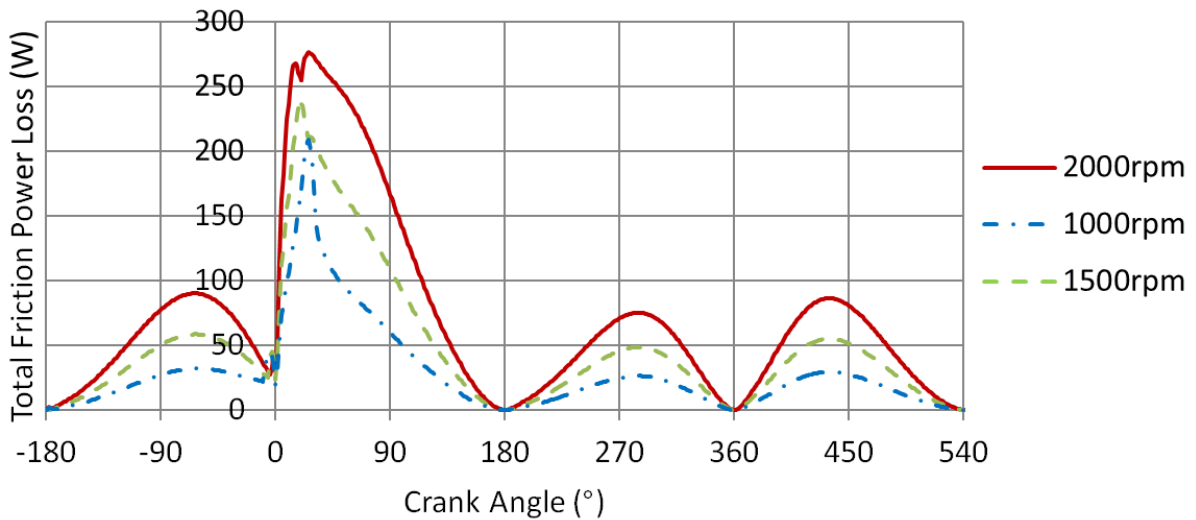


Figure 5.3: Total friction power loss variation (rigid ring analysis) at various engine speeds

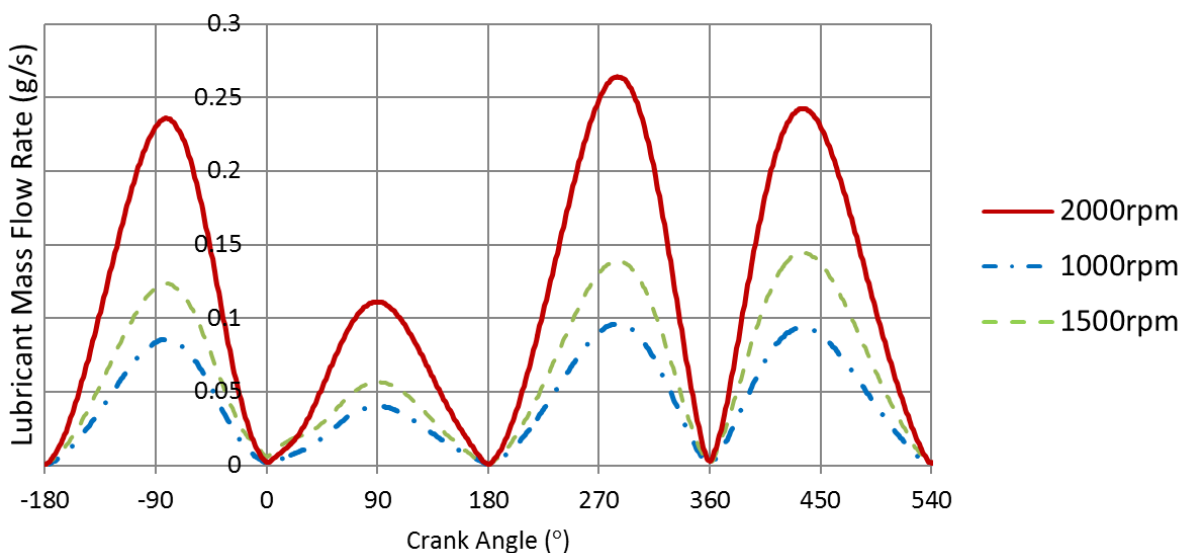


Figure 5.4: Lubricant mass flow rate variation (rigid ring analysis) at various engine speeds

Figures 5.2-5.4 show expected trends with reasonable values for each parameter presented, which suggests that the numerical methodology is representative of the actual noted practical conditions. Preliminary simulations were performed to highlight any differences between the ‘rigid’ ring analysis and that incorporating ring dynamics. Force profiles around critical positions in the engine cycle were extracted and applied to the ring dynamics methodology. The resulting deformation was used in the tribology code and frictional losses were evaluated. This method does not include the time history of ring oscillations, so it may be described as a quasi-static analysis. It is intended as a first step towards complete

coupling with the tribological analysis. The results in figures 5.5 and 5.6 were presented in Baker et al (2012, see Appendix C).

### 5.3. Quasi-static ring deformation

The force profile in ring dynamics is introduced as a Fourier series. An example is shown in figure 5.5. The force profile around the ring is determined by integrating the pressure distribution obtained in the tribological analysis. In the results presented, the ring's profile comprises 64 circumferential nodes and 80 axial nodes (along the ring's facewidth) during the numerical analysis. The computation time and memory size is a determining factor in the number of nodes used. However, the accuracy of the results is not compromised. This gives an 80x64 mesh, which covers the ring's facewidth area. Integration across the 80 axial points at each circumferential step results in the circumferential force profile. This results in a circumferential profile as shown in figure 5.5, which can be used in the dynamics methodology with the use of a Fourier series. A negative value indicates that the net force acts radially outwards.

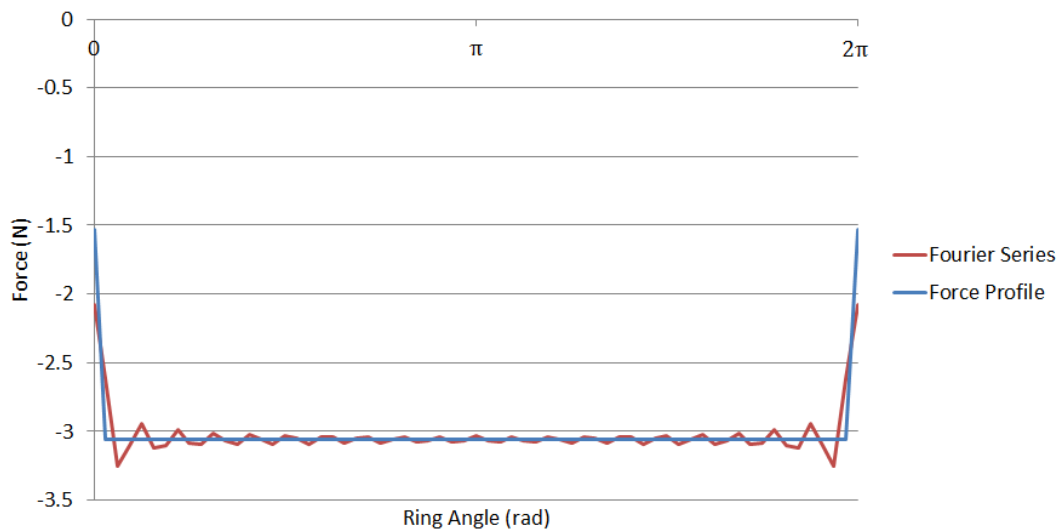
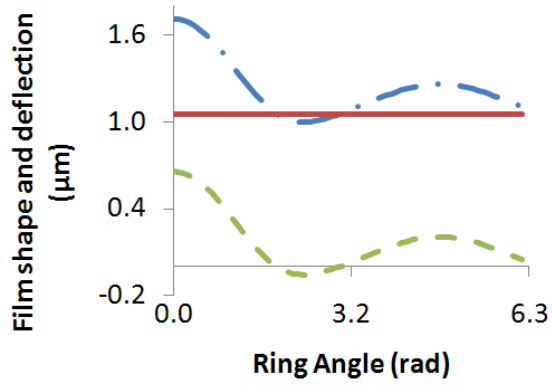
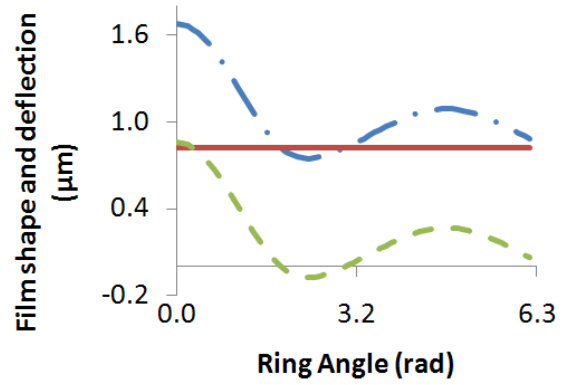


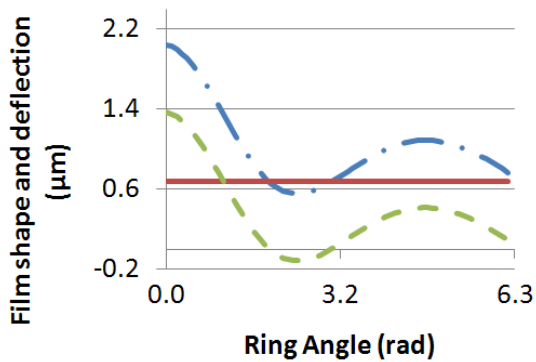
Figure 5.5: Force profile and corresponding Fourier series



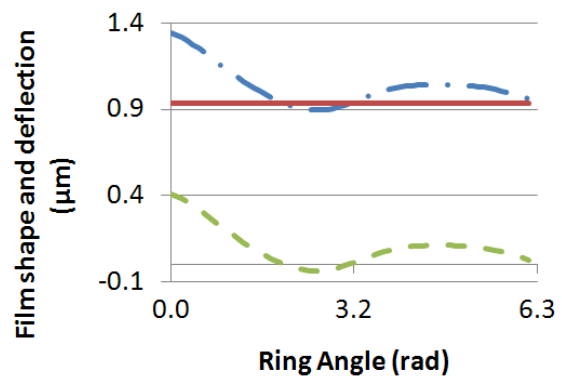
(a): 3° before TDC



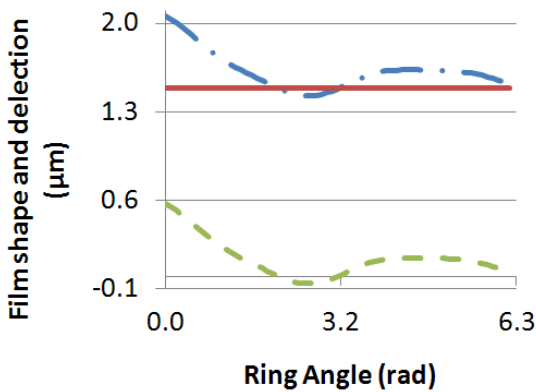
(b): TDC



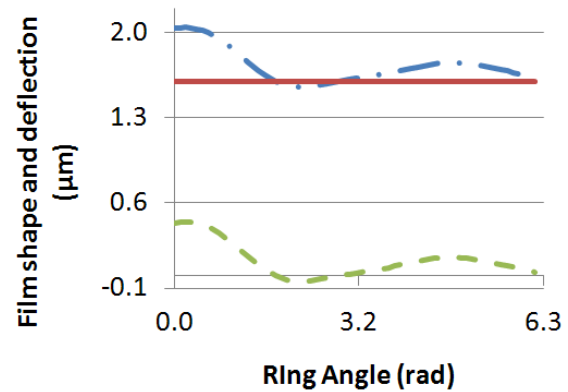
(c): 3° past TDC



(d): 10° past TDC



(e): 20° past TDC, firing point



(f): 22° past TDC

Figure 5.6: Film profile and ring deflection at various crank angle intervals around the TDC and firing point (engine speed = 2000rpm). — rigid film shape, - - - ring deflection, - · - · elastic film shape

Figure 5.6 shows various ring deformation profiles, as well as film thickness comparison with the traditional tribological analysis (i.e. for a rigid, fitted ring). The significant difference between the rigid and elastic profiles suggests that inclusion of ring dynamics is an

important consideration. It also suggests that static conformability analysis is not a realistic approach, because when the piston commences to move, the ring's global deformation constantly alters its conformability to the bore.

It should be stated that this is a quasi-static analysis. Lubricant and asperity carried loads are affected not only by the film thickness at each circumferential point, but also by the local velocity of the ring contributed by the squeeze film term when solving the Reynolds equation. This term embodies the "history" of the lubricant film thickness. The results presented in figure 5.6 demonstrate that ring deformation occurs and the way to account for this effect is by the inclusion of its deformation in a transient numerical analysis.

#### **5.4. In-plane transient ring dynamics**

Whereas the previous section deals with 'snapshots' of the compression ring's dynamic response to excitation experienced within the piston-ring system, a fully transient method is required for complete coupling between tribology and dynamics. An initial minimum film thickness is assumed, as is the case with the rigid ring methodology and the analysis is complete when this minimum film value has converged in the iterative process over the four-stroke cycle. Therefore, the minimum film thickness at the start of a cycle equals to that of the next cycle. This ensures the continuity of the analysis. Figures 5.7-5.9 show a comparison between the rigid and transient elastic ring methodologies. The minimum film thickness, total frictional power loss, and lubricant flow rate are presented. It is interesting to note that the film thickness predictions are lower with the elastic ring analysis, apart from those corresponding to the power stroke. The axial and circumferential film profiles for the points A and B of Figure 5.7 can be seen in Figure 5.10, for the elastic analysis. These points correspond to the TDC and at the mid-stroke and they have been highlighted to illustrate how the pressure profile varies. It can be seen that the circumferential film profile does not change much for either region. However, when the minimum film thickness assumes small values, even these small variations can cause significant changes in the pressure profile around the ring. Observation of figure 5.10a shows that the film profile variation in the circumferential direction is very small. However, pressure changes by over 1MPa from one side of the ring to the other. The assumption of a right cylindrical bore geometry is most probably the reason for the small change in the circumferential film profile, as the force profile acting upon the ring is relatively uniform. A similar plot for the rigid ring case would

show a uniform force circumferentially, whereas the dynamic analysis shows variations due to the ring's dynamic deflection (modal behaviour).

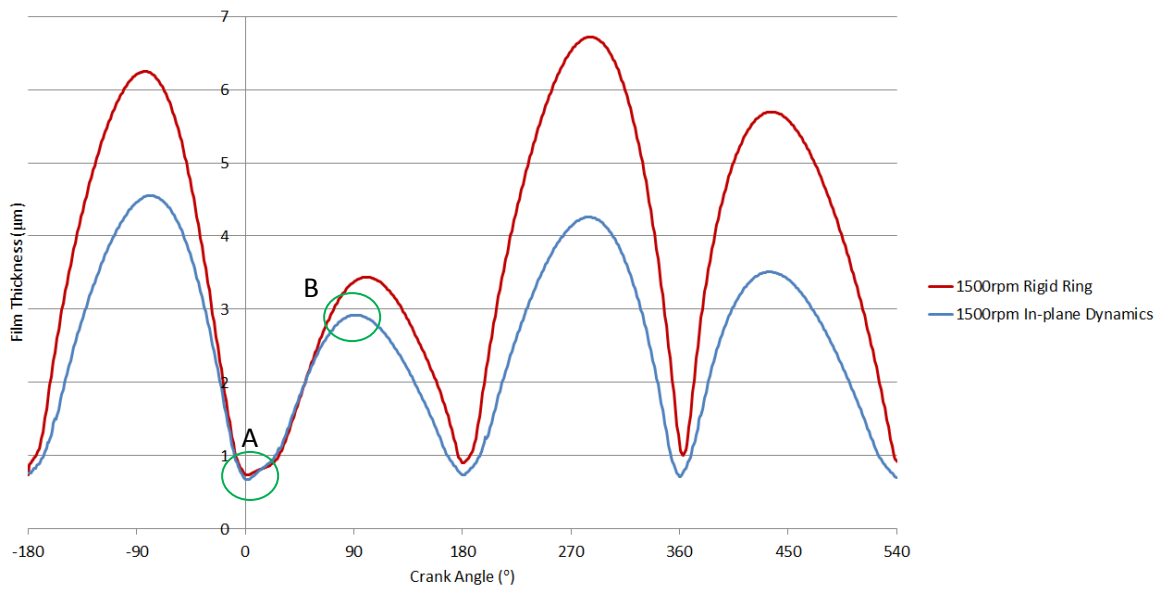


Figure 5.7: Minimum film thickness comparison of rigid and elastic ring analysis

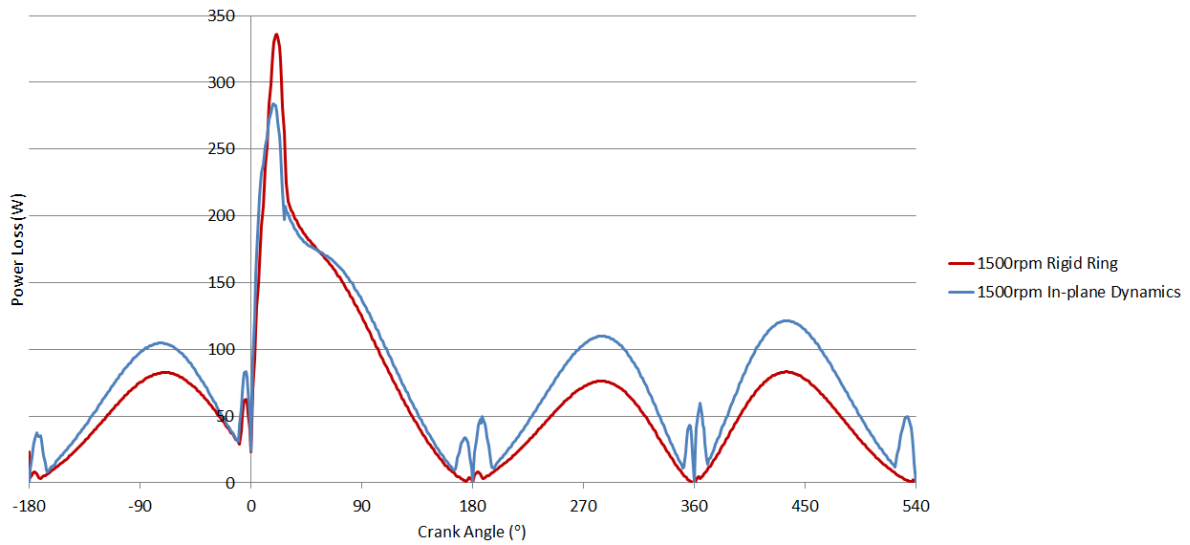


Figure 5.8: Frictional power loss comparison of rigid and elastic ring analysis

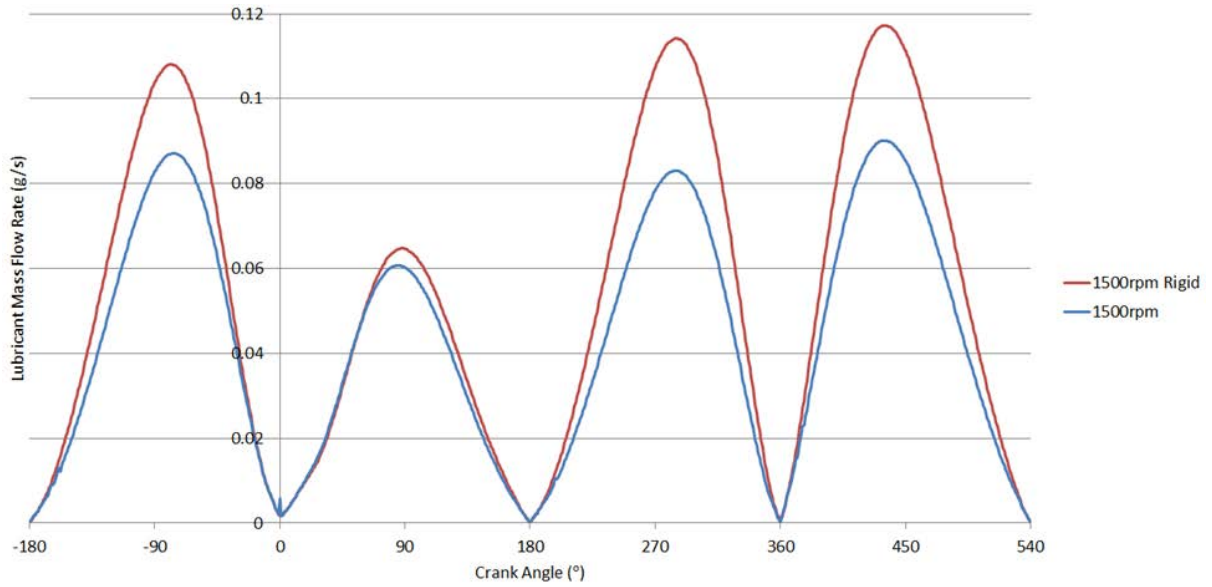


Figure 5.9: Lubricant mass flow rate comparison of rigid and elastic ring analysis at ring's middle cross section. Temperature = 40°C

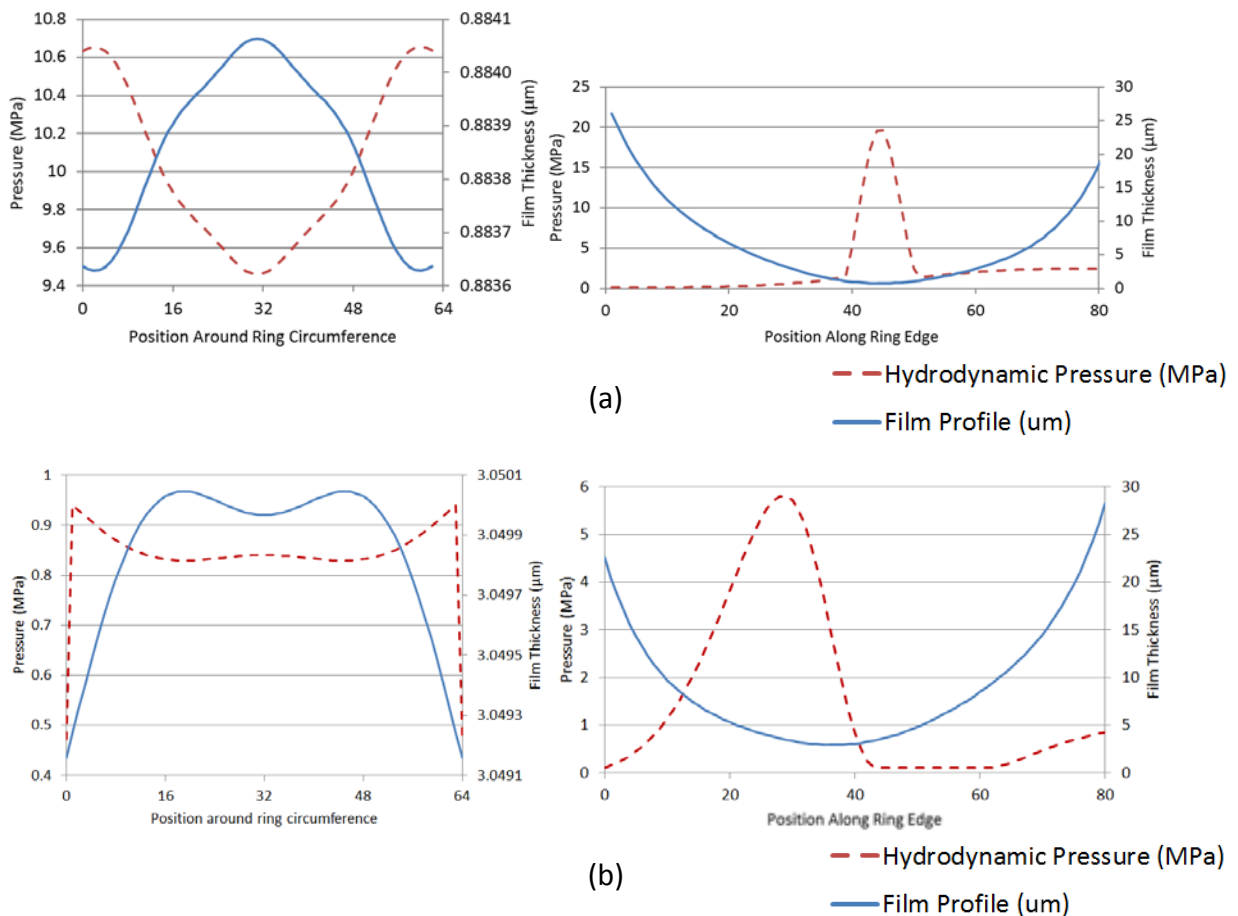


Figure 5.10: Circumferential and axial profiles of the lubricant pressure and film shape at points A and B of figure 5.7



The effect of engine speed on the parameters shown in Figures 5.7-5.9 can also be seen in Figures 5.11-5.13. The rigid ring analysis predicts an increase in the minimum film thickness values at the mid-stroke with increased engine speed (Figure 5.10). This increase is also seen in the elastic ring analysis. Rising speed causes higher frictional losses, as it can be seen in Figure 5.12 (due to increased lubricant shear, the service parameter  $\Delta U/h$ ). The lubricant flow rate follows the trend of the minimum film thickness predictions (Figure 5.13).

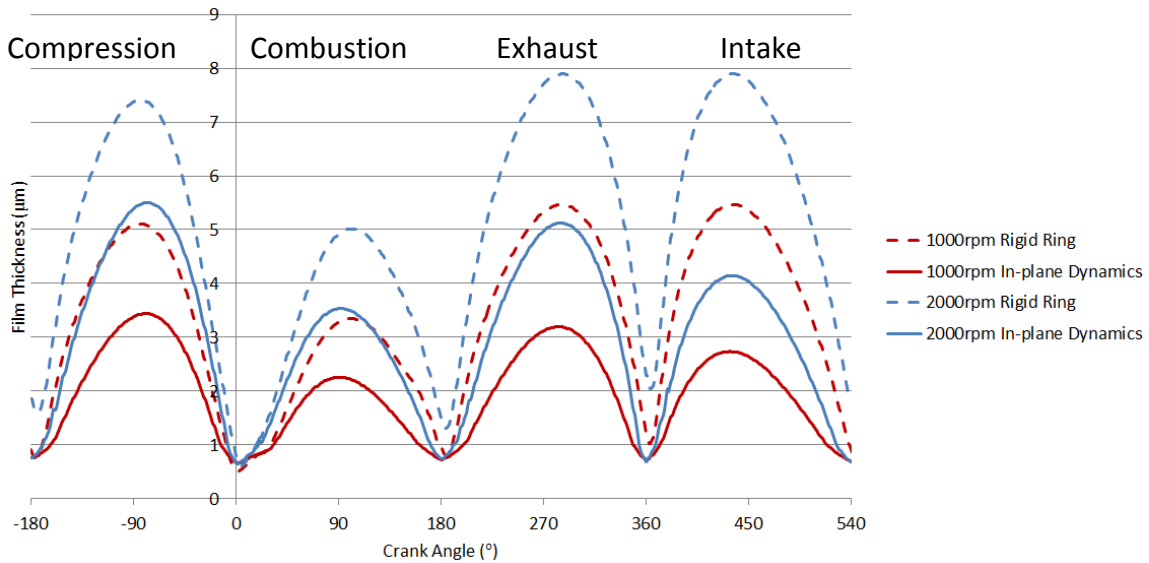


Figure 5.11: Effect of engine speed on the minimum film thickness predictions for both rigid and in-plane elastic ring analysis

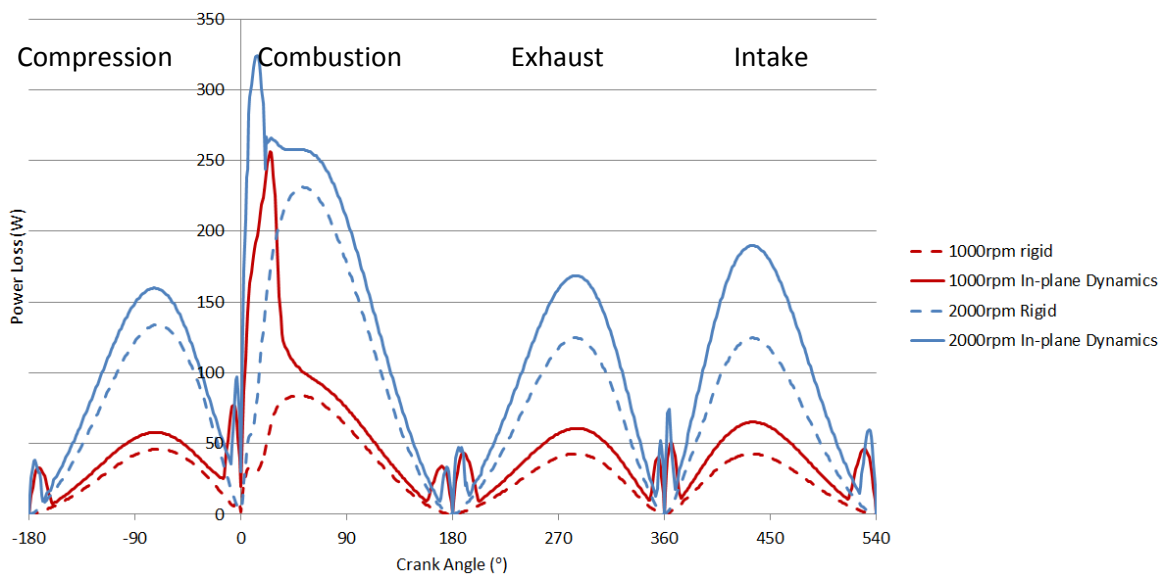


Figure 5.12: Effect of engine speed on frictional power loss predictions for both rigid and elastic ring analysis

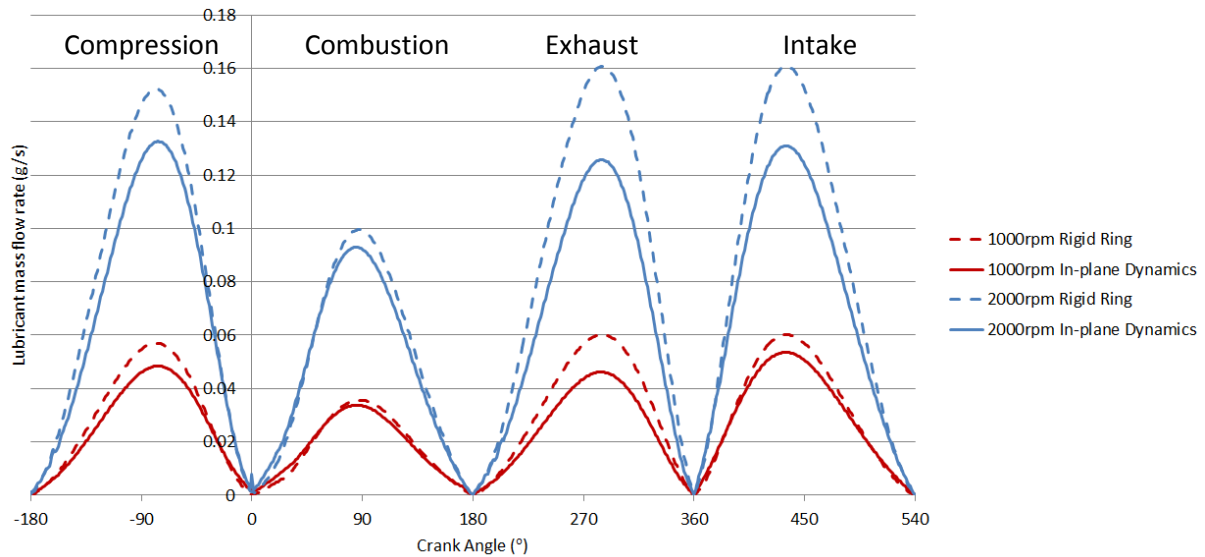


Figure 5.13: Effect of engine speed on lubricant flow rate predictions for both rigid and elastic ring analysis

The effect of oil temperature on the tribological performance of the system is shown in Figures 5.14-5.16. As expected, the film thickness decreases when temperature increases due to lower effective lubricant viscosity. The difference between the rigid and elastic ring analysis appears to be reduced when the lubricant temperature is increased, as shown in figure 5.14. When the film thickness is as thin as that in figure 5.15 at 120°C, any small deviation in film thickness can have a significant effect on the frictional losses. This is due to the contribution of asperity friction, as surface-to-surface contact occurs (spike in the calculated loss in Figure 5.16). Again, the lubricant flow rate depends mainly on the film thickness, so the same trend is noted in figures 5.15 and 5.17.

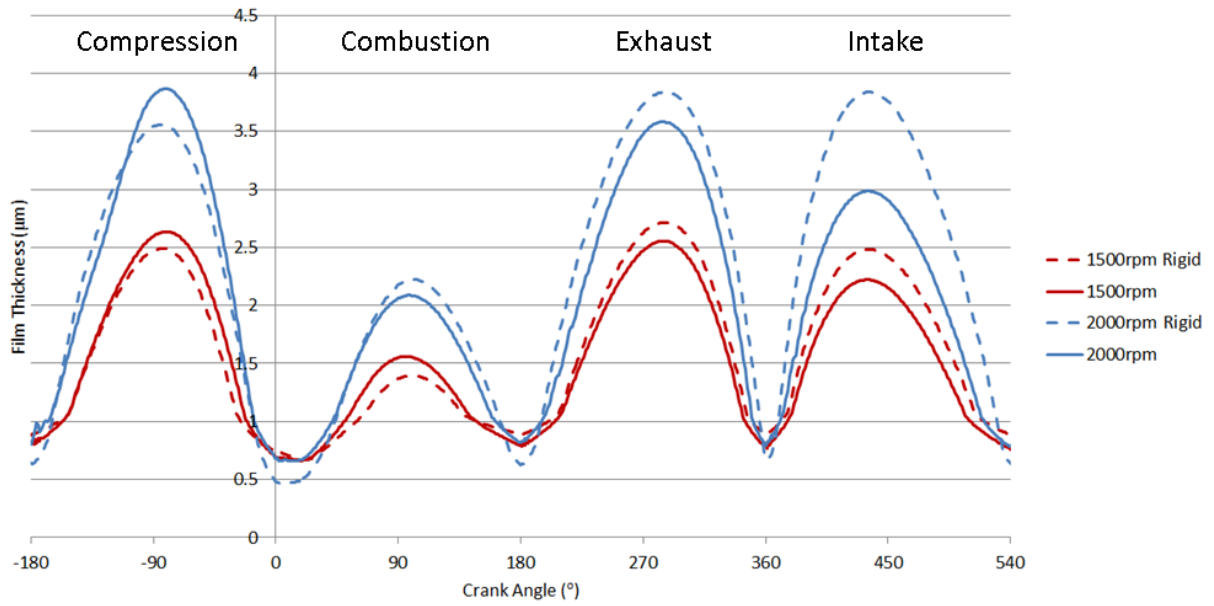


Figure 5.14: Effect of lubricant temperature on the minimum film thickness at different engine speeds for both rigid and elastic analysis. Lubricant temperature = 80°C

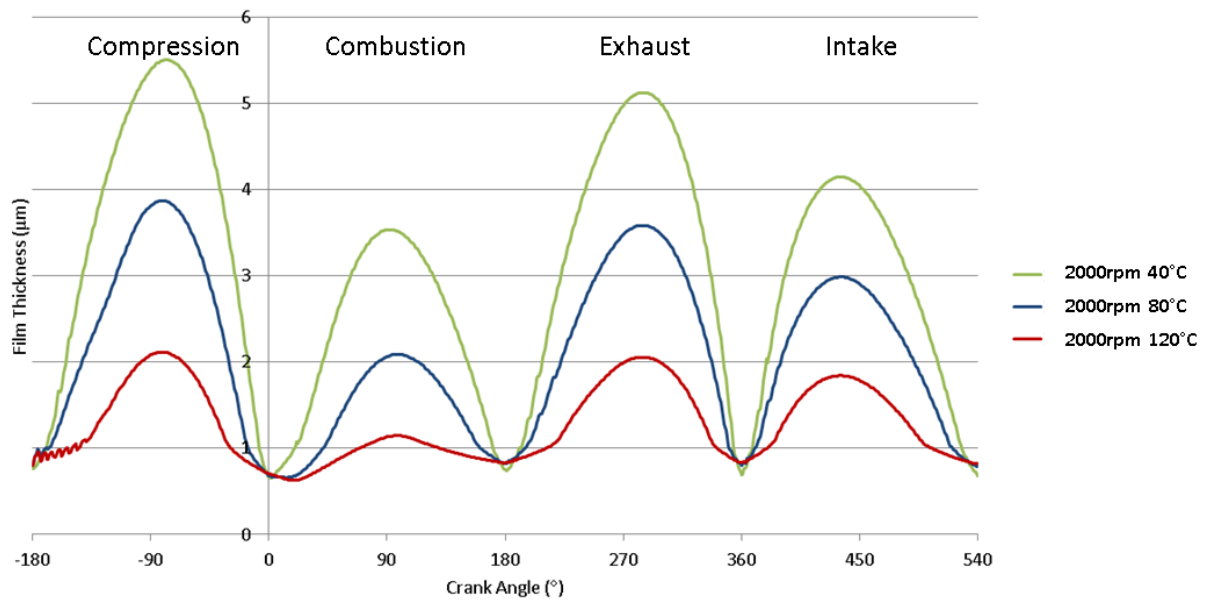


Figure 5.15: Effect of temperature on the minimum film thickness (elastic ring analysis).

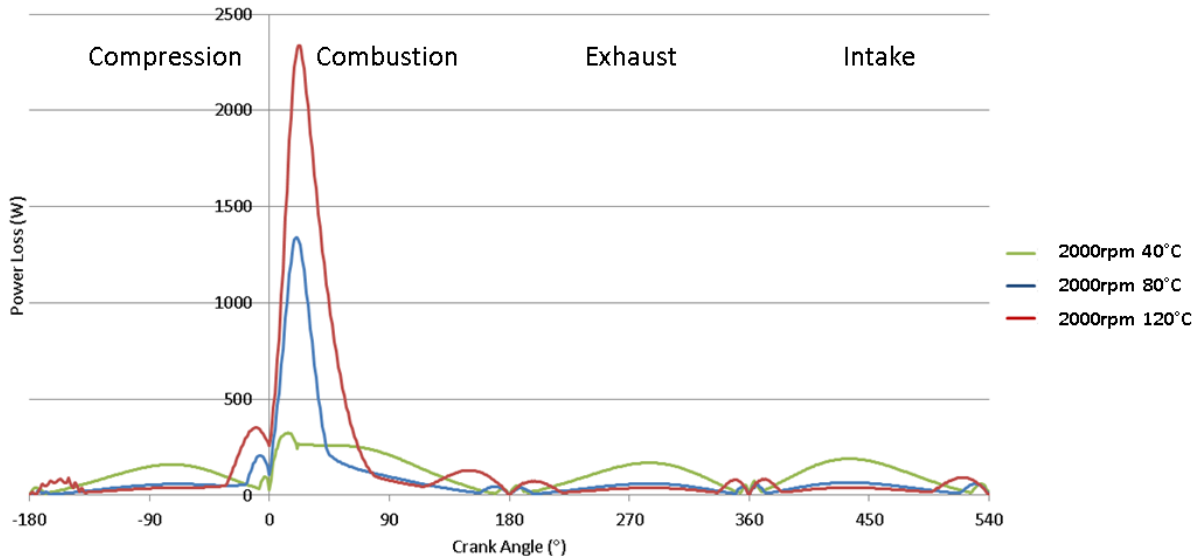


Figure 5.16: Effect of temperature on friction power loss (elastic ring analysis)

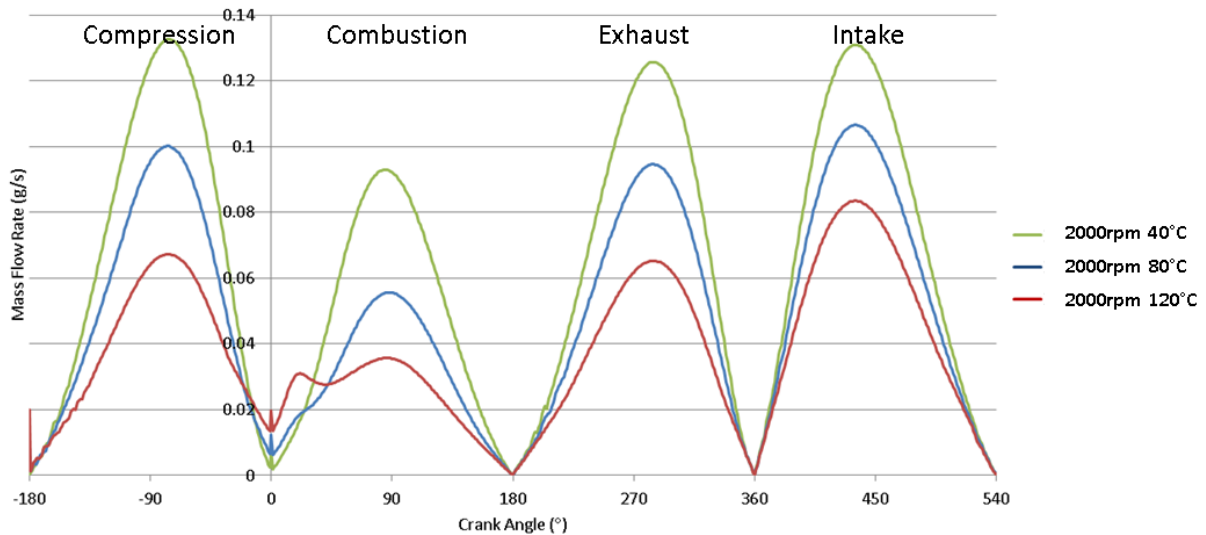


Figure 5.17: Effect of temperature on lubricant mass flow rate (elastic ring analysis)

Figure 5.18 presents a comparison of the frictional power loss for both rigid and elastic ring analyses, as a percentage of the total energy available. The power loss is calculated over a complete engine cycle for different engine speeds and effective temperature values. Over the whole cycle a greater power loss is seen for the elastic analysis, particularly under more demanding conditions. It should be noted, however, that the maximum frictional power loss throughout the engine cycle occurs at the point of maximum pressure. The rigid ring analysis shows a higher peak at these points as shown in figure 5.8. However, over the course of the whole engine cycle, the elastic ring analysis predicts greater frictional losses.

The inset graph to figure 5.18 exhibits the same results, but rotated through 180° for clearer visibility.

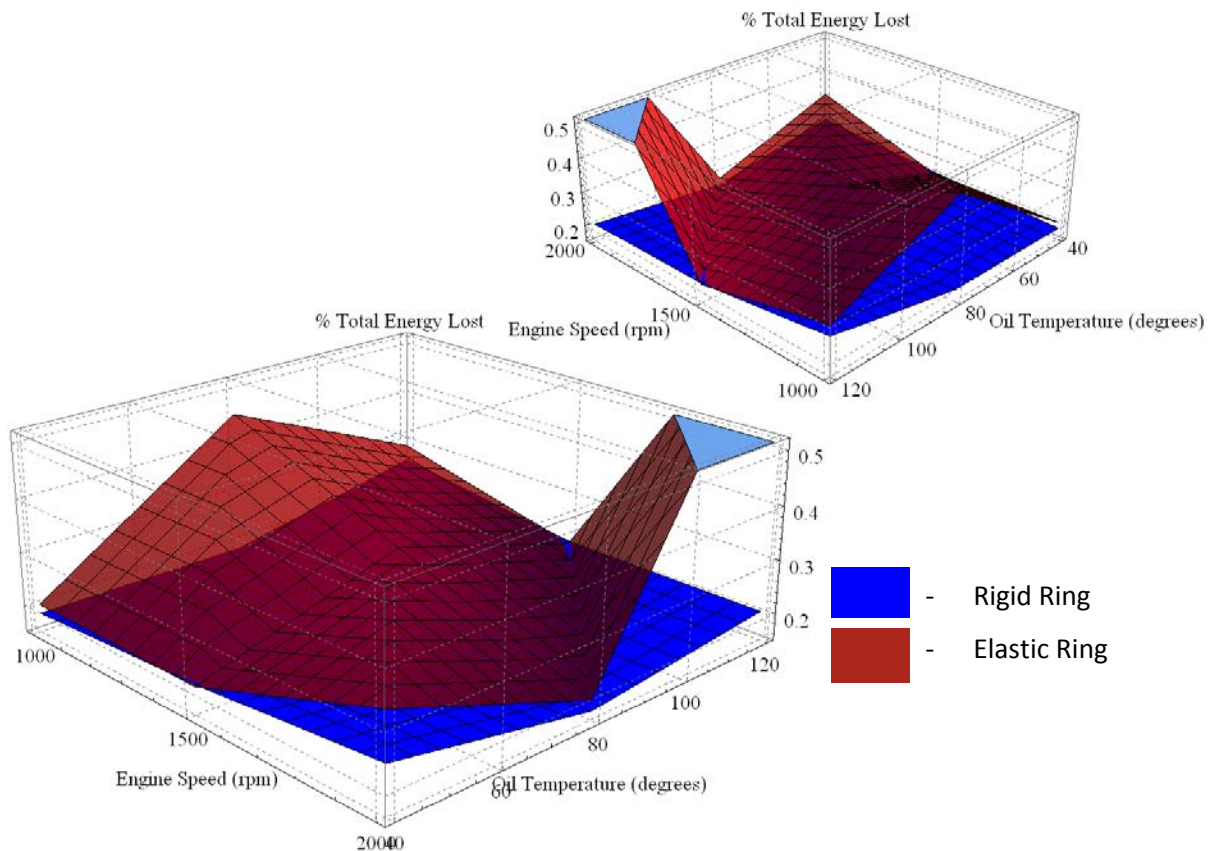


Figure 5.18: Power loss comparison between rigid and in-plane elastic ring analysis, with respect to oil temperature and engine speed

### 5.5. Ring dynamics in two planes

The inclusion of in-plane ring dynamics is a relatively simple solution to envisage. The in-plane deformation acts in the radial direction of the ring, as does the film thickness measurement. This means that the radial ring deflection can be added to the previous profile algebraically to determine the updated film thickness profile. Ring dynamics in the axial plane of the ring are more complicated to couple with the tribological analysis than the in-plane case. The out-of-plane deformation is not accounted for by being simply added to the film thickness value. Instead, the ring's out-of-plane velocity is used to update the speed of entraining motion when solving Reynolds' equation and the incurred twist affects the ring's axial profile with respect to the liner. Figure 5.19 shows an example of this, with the ring profile at two different time steps after undergoing some twisting motion. Without the inclusion of the out-of-plane dynamics, the ring's axial profile will not twist throughout the

engine cycle. An alteration to the ring profile will affect the pressure distribution within the contact.

The inherent assumption, when including ring elastodynamics, is that the lubricant still completely fills the ring-bore conjunction after the ring has undergone deformation. This assumption may not hold true in practice because of lack of lubricant availability or rupture of a meniscus bridge with an increasing gap size between the contacting solid surfaces. However, as fully flooded conditions are used in the tribological analysis, this assumption is seen as reasonable.

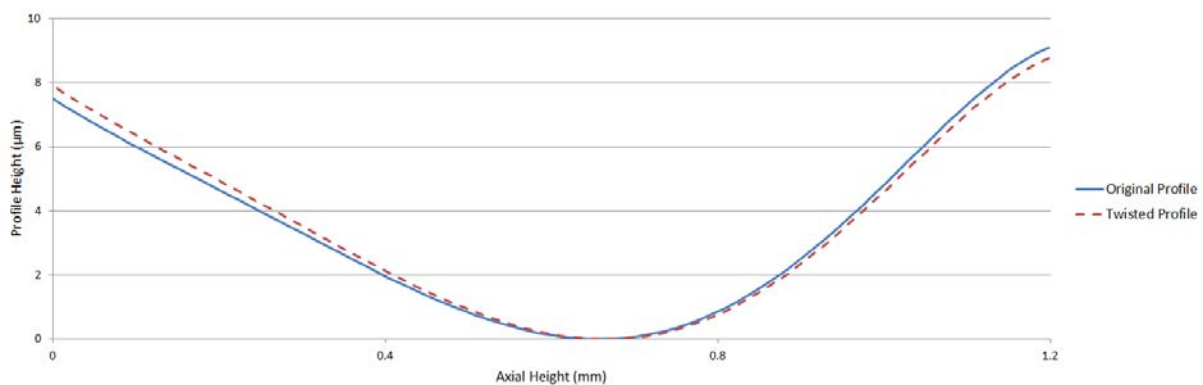


Figure 5.19: Twist of a worn ring's axial profile

Figures 5.20-5.21 show the minimum film thickness and frictional power loss profiles calculated using the rigid ring methodology, the in-plane-only ring dynamics, and the dynamics in both planes. The previous results presented in this chapter showed that the general trend was that the inclusion of in-plane dynamics reduced the film thickness values at the mid-stroke. Since there is no entraining motion at TDC and BDC, the film thickness at these locations for the rigid analysis are thicker than that expected. Inclusion of the out-of-plane response yields lower film thickness predictions at reversal as well as the in-plane methodology, which suggests this to be a more realistic model. The film thickness profiles for both elastic ring analyses are very similar, with the fully dynamic ring yielding slightly lower values. This reduction in film thickness, particularly at reversal, causes asperity interactions to occur, causing 'spikes' in the frictional power loss around TDC and BDC. This is especially noticeable away from the high pressure reversal point just before combustion.

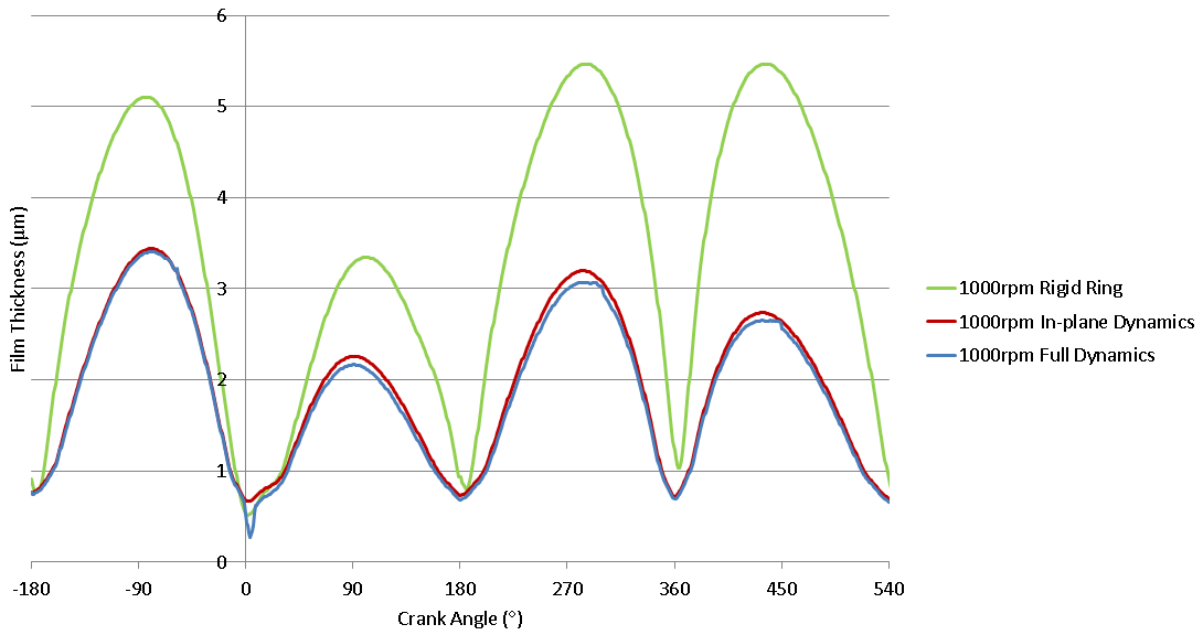


Figure 5.20: Minimum film thickness comparisons for the rigid, in-plane and full dynamic analyses at 1000rpm, lubricant temperature = 40°C

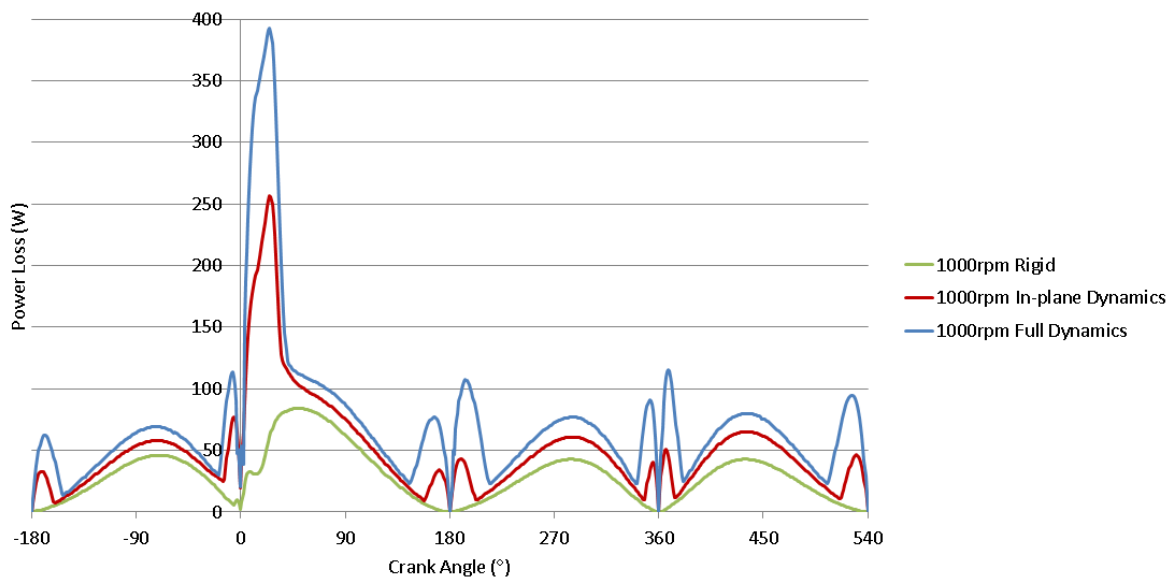


Figure 5.21: Total friction power loss comparisons for the rigid, in-plane and full dynamic analyses at 1000rpm, lubricant temperature = 40°C

Figures 5.22-5.25 show the same results as in figures 5.20-5.21, but at higher engine speeds. The expected trends are present, with a higher speed of entraining motion resulting in a thicker lubricant film. Inclusion of the ring dynamics in both planes gives a similar film thickness result to that with just the in-plane case. This is reflected in the frictional power loss predictions, with very little difference noted between the two methodologies.

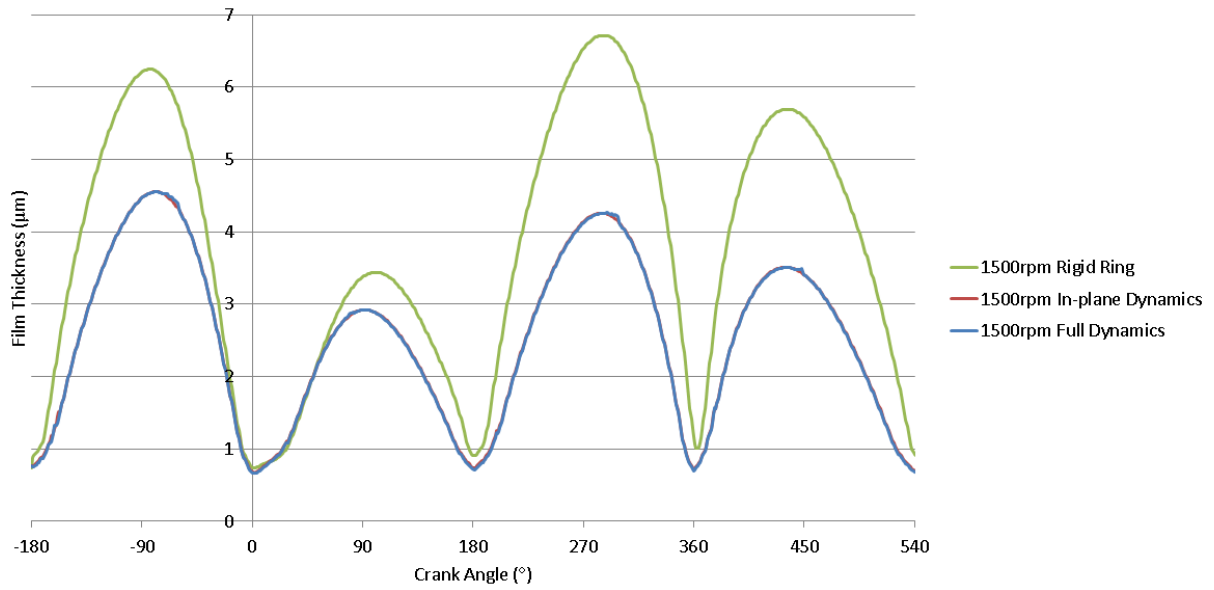


Figure 5.22: Minimum film thickness comparisons for the rigid, in-plane and full dynamic analyses at 1500rpm, lubricant temperature = 40°C

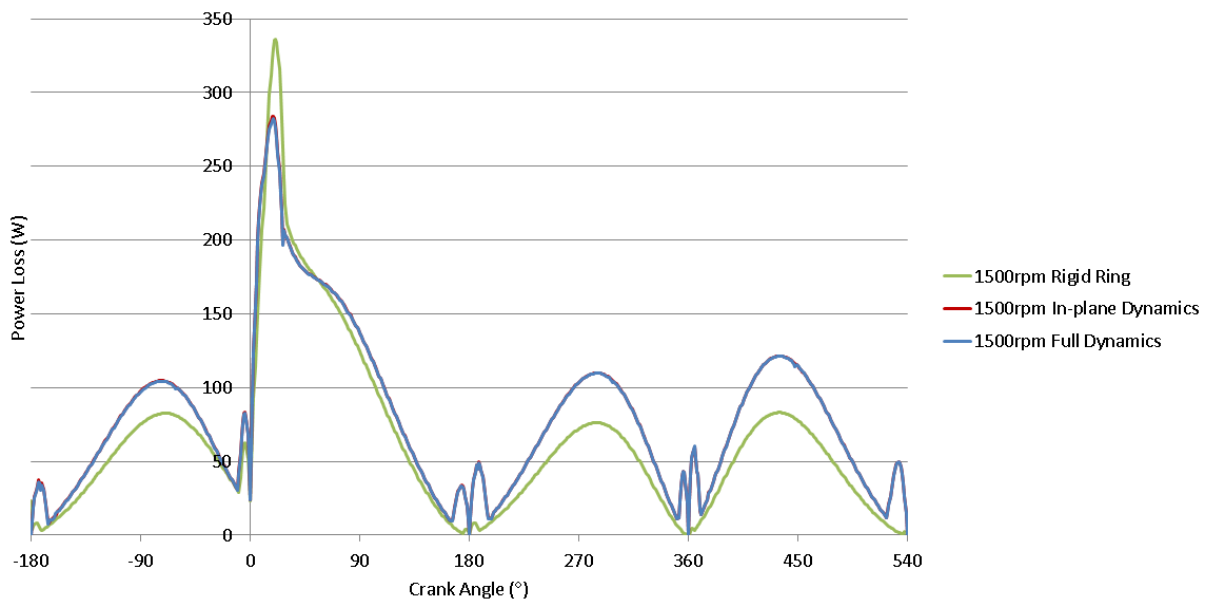


Figure 5.23: Total friction power loss comparisons for the rigid, in-plane and full dynamic analyses at 1500rpm, lubricant temperature = 40°C



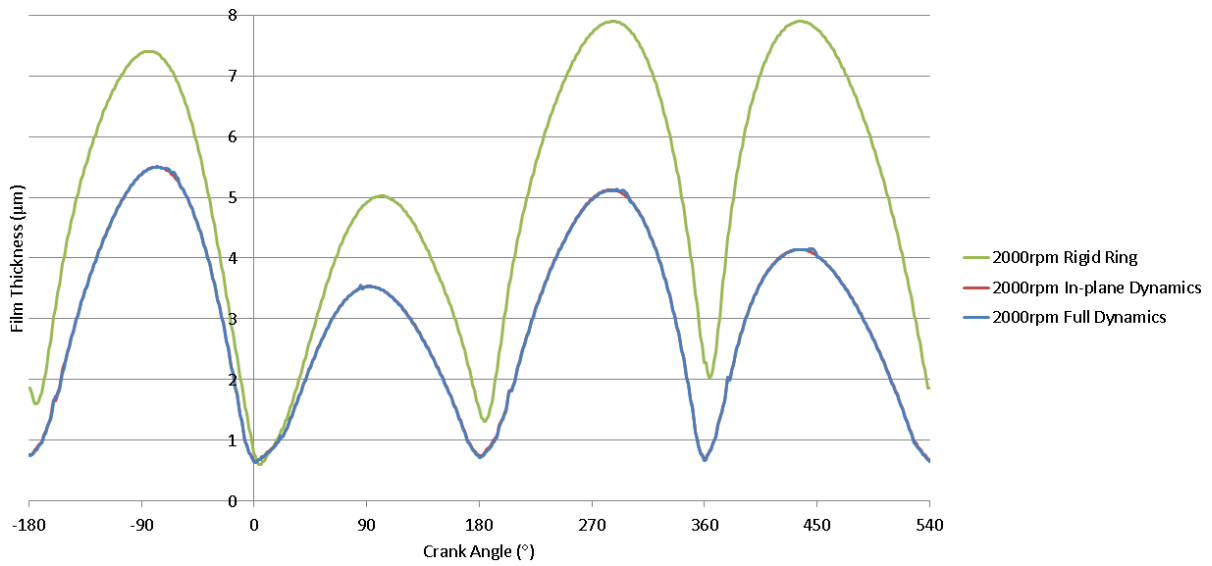


Figure 5.24: Minimum film thickness comparisons for the rigid, in-plane and full dynamic analyses at 2000rpm, lubricant temperature = 40°C

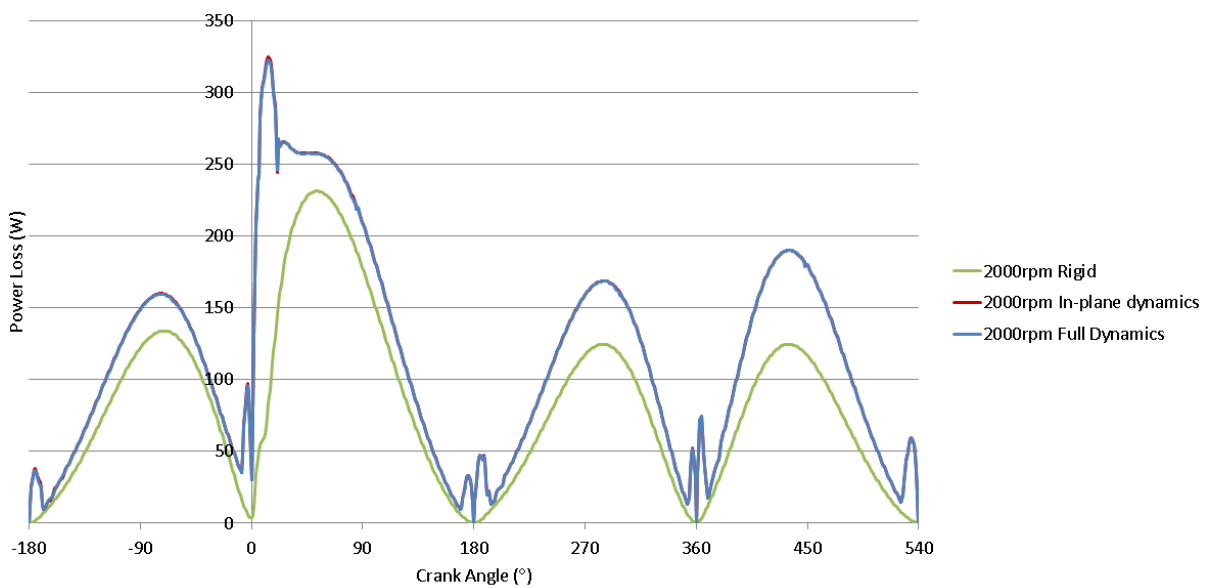


Figure 5.25: Total friction power loss comparisons for the rigid, in-plane and full dynamic analyses at 2000rpm, lubricant temperature = 40°C

Comparisons between the rigid, in-plane and fully dynamic methodologies with higher lubricant temperatures are shown in figures 5.26-5.28, which use oil temperatures of 80°C and 120°C. A very close agreement in prediction is seen between the two dynamic methodologies. This should be expected, since the angle of twist is small, as shown in figure 5.19, meaning that its effect on the ring-liner conjunction is also small. The presented methodology does not include any prediction of gas flow through the ring pack, which

would affect the gas pressure behind the ring. If out-of-plane ring dynamics were included, this gas pressure would alter as the ring moves from the bottom face of the groove to the top. This would subsequently affect the lubricant film thickness. Additionally, accounting for lubricant starvation may also result in a difference between the in-plane and fully dynamic analyses. The combination of higher engine speed and lubricant temperature shows a slightly larger difference between the in-plane and fully dynamic ring analyses, as shown in figure 5.28.

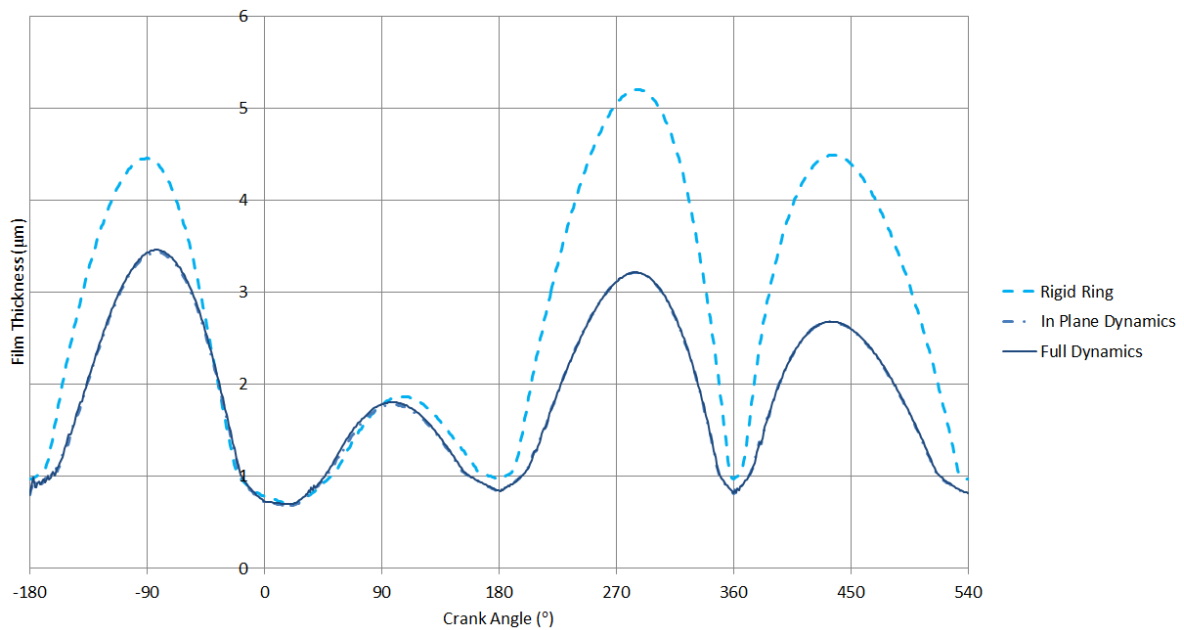


Figure 5.26: Minimum film thickness comparisons for the rigid, in-plane and full dynamic analyses at 1500rpm, lubricant temperature = 80°C

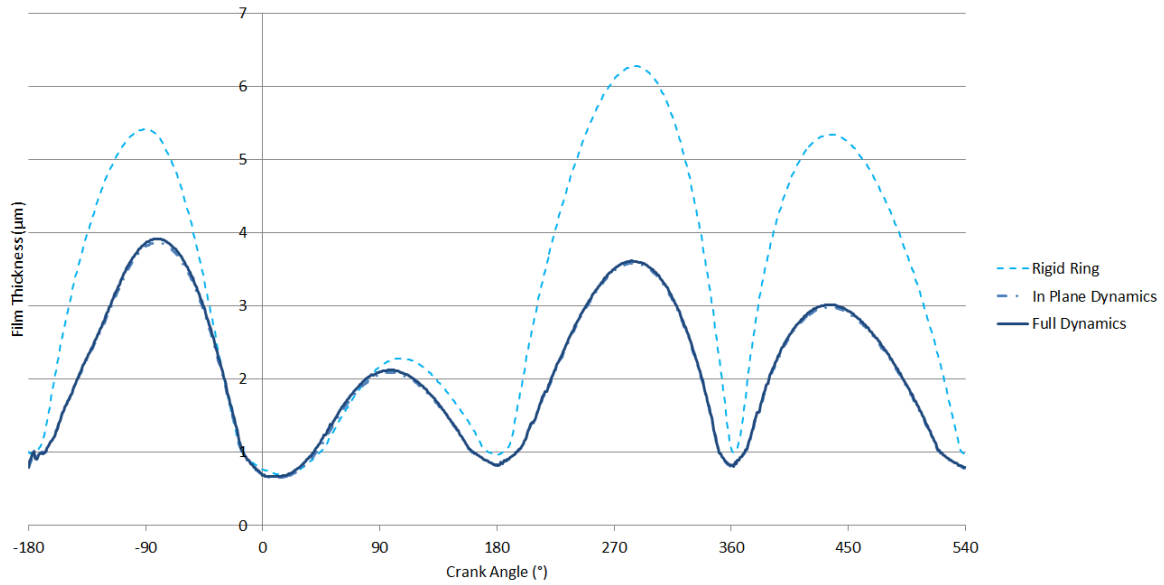


Figure 5.27: Minimum film thickness comparisons for the rigid, in-plane and full dynamic analyses at 2000rpm, lubricant temperature = 80°C

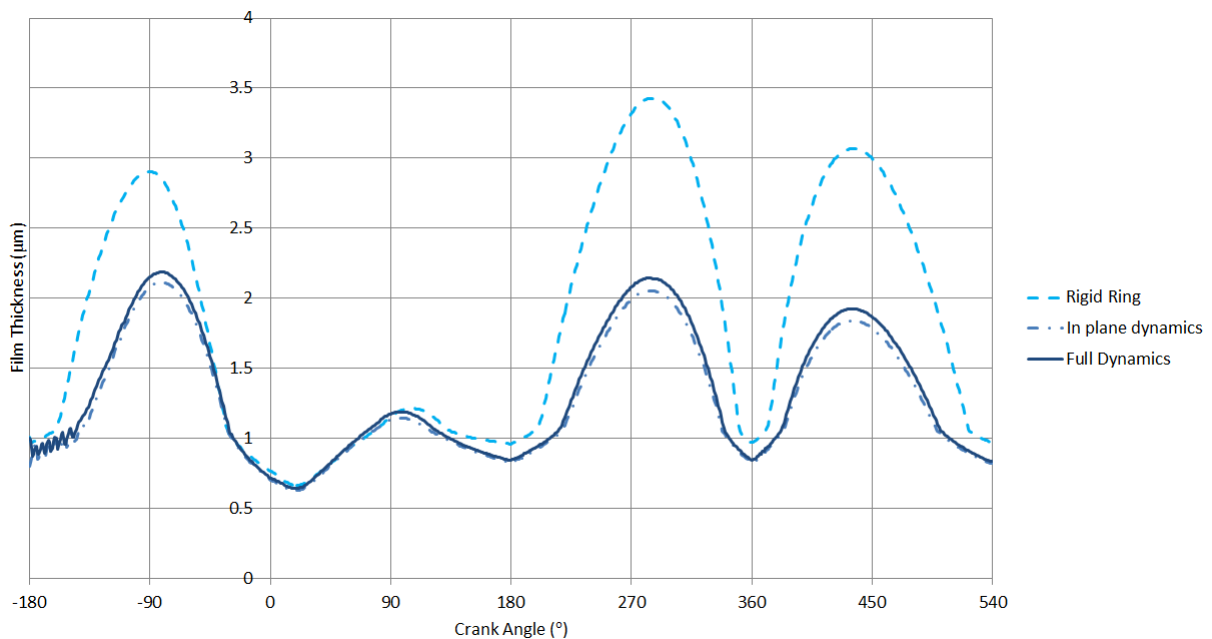
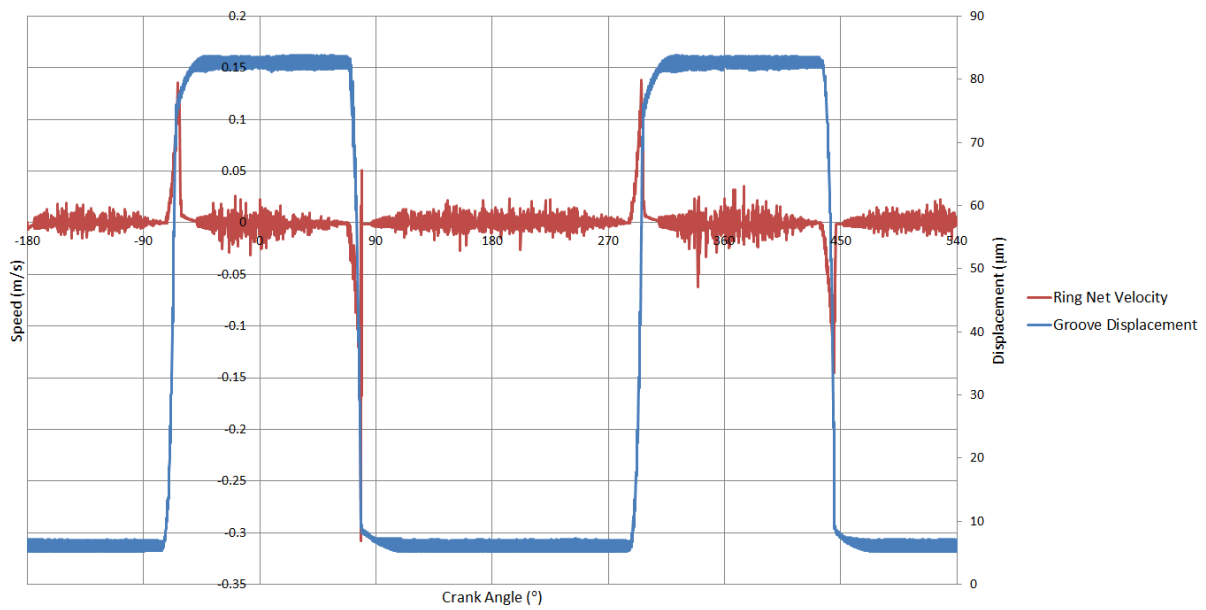


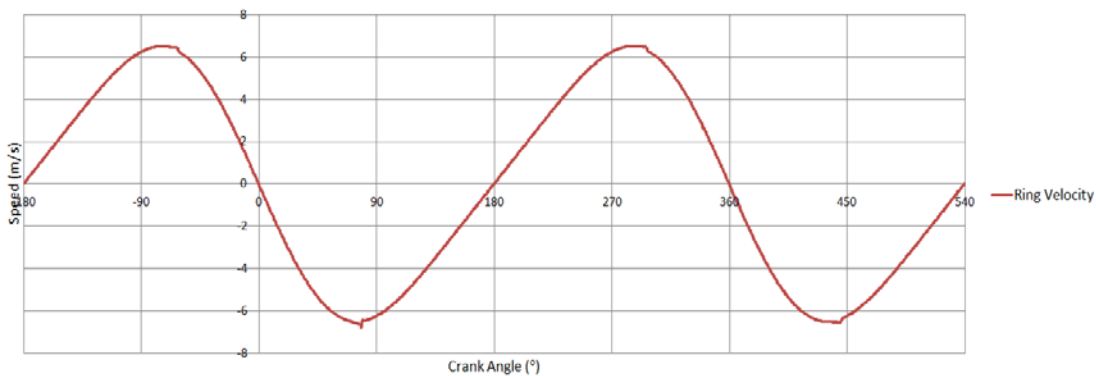
Figure 5.28: Minimum film thickness comparisons for the rigid, in-plane and full dynamic analyses at 2000rpm, lubricant temperature = 120°C

Inclusion of out-of-plane ring dynamics allows for any lateral axial movement with respect to the piston to be taken into account. The piston groove restricts the movement of the ring in the axial direction of the piston. However, there is room for the ring to move rigidly and elastically throughout the engine cycle. From the engine data available, a gap of approximately 89µm remains when the ring’s axial height is subtracted from the groove’s

axial height. It is assumed that a layer of lubricant of thickness  $10\mu\text{m}$  would be present on both faces of the ring. Since fully flooded conditions are assumed for the piston ring-cylinder liner conjunction, it is also assumed that sufficient lubricant is available on the upper and lower faces of the groove. Using Tian's method (1998), the groove lubricant reaction force is calculated when the gap between the ring and the groove becomes less than  $10\mu\text{m}$ . If the gap is greater, the cylinder (top of the ring) or crankcase (bottom of the ring) pressure is used.



(a)



(b)

Figure 5.29: Compression ring motion within the groove throughout the engine cycle. Engine speed = 1500rpm

Figure 5.29a shows the position of the ring within the groove throughout the engine cycle at 1500rpm, alongside the difference in velocity between the piston and the ring. The overall

ring velocity is shown in figure 5.29b, and is seen to largely follow the piston's velocity profile, as would be expected. However, in the instances immediately after the point of maximum velocity in each stroke, there is a deviation from an otherwise smooth curve. These 'spikes' are shown in the net velocity results in figure 5.29a, and occur due to the piston's axial velocity slowing upon approaching the dead centres prior to reversal. The compression ring continues moving at a higher velocity and loses contact with the groove lubricant film. As the ring approaches the opposite face of the groove, lubricant present on this groove surface creates a reaction force which acts upon the ring. This force slows the ring, so that it once again follows the velocity profile of the piston, with some slight local variations. The movement of the ring away from the either grooves' faces causes loss of sealing, as some gas pressure would be lost through the gap behind the ring. This would increase the probability of ring axial oscillations (flutter) and blow-by. Figure 5.30 shows some example ring deformations at different positions throughout the engine cycle. Note the scale in each of the deformed ring profiles, which suggests that there is greater deformation when the ring is in transition between the two groove faces.

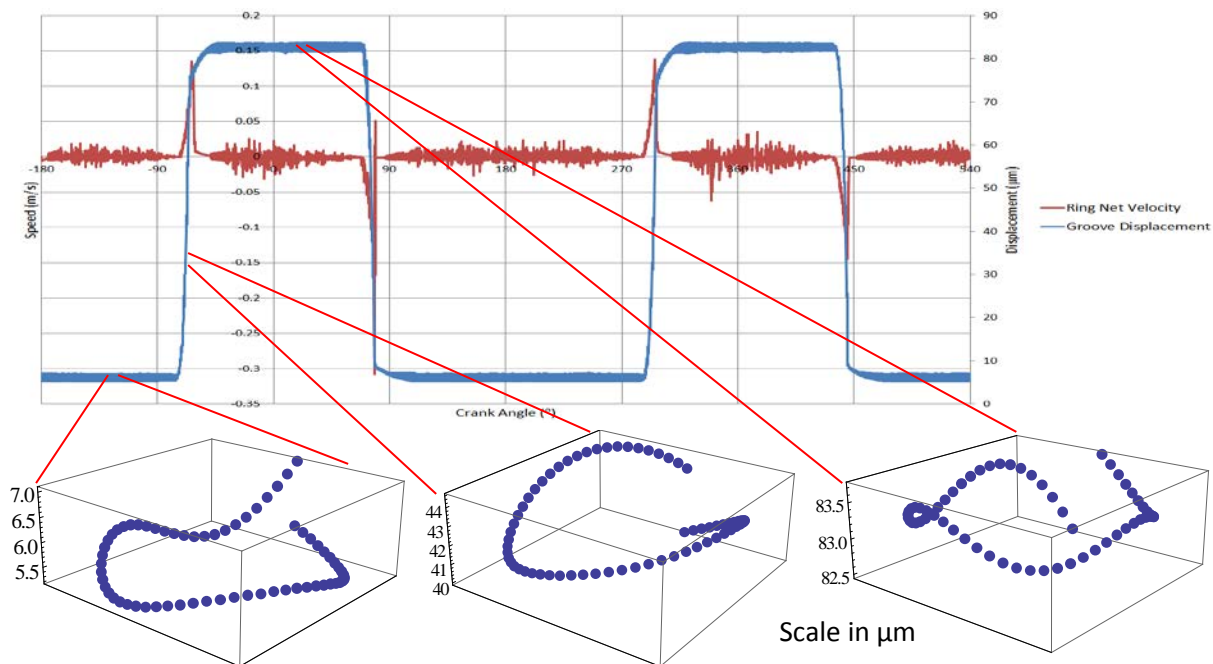


Figure 5.30: Compression ring 3D profiles at different stages of the engine cycle. Engine speed = 1500rpm

Whilst it is seen that the piston speed is the primary cause behind the resultant motion of the ring, certain cases are affected by the combustion pressure, in the results presented.

Figure 5.31 shows the groove displacement and net velocity at 1000rpm and 40°C. At the combustion point, the ring displaces from the top of the groove, even though the piston is still accelerating towards the mid-stroke. This suggests conditions which are even more likely to result in some loss of power, as some of the power from the point of combustion is lost through displacing the compression ring. Therefore, there is a loss of sealing effect.

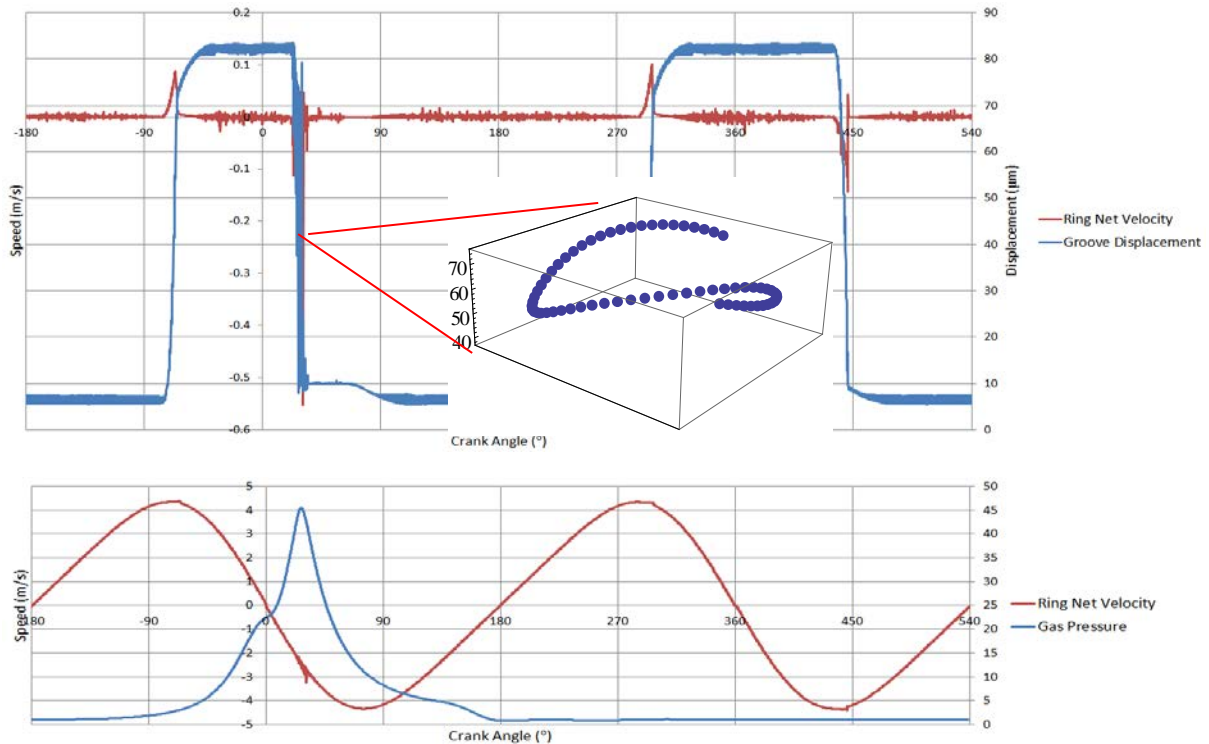


Figure 5.31: The 3D profile when the ring is forced from the groove face due to combustion pressure, even when the piston is increasing in axial velocity. This causes a larger ring deformation (note the scale). Engine speed = 1000rpm, lubricant temperature = 40°C

The effect of an increase in temperature is also shown. Figures 5.32 and 5.33 show the minimum film thickness at 1500rpm and 2000rpm with varying lubricant temperatures. As would be expected, the film thickness decreases with increased temperature, which increases the risk of mixed regime of lubrication and surface interactions. This is shown in figure 5.34, where the frictional power losses are markedly larger than those at lower temperatures at reversal and in the power stroke. The lower lubricant viscosity at higher temperatures means lower viscous friction through the mid-stroke, when comparing the results at the same engine speed. However, friction peaks at reversal and at the point of combustion there are areas where localised wear would be likely.

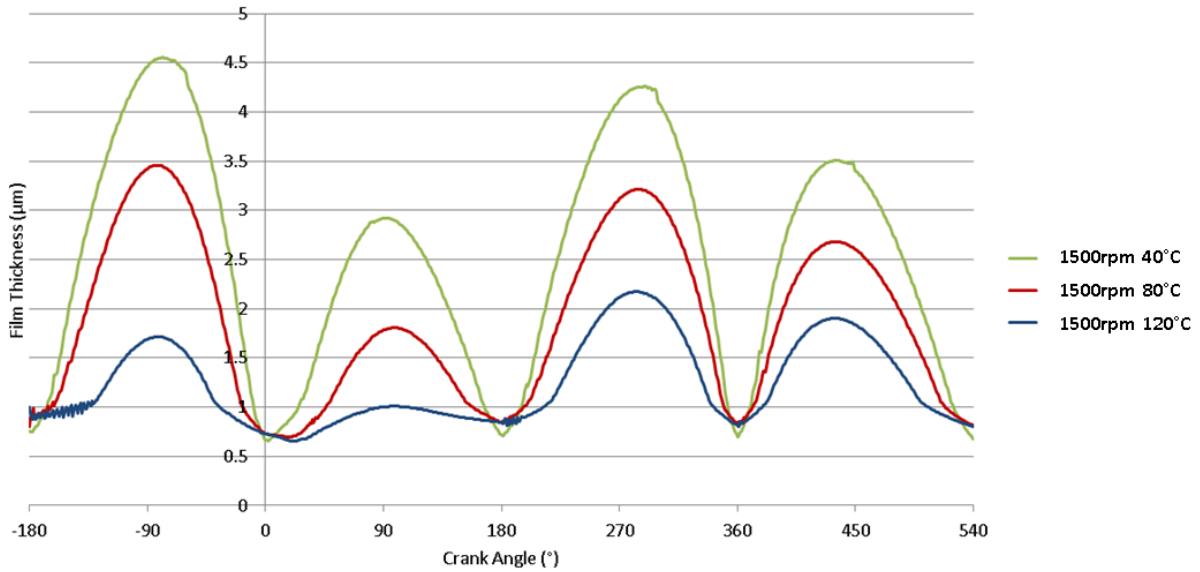


Figure 5.32: The effect of lubricant temperature on film thickness with a fully dynamic ring.

Engine speed = 1500rpm

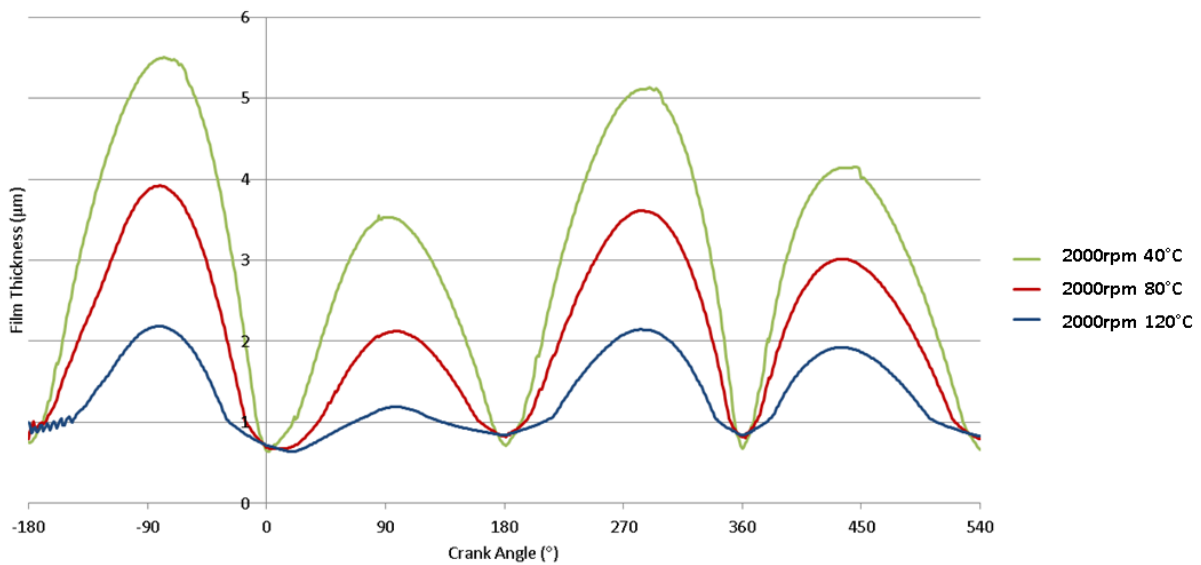


Figure 5.33: The effect of lubricant temperature on film thickness with a fully dynamic ring.

Engine speed = 2000rpm

A difference can be observed between the rigid ring, in-plane and full elastodynamic ring results. However, the variation of engine speed affects the results for each of these cases in different ways. Figure 5.35 shows the full dynamics' results, with a lubricant temperature of 80°C, at different engine speeds.

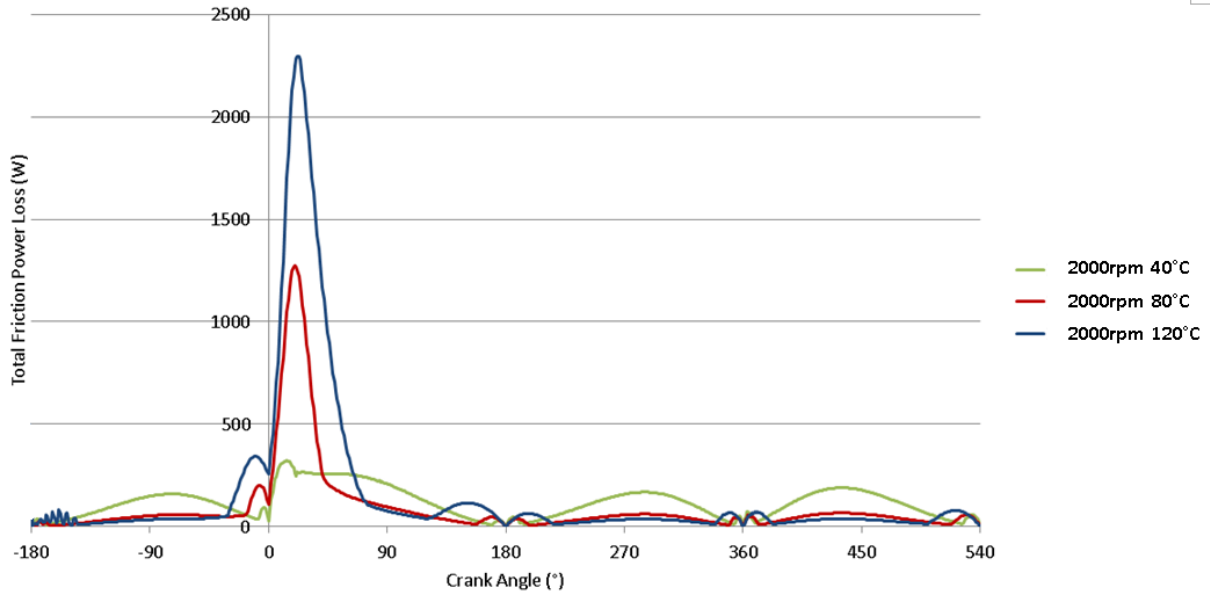


Figure 5.34: The effect of lubricant temperature on friction power loss with a fully dynamic ring. Engine speed = 2000rpm

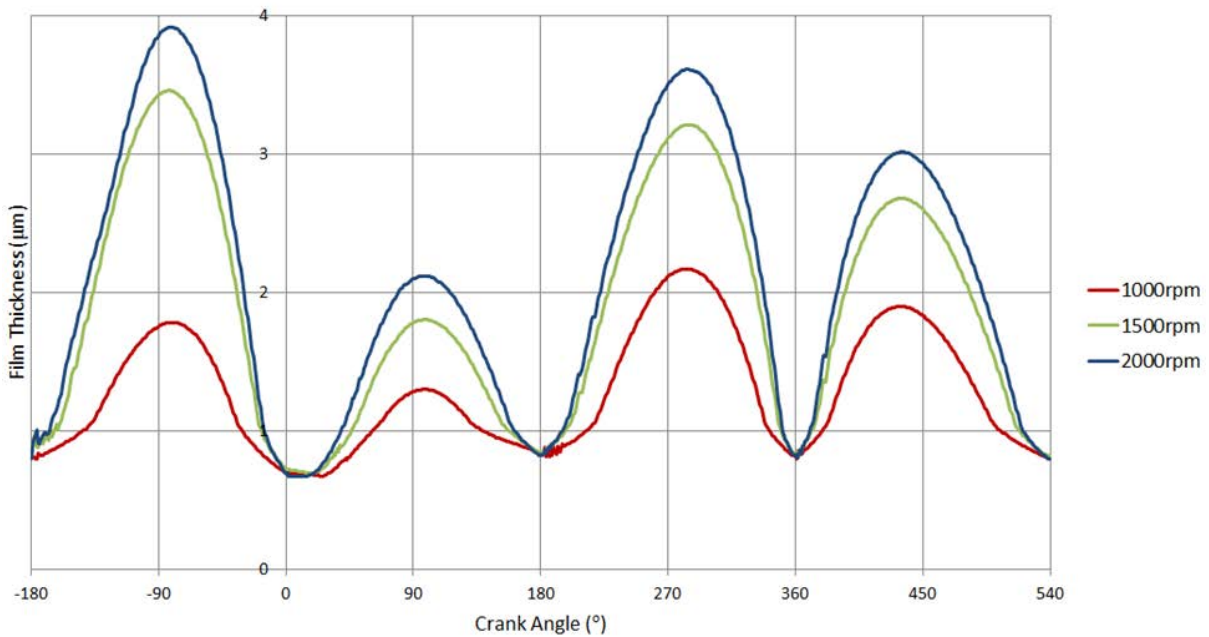


Figure 5.35: The effect of engine speed on film thickness with a fully dynamic ring. Lubricant temperature = 80°C

Figure 5.36 shows the groove displacement profile at an engine speed of 1500rpm with a lubricant temperature of 120°. At the point of combustion the ring is forced away from the top of the groove, losing some of the sealing of the combustion chamber. As shown in figure



5.36, this behaviour causes an increase in ring deformation in the out-of-plane direction. A loss of pressure in the combustion chamber is again likely to occur.

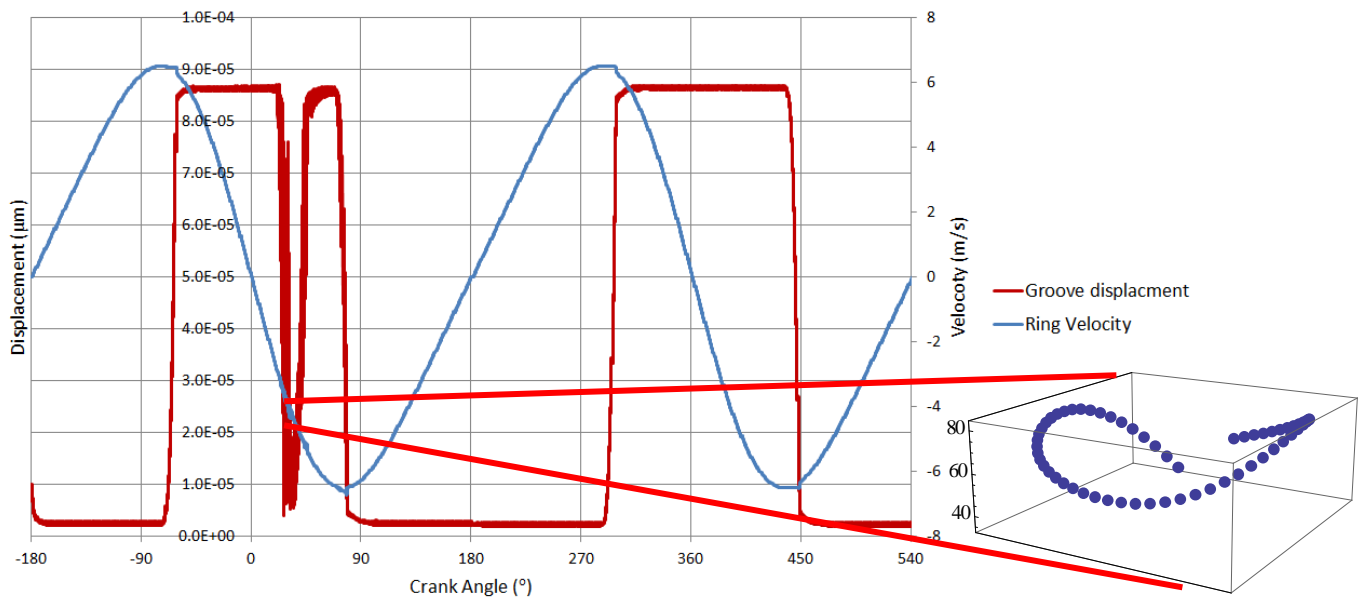


Figure 5.36: Ring displacement throughout the engine cycle. Engine speed = 1500rpm, lubricant temperature = 120°C

Figure 5.37 shows a comparison of the fully dynamic numerical analyses at different engine speeds (up to 6000rpm), with a lubricant temperature of 120°C. It can be seen that over an engine speed of 3000rpm, the piston acceleration towards the mid-stroke causes some drastic motion of the ring. This motion prevents the minimum film thickness from following the expected trend of increasing with an increase in the engine speed, with lower film thickness values predicted for 4000-6000rpm. The corresponding frictional power loss values are shown in figure 5.38. At engine speeds above 3000rpm, significant power loss is predicted just after reversal points, particularly through the power stroke.

Due to the increasing harshness of the conditions at higher engine speeds, the result appears to be a change in the usual trend of increasing film thickness with increasing engine speed. The rigid ring analysis gives results which follow the previously observed trends, as seen in figures 5.39 and 5.40. It can be seen that the power loss predictions are an order of magnitude above those predicted using the rigid ring analysis. As these numerical results have been produced assuming a new compression ring axial profile, it may be indicative of the wear which occurs during the running in period.

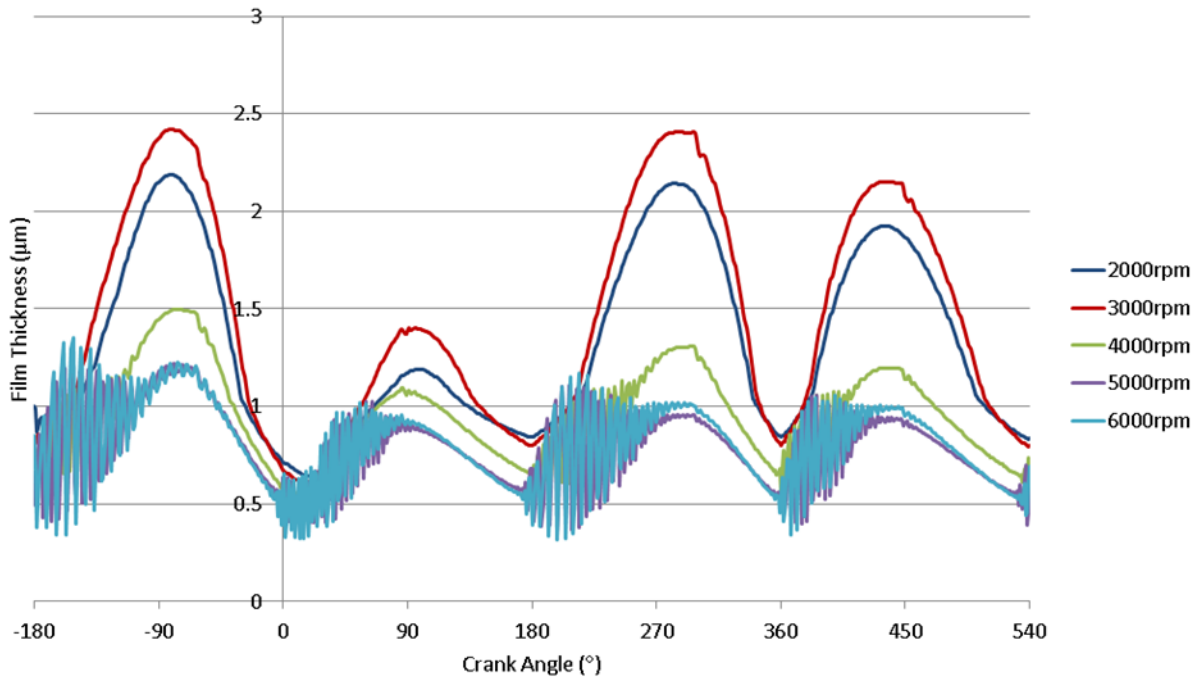


Figure 5.37: The effect of engine speed on film thickness with a fully dynamic ring. Lubricant temperature = 120°C

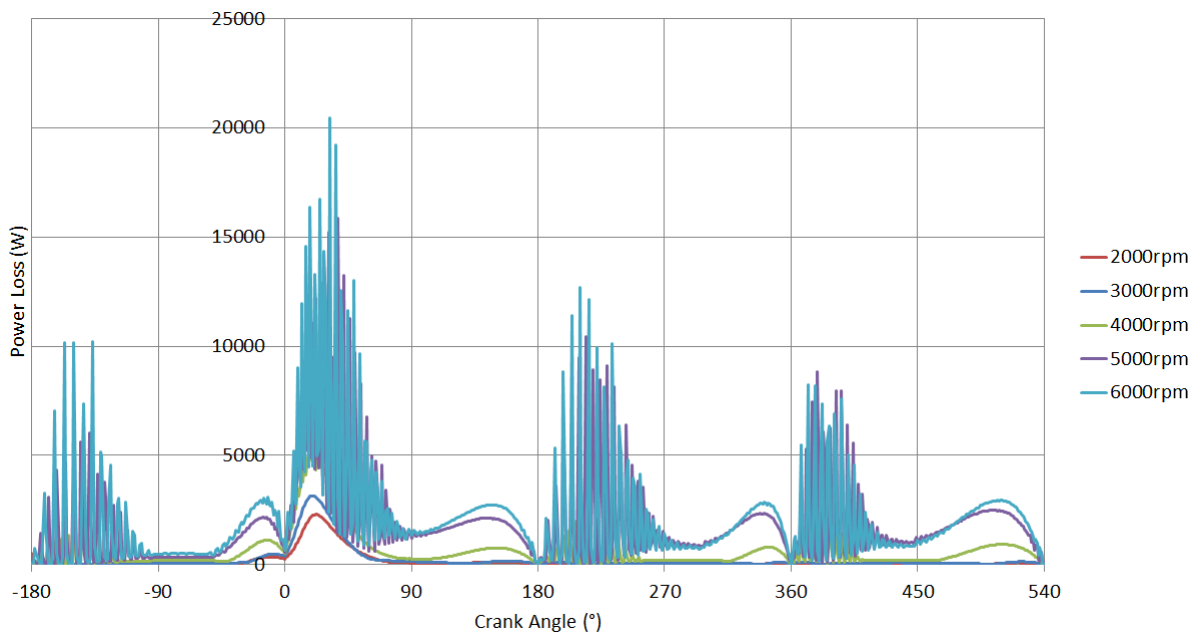


Figure 5.38: The effect of engine speed on friction power loss with a fully dynamic ring. Lubricant temperature = 120°C

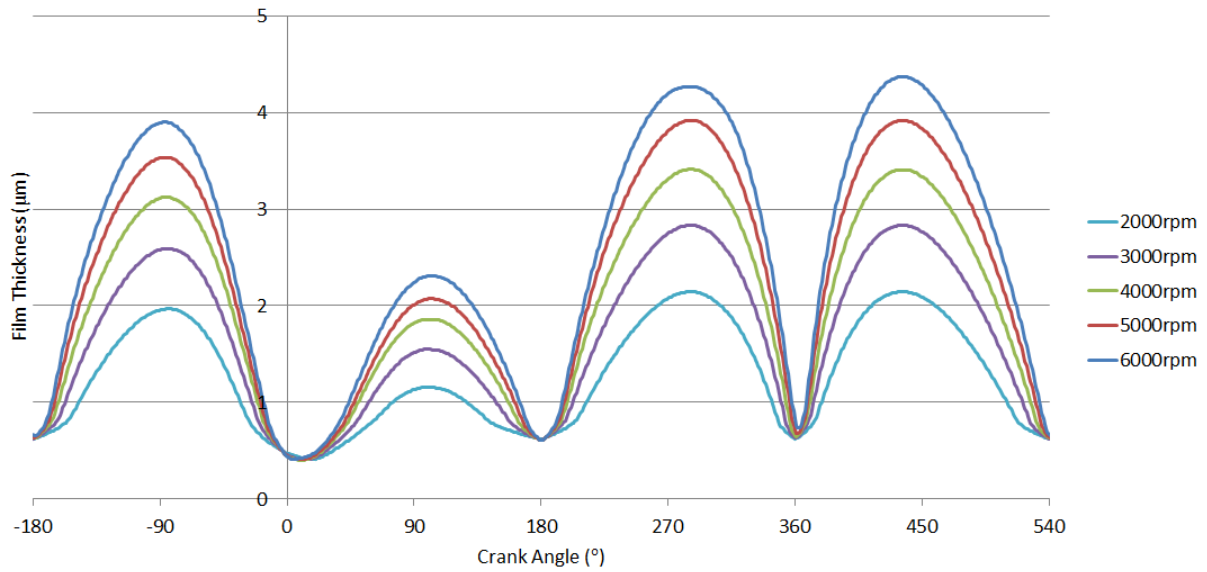


Figure 5.39: The effect of engine speed on film thickness with a rigid ring. Lubricant temperature = 120°C

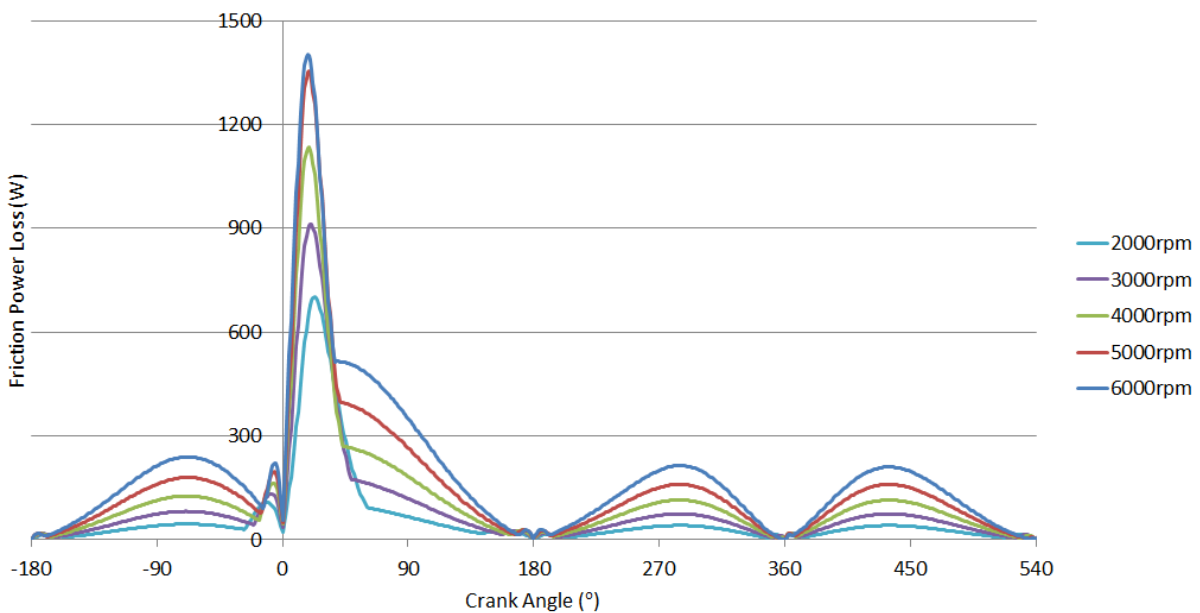


Figure 5.40: The effect of engine speed on friction power loss with a rigid ring. Lubricant temperature = 120°C

The ring profile data provided as part of this project was for a brand new, unused compression ring, as well as a ring which had undergone certain “accelerated harsh” running conditions for 150 hours, thus considered to have reached its useful life. To demonstrate the importance of the ring’s axial profile, as well as providing results which

may represent an intermediate stage of the ring's life, the new measured profile was modified by halving the axial ring profile. This is shown in figure 5.41.

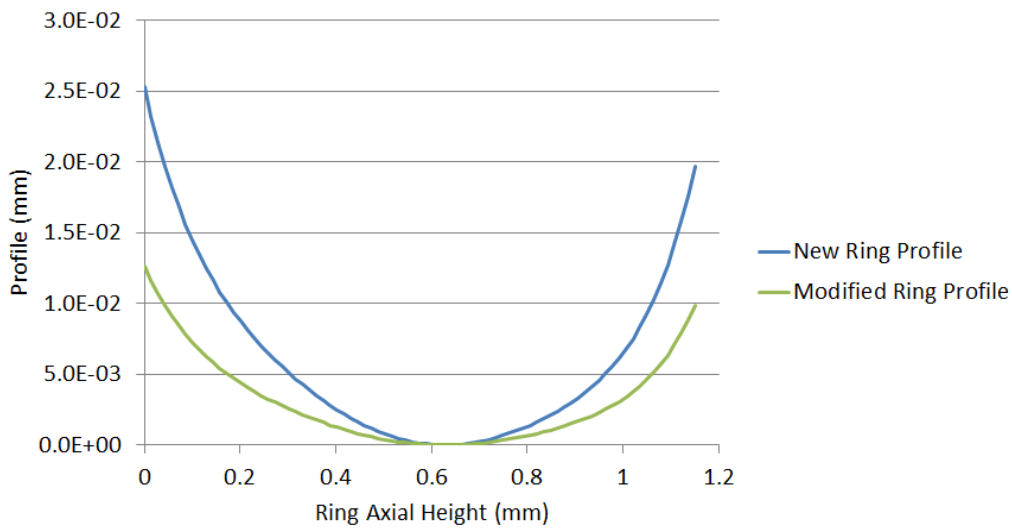


Figure 5.41: Modified new ring axial profile to represent a ring part-way through its life cycle

The modified ring profile in figure 5.41 was used to obtain results at the high load, high temperature conditions which yielded the large perturbations in figures 5.37 and 5.38. These results are shown in figures 5.42-5.43. A more stable result is seen, which is more in keeping with the results obtained at lower speeds and temperatures. This shows that the ring's axial profile plays a significant part in the tribological performance of the compression ring.

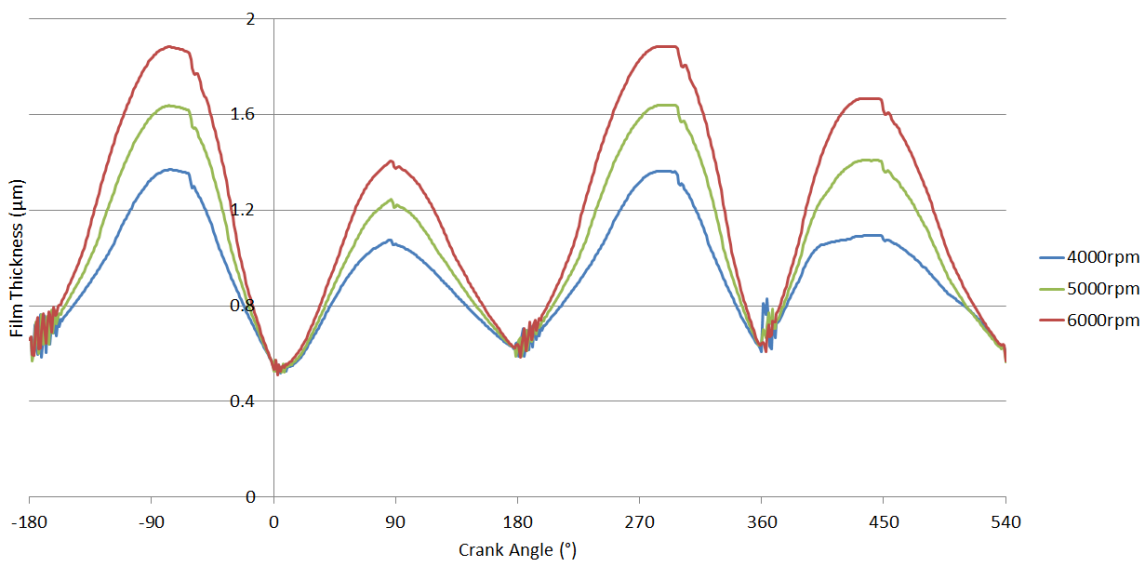


Figure 5.42: Film thickness results using an 'intermediate' ring profile. Lubricant temperature = 120°C

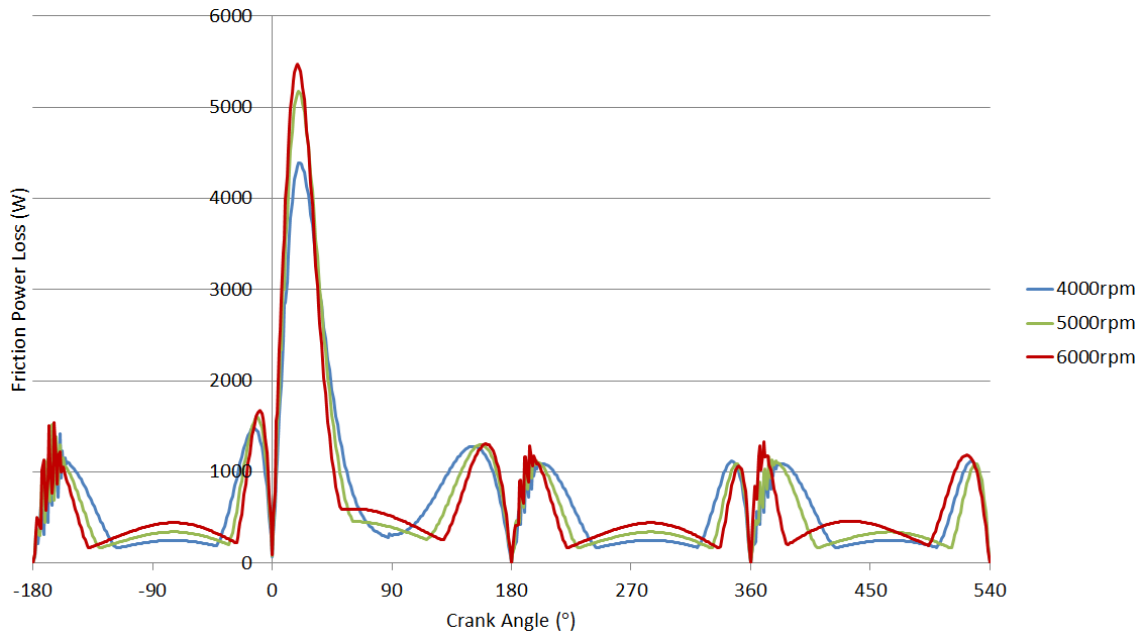


Figure 5.43: Power Loss results using an ‘intermediate’ ring profile. Lubricant temperature = 120°C

Following visual inspection, it can be seen that compression rings suffer through wear of their axial profile (along their face-width) during their useful life. This wear gives an improved film profile through gradual and bedding-in wear when compared with the numerical analysis with a new ring. Figure 5.44 shows the profiles for a new and a worn ring. The worn ring profile is measured after a 150hr high speed test, representing an ‘end of life’ condition. A clear difference between the profiles can be observed.

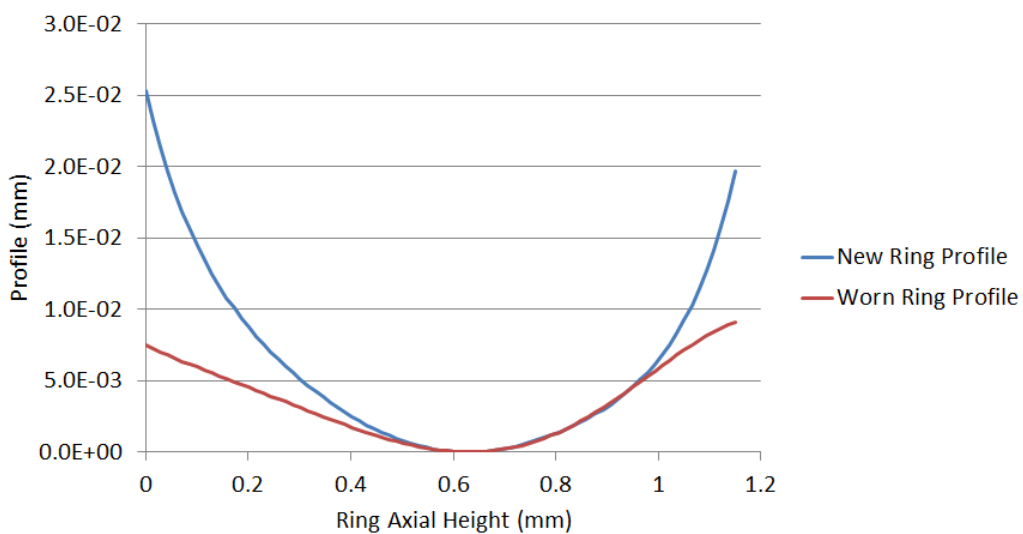


Figure 5.44: New and worn ring axial profiles

The results presented compare a measured new compression ring with a ring at the end of its useful life. With the rigid ring analysis, an improved film thickness is seen through the whole engine cycle. Compared with the new ring analysis for a cold lubricant running condition, a fully dynamic ring analysis with a worn axial profile shows improved film thickness throughout the engine cycle. This is shown in figure 5.45. Correspondingly, figure 5.46 shows the reduced frictional losses due to this worn axial profile. It can be seen that the friction 'peaks' at reversal due to asperity interactions are not present for the worn ring case, giving a smoother power loss curve with lower maximum values at the mid-strokes.

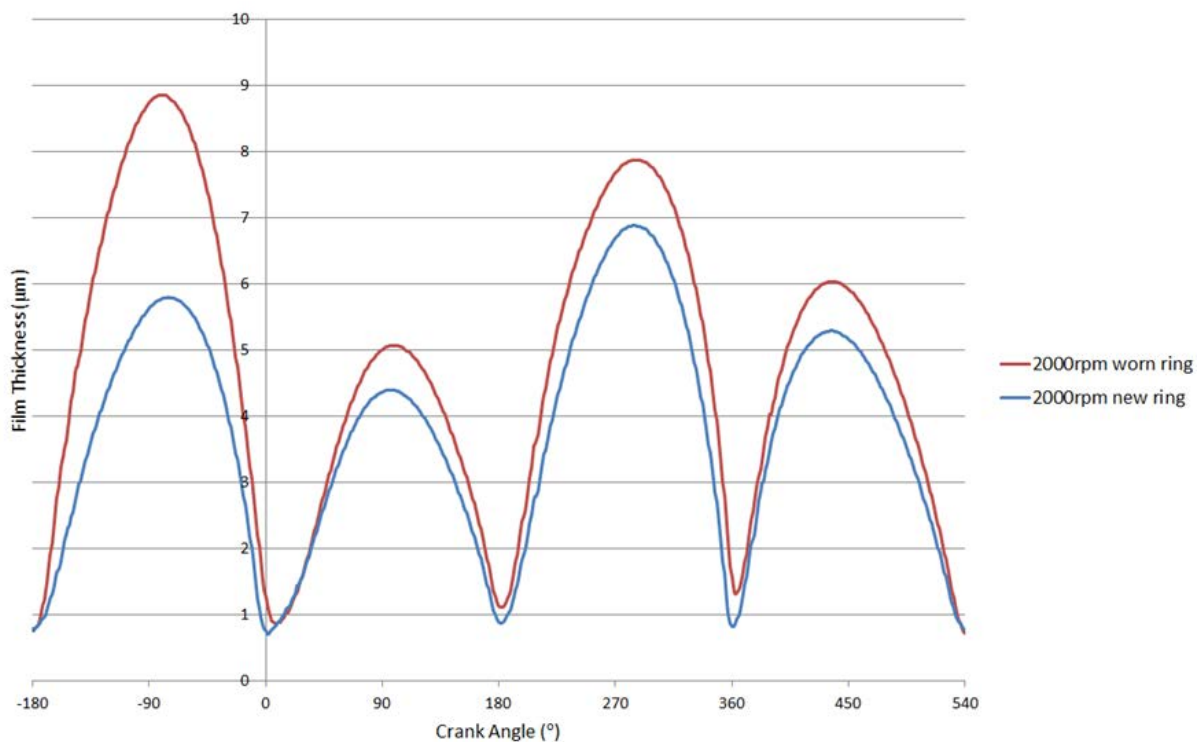


Figure 5.45: Minimum film thickness results for the elastic analysis comparing new and worn ring profiles. Lubricant temperature = 40°C

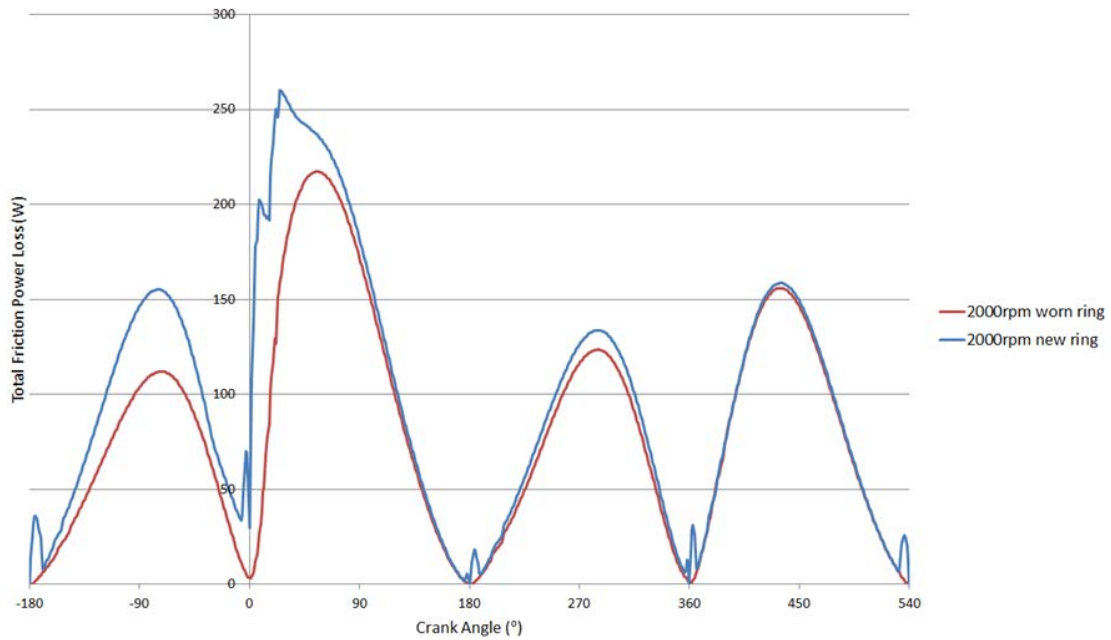


Figure 5.46: Frictional power loss results for the elastic analysis comparing new and worn ring profiles. Lubricant temperature = 40°C

The fact that a worn ring profile shows an improvement in the minimum film thickness is a reasonable result. Most new contact conjunctions with sharp geometrical features go through a running-in wear period, which serves to conform the moving mating parts. In the case of the piston ring-cylinder liner system, it is impossible to manufacture and fit a perfectly circular bore. There may also be imperfections in the connecting rod mechanism. The running-in period allows for these imperfections to be somewhat palliated. For example, at a particular axial position asperity friction may peak due to a loss of film. This would cause the compression ring to wear, therefore removing a small portion of its rough topography. This change of profile may improve the film formation as seen in figure 5.45. Alternatively, the process of frictional losses-to-worn profile continues until the lubrication is sufficient. An “equilibrium” is reached, in which the lubrication at most points around the ring is sufficient to avoid asperity interaction, due to the altered profiles caused by wear. However, when the lubricant temperature is increased the effect on film thickness due to ring profile is reduced. For the elastic ring analysis, the effect of a worn ring profile is not noted, with similar film thickness values obtained in all cases. This suggests that to a certain extent, the lubricant temperature has a greater impact on the film thickness than the axial profile of the ring, provided an inlet wedge shape is still maintained through the process of

gradual wear. This is highlighted in figure 5.47, where a more pronounced difference in film thickness can be seen for the rigid ring analysis, with a minimal change when considering an elastic ring.

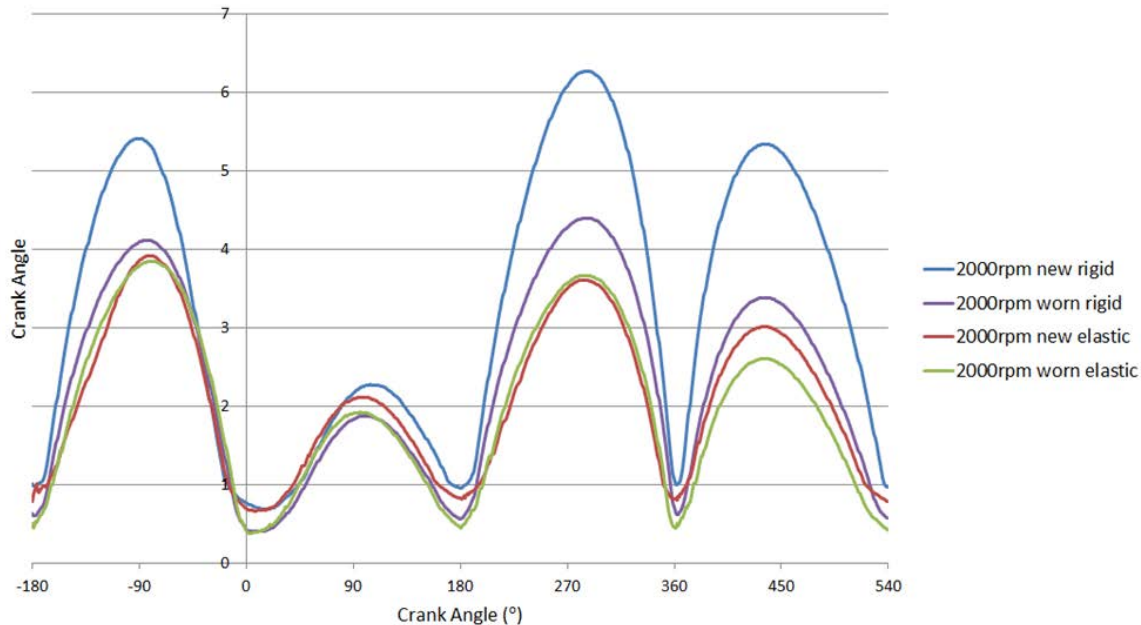


Figure 5.47: Comparisons between rigid and elastic results for a new and worn ring.

Lubricant temperature = 80°C, engine speed = 2000rpm

The results shown in figures 5.37-5.40 were then compared with those under the same conditions, but with a worn ring. It can be seen (figures 5.48-5.49) that the use of a worn ring profile gives a much smoother film thickness profile, and subsequently less friction is generated, provided that a sufficient film thickness is maintained to guard against asperity interactions. The adverse effect of increasing the lubricant film thickness is that the chance of blow-by between the ring and liner is increased. However in the cases presented, it appears that the film thickness is sufficiently thin so as to not dramatically increase this possibility. The first half of each piston stroke, up to the point of maximum sliding velocity, shows an area where wear remains a possibility due to a combination of thin film thickness and increasing entraining velocity. Once this wear has occurred, the rings axial profile changes such that the tribological performance is improved, at least initially. This is shown in figure 5.50, with the power loss from the worn ring analysis being significantly lower than that shown in figure 5.38 for the new ring profile.



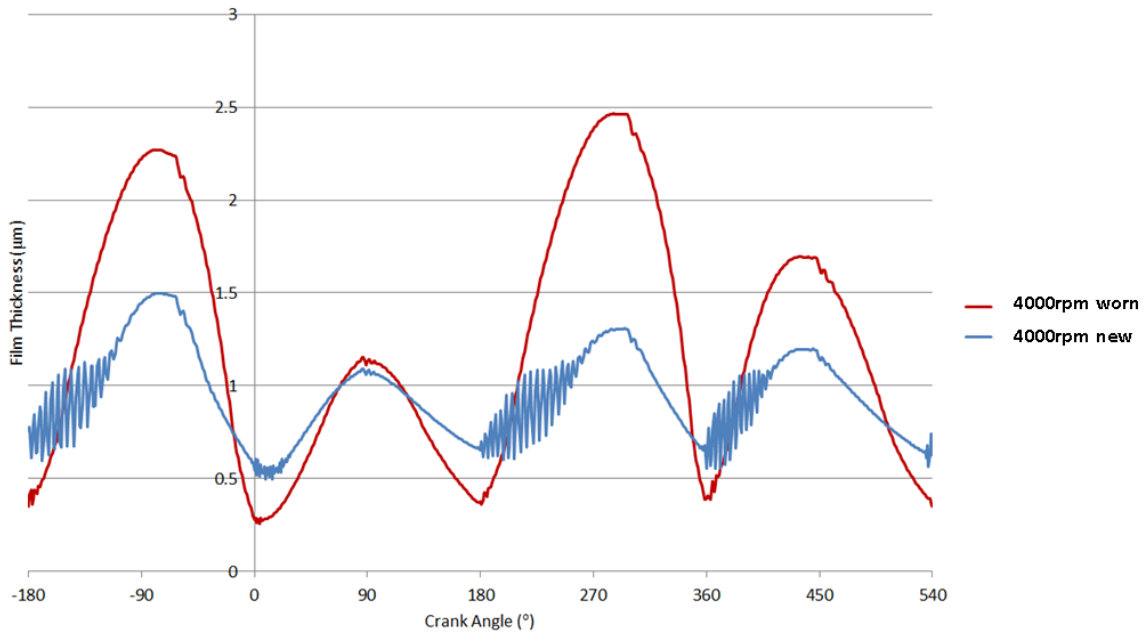


Figure 5.48: Comparison between new and worn ring results. Engine speed = 4000rpm, lubricant temperature 120°C

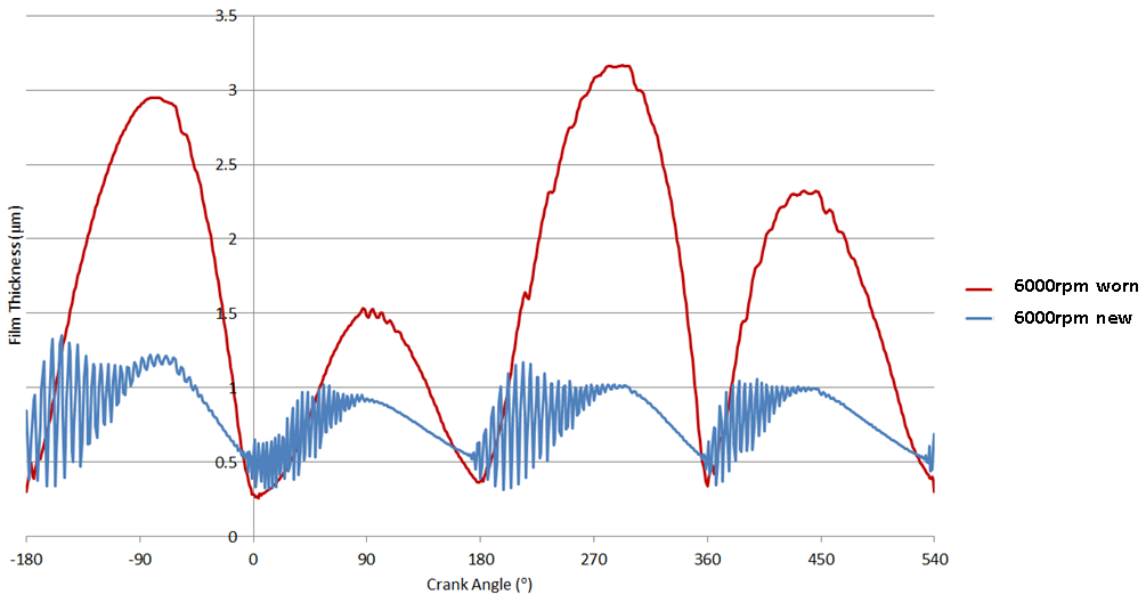


Figure 5.49: Comparison between new and worn ring results. Engine speed = 6000rpm, lubricant temperature 120°C

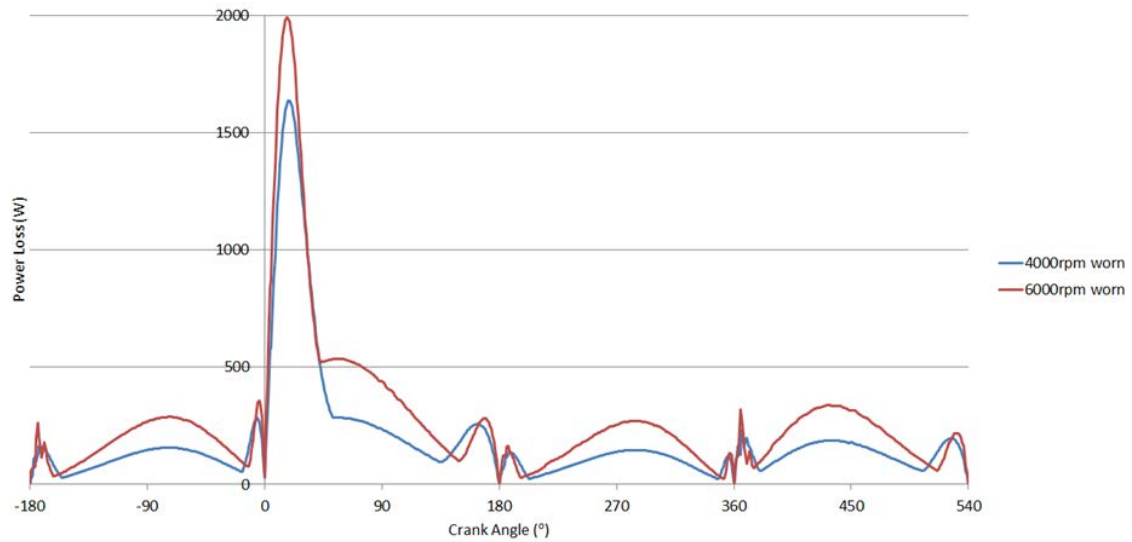


Figure 5.50: Comparison between worn ring power loss results at various engine speeds.

Lubricant temperature 120°C

As shown for the in-plane ring dynamic analysis, the power loss for various engine speeds and lubricant temperatures for rigid, in-plane and fully dynamic cases are shown in figure 5.51. The fully transient ring analysis predicts greater power loss throughout the engine cycle in most instances, when compared with the rigid ring analysis. This is to be expected, due to greater asperity interactions at reversal and a thinner film during the mid-stroke. The percentage total energy lost for all cases falls within the range of 0.06-1.5% reported by Richardson (2000), showing the results to be in line with test results and rational observations.

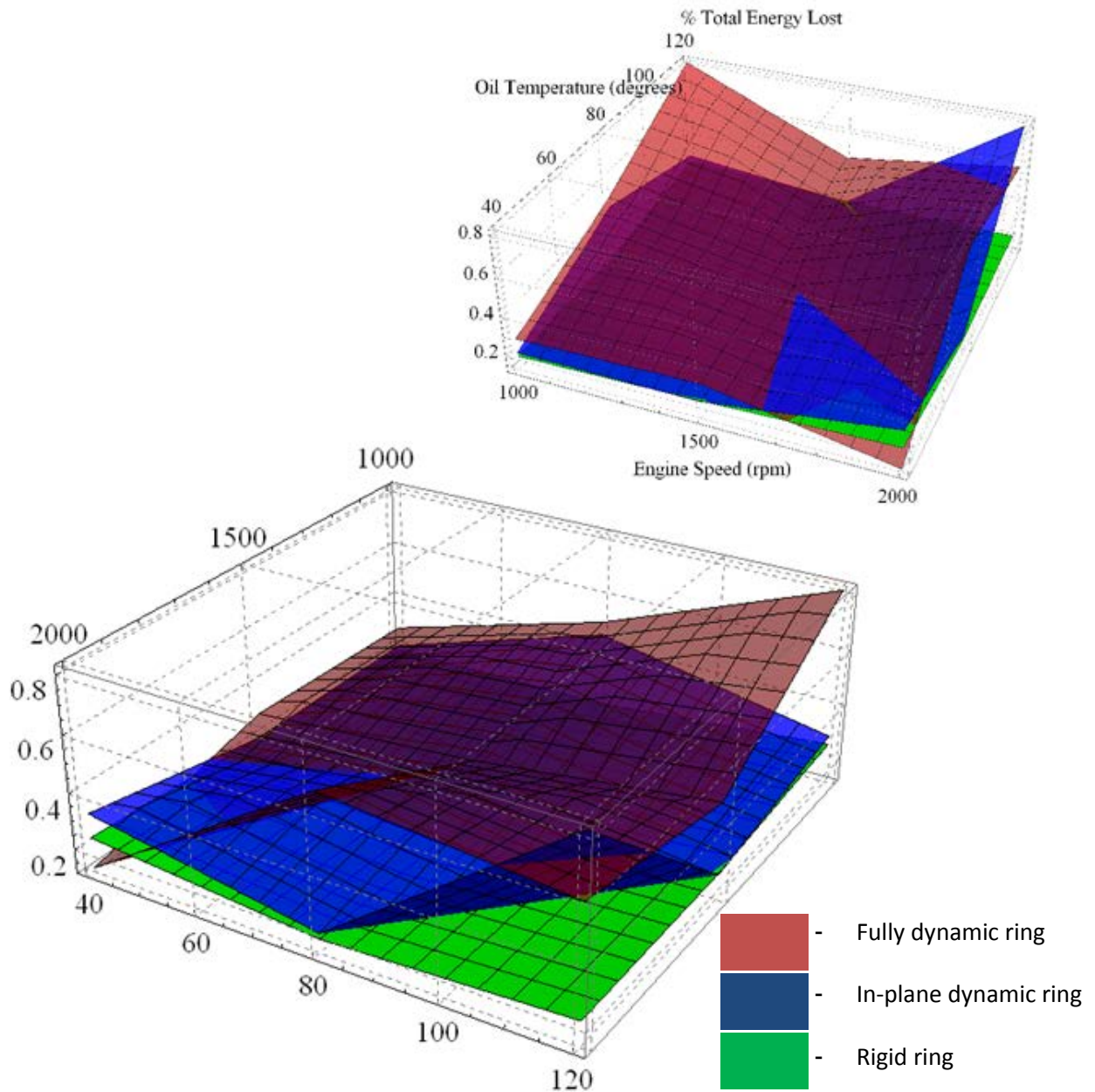


Figure 5.51: Power loss comparison between rigid, in-plane and fully dynamic elastic ring analysis, with respect to oil temperature and engine speed

The Stribeck curve shows the various lubrication regimes which can be encountered in a tribological analysis. Mixed and boundary lubrication give the greater risk of asperity interaction, which can cause wear of the solid surfaces. The compression ring goes through these regimes during the engine cycle. Considering the forces seen by the compression ring, elastohydrodynamic lubrication is unlikely apart from at TDC before the power stroke and the point of maximum pressure (combustion). However, the points indicating reversal in figure 52 show the compression ring appearing to pass through the EHL regime of

lubrication. A temporary stationary point during reversal would mean the coefficient of friction reduces, as there is no sliding motion to generate any friction. Also, the pressures seen may not be significant enough to alter the lubricant viscosity, apart from at the point of combustion. It should be noted that an EHL analysis is not included in the methodology presented.

The power stroke of the engine cycle is depicted by the spike at the left-hand side of figure 5.52, where the coefficient of friction dramatically increases. Hydrodynamic lubrication is dominant throughout the mid-stroke, as seen at the right-hand side of figure 5.52, whilst mixed lubrication regime is seen during reversal.

Figure 5.52 shows the Stribeck curve for both the rigid and elastic ring analysis. The engine speed is 1000rpm with 40°C lubricant temperature. Through the engine cycle, the elastic ring generally has a higher coefficient of friction than the rigid analysis at the corresponding crank angle.

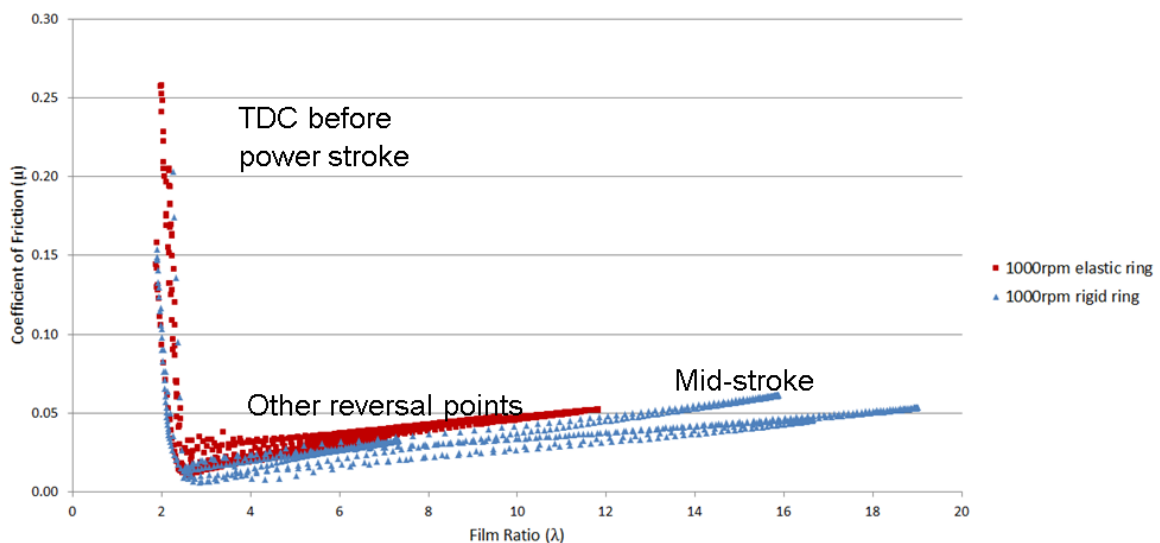


Figure 5.52: Stribeck curve comparisons between rigid and elastic ring analysis. Engine speed = 1000rpm, temperature = 40°C

Figures 5.53 and 5.54 show comparisons between the rigid and elastic ring analyses at 2000rpm for various lubricant temperatures. Again, the Stribeck plots of the elastic analysis have a higher coefficient of friction, usually due to a lower film ratio. A significant difference can be seen when higher temperatures are introduced, with the film ratio remaining at a lower value throughout the engine cycle. The peak coefficient of friction, however, at TDC

before combustion, remains almost the same. Typically, a film ratio between 1 and 3 indicates a mixed regime of lubrication. An increase in the film ratio moves the regime of lubrication in the elastohydrodynamic region, whilst anything above that demonstrates hydrodynamic lubrication. It can be observed from these results that even for lower temperatures and engine speeds that the compression ring moves through these lubrication regimes almost on a perpetual basis. This is seen for the rigid ring analysis as well. However, the friction coefficient predicted using an elastic ring is higher throughout most of the engine cycle.

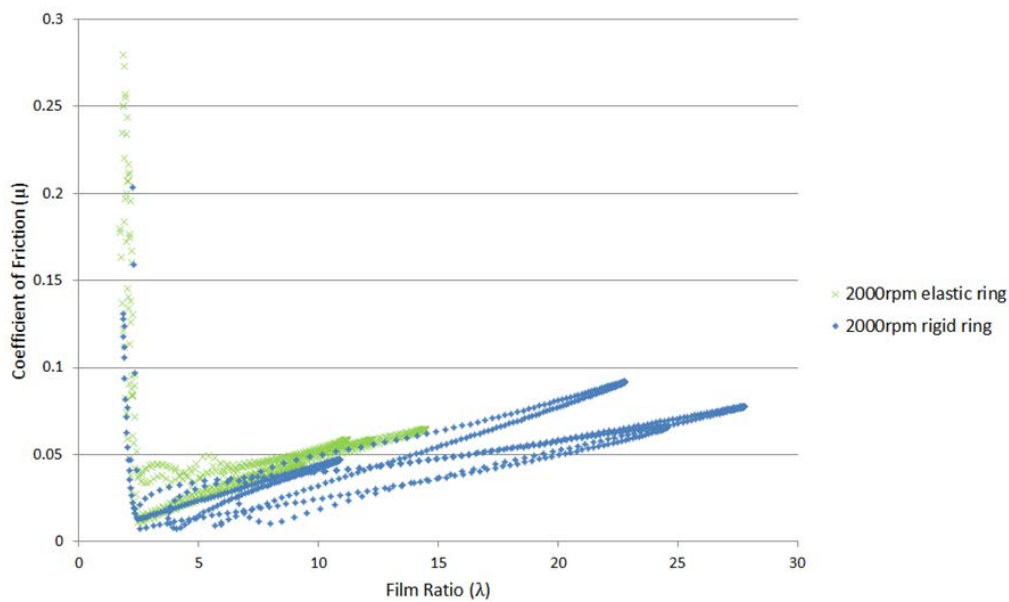


Figure 5.53: Stribeck curve comparisons between rigid and elastic ring analysis. Engine speed = 2000rpm, temperature = 40°C

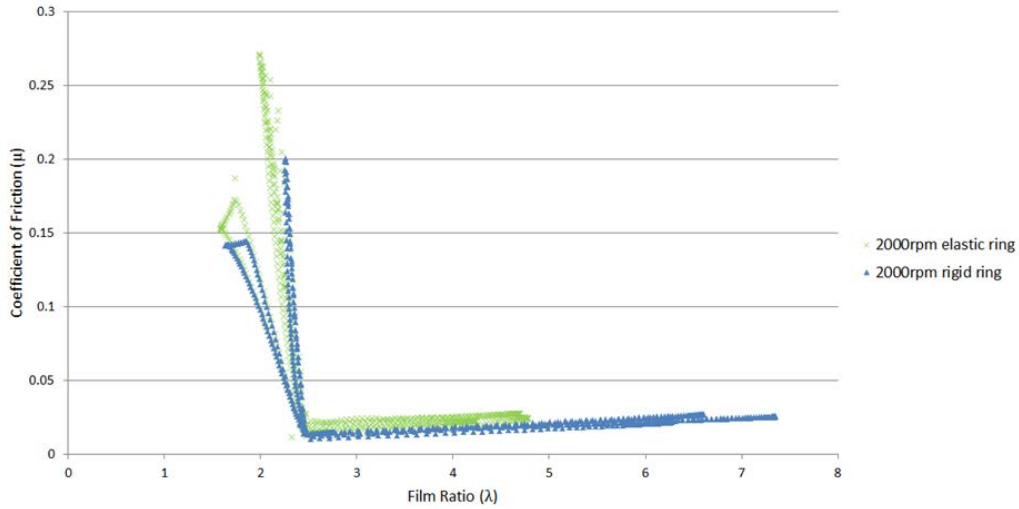


Figure 5.54: Stribeck curve comparisons between rigid and elastic ring analysis at higher temperatures. Engine speed = 2000rpm, temperature = 120°C

Figures 5.55 and 5.56 exhibit the individual friction coefficient contributions due to both asperity and lubricant viscous friction. The engine speed is 1000rpm with 40°C lubricant temperature. As expected, friction through the reversal point, approaching combustion, is dominated by asperity interactions, whereas at the mid-stroke it shows that hydrodynamic losses are prominent. The highest friction coefficients are found when asperity interactions take place, which are also the points where wear is likely to occur. Inclusion of the elastic ring dynamics in both planes of the ring geometry indicates that in most of the engine cycle, a mixed regime of lubrication occurs, with lower film ratios also predicted. Separation of the friction mechanisms in this manner may look different to the composite Stribeck curves. The calculations for the coefficient of friction are as follows:

$$\mu_{asp} = \frac{F_{asp}}{W_{asp}} \quad (5.1)$$

$$\mu_{hydro} = \frac{F_{hydro}}{W_{hydro}} \quad (5.2)$$

$$\mu_{total} = \frac{F_{asp} + F_{hydro}}{W_{asp} + W_{hydro}} \quad (5.3)$$

It can still be concluded from figure 5.54 that asperity interactions dominate the frictional losses at the TDC before combustion. Although the total friction coefficient results show a higher peak value for an elastic ring, comparing asperity interactions only shows a similar coefficient of around 0.3.

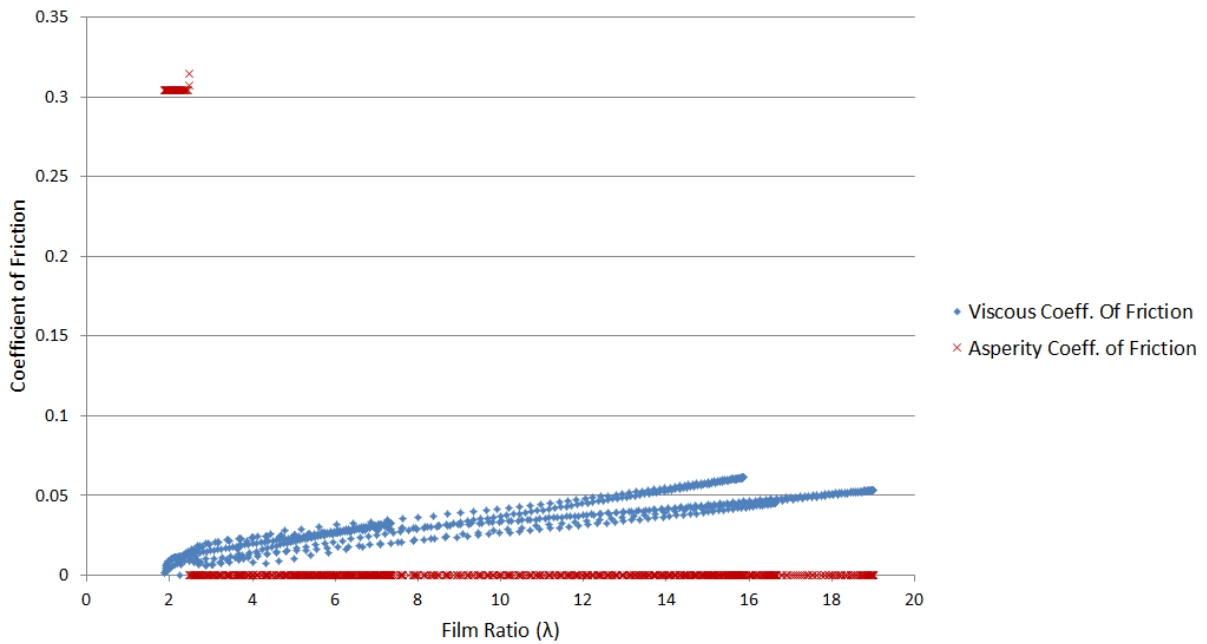


Figure 5.55: Friction coefficient contributions from viscous and asperity losses, for a rigid ring. Engine speed = 1000rpm, temperature = 40°C

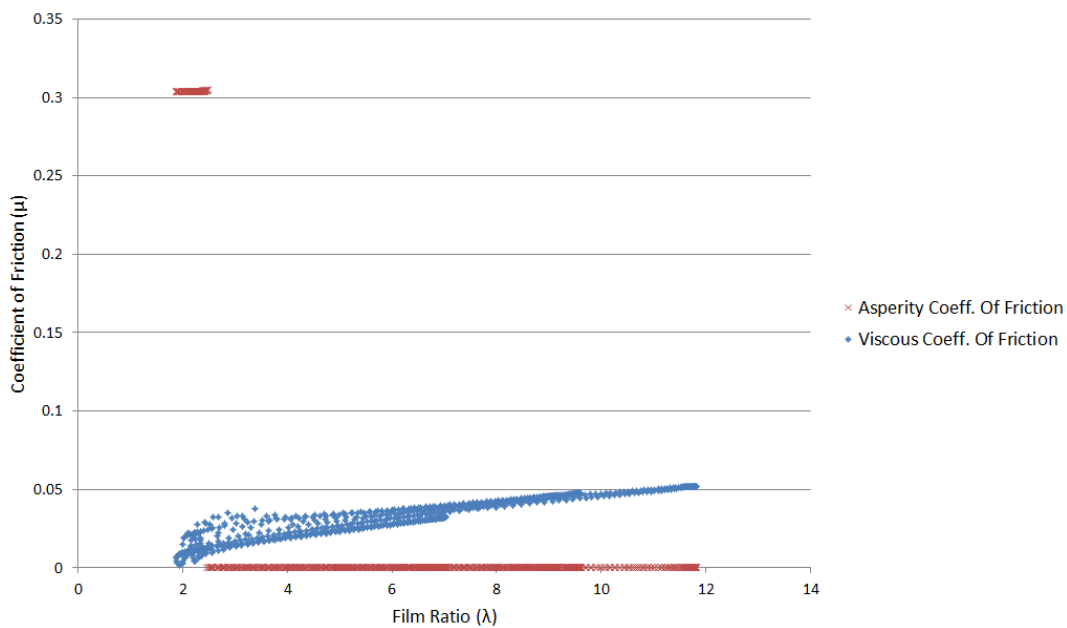


Figure 5.56: Friction coefficient contributions from viscous and asperity losses, for an elastic ring. Engine speed = 1000rpm, temperature = 40°C

Figure 5.57 shows both the viscous and asperity coefficients of friction at a higher engine speed and lubricant temperature in the case of rigid ring case. The higher film thickness predictions are evident in this result, since for a significant portion of the engine cycle, a hydrodynamic lubrication regime is predicted. The lower film thickness values of the elastic

ring analysis are evident in figure 5.58, with a much shorter range of film thickness ratios. A mixed regime of lubrication is predicted for much of the cycle, with asperity interactions occurring at every reversal point.

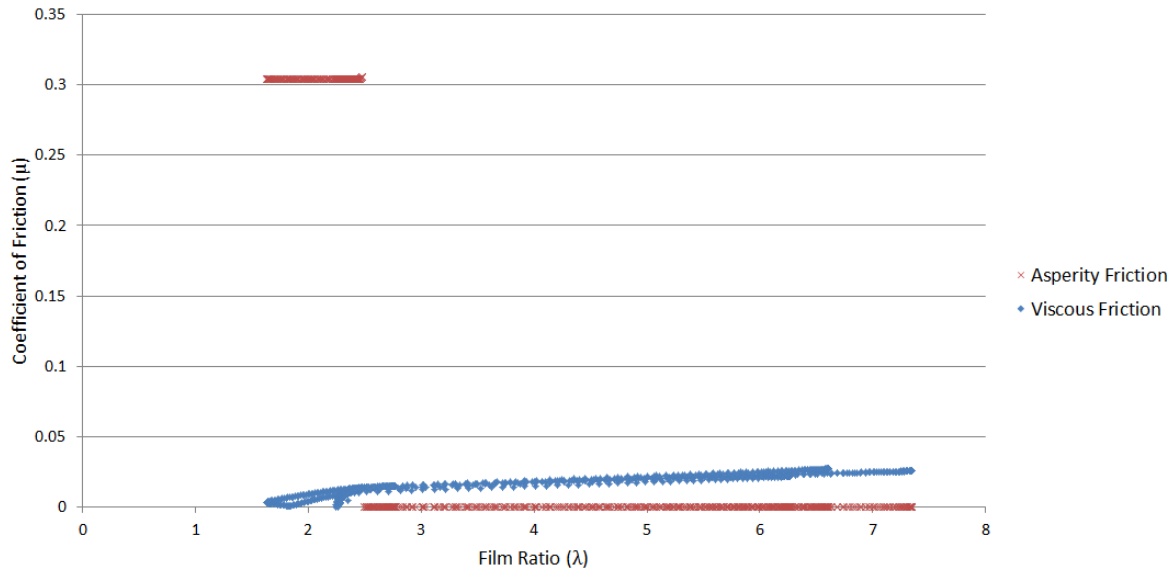


Figure 5.57: Friction coefficient contributions from viscous and asperity losses, for a rigid ring. Engine speed = 2000rpm, temperature = 120°C

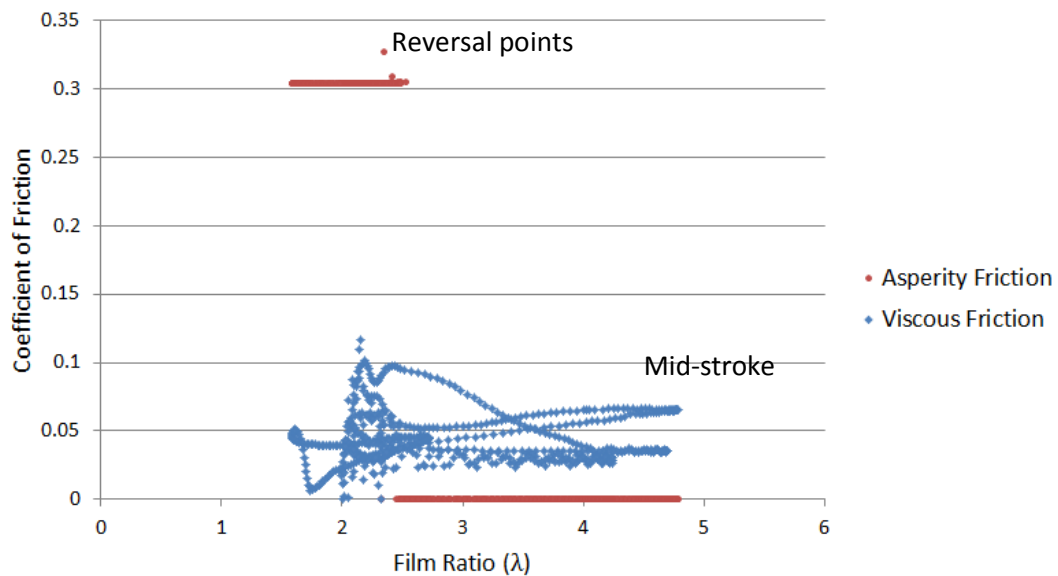


Figure 5.58: Friction coefficient contributions from viscous and asperity losses, for an elastic ring. Engine speed = 2000rpm, temperature = 120°C

The effect of a worn ring profile can be seen on the Stribeck curves in figure 5.59. The increase in film thickness throughout the cycle is sufficient to mitigate any asperity interaction. This is shown by the absence of a sharp increase in friction as the ring reaches



the TDC before combustion. The maximum film ratio seen is also larger due to the increased film thickness through the mid-stroke.

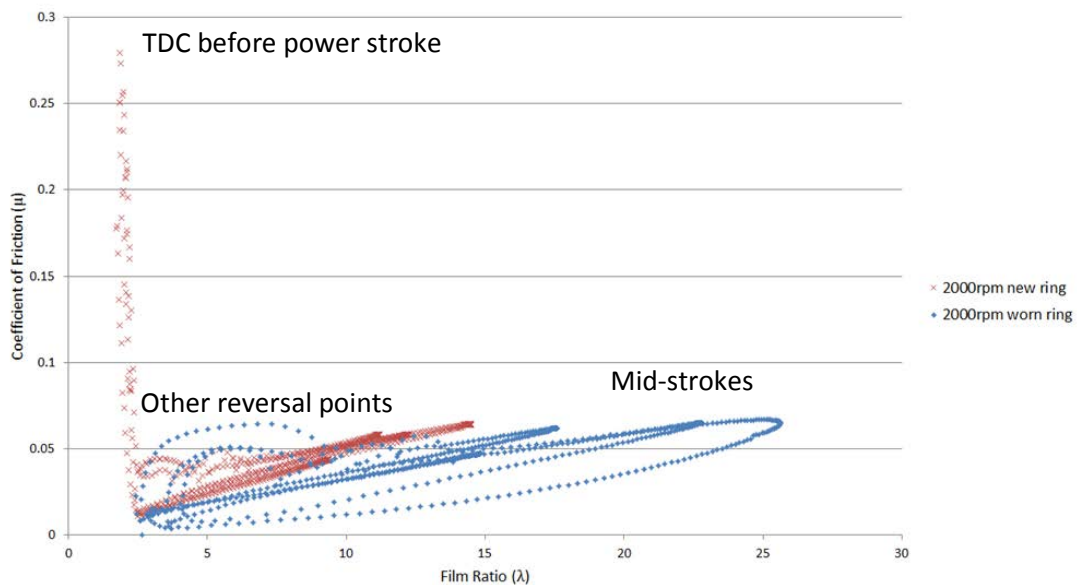


Figure 5.59: Stribeck curve comparisons between new and worn ring analyses, for a fully dynamic ring. Lubricant temperature = 40°C

## 5.6. Closure

This chapter presents results obtained through implementation of the proposed methodology for transient ring elastodynamics. It has been demonstrated that the implementation of this methodology is possible, giving an analysis which has not been hitherto reported in literature. In addition to this, the results presented in this chapter follow expected trends regarding film thickness, with high engine speeds and low lubricant temperatures resulting in higher film thickness predictions, and a mixed regime of lubrication at reversal points. These trends suggest that the results are within an acceptable range. The ring's axial profile is seen to have a significant effect on the film thickness between the ring and the liner, which affects the predicted friction. This is mainly because of alteration in the inlet wedge shape as well as surface topography. The results suggest that the running-in period undertaken during engine testing and manufacture is justified, as the worn profile showed a reduction in friction. The increased likelihood of blow-by and oil consumption with a worn ring was also seen due to the increase in film thickness when applying a worn ring profile to the analysis. The effect on the Stribeck curves for rigid and elastic cases, as well as the contribution of both asperity and viscous friction are also shown.

The next chapter attempts to verify this methodology using data and results from both literature and experimental test rigs.

## 6. Verification of the Numerical Methodology

### 6.1. Introduction

In this chapter, the developed methodology including ring dynamics is validated against direct experimental measurements of lubricant film thickness and in situ in-cylinder friction. Predominantly, this verification process uses experimental data, available in open literature. It also includes some results obtained test rigs fitted with sensors for both friction and film thickness measurements. Furthermore, the developed models using the finite element method allow comparisons with different methods to those presented in this thesis. Agreement of predictions, using completely different methodologies such as numerical and finite element solutions also serves as a form of validation of certain methods.

### 6.2. Results available in the Literature

The validity of the numerical results presented in previous chapters was sought by comparing them with experimentally obtained data. Takiguchi et al (2000) have provided film thickness predictions and measurements, as well as the required input data to replicate the same system with numerical predictions. Compression ring film thicknesses and axial ring motion were measured using a capacitance method. Electrodes were imbedded into the rings to obtain the film thickness between the ring and the liner. They were also embedded into the top groove face to capture ring motion. Takiguchi et al (2000) have also presented numerical predictions compared with their experimental data using an electrode fitted to the thrust side of the compression ring. The cylinder temperature was measured for a variety of speeds and loads, varying around 120°C. Sakhrieh et al (2010) and Nikian et al (2006) performed studies on compression ignition engines of similar size, reporting cylinder temperatures of 400K and 370K, respectively. Figure 1 shows the resulting temperature prediction from Nikian et al (2006) for the cylinder wall. Therefore, a wall temperature of 120°C (393K) was assumed for the numerical analysis here for comparisons with Takiguchi's work. In addition, Howell-Smith (2011) stated that wet aluminium liners in four-stroke high performance engines produce an internal liner temperature of approximately 25°C above that of the coolant temperature. So if the coolant temperature is controllable in a particular experimental setup, the liner temperature can be assumed to within a reasonable degree of reliability. The cylinder used by Howell-Smith (2011) was a

modified Honda 450 CRF single cylinder motocross motorbike gasoline 4-stroke engine. It was modified to a wet liner arrangement from its usual mono-block form. The wet liner arrangement essentially comprises a cylinder block with easily replaceable liner inserts. This arrangement introduces a water jacket surrounding the liner insert which for experimental purposes can ensure a liner temperature of around 120°C where the compression ring passes (inferring a coolant temperature of 95°C). This suggests that 120°C is a reasonable assumption for the liner temperature, and may be even lower if the coolant is controlled to a lower temperature. Clearly, the liner temperature will not be equal to the average temperature of the piston head. Howell-Smith (2011) used heat transfer coefficients from Abbas et al (2004) to create a thermal distribution throughout the piston for the CRF engine. It was predicted to have significantly higher temperatures, rising up to 225°C above the top ring groove. Again, this is an averaged temperature throughout the engine cycle. The temperature which is important with regard to the current analysis is that of the lubricant temperature between the ring and the liner. The compression ring's temperature influences the temperature of the lubricant. However, the liner's larger mass with respect to the ring suggests that the liner temperature is dominant when assuming the oil temperature. Morris et al (2012) reported a control volume thermal mixing model and showed that the critical temperature for the entrant lubricant flow into the contact conjunction is that of the liner surface.

Nikian, M., M. Naghashzadegan, and S. K. Arya. "Modeling of heat losses within combustion chamber of Diesel engines." *IUST International Journal of Engineering Science* 17.3-4 (2006): 47-52. (figure 10)

Figure 6.1: Predicted time-averaged temperature distributions on the cylinder liner wall  
(Nikian et al, 2006)

Figures 6.2 and 6.3 show a comparison between the experimental results of Takiguchi et al versus the tribodynamic analysis presented here (for both rigid and elastic rings). It can be seen that the inclusion of in-plane transient ring dynamics gives a better agreement with experimental measurements throughout the engine cycle, when compared with the rigid ring methodology. Even in the power stroke, where the greatest differences between experimental and numerical results appear, the elastic ring methodology proposed in this

thesis provides better agreement. It should also be noted that whilst the film thickness values found through numerical analysis correspond to the least conjunctural separations (thrust or anti-thrust sides), the experimental measurements are confined to those at the cylinder thrust side. Therefore, with the experimental data the minimum film thickness during the power stroke is unlikely to be those reported by Takiguchi et al as the piston is forced to the anti-thrust side during its downward sense. This would cause the lubricant film at the thrust side to become larger. Since in the present study, piston dynamics are not coupled to the compression ring model, this effect cannot be captured.

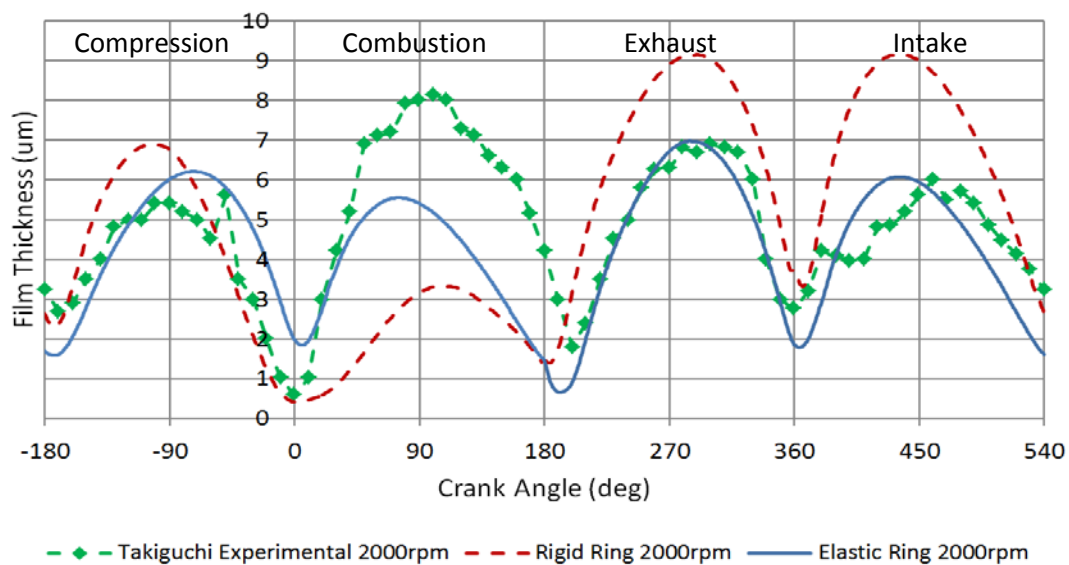


Figure 6.2: Experimental data in comparison with the presented methodology (2000rpm).

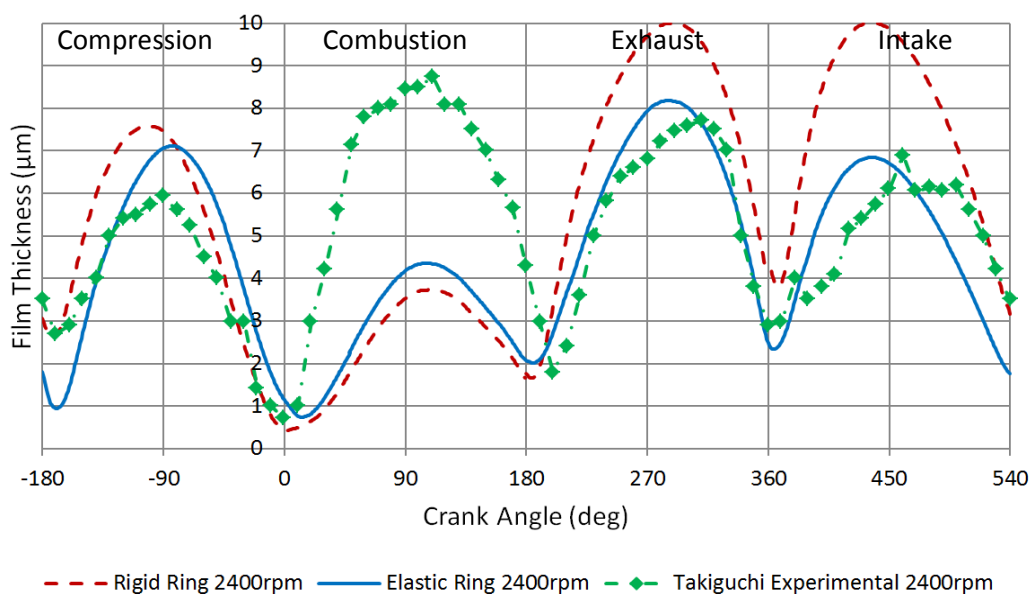


Figure 6.3: Experimental data in comparison with the presented methodology (2400rpm).

Figure 6.4 shows a comparison between the data presented by Takiguchi (2000) and the numerical predictions carried out here, including the out-of-plane ring dynamics. It can be seen that the film thickness prediction is improved through the compression stroke when compared with the case with in-plane dynamics alone. However, a significant difference in film thickness is seen throughout the power stroke, with the inclusion of only in-plane dynamics giving the closest prediction. As previously stated, the measurements by Takiguchi were taken at the thrust side of the liner, whilst during the power stroke the piston would be forced to the anti-thrust side. This tilt and displacement (lateral piston motions) would most likely affect the measurements, especially considering that most literature agree that lower minimum film thickness values are expected during combustion.

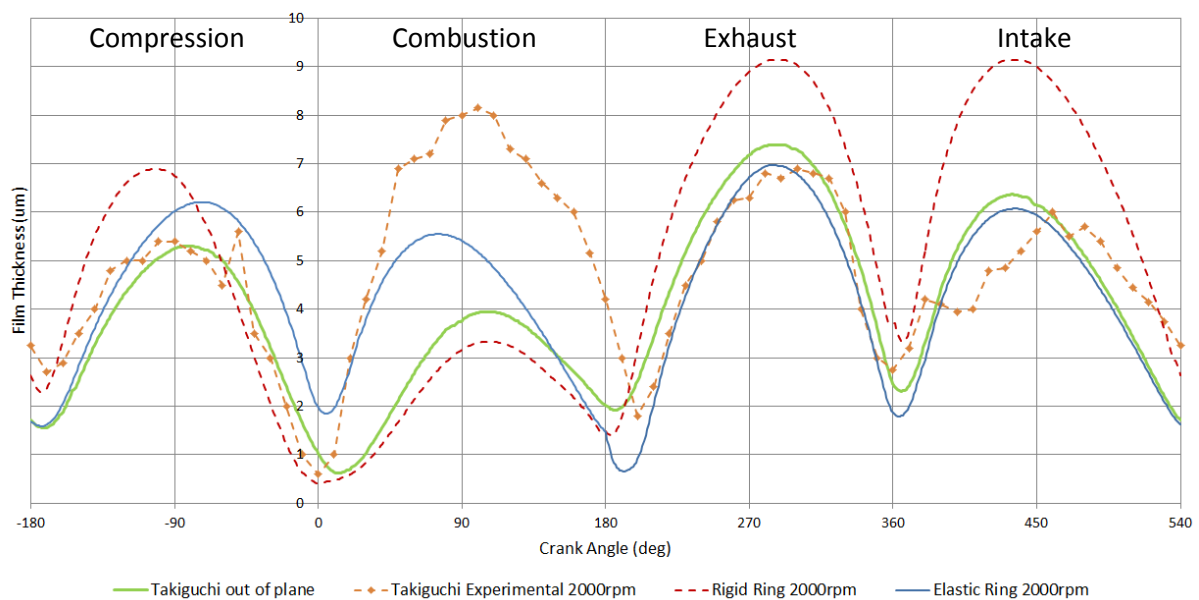


Figure 6.4: Comparison between experimental data (Takiguchi (2000)) and rigid ring, in-plane and full dynamic analysis. Engine speed = 2000rpm, lubricant temperature = 120°C

The groove displacement profiles shown in the numerical results from the previous chapter, such as those in figure 6.5, are comparable to similar results presented in open literature, both from experimental measurements and FEA predictions. Figure 6.6 shows the ring's position within the groove at four positions, 90° apart, as modelled by Kurbet and Kumar (2004) using the finite element method. They investigated piston tilt, which is why such a large difference can be seen between the various sections of the ring. Since the results in this thesis do not account for piston tilt, nor thrust or anti-thrust sides, there is not as much difference circumferentially as would be seen if tilt was included. The general trend gives

excellent agreement between the two methods, with the translation between lower and upper groove surfaces occurring when the piston starts to slow down as it approaches dead centre reversal. This result gives confidence in the groove displacement trends predicted by the current numerical analysis, which shows that the piston motion dominates the ring's dynamic response.

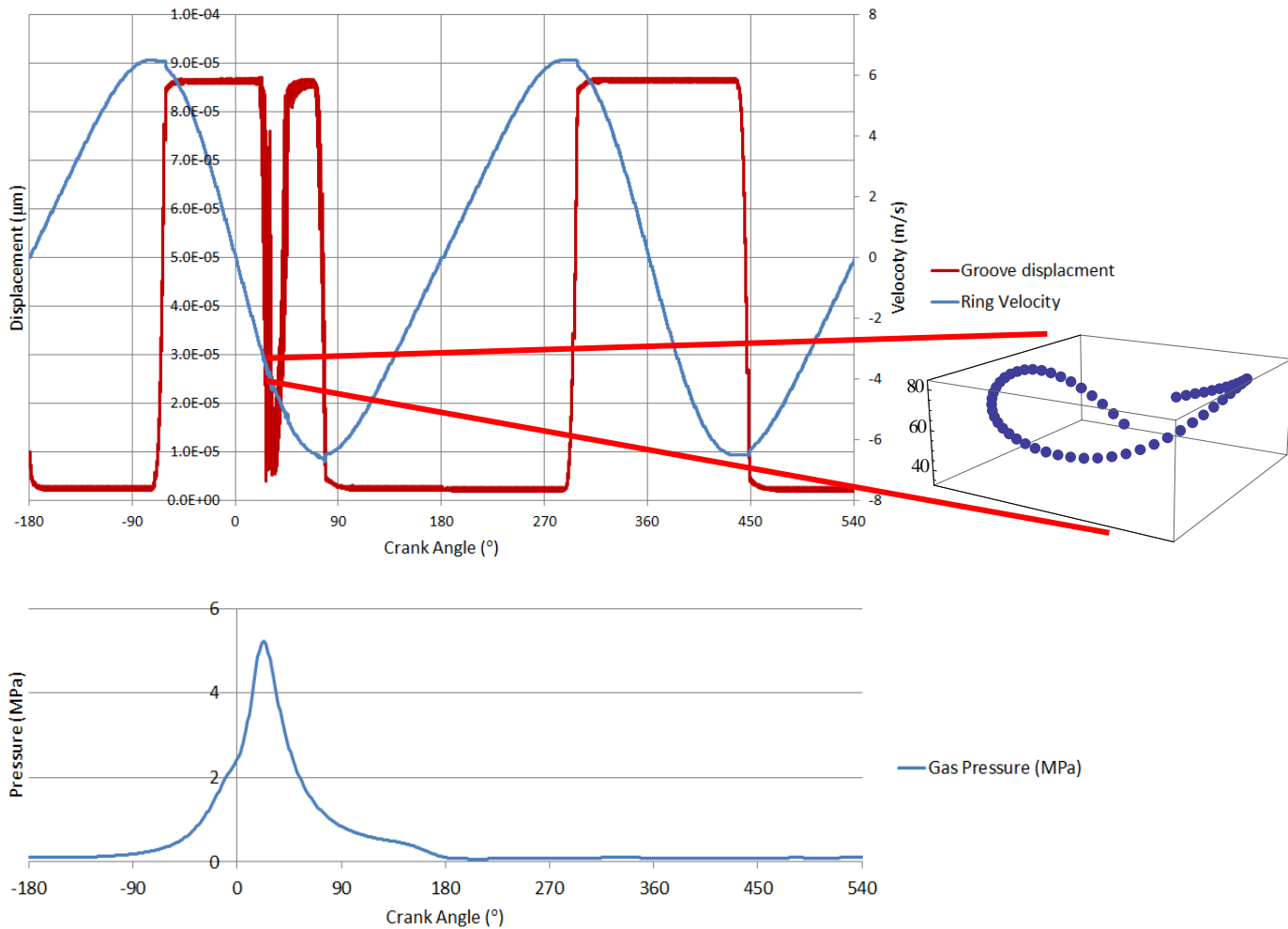


Figure 6.5: Ring displacement throughout the engine cycle, alongside ring axial velocity and cylinder gas pressure. Engine speed = 1500rpm, lubricant temperature = 120°C

Kurbet, S. N., and R. K. Kumar. "A finite element study of piston tilt effects on piston ring dynamics in internal combustion engines." *Proceedings of the Institution of Mechanical Engineers, Part K: Journal of Multi-body Dynamics* 218.2 (2004): 107-117. (figures 3, 6a)

Figure 6.6: Compression ring lift through TDC from an FEA model (Kurbet and Kumar, 2004).

The trend shown is the same as predicted by the numerical model

Figure 6.7a shows the experimental setup used to measure piston ring motion, whilst figure 6.7b shows the results of these measurements in Takiguchi (2000). The motion of the second compression ring is shown, during a cycle with no load. Although these results are from the second ring, the same trend is shown when comparing with the results of the present work. As with the ring-to-liner film thickness measurements, there is a difference between the thrust and anti-thrust sides which cannot be seen in the presented methodology. An additional similarity is seen when examining Takiguchi's result for an engine speed of 2400rpm. At the point of combustion, the ring is forced away from the top groove surface, which would cause loss of sealing. This effect can be seen in figure 6.5.

Although the engine speeds are different, it should be no surprise that engine-to-engine variation will take place, dependent on the dimensions of the ring and piston assembly, as well as gas pressure profiles. An increase in engine speed also shows more stable results, as can be seen when comparing figures 5.30 and 5.31 in the previous chapter. The results in figures 6.6 and 6.7 are important in terms of verifying the presented numerical results. Although they are from the analysis of a different engine, and in the case of Takiguchi (2000) show the second compression ring, the movement of the ring within the groove has not previously been presented for a fully transient case. Additionally, having results from experimental data and an additional FEA model, both in agreement with the numerical analysis, provides additional credence to the developed analysis.

Takiguchi, M., Sasaki, R., Takahashi, I., Ishibashi, F., Furuhashi, S., Kai, R., and Sato, M., "Oil film thickness measurement and analysis of a three ring pack in an operating diesel engine." *SAE paper* (2000): 01-1787. (figure 5)

(a)

Takiguchi, M., Sasaki, R., Takahashi, I., Ishibashi, F., Furuhashi, S., Kai, R., and Sato, M., "Oil film thickness measurement and analysis of a three ring pack in an operating diesel engine." *SAE paper* (2000): 01-1787. (figure 14)

(b)

Figure 6.7: (a) – Experimental schematic diagram and (b) results of the measured groove position of the second compression ring (Takiguchi, 2000).



Verification of the methodology presented in this chapter comes in a variety of forms. Currently available literature enables a comparison between experimental data and the presented methodology, although assumptions may have to be made due to limited information supplied by the other contributors. Similarly, any publications which discuss results from a finite element model of the compression ring within the groove could be useful for comparative purposes, providing that suitable verification of the same had taken place. Internally generated experimental data (as a part of the EPSRC Encyclopaedic Program Grant) allow for a more direct comparison, due to the greater knowledge of the system parameters for the data obtained. A number of test rigs were used to measure film thickness and frictional data using different methods.

### **6.3. Experimental Validation**

In order for reasonable comparisons to be made between numerical and experimental data, a modified CRF 450 single cylinder engine was used. The modified wet liner arrangement instead of the usual mono-block cylinder allows the use of replaceable liner inserts (Gore, et al, 2012). Therefore, a floating liner is used, as described by Gore et al (2012) to directly measure in situ in-cylinder friction. Furthermore, a liner was used by Littlefair et al (2014) which was instrumented with thermocouples for temperature measurement and ultrasonic film thickness measurement sensors (Dwyer-Joyce et al, 2007) to obtain film thickness profiles. The test rig allows control of the engine speed and coolant temperature, meaning a parametric analysis of the system can be carried out. The engine used was a Honda CRF bike engine which could be both motored and fired. This engine was used due to the extreme running conditions which were possible. The high engine speeds, along with high torque and power values, mean that the tribological conditions capable of replicating in this engine will encapsulate those seen in most road vehicle engines. Details of this engine are shown in table 6.1.

Table 6.1: Honda CRF450 engine properties

Property	Value	Unit
Engine Type	4 stroke/4 valve single cylinder	-
Bore/Stroke	96/62.1	mm
Compression Ratio	11.5:1	-
Max rated power/torque	41kW@9000rpm/49.8@7000rpm	
Piston top land diameter	95.4	mm
Top ring groove depth	3.38	mm
Top ring groove height	0.98	mm

Table 6.2: Ring and lubricant properties used in numerical analysis

Property	Value	Unit
Ring Nominal Radius	44.025	mm
Ring Axial Height	0.894	mm
Ring Radial Width	3.075	mm
End Gap	10.92	mm
Ring Elastic Modulus	203	GPa
Poisson Ratio	0.3	-
Coating Elasticity Modulus	400	GPa
Coating Poisson Ratio	0.2	-
Ring Ra value	0.369	Mm
Pressure-viscosity coefficient	$1 \times 10^{-8}$	$\text{m}^2/\text{N}$
Thermal expansion coefficient	$6.5 \times 10^{-4}$	$1/^\circ\text{K}$
Lubricant density	873.0 at 15 [°C]	$\text{kg}/\text{m}^3$
Lubricant kinematic viscosity, $\nu$	95.3 at 40 [°C]	$\times 10^{-6} \text{m}^2/\text{s}$

Running the engine under motorised condition (without combustion) allows for more control over the system, without a plethora of other interactions as the result of cylinder firing. No combustion means the temperatures reached within the cylinder are lower than those with a fired engine, allowing the limit of the sensors and wires to be found gradually. The pressure within the cylinder can be measured for a typical cycle at each engine speed, as can the coolant and oil temperatures. Knowledge of the system's dimensions and lubricant properties coupled with these allows for a reasonable model of the system to be

created. Table 6.2 shows the ring and lubricant properties used in the experimental verification.

#### **6.4. Film Thickness Measurement**

Film thickness measurements of the compression ring were made using ultrasonic sensors. The sensors were placed on the exposed side of the liner, as shown in figure 6.8. The sensors used were ultrasonic pulser-receivers (UPR), as described by Avan et al (2010). These sensors were mounted on the outside of the cylinder liner, with the ultrasonic wave applied through the wall towards the piston. As the sensors can act as both a transmitter and a receiver, the 'echo' of the transmitted signal is captured when the ring passes the sensor's axial position. This echo is captured and amplified, with post-processing allowing for the calculation of the distance between the cylinder and the ring surface, which is the film thickness within the contact.

Avan, Emin Yusuf, Robin Mills, and Rob Dwyer-Joyce. "Ultrasonic Imaging of the Piston Ring Oil Film During Operation in a Motored Engine-Towards Oil Film Thickness Measurement." *SAE International Journal of Fuels and Lubricants* 3.2 (2010): 786-793. (fig. 4)

Figure 6.8: The ultrasonic transducer attached to the wet side of the liner (Avan et al, 2010)

These sensors' width was approximately 10% larger than the ring's axial face-width for the initial experimental results, meaning an average film thickness was obtained at each point due to inadequate resolution. This is shown in figure 6.8. To convert this to a minimum film, a de-convolution process is required, where the measured film thickness is related to an offset of the undeformed ring profile. This allows the 'true' film thickness to be found, as opposed to the initially measured film thickness, as shown in figure 6.9.

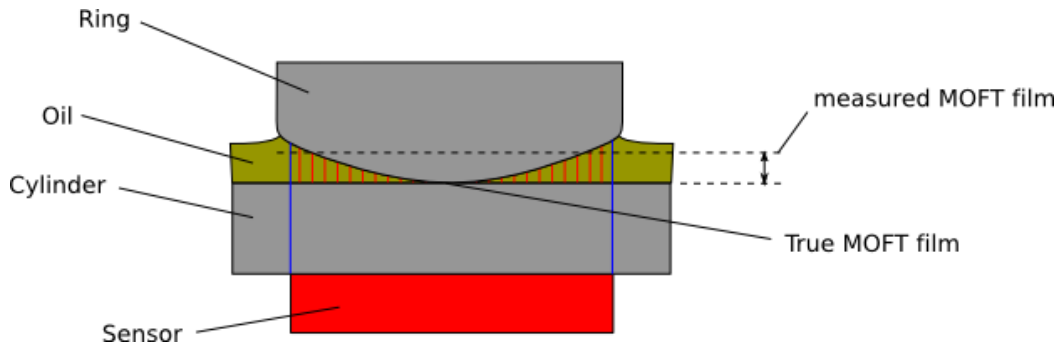


Figure 6.9: Oil film measurement between the ring and the liner. The sensor's size means an 'average' film thickness is measured, resulting in a de-convolution process being required to find the minimum value. MOFT = Minimum Oil Film Thickness

Figure 6.10 shows experimental data from the engine test rig, when compared with both rigid and elastic ring numerical analyses. The engine was run at 3200rpm with a load of 36Nm, and an oil sump temperature of 73°C was measured. Inclusion of elastic ring dynamics shows an improvement in the film thickness prediction for the majority of the data points. Although only a small difference in film thickness is found, this may have a significant effect on the predicted friction, culminating in a significant difference in power loss prediction over many cycles. Negative experimental film thicknesses are found due to the de-convolution processing of the raw data. Whilst a negative film thickness is clearly not possible, this result may indicate very low film thickness values. The temperature used in the numerical analysis was measured when obtaining the numerical results, as was the gas pressure profile used. The low film thickness values observed experimentally at reversal suggest that asperity interaction is likely to occur.

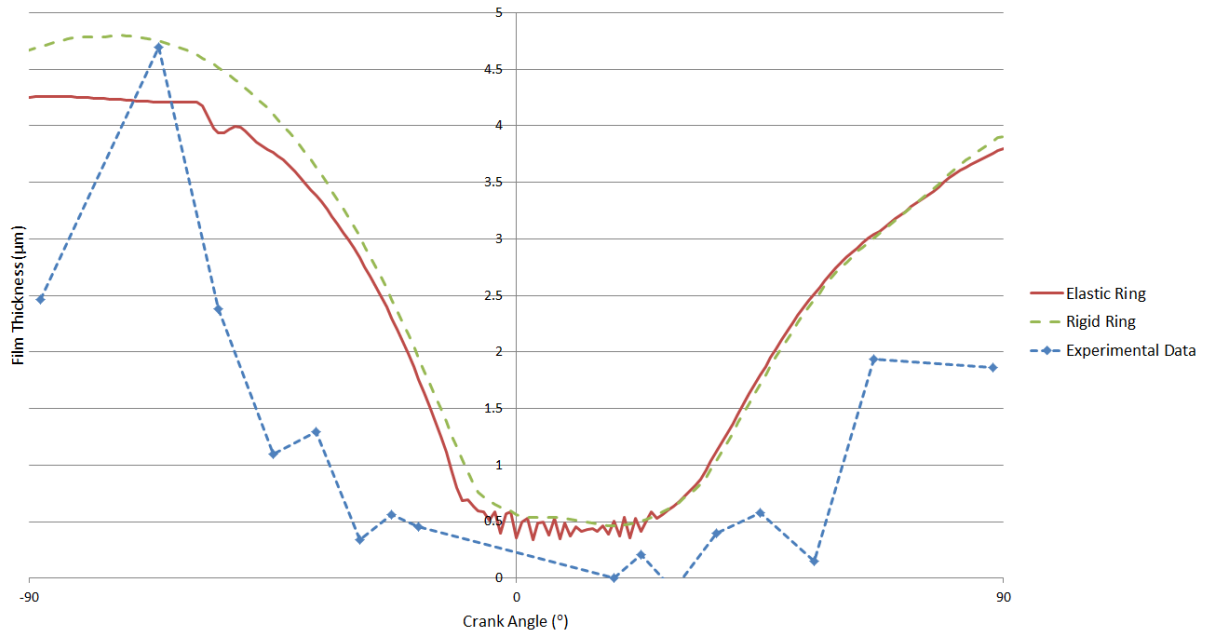


Figure 6.10: Rigid and elastic ring numerical analysis compared to measured data. Engine speed = 3200rpm, Load = 36Nm, lubricant temperature = 73°C

The measured sump oil temperature would not be the same as the temperature within the compression ring-liner contact. Figure 6.11 shows the same load case, but with a more realistic lubricant temperature of 100°C. Whilst the film thickness predictions at reversal do not show much change, the values through the piston stroke are reduced due to lower lubricant viscosity. Once again, the elastodynamic ring analysis gives a lower minimum film at TDC, providing a closer conformance to the experimental values.

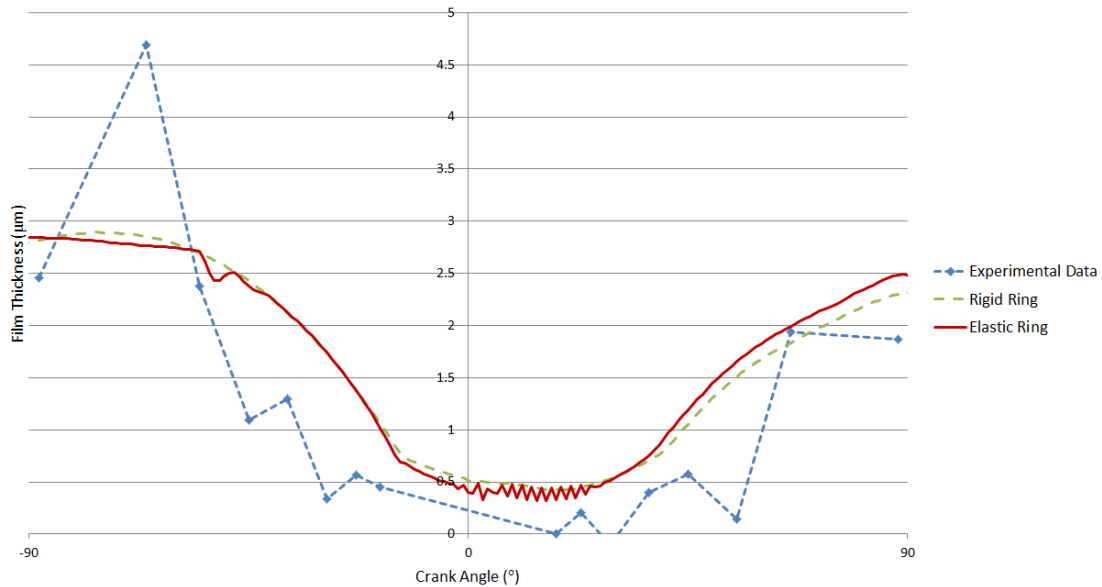


Figure 6.11: Rigid and elastic ring numerical analysis compared to measured data. Engine speed = 3200rpm, Load = 36Nm, lubricant temperature = 100°C

The lubricant film thickness was measured for a different load condition at the same engine speed. Figure 6.12 shows the film thickness comparisons with a load of 25Nm. Again, an improvement in film thickness prediction is seen for the elastic ring analysis. When considering figures 6.10-6.12, it is important to note that there will be a degree of error in both the experimental and numerical data, either due to equipment and measurement limitations, or assumptions made when constructing the numerical model, such as a fully flooded inlet. Clearly in figure 6.10, the difference between both numerical predictions and the experimental data is significant. However, these numerical assumptions are recognised as potential future investigations, and accuracy is part of every experimental measurement in all subject areas. Assumptions such as fully flooded conditions are made, when in reality there would be a degree of starvation, particularly during reversal at the TDC. The inclusion of a starvation model would invariably reduce the film thickness predictions, moving them closer to the measured data. The experimental results in figures 6.10-6.12 all suggest that contact between the two surfaces may occur. This is to be expected due to wear patterns which can be seen from used piston rings and liners. It also reinforces the point that TDC is a critical area when attempting to improve the efficiency of the system and that it is reasonable to include asperity reaction and friction forces in the numerical analysis.

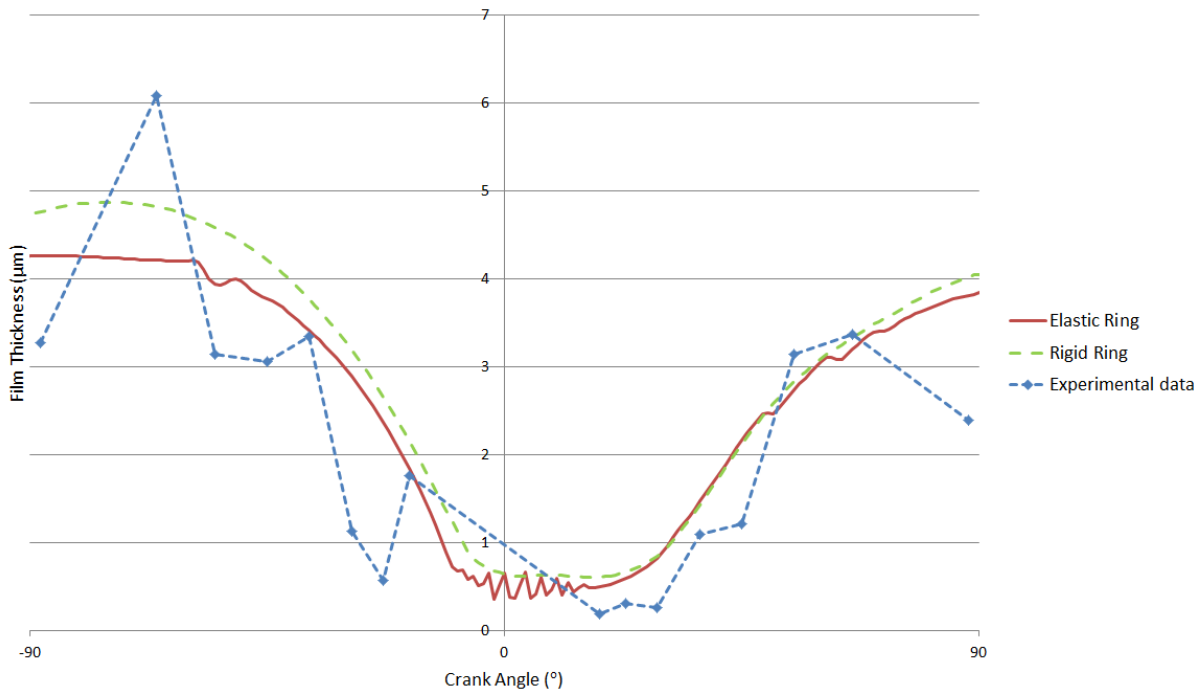


Figure 6.12: Rigid and elastic ring numerical analysis compared to measured data. Engine speed = 3200rpm, Load = 25Nm, lubricant temperature = 73°C

Further film thickness measurements were undertaken, using new sensors in different positions both axially and circumferentially. However, these were made using larger sensors than the previous tests, meaning that the measurement resolution was reduced when compared with figures 6.10-6.12. Previous results were obtained using sensors which were 10% wider than the ring itself, meaning deconvolution of the results would be reasonably accurate. Figure 6.13 demonstrates the difference in sensor size between the two sets of results. The sensor was approximately twice the width of the ring itself, which means the deconvolution method used to attain the 'real' film thickness from the observed data becomes less reliable. This change to sensor width was made to improve the resolution for measurement of the piston skirt film thickness, for the benefit of studies that are out of the scope of this thesis. However, trends in the circumferential film profile, as well as with respect to crank angle, may be observed.



Figure 6.13: Representation of the sensor size for both sets of film thickness results. A sensor width approximately 10% larger than the ring's width (a) allows for reasonable deconvolution results, whereas double the ring's width (b) reduces the reliability of these results.

### 6.5. Friction Measurement

As well as film thickness values, friction was measured in the Honda CRF engine. A floating liner with a wet barrel arrangement was used, allowing the friction due to motion of the liner to be captured from the bore. As described by Gore et al (2012), the floating liner principle suspends the cylinder liner so that any points of contact are with load cells. Throughout the engine cycle, any forces applied to the liner will be captured by the load cells, allowing friction to be measured (O'Rourke et al, 2010). The inertial force, being equal to the total friction less pressure loading on the top rim of the floating liner, was captured by load cells. It is important for any side loading that may occur to be removed from the results. Also, any gas pressure acting on the cylinder liner top surface should be accounted for when processing the results, so the remaining results are due to friction only (Gore et al, 2012).

The friction was measured using quartz piezo-electric miniature force transducers. The load cells were positioned  $120^\circ$  apart as shown in figure 6.14, with 3 pairs of two sensors positioned as shown. This was undertaken to negate stiffness variation between the cylinder and the block (Howell-Smith, 2011).



Gore, M., Howell-Smith, S. J., King, P. D. and Rahnejat, H., “Measurement of In-cylinder Friction using the Floating Liner Principle”, *Proceedings of the ASME ICED Spring Technical Conference, ICES2012-81028* (2012) (figure 1)

Figure 6.14: Sensor position for friction measurements. The transducers were arranged in pairs (two above, two below) 120° apart

The force applied to the liner is calculated using equation (6.1) (Gore et al, 2012):

$$\Delta F = \frac{(\Delta F_{T1} + \Delta F_{B1})}{2} + \frac{(\Delta F_{T2} + \Delta F_{B2})}{2} + \frac{(\Delta F_{T3} + \Delta F_{B3})}{2} \quad (6.1)$$

This equation takes into account the difference between both upper (T) and lower (B) sensors at each point, producing a force value at each position. To prevent the gas pressure within the chamber directly affecting the sensors a labyrinth seal was used. This ensures a de-coupling of the seal clamping load from the liner, allowing the liner to ‘float’ in an unconstrained manner (Gore et al, 2012). This setup is shown in figure 6.15. The alternative to this is using a spring-damper system to negate liner loading other than friction, however this would mean losses through the spring-damper which are unaccounted for. The labyrinth seal solves this issue but it may allow for side leakage of the gas pressure through the leakage orifice. This leakage is measured using a pressure transducer, and it is used to update the actual pressure applied to the ring.

Gore, M., Howell-Smith, S. J., King, P. D. and Rahnejat, H., “Measurement of In-cylinder Friction using the Floating Liner Principle”, *Proceedings of the ASME ICED Spring Technical Conference, ICES2012-81028* (2012) (figure 3)

Figure 6.15: Cross-section view of the floating liner assembly, showing the seal ring in green (Gore et al, 2012)

Verification of the testing process is shown by Gore et al (2012). The experimental results presented in this chapter have been smoothed using a 11-point moving average to reduce the noise and allow for better comparisons of trends. This is demonstrated in figure 6.16. The equation used for averaging the points is shown in equation (6.2):

$$F_{avg}(\varphi) = \frac{SUM(F(\varphi-5):F(\varphi+5))}{11} \quad (6.2)$$

Where  $F_{avg}$  is the averaged friction value, and  $\varphi$  is the crank angle.

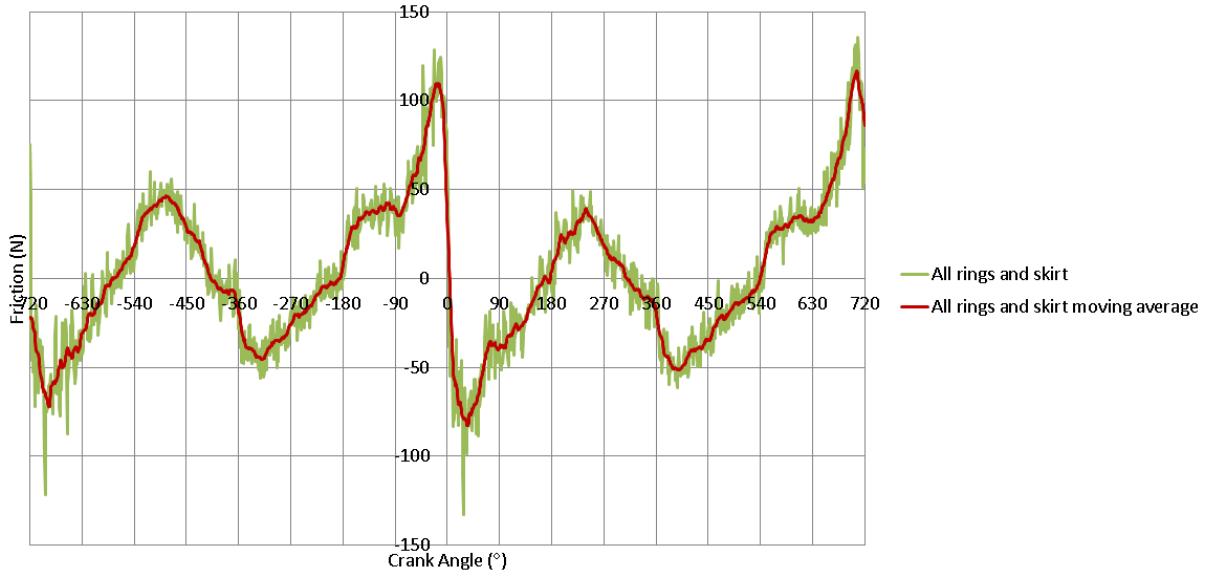


Figure 6.16: Experimental data before and after averaging. Engine speed = 2000rpm, motored running conditions

### 6.5.1. Motored Case

Figure 6.17 shows friction data captured from the engine and compared with numerical predictions for the top compression ring, both for elastic and rigid ring analyses. The test rig was run at 2000rpm using a transient dynamometer which can drive the engine in motored configuration, while the lubricant temperature was assumed to be at 35°C, which is a reasonable representation of the temperature seen under short-test motored conditions. It must be noted that the friction measured is a total friction value, which includes the piston skirt and the oil control ring, as well as the compression ring in this 2-ring engine. Therefore, an exact agreement between experimental and numerical values would not be expected. In both cases the order of magnitude of the numerical results appears to be reasonable, with the increase at 0° crank-angle (TDC position in transition from compression to power stroke, in this case with developed pressure due to the swept volume of air) seen. The asperity friction predictions at the reversal points are not captured through experimental analysis, however the numerical analysis shows asperity interaction at reversal points. This gives a difference between both the rigid and elastic ring methodologies and the experimental data, as the ‘spikes’ at reversal are not measured. This may be down to measurement

inaccuracies or assumptions within the numerical analysis which misrepresent the conditions at reversal. However, thin films would be expected when axial motion of the ring temporarily ceases, which would cause asperity interaction. Observation of all the strokes, excluding that of compression show higher friction as the piston accelerates towards the mid-stroke, with this reducing as the piston approaches reversal. This may be due to an offsetting of the experimental results, which would explain why the graph does not pass through zero at the expected crank angles ( $-180^\circ$ ,  $0^\circ$ ,  $180^\circ$ ,  $360^\circ$ ). It may also be the skirt contribution, which cannot be captured in the numerical analysis presented. Whilst the experimentally measured friction results are for both ring and skirt contributions, the numerical results from the presented methodology show top ring predictions only.

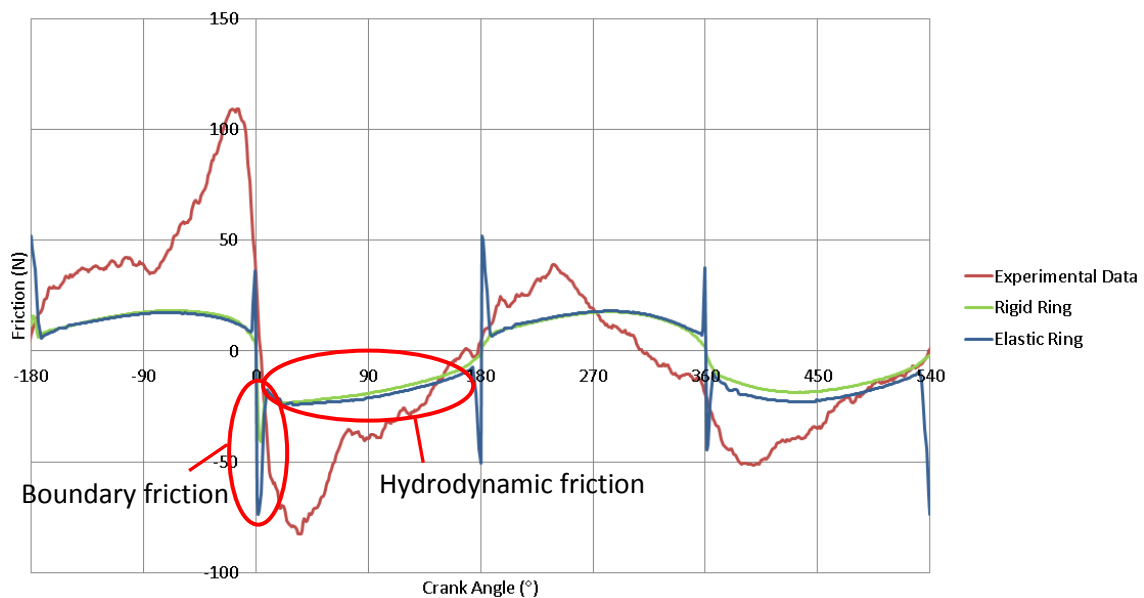


Figure 6.17: Friction comparison between numerical analysis and total measured friction in a motored engine. Engine speed = 2000rpm, Lubricant temperature =  $35^\circ\text{C}$

Regarding the comparison of both numerical methodologies, there is very little difference between the predicted friction values through the mid-stroke. However, the elastic ring analysis shows asperity friction at the reversal points. The peak created by this asperity friction is comparable in magnitude to the measured experimental friction at TDC before the power stroke. The difference would certainly be within the experimental margin of error, meaning a conclusive improvement in friction prediction cannot be claimed from these results. However, film thickness comparisons shown previously in the chapter would suggest that the elastic ring methodology gives a more accurate lubricant film prediction. This

suggests that the elastic ring friction predictions would also be more accurate. The peak friction force predicted is higher for a rigid ring analysis at low temperatures; however an increase in temperature causes the elastic ring methodology to predict greater friction, closer to the experimental data. It is important to note that the measured friction data accounts for the full ring pack and skirt frictional losses, so the numerical friction predictions should be less than the measured data.

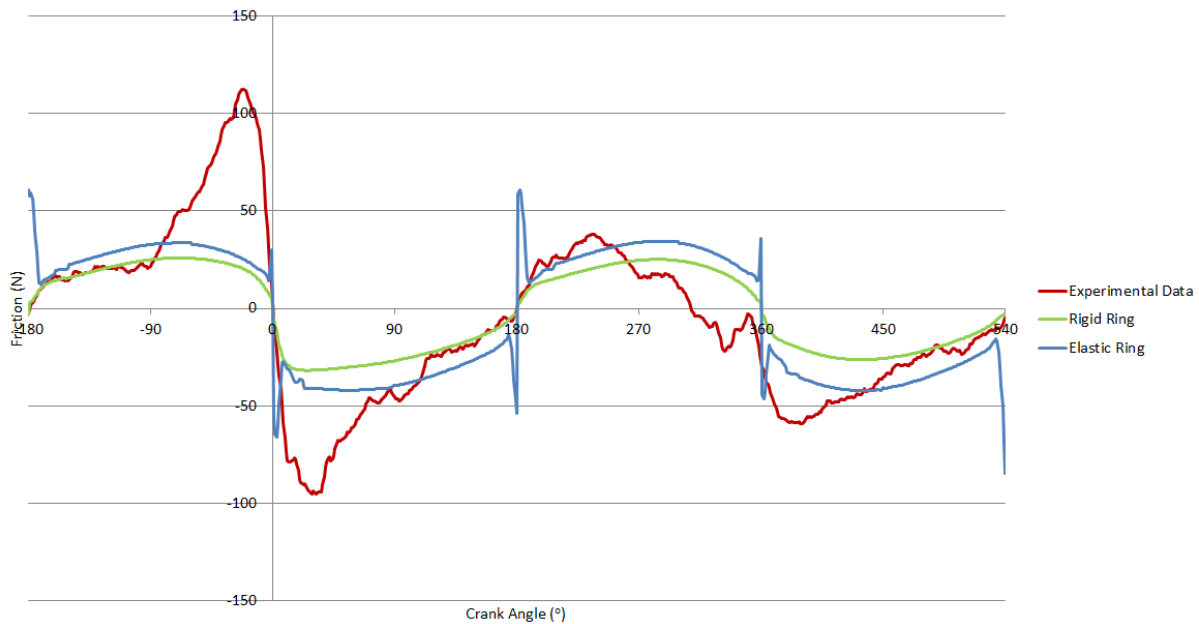


Figure 6.18: Friction comparison between numerical analysis and total measured friction in a motored engine. Engine speed = 2500rpm, lubricant temperature = 25°C

Further motored results were obtained using the Honda CRF engine at higher speeds. Figures 6.18 and 6.19 show the experimental friction data for the full ring pack and piston skirt, compared with the numerical results with rigid and elastic ring analyses. The engine speed in figures 6.18 and 6.19 is 2500rpm and 3000rpm, respectively. As these results were obtained without long engine operation, and as these correspond to motored conditions, a low temperature was measured in the oil sump and outside the liner. This meant a low temperature lubricant was assumed in the numerical analysis.

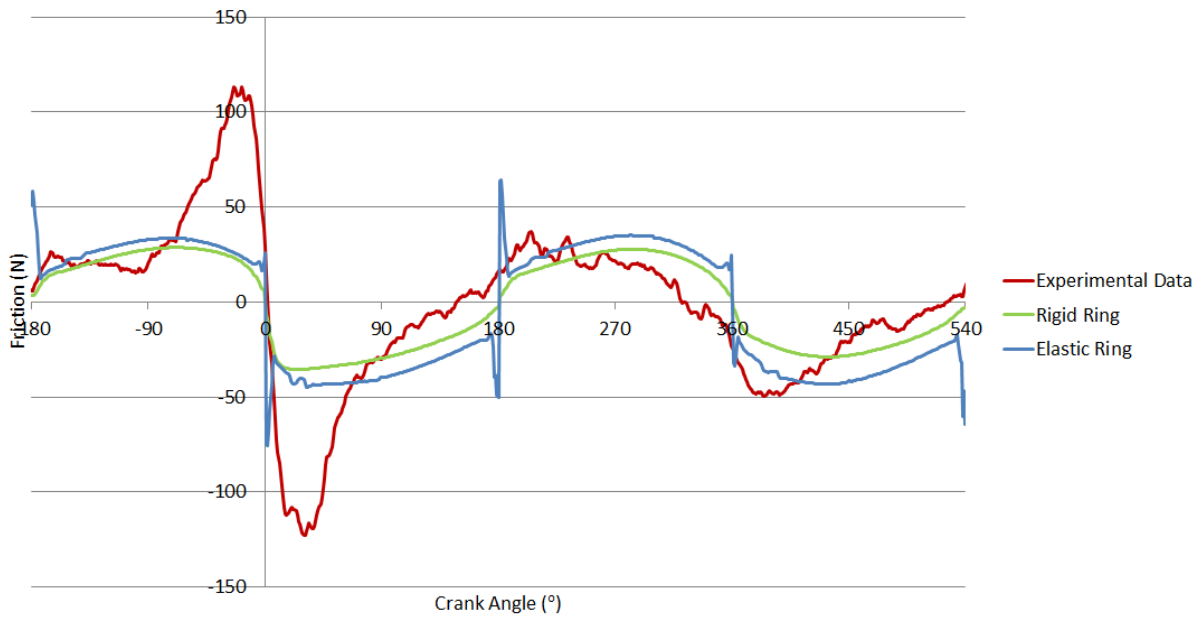


Figure 6.19: Friction comparison between numerical analysis and total measured friction in a motored engine. Engine speed = 3000rpm, lubricant temperature = 25°C

It can be seen from the experimental data obtained that engine speed has very little effect on the measured friction, apart from at the point of maximum pressure. Figure 6.20 shows the measured friction results at different speeds. It should also be noted that above an engine speed of 3000rpm, the accuracy and reliability of the experimental data is less certain. With the use of a floating liner with a labyrinth seal as described above, an increase in piston speed and load will likely cause more gas to leak into the environment, affecting the assumed pressure loading of the floating liner as well as placing more stress on the transducers. This situation pertains to a lack of reliability under extreme conditions. What can be seen however is that the results are repeatable to an acceptable degree with the friction values following piston velocity through the engine cycle.

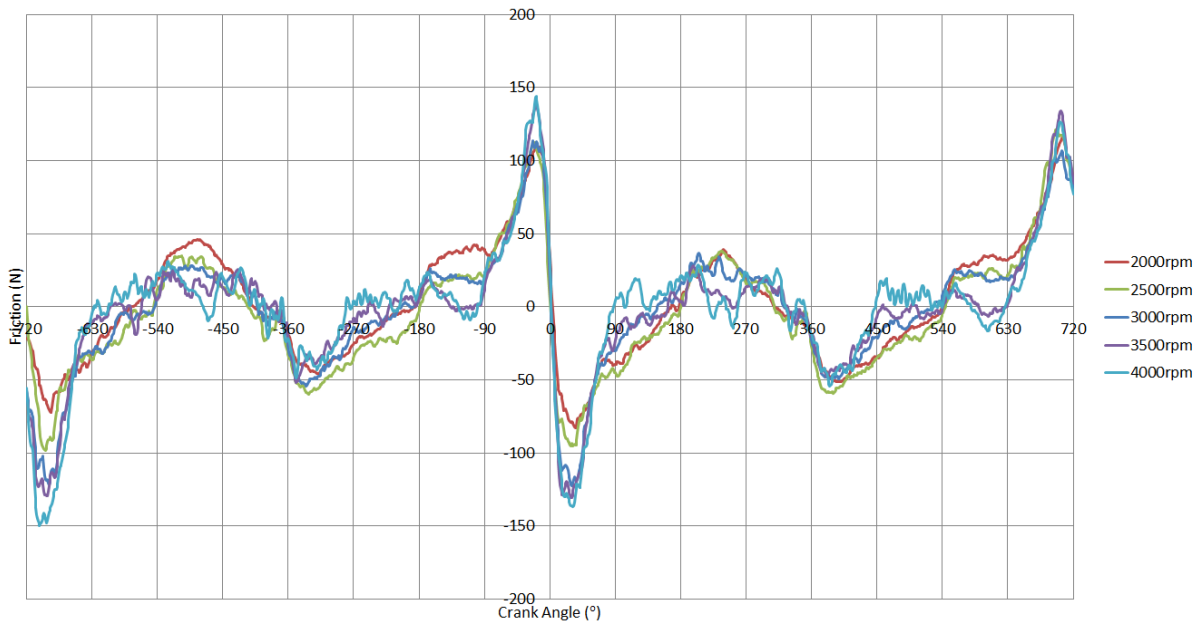


Figure 6.20: Measured friction results for different engine speeds

Whilst the individual friction values at each crank angle are a good indication of the accuracy of the numerical analyses through the cycle, examination of the average friction value in each case may also give insight into the results. Table 6.3 shows the average friction values for the results presented in figures 6.17-6.19. In each case the elastic ring methodology yields a closer average value than the rigid ring analysis. Figure 6.21 shows the results of both methodologies as a percentage of the measured friction value. Again, the inclusion of ring elastodynamics gives a closer approximation of friction throughout the four-stroke cycle. It must be reiterated that the measured friction is a total value, including losses due to oil control ring and piston skirt contributions. The numerical analyses consider the top compression ring only. However, inclusion of the full ring pack and piston skirt would dramatically increase the complexity and therefore the computation time of any numerical analysis. If a reasonable approximation of the average friction for a particular engine set up was possible, it may be beneficial to manufacturers even if the skirt and oil ring are not included in the analysis. Referring to figure 6.21, if one can predict with reasonable accuracy the average friction at a certain speed, this could allow for power loss calculations without the costs incurred through use of engines or other experimental test rigs.

Gas pressure loading applied behind the inner rim of the compression ring increases its contribution to overall piston-cylinder friction. Therefore, under motored conditions the contribution of compression ring to friction would be less than that under engine fired

conditions with higher gas pressures. The difference between the numerical results and those measured in table 6.3 is an indicative of this trend, as the ring friction is less than the measured friction. It is, therefore, important to make comparisons under fired conditions.

Table 6.3: Average friction comparison between experimental measurements and numerical analyses, motored case

Engine Speed (rpm)	Experimental Data (N)	Rigid Ring (N)	Elastic Ring (N)
2000	33.86	20.37	20.76
2500	34.96	20.31	31.79
3000	31.27	22.35	29.59

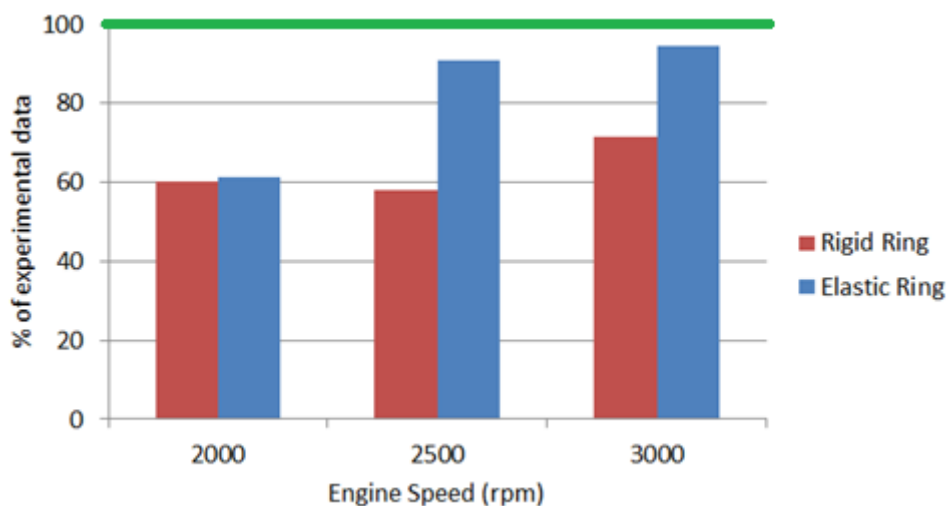


Figure 6.21: Numerical comparisons to motored experimental data as a percentage of average friction

### 6.5.2. Engine fired case

Fired friction data were also obtained from the Honda CRF with fitted floating liner. Figure 6.22 shows the results from a low load case at an engine speed of 2000rpm with the liner being relatively cold. Therefore, a lubricant temperature of 40°C was assumed in the numerical analysis. Lower friction is measured than from the motored case due to the low loading. The peak measured friction has moved to just after the top dead centre due to the point of combustion. The predicted friction from both numerical analysis methods peaks at approximately the same value; however the elastic analysis again predicts a higher friction value.

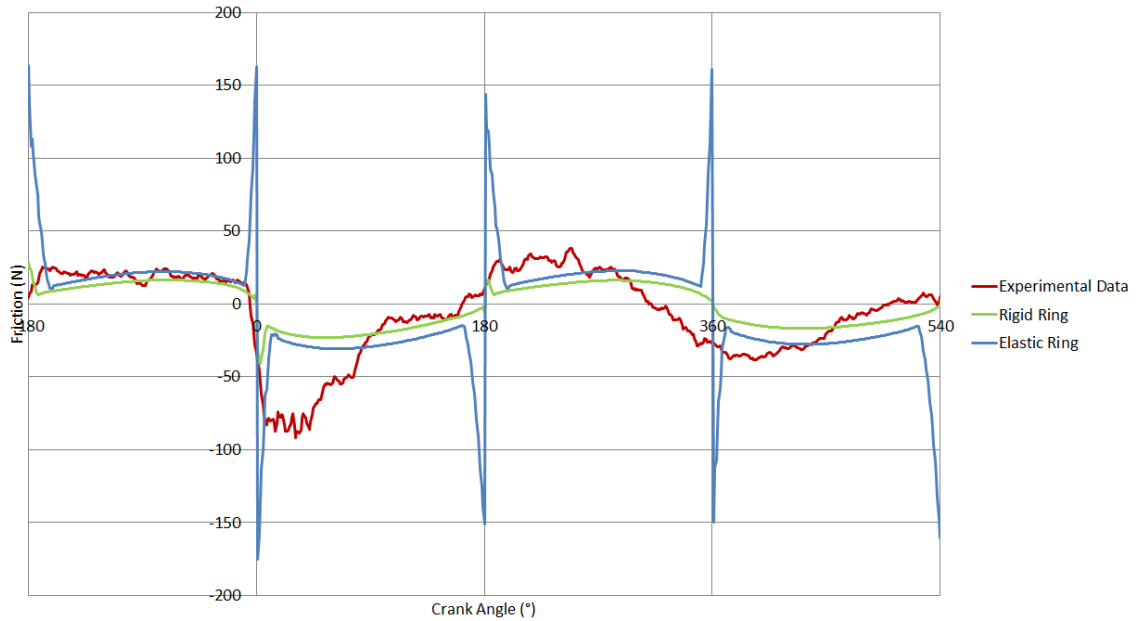


Figure 6.22: Friction comparison between numerical analysis and total measured friction in a fired engine. Engine speed = 2000rpm, lubricant temperature = 40°C, dyno load = 30Nm

Figures 6.23-6.24 show the same load cases but at higher engine speeds, 2500rpm and 3000rpm respectively. The measured friction increases at the point of maximum pressure. An increase is seen for both rigid and elastic analyses at the mid-stroke. However, the rigid ring analysis does not show any asperity interaction at reversals at these higher speeds. Furthermore, the friction value measured at 3000rpm does not show the expected trend between approximately 90° and 270° past TDC, even when the averaging of results has occurred. This suggests results at higher speeds may not be as reliable as in lower speed cases.



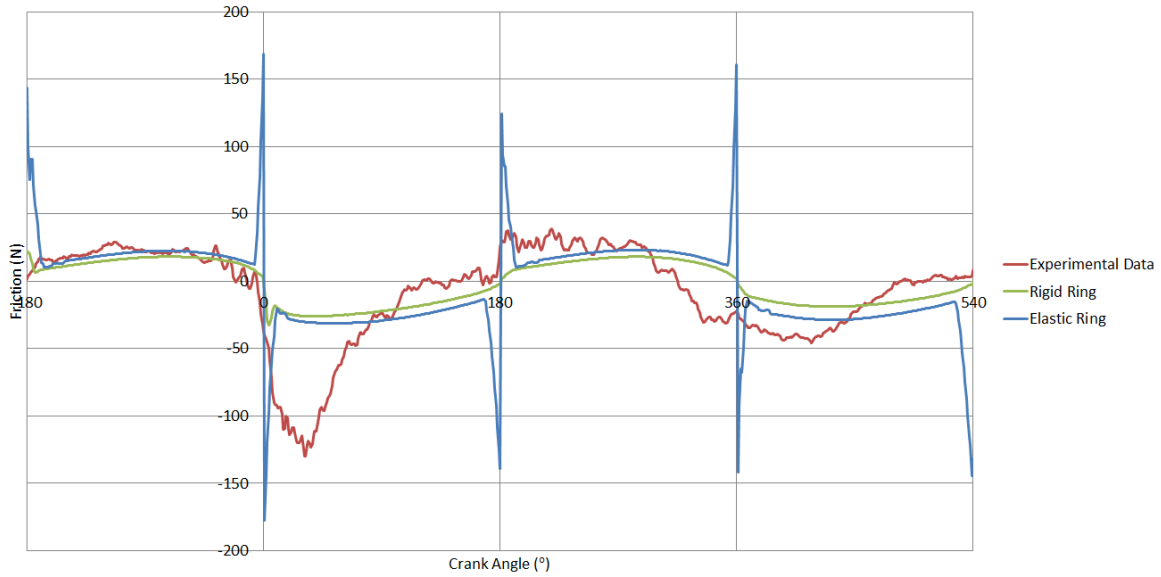


Figure 6.23: Friction comparison between numerical analysis and total measured friction in a fired engine. Engine speed = 2500rpm, lubricant temperature = 40°C, dyno load = 30Nm

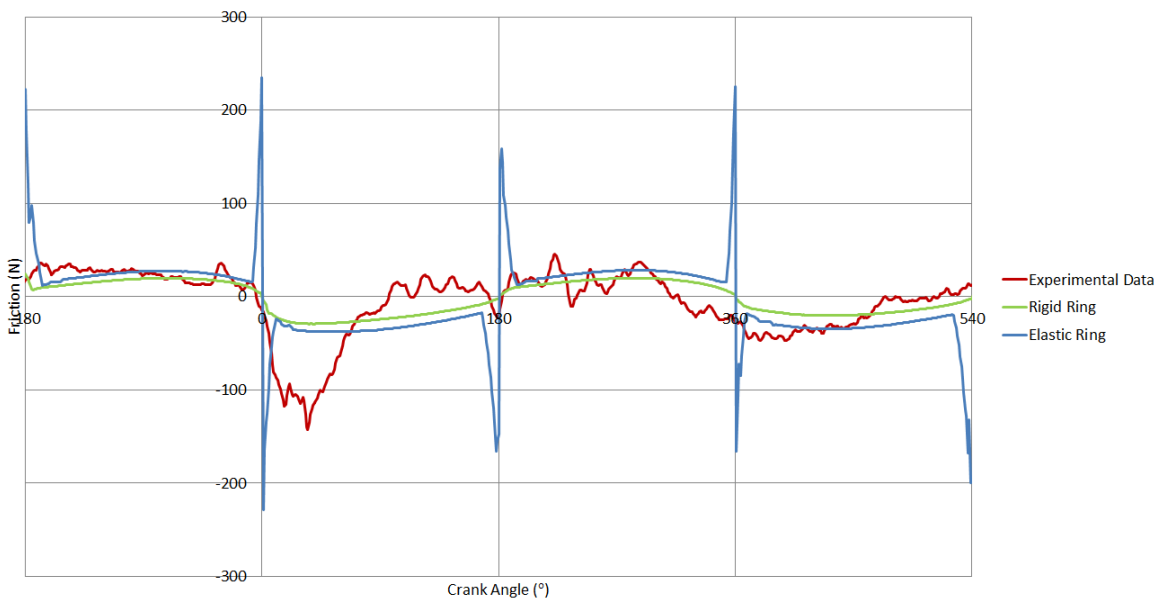


Figure 6.24: Friction comparison between numerical analysis and total measured friction in a fired engine. Engine speed = 3000rpm, lubricant temperature = 40°C, dyno load = 30Nm

Figures 6.22-6.24 show that asperity friction is predicted from the elastic ring analysis, as represented by the ‘spikes’ at reversal. This phenomenon is not demonstrated in the experimental data. However, when the averaging of the experimental results is removed, the peak friction value is seen to be closer to the numerical analysis for an elastic ring. Figures 6.25-6.27 show the experimental data without the moving average applied, in comparison with the elastic ring numerical analysis. This suggests that whilst the ‘spike’ in

numerical data is not captured when the moving average is plotted, it is not an unreasonable result when compared with the raw experimental data, particularly around the point of maximum pressure.

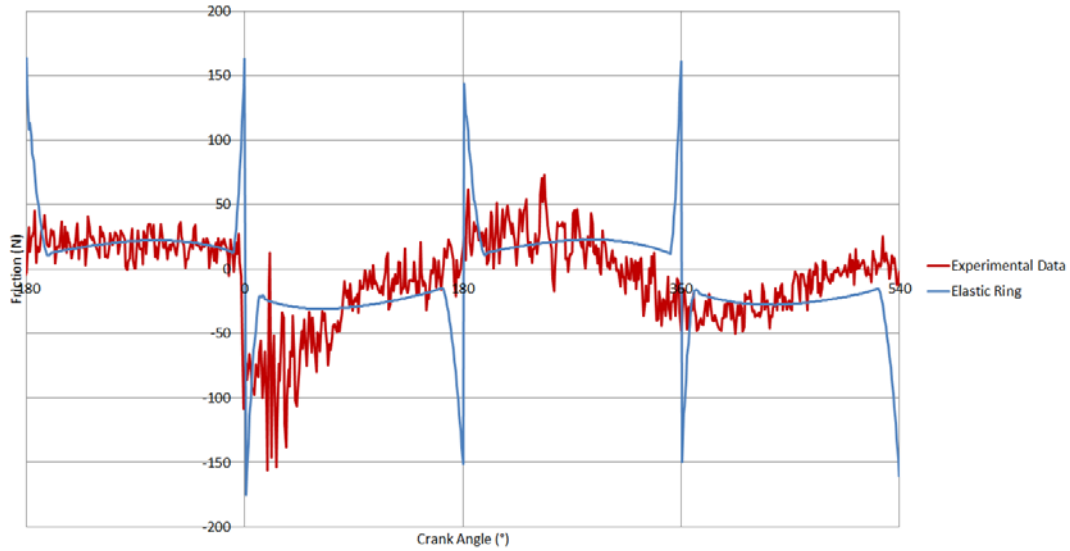


Figure 6.25: Comparison between numerical analysis and un-averaged friction from figure 6.26. Engine speed = 2000rpm, lubricant temperature = 40°C, dyno load = 30Nm

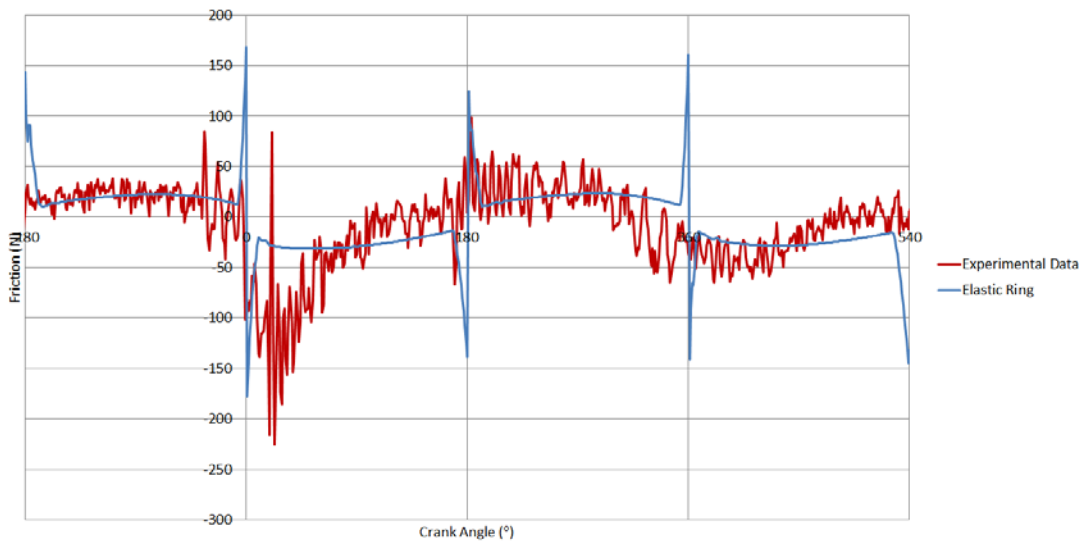


Figure 6.26: Comparison between numerical analysis and un-averaged friction from figure 6.27. Engine speed = 2500rpm, lubricant temperature = 40°C, dyno load = 30Nm

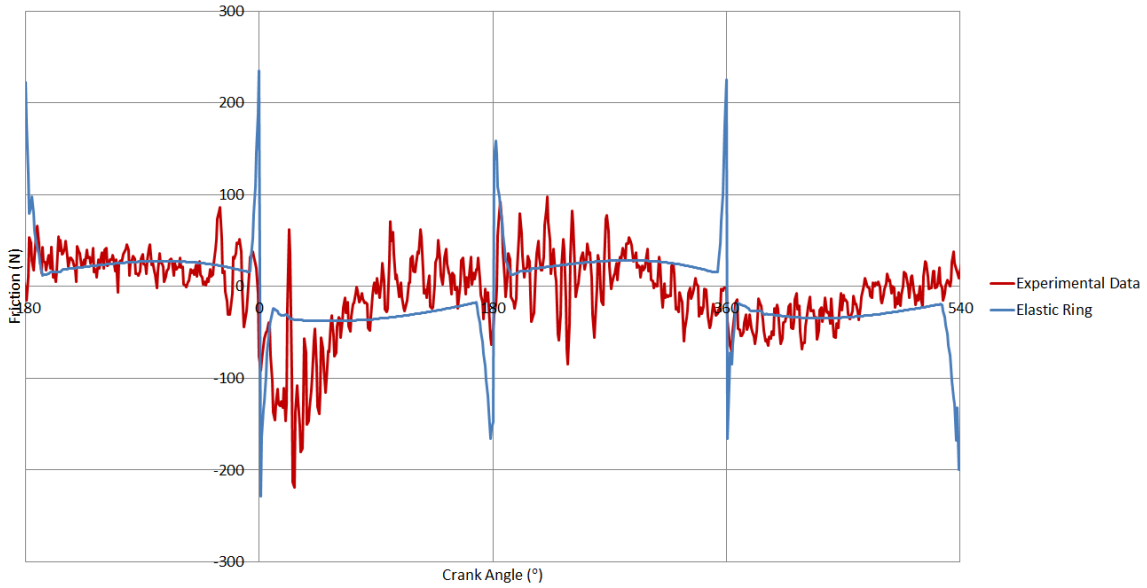


Figure 6.27: Comparison between numerical analysis and un-averaged friction from figure 23. Engine speed = 3000rpm, lubricant temperature = 40°C, dyno load = 30Nm

Further to these results, when the numerical data is averaged using the same moving average, the experimental and numerical results show reasonably good agreement. This can be seen in figure 6.28.

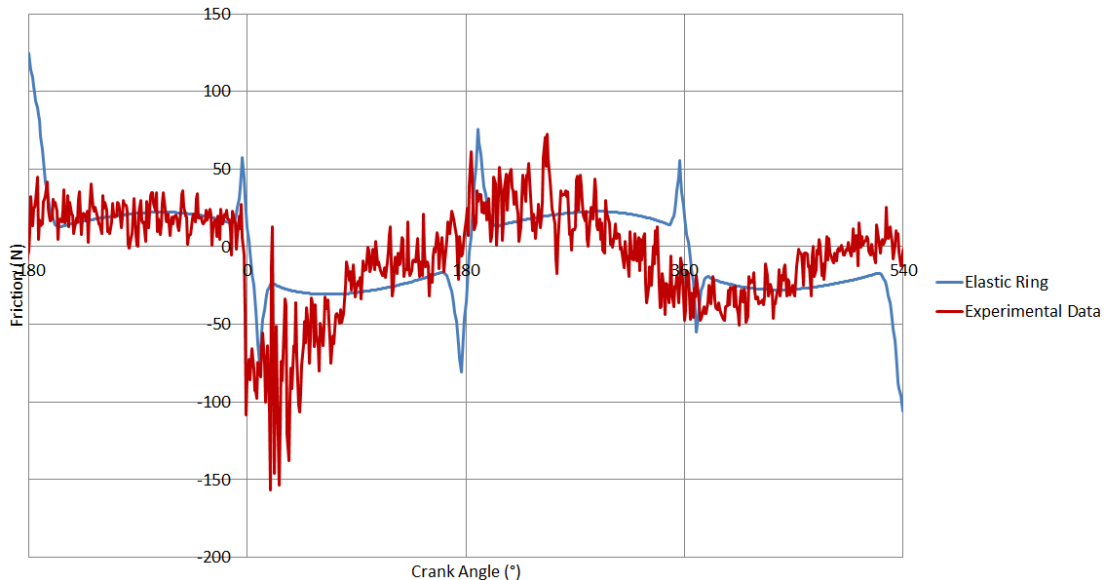


Figure 6.28: Comparison between averaged numerical analysis and un-averaged friction from figure 6.25. Engine speed = 2000rpm, lubricant temperature = 40°C, dyno load = 30Nm

Figure 6.29 gives the same friction comparison as for the motored data, with the numerical results presented as a percentage of the measured friction value. As opposed to the

motored comparisons, the average friction predicted from the elastic ring analysis is higher than the averaged measured value. This corroborates the argument that increased pressure loading of the compression ring increases its contribution to the overall piston-cylinder friction as noted in the previous section. In each case, the predicted value is closer to the experimental measurements for the elastic ring analysis than when a rigid ring is considered. Table 6.4 gives the numerical values for the cases in figure 29. The results show that the compression ring may almost account for the entire friction when its elasticity conforms it to the liner surface. With the rigid ring the compression ring contribution is around 50% of the overall average friction. In practice, the compression ring contribution may reside somewhere between these extremes as noted measured by Federal Moghul, who have not published their work or their method of measurement.

Table 6.4: Average friction comparison between experimental measurements and numerical analyses, fired case

Engine Speed (rpm)	Experimental Data (N)	Rigid (N)	Elastic (N)
2000	23.82882	14.12903	29.66429
2500	26.19526	15.43266	27.60714
3000	26.01748	16.63153	34.67723

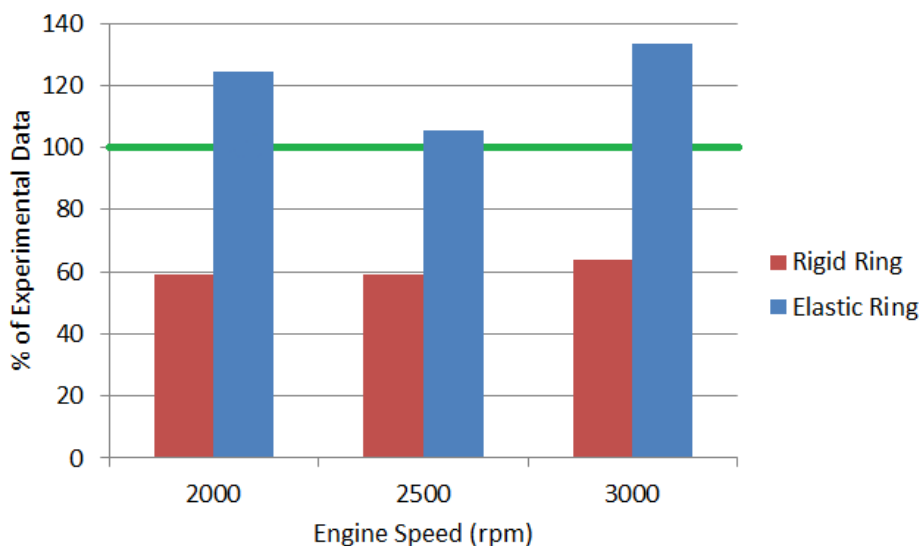


Figure 6.29: Numerical comparisons to experimental fired data as a percentage of average friction. Lubricant temperature = 40°C, dyno load = 30Nm

Further experimental data was gathered at the same engine speed range as previously, with a higher applied load. With increased loading one would expect greater applied gas pressure to the compression ring and consequently a greater contribution from it to the overall cylinder friction. Figure 6.30 shows the results at an engine speed of 2500rpm, with a dyno load of 130Nm (actual engine load of approximately 32.5Nm, because the engine is driven through an engaged clutch with a transmission ratio of 4.02:1). The increase in load can be seen to have a significant effect on the generated friction force through the power stroke. As with previous results, the elastic ring analysis gives a closer approximation to the measured friction than the rigid ring analysis.

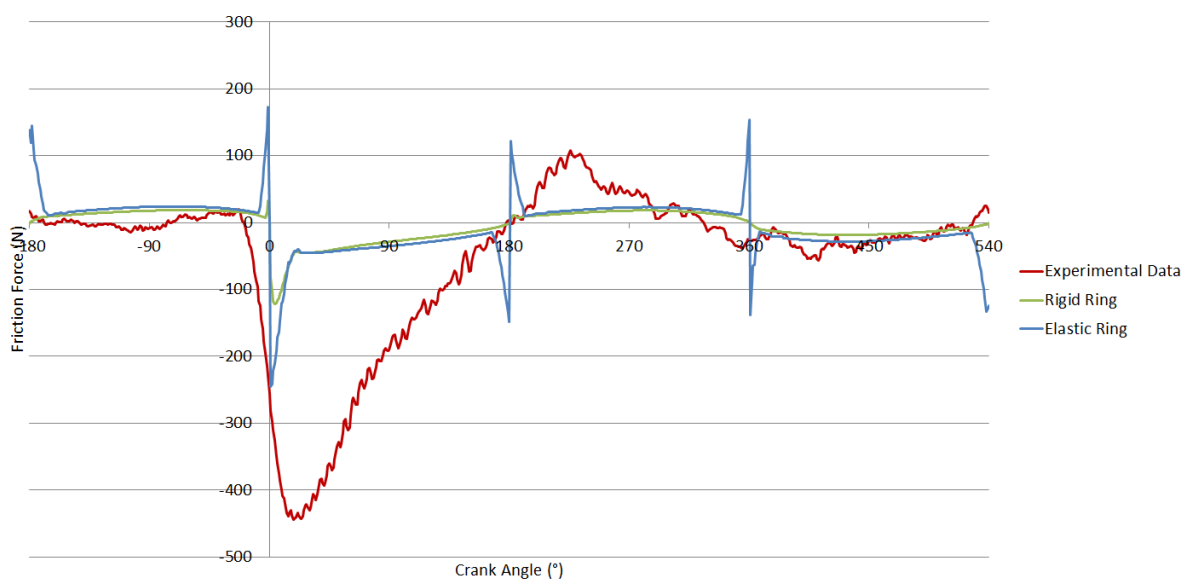


Figure 6.30: Comparison between numerical analysis and averaged friction. Engine speed = 2500rpm, lubricant temperature = 40°C, dyno load = 130Nm

With increasing engine speed, the difference between rigid and elastic ring analyses increases. This increase brings the friction value closer to the experimentally measured results as would be expected and discussed above. However, an increase in load also significantly increases the experimentally measured results, moving the peak friction away from the numerically predicted values. The results presented above, from both rigid and elastic numerical methodologies, do not give 100% agreement with the experimental and previously published data. However, there is consistency throughout the numerical results, with increases in frictional losses seen for higher engine speeds and loads.

## 6.6. Closure

This chapter compares the numerical predictions with those available in open literature. An improvement in film thickness prediction was seen when attempting to replicate published results, compared with the previous rigid ring analysis. As the out-of-plane ring motion is captured using this methodology, it was possible to compare any published ring motion predictions within the groove. The trend shown is in excellent agreement with both experimental and FEA results, with the ring's motion mostly dominated by the piston speed, as well as occasions where the cylinder gas pressure is sufficient to force the ring from the groove, reducing sealing. This result suggests correct coupling of the out-of-plane dynamics methodology to the tribological model.

The methodology was then compared with experimental measurements from a Honda CRF engine. Film thickness and frictional measurements were obtained. Again, the elastodynamic model showed an improvement in film thickness prediction when compared with the rigid ring analysis. Comparisons with friction measurements were made, showing ring friction numerical analysis against the total friction force data, which includes skirt and ring pack contributions. The magnitude of the numerically predicted friction was reasonable for both rigid and elastic ring analyses, even though the results did not follow the same exact profile through the four-stroke cycle as the experimental data. This was consistent even when the engine load was increased. However, limitations and assumptions used in both experimental and numerical analysis mean that complete conformance between the results is highly unlikely. When the average friction per crank angle was compared with experimental and numerical cases, the elastic ring analysis produced a closer average than when ring dynamics were not included. This result was consistent for all cases examined; indicating again that the inclusion of ring elastodynamics is beneficial to the numerical modelling of the compression ring.

## 7. Conclusions

### 7.1. Overall conclusions

The research undertaken as part of this thesis has drawn attention to the complex nature of the compression ring's dynamic behaviour throughout the engine cycle. The solution combines two different disciplines (tribology and dynamics), which are coupled to yield a solution. Therefore, it can be described as a multi-physics approach.

Modelling of the ring elastodynamic behaviour is based on previous literature using an analytic approach to determine the modal response of curved bars and incomplete rings. It has been noted that the in-plane (radial plane) and out-of-plane ring modal responses can be de-coupled, due to non-common degrees of freedom in their corresponding equations of motion, as well as relatively small deflections. This enables the overall ring dynamics solution to be treated as two distinct problems from a mathematical viewpoint. The solutions in each plane are then modified to augment rigid body responses of the ring in the radial and axial directions, verified by equivalent FEA results. This verification has shown that the mode shapes and natural frequencies show remarkable agreement between the analytical and FEA results. Application of a force function to the ring also provided good correlation between the two methods, giving confidence that the stand-alone dynamics models can be regarded as accurate.

The dynamics models in both planes were then coupled with the tribological analysis. Essentially, the forces acting upon the ring throughout the engine cycle are algebraically summed to give a net resultant, in both the ring's planes. These force profiles were extracted for application as the excitation force. The resultant deformed ring profiles, along with localised ring-bore kinematics are used in the tribology models to update the film thickness and squeeze velocity profiles. For the out-of-plane case, the film thickness and squeeze velocity values also include the ring-piston groove lands' conjunctions. A layer of lubricant was assumed to be present between the ring and the groove lands, as had been previously assumed by Tian (1998). This is considered to be a reasonable assumption. Due to the relatively small amount of radial movement with respect to the piston, the primary cause of the groove lubricant reaction force is the squeeze between the ring and piston, caused by the piston's primary motion and any localised twisting motion. This method gives

the ring's out-of-plane velocity, which largely follows that of the piston as would be expected. However, as the piston velocity decreases upon its approach to the dead centre reversals, the ring appears to 'jump' from one piston groove face to the other, due to its acceleration as the piston reaches the mid-stroke. The ring's local velocity values are used in the calculation of friction between the ring and the cylinder liner, giving a more accurate representation of the generated contact friction.

Overall, the results show that a hydrodynamic regime of lubrication is usually seen prevalent through the mid-strokes in an engine cycle. At reversals, a mixed regime of lubrication is encountered as the film thickness decreases, with EHL conditions potentially occurring around the point of maximum pressure.

The inclusion of ring elastodynamics generally resulted in an improved film thickness prediction, when compared with the alternative methods. Generally, the elastic ring analysis returned more accurate minimum film thickness values, bringing the predictions closer to those seen experimentally. The verification was achieved by comparison with results available in open literature, as well as experimentally obtained data using test rigs designed as part of this body of research. Friction predictions also compared favourably with the elastic numerical analysis. Although it must be noted that the numerical analysis represents the top ring only, whereas the measured friction is that of the entire piston assembly, the inclusion of ring dynamics improves the correlation between numerical and experimental results with respect to the previous methodology. Furthermore, the average friction predicted shows a closer agreement to the experimental data.

The out-of-plane motion of the top compression ring is a source of power loss, as the sealing capability of the ring is lost when it moves between the upper and lower groove faces. This suggests that the ability to limit both the ring's motion, and the distance between the lands, would reduce the time when the chamber is not adequately sealed. Further investigation into the design of the compression ring and piston groove, with this result in mind, may yield an improvement in the sealing capabilities of the ring.

### **7.2. Achievement of aims**

The major aim of research was the inclusion of transient compression ring elastodynamics into the tribological analysis of the ring-liner interface. Previous reported analyses of the



compression ring-cylinder liner conjunction had not considered the ring's transient deflection throughout the engine cycle. Instead, a force balance between the external (gas and elastic/ring tension) and internal (lubricant and asperity reaction) forces is usually assumed, with the minimum film thickness predicted, corresponding to this state of instantaneous equilibrium (quasi-static).

The aim of this thesis was to incorporate transient ring dynamics, both in-plane and out-of-plane, when considering the tribological performance of the compression ring. This aim has been achieved. Not only has this primary aim been achieved, but also the inclusion of ring dynamics has been shown to improve film thickness predictions, reasonable ring motion within the groove, and friction predictions of similar magnitude to those seen experimentally. Therefore, the aim of the research has been realised.

### **7.3. Contributions to Knowledge**

The points raised herein are regarded as the key contributions of the thesis, although these may not be entirely exhaustive.

The verification of a transient ring dynamics model has not hitherto been presented in literature, and can therefore be considered as novel in its detail and thorough implementation and reporting. Previous publications in open literature had shown some verified mode shapes and natural frequencies. However, a systematic study including both modal and forced responses had not been demonstrated as it is presented in this thesis. The thesis demonstrates verified forced response results, both in-plane and out-of-plane, with the inclusion of rigid body modes, achieved through modification of the elastodynamic equations of motion.

Furthermore, the coupling of transient ring dynamics and transient mixed hydrodynamic analysis of the compression ring-to-cylinder liner conjunction is a methodology generated in this thesis, and it represents a unique solution for the fully transient behaviour of the top compression ring. It is the culmination of two separate theoretical areas of research, coupled within a unified methodology which reflects the physical reality in a plausible manner. The thin nature of compression rings means that they are highly likely to behave in an elastic manner. Aside from any verification, the methodology is novel on its own accord.

Verification of the presented methodology was possible, both from results available in open literature and experimental data collection as part of this research. The results presented (comparisons with other sources, and conclusions from this study) are novel. The ring's position within the groove had previously been observed experimentally and predicted using an FEA model of the ring's dynamic response. However, a closed form analytical method studying this phenomenon has not hitherto been produced, providing further contribution to knowledge.

### **7.4. Suggestions for future work**

The work carried out in this thesis leaves a number of areas of research which can be investigated in addition to the inclusion of ring dynamics. Previous studies on the tribological performance of the top compression ring have taken into account many different aspects, all of which could be combined with the above research to yield further interesting results and conclusions.

Mechanical bore distortion and ring conformability was discussed by Ma et al (1997). The inclusion of a variable liner profile, both circumferentially and axially, would give an added complexity to the ring elastodynamics. This would likely be shown in the ring's response throughout the engine cycle, as a more complex liner shape gives a constantly changing force profile, which would excite a larger variety of ring mode shapes. The phenomenon of blowby is attributed to gaps between the ring and the liner, as well as around the back of the ring, which allows gas to escape from the combustion chamber causing a loss of power. A study which includes both ring and bore deformation would give better indication of the conditions at which blowby and ring flutter can occur. Therefore, a further addition to this work, allowing for improved analysis of the piston ring pack, would be a gas blowby model. The gas pressure acting upon the back of the ring would vary as a percentage of the cylinder pressure throughout the engine cycle, depending on the ring's position within the groove. Previous attempts to create a gas flow model use quasi-static, rigid ring motion, which is a simplistic view of the ring's likely motion. Incorporating transient ring elastodynamics would provide a more complex, but realistic model, leading to improved understanding of gas blowby.

Other future work concerns the lubricant models used within the tribodynamic analysis. The presented results in this thesis assume fully flooded conditions in the numerical analysis (an assumption which is also used when deconvoluting the film thickness ultrasound measurements). In reality, there would be a finite amount of lubricant available to the ring-liner contact, particularly at reversal points. Han and Lee (1998) implemented a starvation model, which would be a potential area of research in conjunction with ring elastodynamics. The entraining lubricant affects the hydrodynamic reaction force, and consequently the generated friction. There may also be the potential to account for the lubricant on each groove face. This would affect the ring's axial motion within the groove, and may influence the predicted sealing capabilities of the system.

EHL analysis of the piston ring was carried out by Ruddy et al (1981). Localised deflections of the cylinder liner would only occur when high pressures were seen; meaning the majority of the piston's cycle would not encounter EHL conditions. However, the point of maximum pressure is a critical area when considering the tribological performance of the compression ring. Ruddy et al (1981) suggested that localised deformations may be a source of blowby. Inclusion of transient ring dynamics would help to further investigate this supposition, with the amalgamation of ring and bore localised deflection.

The conditions described above were not considered for this thesis, as the focus on ring dynamics was the key area of interest. Many previous studies of piston ring tribology do not include EHL analysis, so this was deemed a reasonable assumption for this research. Each factor increases the complexity of the analysis, but providing a more accurate representation of the real conditions which would affect the ring throughout the engine cycle. The inclusion of research areas such as these will further contribute to the understanding of the piston ring pack assembly.

Aside from the previously explored areas of research concerned with the piston ring pack, an area where progression would be possible is with the implementation of the groove lubricant reaction force. The results presented in this thesis applied a one-dimensional analytical Reynolds' equation solution, integrated along the ring's radial width to find the force at each circumferential position. The development into a transient, two-dimensional analysis would represent a further enhancement of the methodology. This could potentially

be coupled with the lubricant starvation model, to give a more accurate approximation of the available lubricant on each groove face.

The research presented was undertaken in conjunction with a number of industrial partners, who provided information such as the piston ring pack dimensions, lubricant properties and engine running conditions. Sample compression rings were also provided, allowing for more accurate measurement of the ring's dimension. This is particularly important in the case of the ring's axial profile. The axial profile is altered via the mechanism of wear throughout the ring's working life, and relatively small changes to the profile can have a significant effect on the friction predictions. A brand new and an end-of-life compression ring were provided, to allow measurement and comparison of results, which is seen to be significant. Any future research in this area may be enhanced by a more comprehensive range of top ring axial profiles. This would allow the wearing of the ring to be documented, if measurements were taken after known running times. The ring's axial profile could be plotted at each instance, as well as the corresponding friction/power loss predictions. A methodology such as this would improve the understanding of how the ring wears over its useful time, as well as the effect of gradual wearing upon the power output of the engine.

## 8. References

Akalin, Ozgen, and Golam M. Newaz. "Piston ring-cylinder bore friction modelling in mixed lubrication regime: part I—analytical results." *Journal of tribology* 123 (2001): 211.

Andersson, B. S. "Paper XVIII (iii) Company Perspectives in Vehicle Tribology-Volvo." *Tribology Series* 18 (1991): 503-506.

Andersson, P., Tamminen, J., and Sandström, C., "Piston ring tribology." *A literature survey. VTT Tiedotteita-Research Notes* 2178.1 (2002).

Archer, Robert R. "Small vibrations of thin incomplete circular rings." *International Journal of Mechanical Sciences* 1.1 (1960): 45-56.

Auciello, N. M., and M. A. De Rosa. "Free vibrations of circular arches: a review." *Journal of Sound and Vibration* 176.4 (1994): 433-458.

Avan, Emin Yusuf, Robin Mills, and Rob Dwyer-Joyce. "Ultrasonic Imaging of the Piston Ring Oil Film During Operation in a Motored Engine-Towards Oil Film Thickness Measurement." *SAE International Journal of Fuels and Lubricants* 3.2 (2010): 786-793.

Baker, C. E., Rahmani, R., Theodossiades, S., Rahnejat, H., "Analytical Evaluation of Fitted Piston Compression Ring: Modal Behaviour and Frictional Assessment", *SAE Technical Paper 2011-01-1535*, (2011).

Baker, C. E., Rahmani, R., Theodossiades, S., Rahnejat, H., and Fitzsimons, B., "Thermo-Elastohydrodynamics of a Rough Piston Compression Ring-to-Cylinder Bore Conjunction," *Proc. STLE 66th Annual Conference, Atlanta, GA, 15–19 May* (2011).

Baker, C. E., Theodossiades, S., Rahnejat, H., and Fitzsimons, B., "Influence of In-Plane Dynamics of Thin Compression Rings on Friction in Internal Combustion Engines." *ASME Journal of Engineering for Gas Turbines and Power* Vol. 134 (2012): 092801.

Baker, C. E., Theodossiades, S. and Rahnejat, H., "Friction under transient mixed regime of lubrication in conjunction of an elastic ring within a real cylinder", *Proc. ASME ICED Spring Tech. Conference, ICES2012-81045, 6-9 May* (2012)

Balakrishnan, S., and H. Rahnejat. "Isothermal transient analysis of piston skirt-to-cylinder wall contacts under combined axial, lateral and tilting motion.", *Journal of Physics D: Applied Physics* 38.5 (2005): 787.

Balakrishnan, S., "Transient Elastohydrodynamic Analysis of Piston Skirt Lubricated Contact Under Combined Axial, Lateral and Tilting Motion", PhD Thesis, Loughborough University (2002)

Barus, Carl. "Isothermals, isopiestic and isometrics relative to viscosity." *American Journal of Science, 3<sup>rd</sup> Series*, 45, (1893): 87-96

BBC website, 27 September 2013. Available at <http://www.bbc.co.uk/news/science-environment-24292615>

Brown, Fred H. "Lateral vibration of ring-shaped frames." *Journal of the Franklin Institute* 218.1 (1934): 41-48.

Burington, R. S., "Handbook of Mathematical Tables and Formulas", 3<sup>rd</sup> Ed., *Handbook Publishers, Ohio*, (1958)

Cameron, A., (1967) "*Basic Lubrication Theory*" London, Longman Ltd

Castleman, R. A. "A hydrodynamical theory of piston ring lubrication." *Journal of Applied Physics* 7.9 (1936): 364-367.

Challamel, Noël, Charles Casandjian, and Jean Lerbet. "On the occurrence of flutter in the lateral-torsional instabilities of circular arches under follower loads." *Journal of Sound and Vibration* 320.3 (2009): 617-631.

Chittenden, R. J., and M. Priest. "Analysis of the piston assembly, bore distortion and future developments." *Tribology Series* 26 (1993): 241-241.

Coy, R. C. "Practical applications of lubrication models in engines." *Tribology international* 31.10 (1998): 563-571.

Dowson, D., and G. R. Higginson. "A numerical solution to the elasto-hydrodynamic problem." *Journal of Mech. Engineering Science* 1.1 (1959): 6-15.

Dowson, D., Economou, P. N., Ruddy, B. L., Strachan, P. J., and Baker, A. J. S., "Piston ring lubrication. Part II: theoretical analysis of a single ring and a complete ring pack." *ASME Energy Conservation through fluid film lubrication technology: Frontiers in research and design* (1979): 23-52.

Dowson, D. "Piston assemblies; background and lubrication analysis." *Tribology Series 26* (1993): 213-240.

De Rosa, M. A., and C. Franciosi. "Exact and approximate dynamic analysis of circular arches using DQM." *International Journal of Solids and Structures* 37.8 (2000): 1103-1117.

Den Hartog, J. P. "XL. The lowest natural frequency of circular arcs." *The London, Edinburgh, and Dublin Philosophical Magazine and Journal of Science* 5.28 (1928): 400-408.

Dunaevsky, V. V. "Analysis of distortions of cylinders and conformability of piston rings." *Tribology Transactions* 33.1 (1990): 33-40.

Dunaevsky, Valery V., Sergei Alexandrov, and F. Barlat. "Analysis of three-dimensional distortions of the piston rings with arbitrary cross-section." *SAE Technical Paper* (2000): 01-3453.

Dunaevsky, V. V., S. Alexandrov, and F. Barlat. "Fundamentals for analysis of three dimensional distortions of the piston rings." *Proceedings of the 2000 Fall Technical Conference of the ASME Internal Combustion Engine Division*. (2000): 15-22

Dunaevsky, V. V. and Alexandrov, S., and Barlat., F., "The effect of contact pressure on piston ring twist." *SAE Technical Paper* (2001): 01-2720.

Dunaevsky, V. V. and Alexandrov, S., "Three-dimensional engineering approach to conformability analysis of piston rings." *Tribology Trans.* 48.1 (2005): 108-118.

Dwyer-Joyce, R. S., Green, D. A., Balakrishnan, S., Harper, P., Lewis, R., Howell-Smith, S. and Rahnejat, H. "2006-01-0648 The Measurement Of Liner-Piston Skirt Oil Film Thickness by an Ultrasonic Means." *SAE Trans.* 115.3 (2007): 348.

Eddington, Sir Rod. "The Eddington transport study: the case for action: Sir Rod Eddington's advice to Government.", *HMSO* (2006).

Eilon, Samuel, and O. A. Saunders. "A study of piston-ring lubrication.", *Proceedings of the Institution of Mechanical Engineers* 171.1 (1957): 427-462.

Encyclopaedic.org, 2009. Available at <http://www.encyclopaedic.org/Pages/default.aspx>

Evans, H. P., and Snidle, R. W., The elastohydrodynamic lubrication of point contacts at heavy loads. *Proceedings of the Royal Society of London. A. Mathematical and Physical Sciences, Vol. 382, No. 1782* (1982), 183-199.

Fox, Malcolm F., et al. "The 'limits of lubrication' concept applied to the piston ring zone lubrication of modern engines." *Tribology Letters*, 3.1 (1997): 99-106.

Furuhama, S., "A dynamic theory of piston-ring lubrication: 1<sup>st</sup> report, calculation", *Bulletin of JSME*, 2.7, (1959): 423-428

Furuhama, S., "A dynamic theory of piston-ring lubrication: 2st report, experiment", *Bulletin of JSME*, 3.10, (1960): 291-297

Furuhama, S., "A dynamic theory of piston-ring lubrication: 3rd report, measurement of oil film thickness", *Bulletin of JSME*, 4.16, (1961): 744-752

Furuhama, Shoichi, and Shinichi Sasaki. *New device for the measurement of piston frictional forces in small engines*. SAE Paper No. 831284, (1983).

Gohar, R. and Rahnejat, H., (2008) *"Fundamentals of Tribology"*, London: Imperial College Press

Gore, M., Howell-Smith, S. J., King, P. D. and Rahnejat, H., "Measurement of In-cylinder Friction using the Floating Liner Principle", *Proceedings of the ASME ICED Spring Technical Conference, ICES2012-81028* (2012)

Greenwood, J. A., and J. H. Tripp. "The contact of two nominally flat rough surfaces." *Proceedings of the Institution of Mechanical Engineers* 185.1 (1970): 625-633.

Grubin, A. N. "Fundamentals of the hydrodynamic theory of lubrication of heavily loaded cylindrical surfaces." *Investigation of the Contact Machine Components* 30 (1949): 115-166.



Hamilton, G. M., and S. L. Moore. "First Paper: Measurement of the Oil-Film Thickness between the Piston Rings and Liner of a Small Diesel Engine," *Proceedings of the Institution of Mechanical Engineers* 188.1 (1974): 253-261.

Han, D. C. and Lee, J. S., "Analysis of the piston ring lubrication with a new boundary condition." *Tribology international* 31.12 (1998): 753-760.

Hertz, Heinrich. "On the contact of elastic solids." *J. reine angew. Math* 92.156-171 (1881): 110.

Henrych, Josef. *The dynamics of arches and frames*. Ed. Rudolph Major. Academia, 1981.

Hill, Stephen H., and Brian A. Newman. *Piston ring designs for reduced friction*. No. SAE-TP-841222. Society of Automotive Engineers, Inc., Warrendale, PA, 1984.

Houpert, L., and P. Leenders. "A theoretical and experimental investigation into Rolling Bearing Friction." *Proc. of Eurotrib Conference, Lyon*. 1985.

Howell-Smith, S., "Tribological optimisation of the internal combustion engine piston to bore conjunction through surface modification", PhD thesis, Loughborough University (2011)

Hu, Y., Cheng, H.S., Arai, T. and Kobayashi, Y., "Numerical simulation of piston ring in mixed lubrication – A nonaxisymmetrical analysis", *Trans. ASME, J. Tribology*, 116, 470-478 (1994)

Inman, Daniel J. (2001) "*Engineering vibration*", Prentice-Hall

IPCC, 2007: Climate Change 2007: Synthesis Report. Contribution of Working Groups I, II and III to the Fourth Assessment Report of the Intergovernmental Panel on Climate Change [Core Writing Team, Pachauri, R.K and Reisinger, A. (eds.)]. IPCC, Geneva, Switzerland, 104 pp.

Kang, K. J., C. W. Bert, and A. G. Striz. "Vibration and buckling analysis of circular arches using DQM." *Computers and structures* 60.1 (1996): 49-57.

Kang., K. J., "Vibration analysis of thin-walled curved beams using DQM." *Journal of mechanical science and technology* 21.8 (2007): 1207-1217.

Karthikeyan, B. K., Teodorescu, M., Rahnejat, H., and Rothberg, S. J., "Thermo-elastohydrodynamics of grease-lubricated concentrated point contacts." *Proceedings of the Institution of Mechanical Engineers, Part C: Journal of Mechanical Engineering Science* 224.3 (2010): 683-695.

King, Julia. *The King Review of low-carbon cars: part I: the potential for CO2 reduction*, HMSO, 2007.

Knoll, G. D., and H. J. Peeken. "Hydrodynamic lubrication of piston skirts." *Journal of Lubrication Technology* 104 (1982): 504.

Kurbet, S. N., and R. K. Kumar. "A finite element study of piston tilt effects on piston ring dynamics in internal combustion engines." *Proceedings of the Institution of Mechanical Engineers, Part K: Journal of Multi-body Dynamics* 218.2 (2004): 107-117.

Lamb, H., "On the Flexure and the Vibrations of a Curved Bar." *Proceedings of the London Mathematical Society* 1.1 (1887): 365-377.

Lang, T. E. "Vibration of thin circular rings." *Jet Propulsion Laboratory Technical Report* 32-261 (1962).

Lee, Sen-Yung, and Jeng-Chung Chao. "Out-of-plane vibrations of curved non-uniform beams of constant radius." *Journal of sound and vibration* 238.3 (2000): 443-458.

Littlefair, B., De la Cruz, M., Mills, R., Theodossiades, S., Howell-Smith, S., Rahnejat, H. and Dwyer-Joyce, R., "Lubrication of a Flexible Piston Skirt Conjunction subjected to Thermo-elastic Deformation: a Combined Numerical and Experimental Investigation" *Proceedings of the Institution of Mechanical Engineers, Part J: Journal of Engineering Tribology*, 228.1 (2014): 69-81.

Love, A. E. H. *A treatise on mathematical theory of elasticity*, 1944 (Dover, New York).

Ma, M. T., Sherrington, I. and Smith., E. H., "Analysis of lubrication and friction for a complete piston-ring pack with an improved oil availability model: Part 1: Circumferentially uniform film." *Proceedings of the Institution of Mechanical Engineers, Part J: Journal of Engineering Tribology* 211.1 (1997): 1-15.

Mayer, R. Uber Elastizitat und Stabilitat des geschlossenen und offenen Kreisbogens. *Zeitschr.f.angewandte Math.u.Phys.*, 1921, Bd.61, 246–322.

Mishra, P. C., Homer Rahnejat, and P. D. King, "Tribology of the ring—bore conjunction subject to a mixed regime of lubrication." *Proceedings of the Institution of Mechanical Engineers, Part C: Journal of Mechanical Engineering Science* 223.4 (2009): 987-998.

Morley, L. S. D. "The Flexural Vibrations of a Cut Thin Ring." *The Quarterly Journal of Mechanics and Applied Mathematics* 11.4 (1958): 491-497.

Morris, N., Rahmani, R., Rahnejat, H., King, P. D., & Fitzsimons, B., "Tribology of piston compression ring conjunction under transient thermal mixed regime of lubrication." *Tribology International Vol. 59* (2012): 248-258

Namazian, M., and J. B. Heywood. "Flow in the Piston—Cylinder Ring Crevices of a SI Engine." *SAE paper 820088* (1982).

Natsavias, S., *Vibrations of Mechanical Systems, Thessaloniki*, 2001, ISBN960-431-712-1

Navier, C. L. M. H., "Mémoire sur les lois du mouvement des fluides." *Mémoires de l'Académie Royale des Sciences de l'Institut de France* 6 (1823): 389-440

Nikian, M., M. Naghashzadegan, and S. K. Arya. "Modeling of heat losses within combustion chamber of Diesel engines." *IUST International Journal of Engineering Science* 17.3-4 (2006): 47-52.

Ojalvo, I. U. "Coupled twist-bending vibrations of incomplete elastic rings." *International Journal of Mechanical Sciences* 4.1 (1962): 53-72.

Okamoto, Michio, and I. Sakai. "Contact pressure distribution of piston rings—calculation based on piston ring contour." *SAE Technical Paper 2001-01-0571* (2001)

O'Rourke, B., Radford, D. and Stanglmaier, R., "Tri-Axial Force Measurements on the Cylinder of a Motored SI Engine Operated on Lubricants of Differing Viscosity." *Journal of engineering for gas turbines and power* 132.9 (2010)

Owen, N. J., and R. L. Gordon. "Carbon to Hydrogen" Roadmaps for Passenger Cars: Update of the Study for the Department for Transport and the Department of Trade and Industry. Ricardo Consulting Engineers, UK, 2003.

Patir, Nadir, and H. S. Cheng. "An average flow model for determining effects of three-dimensional roughness on partial hydrodynamic lubrication." *ASME, Transactions, Journal of Lubrication Technology* 100 (1978): 12-17.

Petrusevich, A. I. "Fundamental conclusions from the contact-hydrodynamic theory of lubrication." *Izv. Akad. Nauk. SSSR (OTN)* 2 (1951): 209.

Priest, M., and C. M. Taylor. "Automobile engine tribology—approaching the surface." *Wear* 241.2 (2000): 193-203.

Protocol, Kyoto. "United Nations framework convention on climate change." *Kyoto Protocol, Kyoto* (1997).

Quan-bao, Zhou, Zhu Tie-zhu, and Wang Rong-sheng. "A full lubrication model for rough surface piston rings." *Tribology international* 21.4 (1988): 211-214.

Rahmani, Ramin, Theodossiades, S., Rahnejat, H., and Fitzsimons, B., "Transient elastohydrodynamic lubrication of rough new or worn piston compression ring conjunction with an out-of-round cylinder bore", *Proceedings of the Institution of Mechanical Engineers, Part J: Journal of Engineering Tribology* 226.4 (2012): 284-305.

Rahnejat, Homer, Balakrishnan, S., King, P. D., and Howell-Smith, S., "In-cylinder friction reduction using a surface finish optimization technique." *Proceedings of the Institution of Mechanical Engineers, Part D: Journal of Automobile Engineering* 220.9 (2006): 1309-1318.

Rao, S. S. "Effects of transverse shear and rotatory inertia on the coupled twist-bending vibrations of circular rings." *Journal of Sound and Vibration* 16.4 (1971): 551-566.

Reynolds, Osborne. "On the dynamical theory of incompressible viscous fluids and the determination of the criterion." *Philosophical Transactions of the Royal Society of London. A* 186 (1895): 123-164.

Richardson, D. E. "Review of power cylinder friction for diesel engines." *Journal of engineering for gas turbines and power* 122.4 (2000): 506-519.

Roelands, C. J. A., "Correlational aspects of the viscosity-temperature-pressure relationship of lubricating oils." Doctoral Thesis, Delft University of Technology, (1966).

Ruddy, B. L., Dowson, D., Economou, P. N., and Baker, A. J. S., "Piston-ring lubrication—part III. The influence of ring dynamics and ring twist." *ASME Energy Conservation through fluid film lubrication technology: Frontiers in research and design* (1979).

Ruddy, B. L., D. Dowson, and P. N. Economou. "A theoretical analysis of the twin-land type of oil-control piston ring." *Journal of Mechanical Engineering Science* 23.2 (1981): 51-62.

Sakhrieh, A., Abu-Nada, E., Al-Hinti, I., Al-Ghandoor, A., and Akash, B., "Computational thermodynamic analysis of compression ignition engine." *International Communications in Heat and Mass Transfer* 37.3 (2010): 299-303.

Sommerfeld, A. "The hydrodynamic theory of lubrication friction." *Math. And Phys* 50.1-2 (1904): 97-155.

Smedley, "Piston Ring Design for Reduced Friction in Modern Internal Combustion Engines", *Thesis, Massachusetts Inst. Technology, 2004*

Spencer, A. Almqvist, A. and Larsson, R., "A numerical model to investigate the effect of honing angle on the hydrodynamic lubrication between a combustion engine piston ring and cylinder liner." *Proceedings of the Institution of Mechanical Engineers, Part J: Journal of Engineering Tribology* 225.7 (2011): 683-689.

Spencer, A., Almqvist, A. and Larsson, R., "A semi-deterministic texture-roughness model of the piston ring–cylinder liner contact." *Proceedings of the Institution of Mechanical Engineers, Part J: Journal of Engineering Tribology* 225.6 (2011): 325-333.

Stachowiak, G. W. and Batchelor, A. W., "Engineering Tribology", 2<sup>nd</sup> Ed., *Butterworth-Heinemann Ltd* (2001)

Stokes, G. G., "Sound attenuation due to viscosity." *Trans. Camb. Phil. Soc* 8 (1845): 75-102

Takiguchi, M., Sasaki, R., Takahashi, I., Ishibashi, F., Furuhashi, S., Kai, R., and Sato, M., "Oil film thickness measurement and analysis of a three ring pack in an operating diesel engine." *SAE paper* (2000): 01-1787.

Taylor, C. M. "Automobile engine tribology—design considerations for efficiency and durability." *Wear* 221.1 (1998): 1-8.

Teodorescu, M., S. Balakrishnan, and H. Rahnejat. "Integrated tribological analysis within a multi-physics approach to system dynamics." *Tribology and Interface Engineering Series* 48 (2005): 725-737.

Tian, T., "Dynamic behaviours of piston rings and their practical impact. Part 1: ring flutter and ring collapse and their effects on gas flow and oil transport." *Proceedings of the Institution of Mechanical Engineers, Part J: Journal of Engineering Tribology* 216.4 (2002): 209-228.

Tian, T., "Dynamic behaviours of piston rings and their practical impact. Part 2: oil transport, friction and wear of ring/liner interface and the effects of piston and ring dynamics." *Proceedings of the Institution of Mechanical Engineers, Part J: Journal of Engineering Tribology* 216.4 (2002): 229-248.

Tian, T., Noordzij, L., Wong, V. W., and Heywood, J. B., "Modeling piston-ring dynamics, blowby, and ring-twist effects." *Journal of Engineering for Gas Turbines and Power* 120.4 (1998): 843-854.

Timoshenko, S., and D. H. Young. "Vibration Problems in Engineering. 1955." *Van Nostrana*.

Tomanik, Eduardo. "Piston ring conformability in a distorted bore." *SAE paper* 960356 (1996).

Tung, Simon C., and Michael L. McMillan. "Automotive tribology overview of current advances and challenges for the future." *Tribology International* 37.7 (2004): 517-536.

Uras, H. M. and Patterson, D. J., "Measurement of piston and ring assembly friction instantaneous IMEP method". *SAE Paper No. 830416*. (1983).

## References

---

Volterra, E., and J. D. Morell. "Lowest natural frequency of elastic arc for vibrations outside the plane of initial curvature." *Journal of Applied Mechanics* 28 (1961): 624.

Wang, T. M., R. H. Nettleton, and B. Keita. "Natural frequencies for out-of-plane vibrations of continuous curved beams." *Journal of Sound and Vibration* 68.3 (1980): 427-436.

Williams, H. E. "On the equations of motion of thin rings." *Journal of Sound and Vibration* 26.4 (1973): 465-488.

Wing, R. D., and Owen Saunders. "Oil film temperature and thickness measurements on the piston rings of a diesel engine." *Proceedings of the Institution of Mechanical Engineers* 186.1 (1972): 1-9.

## 9. Appendices

### 9.1. Appendix A – SAE technical paper

Baker, C. E., Rahmani, R., Theodossiades, S., Rahnejat, H., “Analytical Evaluation of Fitted Piston Compression Ring: Modal Behaviour and Frictional Assessment”, *SAE Technical Paper 2011-01-1535*, (2011).



## 9.2. Appendix B – STLE Annual Conference extended abstract

Baker, C. E., Rahmani, R., Theodossiades, S., Rahnejat, H., and Fitzsimons, B., “Thermo-Elastohydrodynamics of a Rough Piston Compression Ring-to-Cylinder Bore Conjunction,” *Proc. STLE 66th Annual Conference, Atlanta, GA, 15–19 May (2011)*.

### 9.3. Appendix C – ASME journal paper

Baker, C. E., Theodossiades, S., Rahnejat, H., and Fitzsimons, B., "Influence of In-Plane Dynamics of Thin Compression Rings on Friction in Internal Combustion Engines." *ASME Journal of Engineering for Gas Turbines and Power* 134 (2012): 092801.

